Katharina Goth

Highly Repetitive 2 µm Holmium Solid-State Lasers

Power Scaling, Mechanical Stability, and Nonlinear Conversion
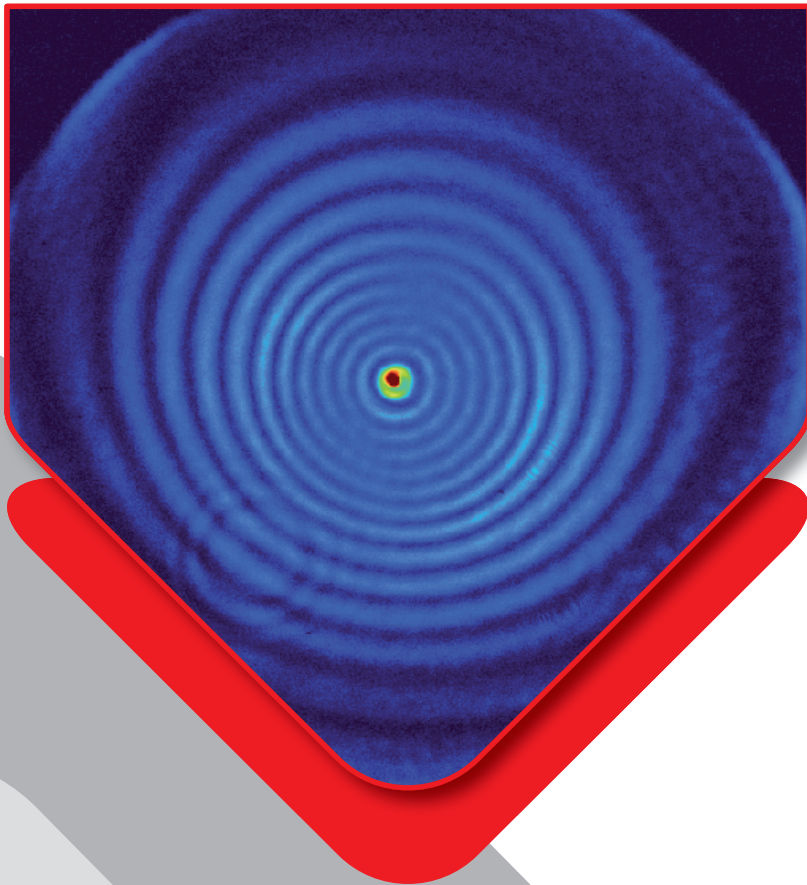

KIT
Karlsruher Institut für Technologie

Katharina Goth

Highly Repetitive 2 µm Holmium Solid-State Lasers

Power Scaling, Mechanical Stability, and Nonlinear Conversion

Lasers and Optronics:
Materials, Technologies and Applications
Volume 4.2024

Editor: Prof. Dr. rer. nat. habil. Marc Eichhorn

Professur für Optronik am
Karlsruher Institut für Technologie (KIT)

Fraunhofer-Institut für Optronik, Systemtechnik
und Bildauswertung (IOSB)

Highly Repetitive 2 µm Holmium Solid-State Lasers

Power Scaling, Mechanical Stability,
and Nonlinear Conversion

by
Katharina Goth

Karlsruher Institut für Technologie
Institut für Regelungs- und Steuerungssysteme

Highly Repetitive 2 µm Holmium Solid-State Lasers:
Power Scaling, Mechanical Stability, and Nonlinear Conversion

Zur Erlangung des akademischen Grades eines Doktors der Ingenieurwissenschaften von der KIT-Fakultät für Elektrotechnik und Informationstechnik des Karlsruher Instituts für Technologie (KIT) genehmigte Dissertation

von Katharina Leonie Goth, M.Sc.

Tag der mündlichen Prüfung: 23. Juli 2024
Hauptreferent: Prof. Dr. rer. nat. habil. Marc Eichhorn
Korreferent: Prof. Dr. rer. nat. Uli Lemmer

Highly Repetitive 2 µm Holmium Solid-State Lasers

Power Scaling, Mechanical Stability, and Nonlinear Conversion

Zur Erlangung des akademischen Grades eines

DOKTORS DER INGENIEURWISSENSCHAFTEN (Dr.-Ing.)

von der KIT-Fakultät für Elektrotechnik und Informationstechnik des

Karlsruher Instituts für Technologie (KIT)

angenommene

DISSERTATION

von

Katharina Leonie Goth, M.Sc.

geboren am 29.09.1994 in Freiburg im Breisgau

Tag der mündlichen Prüfung: 23.07.2024

Hauptreferent: Prof. Dr. rer. nat. habil. Marc Eichhorn

Korreferent: Prof. Dr. rer. nat. Uli Lemmer

Kurzfassung

Laser haben vielfältige Anwendungen, unter anderem in der Medizin, Messtechnik, Material-bearbeitung, Telekommunikation und Verteidigung. Je nach Anwendung variieren die spezifis-chen Anforderungen an die Laserquelle in Bezug auf die Laserparameter wie Leistung oder Emissionswellenlänge. In den letzten Jahrzehnten wurde ein hoher Aufwand für die Forschung und Entwicklung von Laserquellen betrieben, die im 1 µm-Bereich emittieren. Dies wurde durch ein starkes industrielles Interesse und die für bestimmte Anwendungen günstigen Eigenschaften der Lasermaterialien in diesem Bereich vorangetrieben. In jüngster Zeit hat auch die Forschung an Laserquellen im 2 µm-Bereich ein zunehmendes Interesse geweckt, da damit spezifische Absorptions- und Transmissionscharakteristiken von Materialien oder der Atmosphäre aus-genutzt werden können. Neben Anwendungen, die eine Ausbreitung im freien Raum erfordern, finden diese Laser auch eine Anwendung in der Materialbearbeitung oder Medizin, ebenso wie bei ihrer nichtlinearen Konversion in den mittleren Infrarotbereich.

Im 2 µm-Bereich wird derzeit sowohl an Faserlasern wie auch an Kristalllasern, jeweils dotiert mit Thulium- oder Holmium-Ionen, geforscht. Holmium-dotiertes Yttrium-Aluminium-Granat (Ho^{3+}:YAG) erweist sich auf dem Gebiet der Festkörperlaser aufgrund seines effizien-ten Pumpschemas, seiner langen Lebensdauer des oberen Zustands sowie der guten thermo-optischen Eigenschaften und des ausgereiften Herstellungsprozesses des Wirtsmaterials als besonders vielversprechend. Ein Großteil der Forschung hat sich dabei auf die Untersuchung der Materialeigenschaften, Lasern mit verschiedenen Resonatorgeometrien und Pulserzeu-gungsmechanismen sowie Laser-/Ver-stärker-Kombinationen zur Leistungssteigerung konzen-triert. Um die Forschung an Ho^{3+}:YAG-Lasern weiter voranzutreiben, können Konzepte, die sich bei anderen Materialien, beispielsweise Nd^{3+}:YAG, bewährt haben, auch auf Ho^{3+}:YAG-Laser angewendet werden. Hier sind eingehende Untersuchungen und Experimente erforderlich,

um festzustellen, ob die übertragenen Konzepte zu verbesserten Eigenschaften der Laserquellen führen.

In dieser Arbeit wird zunächst die Leistungsskalierung von Ho^{3+}:YAG-Lasern unter dem Gesichtspunkt eines verbesserten Temperaturmanagements innerhalb des Laserkristalls durch eine segmentierte Dotierung betrachtet. Das Ziel einer solchen segmentierten Dotierung besteht darin, eine gleichmäßigere Absorption des Pumplichts zu erzeugen, um niedrigere Spitzentemperaturen und damit auch geringere thermische Verspannungen zu erzeugen. In diesem Kontext werden segmentierte Kristalle theoretisch beschrieben, um mithilfe einer numerischen Optimierung ein optimales Design für sie zu finden. Obwohl mit dem segmentierten Kristall eine Reduktion der maximalen Kristalltemperatur gezeigt werden kann, wird im Gegensatz zu anderen in der Literatur untersuchten Lasermaterialien bei Ho^{3+}:YAG keine Verbesserung der Laserperformance festgestellt. Dies wird auf die im Vergleich zu Publikationen basierend auf Nd^{3+}:YAG-Kristallen deutlich niedrigeren Temperaturen im Laserkristall zurückgeführt, die aus den ausgezeichneten thermischen Eigenschaften von Ho^{3+}:YAG resultieren. Im Hinblick auf die Leistungsskalierung wird neben der segmentierten Kristalldotierung auch ein Laser-/Verstärkersystem untersucht. Bei der Untersuchung verschiedener Pumpschemen erweist sich das Kopumpen als das Pumpschema mit der höchsten differenziellen Effizienz von fast 70 %. Da die höchste Pumpleistung im beidseitig gepumpten Schema verfügbar ist, ermöglicht dies eine Skalierung der Ausgangsleistung um den Faktor 2 auf über 120 W und stellt somit einen vielversprechenden Ansatz dar, wenn sowohl eine Leistungsskalierung als auch eine Erhaltung der Strahlqualität gewünscht sind.

Neben der Leistungssteigerung wird auch die Verbesserung der mechanischen Stabilität durch die Verwendung von Porro-Prismen anstelle der Resonatorendspiegel untersucht, um so den Einsatz in anspruchsvollen Umgebungen zu ermöglichen. Die Untersuchung der Prismen zeigt, dass für einen Einsatz im Laserresonator eine hohe Qualität der Prismenkante ausschlaggebend ist. Zudem ist es essenziell, ein geeignetes Resonatordesign zu finden, welches zu den kleinen Modendurchmessern passt, die zum einen aufgrund der Quasi-Drei-Niveau-Eigenschaft des Laserkristalls und zum anderen aufgrund der Bedingung einer guten Strahlqualität erforderlich sind. Dazu wird in dieser Arbeit ein teleskopisches Design vorgeschlagen, wodurch der Laser bei deutlich höheren Ausgangleistungen als bisher in der Literatur gezeigt betrieben werden kann. Darüber hinaus vergrößert sich die Justagetoleranz bis zu einem Faktor von 200 im Vergleich zu einem als Referenz dienenden konventionellen Spiegelresonator.

Aufgrund der ausgezeichneten Eignung von Ho^{3+}:YAG-Lasern für das Pumpen von optisch parametrischen Oszillatoren basierend auf Zink-Germanium-Phosphid wird im letzten Teil der Arbeit ein solcher Oszillator ausgelegt und optimiert. Durch das Einfügen einer negativen Linse in den Resonator können Pump- und Resonatormode so aneinander angepasst werden, dass eine signifikante Verbesserung der Strahlqualität erzielt wird. Diese Strategie spielt vor allem bei der Verbesserung der Brillanz der optisch parametrischen Oszillatoren eine zentrale Rolle, insbesondere wenn Pumpquellen mit einer hohen Pulsenergie verwendet werden.

Abstract

Lasers have diverse applications including medicine, metrology, material processing, telecommunications, and defense. Depending on the application, the specific requirements for the laser source vary in terms of the laser parameters like power or emission wavelength. Driven by a high industrial interest and favorable properties of the laser materials emitting in the 1 µm range, a high effort has been devoted to the research and development of laser sources emitting in this region in the last decades. More recently, research on laser sources in the 2 µm range has gained increasing attention, as it allows for the exploitation of specific absorption and transmission characteristics of materials or the atmosphere. In addition to applications requiring free space propagation, these lasers also find applications in material processing or medicine, as well as in their nonlinear conversion to the mid-wave infrared range.

In the 2 µm range, research currently advances on both fiber and crystal lasers doped with thulium and holmium ions. Holmium-doped yttrium aluminum garnet (Ho^{3+}:YAG) is a particularly promising material in the field of solid-state lasers due to its efficient pumping scheme, its long upper-state lifetime as well as its excellent thermo-optic properties, and the mature manufacturing process of the host material. A significant part of the research has focused on the investigation of its material properties, lasers with different resonator geometries and pulse generation mechanisms as well as master oscillator power amplifier (MOPA) systems for power scaling. To further push the research on Ho^{3+}:YAG lasers forward, concepts proven successful with other laser materials, e.g. Nd^{3+}:YAG, can be applied to Ho^{3+}:YAG lasers. In-depth investigations and experiments are necessary to determine the extent to which these transferred concepts lead to improved properties of the laser sources.

In this work, the power scaling of Ho^{3+}:YAG lasers is initially investigated from the perspective of an improved temperature management within the laser crystal through a segmented doping

concentration. The goal of a segmented doping concentration is to achieve a more uniform absorption of the pump light, resulting in lower peak temperatures and reduced thermal stresses. In this context, segmented crystals are theoretically described to enable their optimal design through numerical optimization. Although a reduction in the maximum crystal temperature can be demonstrated with the segmented crystal, unlike experiments with other laser materials investigated in the literature, no improvement in laser performance is observed in the case of Ho^{3+}:YAG. This is attributed to the significantly lower temperatures in the laser crystal compared to publications based on Nd^{3+}:YAG crystals, resulting from the excellent thermal properties of Ho^{3+}:YAG. Regarding further power scaling, a MOPA system is investigated in addition to a segmented doping concentration. Among different pumping schemes, co-pumping proves to be the most efficient pumping scheme with the highest slope efficiency of almost 70 %. As the highest pump power is available in the dual-end-pumping scheme, this enables an output power scaling by a factor of 2 to over 120 W, making it the most promising approach when both power scaling and a beam quality preservation are desired.

In addition to power scaling, the improvement of the mechanical stability through the use of Porro prisms instead of the resonator end mirrors is investigated, which aims to enable the operation of the laser in demanding environments. The investigations of the prisms indicate that high-quality prism apexes are crucial for their use in laser resonators. It is also essential to find a suitable resonator design that matches the small mode diameters required due to both the quasi-three-level nature of the laser crystal and the requirement of a good beam quality. In this work, a telescopic design is proposed, which allows the laser to be operated at significantly higher output powers than previously shown in the literature. Furthermore, the alignment tolerance is enhanced by a factor of up to 200 compared to a conventional mirror resonator serving as a reference.

Due to the excellent suitability of Ho^{3+}:YAG lasers for pumping zinc germanium phosphide based optical parametric oscillators (OPOs), the last part of the thesis focuses on the design and optimization of such an oscillator. By inserting a negative lens into the resonator, the pump and resonator mode matching is improved, resulting in a significant enhancement in beam quality. This strategy plays a central role in improving the brightness of OPOs, especially when high-pulse-energy pump sources are used.

Contents

1   Introduction

Since the demonstration of the first ruby laser by Theodore Maimain in 1960, a wide variety of laser materials has been investigated, spanning the wavelength range from the ultraviolet over the mid-wave infrared (MWIR) region to the THz range [1]. Lasers have become an integral part of modern life with plenty of applications in the fields of medicine, material processing and manufacturing, optical metrology, lidar sensor technologies as well as everyday devices like laser printers, barcode readers, laser pointers, and the internet. In the last decades, a wide variety of laser gain media has been extensively studied, and driven by a substantial industrial interest, lasers emitting around 1 μm have been pushed to their limits [2]. This mainly encompasses Nd^{3+}- and Yb^{3+}-doped solid-state and fiber lasers, which find applications in laser drilling, welding, cutting, and marking, among other things [3–6]. Considering that 1 μm lasers have already become a mature technology, research on lasers in other wavelength ranges, particularly in the 2 μm region, becomes relevant not only due to scientific curiosity but also for other reasons.

The 2 μm range offers distinct properties that cannot be achieved with other wavelengths, due to specific transmission and absorption characteristics of the atmosphere and certain materials. Firstly, materials that are transparent around 1 μm can have absorption features around 2 μm, facilitating direct laser processing [7]. This, for example, applies to biological tissue or plastics, which become processable without absorptive additives in the material [8]. Secondly, free space applications including wind and chemical sensing, active imaging, or range finding, among others [9–11], can be realized with 2 μm lasers, as an atmospheric transmission window is located around 2.2 μm (see Figure 1.1). In addition, Rayleigh scattering is significantly diminished at the longer 2 μm wavelength, making these lasers especially well-suited for applications requiring long propagation paths through the atmosphere. In contrast to 1 μm lasers, using 2 μm lasers for free space applications comes with another advantage: their eye-safe
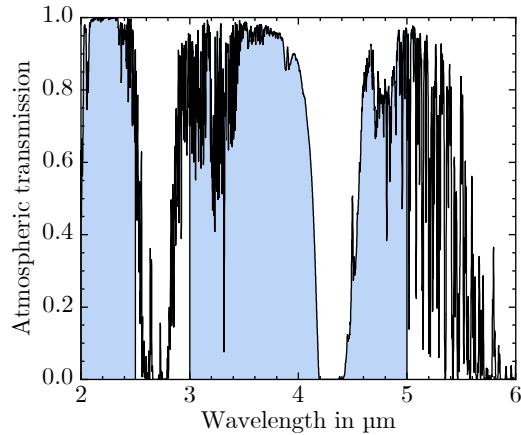
Figure 1.1: Atmospheric transmission in the 2–6 µm range. The data were produced by the IRTRANS4 program and obtained from the UKIRT worldwide web pages [17].

nature [12]. While 2 µm radiation is absorbed in the vitreous body of the eye, light from a 1 µm laser is absorbed in the retina, causing irretrievable damage [8]. Furthermore, 2 µm lasers serve as excellent pump sources for nonlinear down-conversion into the 3–5 µm range mainly for two reasons: Firstly, the converted light is entirely located in the 3–5 µm wavelength range, whereas with a 1 µm pump source only a portion of the converted light is in this wavelength range. Secondly, only 2 µm pump light enables the use of nonlinear crystals with a high nonlinear coefficient that are transparent over the entire 3–5 µm range but cannot be pumped with a 1 µm source due to strong absorption at this wavelength [13]. In addition to the 2 µm light, the 3–5 µm wavelength range is of particular interest for remote sensing, defense applications, and free space optical communications due to the atmospheric transmission window around 3–5 µm [14–16]. Figure 1.1 illustrates the atmospheric transmission from 2–6 µm, highlighting the transmission windows around 2.2 µm and 3–5 µm in blue.

Laser sources emitting around 2 µm are mainly Tm^{3+}- and Ho^{3+}-doped solid-state and fiber lasers. An advantage of Tm^{3+}-based lasers is their ability to be pumped with compact laser diodes, whereas Ho^{3+}-doped solid-state lasers stand out due to their significantly higher emission cross-section, making them well-suited for generating short pulses. This thesis focuses on holmium-doped yttrium aluminum garnet (Ho^{3+}:YAG) crystal lasers, as they have a number of favorable properties. Firstly, the host material yttrium aluminum garnet (YAG) exhibits excellent thermo-optic properties and benefits from a mature fabrication process [18]. Secondly,

the $^5I_8 \rightarrow {}^5I_7$ transition in Ho^{3+}:YAG lasers can be resonantly pumped by Tm^{3+}-doped lasers emitting at 1908 nm [19]. Due to a high quantum efficiency of around 91 %, the heat generation is significantly lower than, for example, in Nd^{3+}:YAG, which is typically pumped at 808 nm and emits at 1064 nm, resulting in a quantum efficiency of 76 %. In addition, a long upper-state lifetime of 7.8 ms, which is roughly an order of magnitude higher than in Nd^{3+} and Yb^{3+}, enables a high energy storage capacity, which is favorable for Q-switching [20]. These features make Ho^{3+}:YAG a promising candidate for the power and energy scaling in the 2 µm region. A challenge for the optimization of Ho^{3+}:YAG lasers is their quasi-three-level nature, which requires a pump threshold to be overcome prior to lasing due to reabsorption at the laser wavelength [20]. This necessitates small pump diameters to achieve high pump intensities and ensure an efficient operation, which leads to challenges that will be adressed later on in detail.

To provide context, a brief overview over the history of Ho^{3+}-based crystal lasers is given in the following passage. The first Ho^{3+}-doped flashlamp-pumped crystal laser was introduced as early as 1965 [21]. Up to now, flashlamp-pumped Ho^{3+}-doped lasers have widely been used in medical lasers [22]. However, their efficiency is limited due to an inefficient absorption. In addition to flashlamp-pumping, diode-pumping of Tm^{3+}-codoped Ho^{3+}:YAG lasers was investigated in the 1980s [23]. Due to detrimental interionic processes generating additional heat in these codoped crystals, direct pumping with Tm^{3+}-doped lasers paved the way for the further optimization of Ho^{3+}:YAG lasers [8, 19]. Over the past 20 years, significant progress has been made in the development of Ho^{3+}:YAG lasers. The following passage summarizes some of them with a particular focus on highly-repetitive systems. Notable achievements include an exceptional slope efficiency of 80 %, demonstrated by Mu et al. in a four-pass end-pumped continuous wave (CW) Ho^{3+}:YAG laser with an average output power of 18.7 W [24]. In terms of a high output power, Yao et al. achieved a CW output power of 142 W with a single crystal single-end-pumped by a 1931 nm Tm^{3+}-doped fiber laser, thus resulting in a comparably low slope efficiency of 56.7 % [25]. Duan et al. developed a more complex setup involving two slab crystals, both dual-end-pumped, and achieved an output power of 146 W [26]. In recent years, several Q-switched high-power lasers have been presented. With a single Ho^{3+}:YAG crystal in a double-pass pumping scheme, Lippert et al. demonstrated an average output power of 42 W at 45 kHz repetition rate in 2010 [27]. Two years later, Shen et al. further increased the output power to 58.7 W by employing a dual-end-pumping scheme with two Tm^{3+}-doped fiber lasers [28]. Further power scaling to an average output power above 100 W was achieved with the same pumping scheme by Duan et al. in 2018 [29] and by Liu et al. in 2021 [30]. The

highest Q-switched average output power of 141 W was achieved with the laser containing two dual-end-pumped slab crystals, producing 2.8 mJ pulses with a duration of 39 ns [26]. In terms of pulse energy scaling at high average output powers, Ganija et al. presented impressive results in a cryogenically cooled setup. At a repetition rate of 100 Hz, they achieved 80 ns pulses with an energy of 470 mJ, corresponding to an average power of 47 W [31].

The majority of lasers discussed in the previous passage adhere to conventional crystal and resonator designs. In particular with regard to more advanced designs that have already been investigated with other laser materials in the literature, there is a noticeable lack of research on Ho^{3+}:YAG lasers. This includes innovative techniques such as using crystals with a varying doping concentration along the crystal axis as well as the implementation of prism based resonators [32, 33]. The objective of this thesis is the investigation and optimization of highly-repetitive Ho^{3+}:YAG lasers, aiming for a near-diffraction-limited beam quality and a nonlinear conversion to the MWIR range. The focus is particularly on power scaling and enhancing the mechanical stability through novel approaches. Both theoretical considerations and experimental studies are employed to explore these approaches. This involves the numerical modeling of laser resonators, theoretical analysis of the novel components' properties, and characterizing the unique properties of these components in experiments. These characterizations are intended to provide insight into the optimal utilization of these new components in laser resonators.

After a thorough investigation of both the components and laser resonators, this thesis is intended to provide information on the following key points:

1. Strategies for power scaling of Ho^{3+}:YAG resonators with a near-diffraction-limited beam quality:
   For the power scaling, it is essential to understand the thermal properties inside the laser crystal and evaluate how an improved thermal management inside the crystal influences the performance of the laser. Additionally, the optical gain properties of a master oscillator power amplifier (MOPA) system are investigated to provide insight on the power scaling capability of such a system.

2. Increase of the mechanical stability by employing a prism based resonator design:
   The objective is to acquire a comprehensive understanding of the fundamental properties of Porro prisms in relation to their utilization in laser resonators to design resonators that are robust against mechanical instabilities.

3. Application of a suitable Ho^{3+}:YAG source for pumping a zinc germanium phosphide (ZGP) optical parametric oscillator (OPO):
   In addition to identifying optimal pump parameters, the objective is to thoroughly investigate the power scaling capabilities and beam quality of the OPO. Moreover, strategies for improving the resonator geometry with regard to an enhanced beam quality are examined.

Outline of the Thesis

In Chapter 2, the essential theoretical foundations that underly this thesis are established. It begins with providing a general overview of the laser principle, followed by an explanation of the properties of rare-earth doped crystal lasers and the generation of highly-repetitive Q-switched pulses using an acousto-optic modulator (AOM). Additionally, the theoretical framework for the nonlinear conversion into the MWIR range is established, encompassing the nonlinear wave equation and the working principle of OPOs.

In Chapter 3, the theoretical and experimental methods employed in this thesis are presented. Emphasis is set on the numerical simulation and the experimental determination of the thermal lens. Furthermore, the measurement devices and methods are described, and a comprehensive characterization of a Ho^{3+}:YAG resonator is conducted using these techniques. Finally, the thermal blooming of the pump beam is qualitatively investigated, as this effect can have a detrimental effect on the performance of the Ho^{3+}:YAG resonators.

Chapter 4 is dedicated to the power scaling of Ho^{3+}:YAG lasers. The investigation focuses on how an improved temperature management in the crystal offers opportunities for power scaling. Additionally, the power scaling is investigated in a MOPA setup, with a particular focus on investigating the optical gain properties.

In Chapter 5, Porro prisms are investigated theoretically and experimentally regarding their reflective properties and apex characteristics. Different Porro resonators are subsequently examined with a focus on the power scaling and the alignment tolerance.

Chapter 6 presents results on a ZGP OPO pumped by the laser investigated in Chapter 4. In addition to investigating the impact of different pump parameters on the performance of the OPO, a novel design is introduced to enhance the beam quality, thereby increasing the brightness of the coherent source.

Finally, Chapter 7 concludes with a summary of the key findings and provides indications for further research on Ho^{3+}:YAG lasers and their nonlinear conversion.

2 Theoretical Fundamentals

This chapter describes the theoretical background to understand crystal lasers and OPOs. It begins with an explanation of the basic laser principle in Section 2.1, followed by a more detailed view on holmium-doped crystal lasers in Section 2.2, including the development of energy levels, the laser rate equations, and thermal lensing. In particular, the quasi-three-level laser material Ho^{3+}:YAG is considered here. In Section 2.3, Q-switching is described as a method for generating pulses in the ns regime. Finally, fundamentals of OPOs as a way to convert the 2 μm laser radiation to the 3–5 μm spectral region are explained in Section 2.4 while setting the focus to the nonlinear crystal ZGP.

2.1 Basic Laser Principle

The laser principle is based on the optical amplification by stimulated emission (see Section 2.1.1). This requires an inversion in the laser medium (see Section 2.1.2), which is generated by pumping the laser medium.

2.1.1 Optical Amplification

The underlying principle of a laser (acronym for Light Amplification by Stimulated Emission of Radiation [34]) is based on the interaction of light with the energy levels of an atom, ion, or molecule. In 1958, Schawlow and Townes theoretically developed the principle of the laser, which emits radiation in the optical and infrared spectral range, based on the principle of a maser, which was first demonstrated in 1954 [35, 36]. In addition to stimulated emission, which amplifies the incoming photons, absorption and spontaneous emission play a central role in the
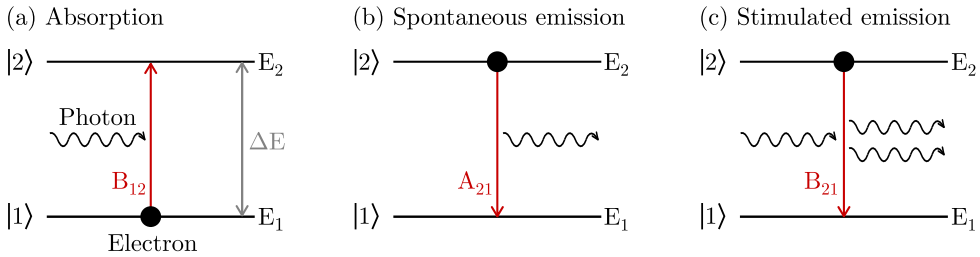
Figure 2.1: Schematic representation of the fundamental processes (a) absorption, (b) spontaneous emission, and (c) stimulated emission (adapted from [38]).

light-matter interaction. These three processes are closely related and all of them are relevant for the operation and understanding of a laser.

To explain these processes in detail, Figure 2.1 shows the interaction of a photon with a two-level system. The two-level system consists of two energetic states, the ground state $|1\rangle$ with energy E_1 and the excited state $|2\rangle$ with energy E_2. The incoming photon is assumed to have an energy of $\Delta E = h\nu = E_2 - E_1$. When the electron is in the ground state and the photon is incident on the two-level system, it is absorbed with a probability proportional to the Einstein coefficient B_{12} and the electron is transferred to the excited state (see Figure 2.1(a)) [37]. In the process of spontaneous emission, an electron in the excited state transitions to the ground state with a probability proportional to the Einstein coefficient A_{21} while a photon with energy ΔE is emitted from the two-level system. The cause for this process are vacuum fluctuations, which result directly from Heisenberg's uncertainty relation $\Delta E \cdot \Delta t \geq \frac{\hbar}{2}$ stating that a photon with energy $\Delta E = h\nu$ can exist for a short time period $\Delta t \leq \frac{1}{4\pi\nu}$. When a photon is incident on a two-level system in its excited state, stimulated emission occurs, which is described by the Einstein coefficient B_{21}. This means that the electron transitions to the ground state while emitting another photon that has identical properties (wavelength, phase, polarization, propagation direction) as the incident photon [37]. [38, 39]

In a laser, the stimulated emission process is used by placing a gain medium, which provides the necessary energy level structure and inversion, inside a resonator (see Figure 2.2). In the simplest case, a resonator consists of two parallel end mirrors, one of which is highly reflective (HR) and the other is partially reflective, therefore it is referred to as output coupling (OC) mirror. Initially, the gain medium spontaneously emits photons, which are reflected back and forth in the resonator. With each pass of the gain medium, they are amplified by stimulated emission

Figure 2.2: Schematic representation of a simple ideal laser resonator. The photons are amplified with each pass through the gain medium. The OC mirror is partially reflective which allows some of the photons to leave the resonator (adapted from [38]).

and a fraction is coupled out of the resonator at the OC mirror. In a stable laser operation, the photon density must reproduce itself after one cavity round-trip. Consequently, the following relation must hold true

$$R_{\mathrm{HR}} G^2 R_{\mathrm{OC}} (1 - \Lambda) = 1 \quad \Leftrightarrow \quad G = (R_{\mathrm{HR}} R_{\mathrm{OC}} (1 - \Lambda))^{-1/2} \ . \tag{2.1}$$

R_{HR} and R_{OC} are the reflectivities of the HR and OC mirror, G is the relative increase of the optical signal when the gain medium is passed once and Λ are all other parasitic cavity losses. [38]

When the incoming light passes the gain medium once, it experiences the effective gain

$$G(z, \lambda) = \exp\left(\sigma_{\mathrm{e}}(\lambda) N_2 - \sigma_{\mathrm{a}}(\lambda) N_1\right) \ . \tag{2.2}$$

In this equation, N_1 and N_2 are the population densities of the ground and excited state and $\sigma_{\mathrm{e}}(\lambda)$ and $\sigma_{\mathrm{a}}(\lambda)$ are the emission and absorption cross-sections at the wavelength λ, respectively. Amplification occurs when the condition $G > 1$ is met. This is equivalent to

$$N_2 > \frac{\sigma_{\mathrm{a}}(\lambda)}{\sigma_{\mathrm{e}}(\lambda)} N_1 \ . \tag{2.3}$$

In the simple two-level system from Figure 2.1, the absorption and emission cross-section are equal, simplifying Equation (2.3) to $N_2 > N_1$. This, however, can neither be fulfilled in thermal equilibrium nor under optical pumping, as the symmetry between stimulated emission and absorption is broken by spontaneous emission. [38] Consequently, more complex energy level schemes like three- and four-level systems are required to generate a population inversion and to achieve an optical amplification.

2.1.2   Creation of Population Inversion

Figure 2.3(a) depicts an exemplary three-level system with the energy states $|1\rangle$, $|2\rangle$, and $|3\rangle$ and the respective energies E_1, E_2, and E_3. Under optical pumping, electrons are excited to energy level $|3\rangle$ at a pump rate W_p. From level $|3\rangle$ to level $|2\rangle$, the electrons relax in a fast radiationless process via the interaction with phonons. Between the energy levels $|1\rangle$ and $|2\rangle$, three processes take place: stimulated emission with a probability W_{12}, reabsorption on the laser wavelength with a probability W_{21}, and spontaneous emission with a probability A_{12}. Because the lower laser level $|1\rangle$ is populated in this type of three-level laser, an inversion requires at least half of the total population to be pumped into the upper laser level. Additionally, spontaneous emission leads to a depopulation of the upper laser level, which is especially pronounced in laser media with short upper-state lifetimes. Therefore, high pump intensities are required, which decreases the overall optical efficiency of this type of laser. Furthermore, because the lower laser level is populated, reabsorption at the laser wavelength occurs, which, however, saturates in the case of high laser intensities. [38, 39]

Figure 2.3(b) shows a four-level system with the energy levels $|1\rangle$, $|2\rangle$, $|3\rangle$, and $|4\rangle$. When a four-level laser is pumped at a pump rate W_p, electrons are excited from level $|1\rangle$ to level $|4\rangle$. Between level $|4\rangle$ and level $|3\rangle$ and between level $|2\rangle$ and level $|1\rangle$, fast decays via phonon interactions take place. Therefore, level $|4\rangle$ and level $|2\rangle$ are assumed to be unpopulated, thus reabsorption on the laser wavelength (with a probability W_{23}) does not play a role in four-level lasers. Like in a three-level laser, three processes take place between the levels $|1\rangle$, $|2\rangle$, and $|3\rangle$: stimulated emission between level $|3\rangle$ and $|2\rangle$ with a probability W_{32} and spontaneous emission from level $|3\rangle$ to level $|2\rangle$ and to level $|1\rangle$ with probabilities A_{32} and A_{31}, respectively. Four-
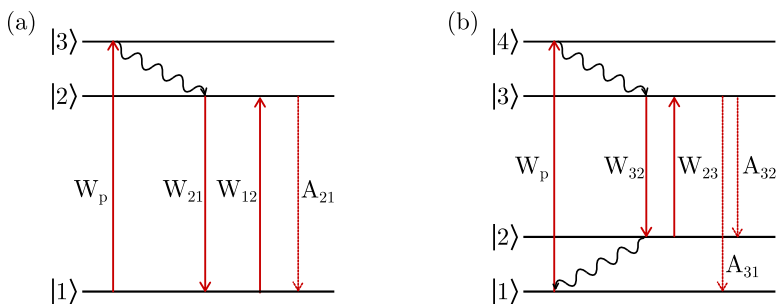

Figure 2.3: Energy level schemes of (a) an exemplary three- and (b) a four-level laser.

level lasers have a crucial advantage over three-level lasers: Because the lower laser level $|2\rangle$ is unpopulated, an inversion is created even for low pump intensities. Consequently, these laser media exhibit the lowest pump thresholds. [38, 39]

2.2 Ho^{3+}-Doped Crystal Solid-State Lasers

In this thesis, holmium-doped crystal lasers, which belong to the quasi-three-level lasers, are investigated. This section describes the development of energy levels when a crystal host material is doped with holmium ions in Section 2.2.1. Building on that, the basic laser rate equations are derived in Section 2.2.2, followed by an overview over the contributions that lead to thermal lensing in Section 2.2.3.

2.2.1 Development of Energy Levels

Because the preferred optical transitions occur in laser-active ions, they are embedded in a host material. As host material, glasses, ceramics, or crystals, which are characterized by a particularly regular environment, are used. The host material is either doped with divalent transition-metal ions or with trivalent rare-earth ions like Nd^{3+}, Tm^{3+}, Er^{3+}, or Ho^{3+} [40], which belong the chemical group of lanthanides [39]. The energy level splitting of transition-metal ions and rare-earth ions is fundamentally different, as the laser-active electrons are shielded from the electric field of the surrounding host to varying degrees: The laser-active electrons lie in outer shells in transition-metal ions, therefore experiencing a strong crystal field, whereas the influence of the crystal field is lower for lanthanides, as the laser-active ions are located on the inner shells [38]. As a consequence of the shielding, rare-earth ions have significantly longer upper level lifetimes compared to transition-metal ions. In the following section, the development of energy levels is discussed on the basis of a Ho^{3+}:YAG crystal.

A characteristic of lanthanides are the filled 4d, 5s, 5p, and 6s subshells. The optically active valence electrons are located in the 4f subshell [40]. The electron configuration of a holmium atom is given by [Xe].4f^{11}.6s^2 and changes to [Xe].4f^{10} in the trivalent Ho^{3+}-ion, thus ten electrons are in the 4f subshell. In the free ion, the energy level splitting into subshells results from the Coulomb interaction of the electrons with the atomic core [40]. Secondly, the interaction of the optically active electron with the non-centrosymmetric Coulomb potential
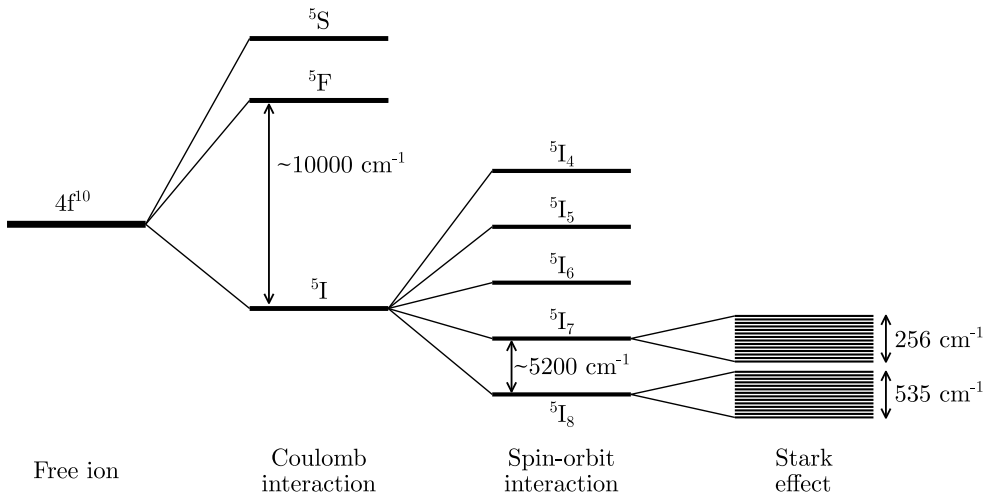
Figure 2.4: Development of the energy levels in a YAG crystal doped with holmium ions starting from the free ion (adapted from [40], numbers from [20]).

of all other electrons results in a further splitting of $\sim 10000\,\mathrm{cm}^{-1}$ as shown in Figure 2.4. Thirdly, the spin-orbit coupling splits the energy levels further. This relativistic effect describes the interaction of the orbital angular momentum of the electron and its spin. These three contributions are already present in a Ho^{3+}-ion in absence of external electric and magnetic fields. When the ion is brought into a crystalline material, for example YAG, a further energy level splitting can occur, which results from the static electric field at the particular lattice site inside the crystal host. This crystal field arises from the crystal structure of the respective host and the resulting asymmetric charge distribution in the direct vicinity of the doping site. The interaction between the Ho^{3+}-ion and the crystal field is called Stark effect [41]. In lanthanides, the interaction between the crystal field and the electron is, however, small because the optically active 4f electrons are shielded from the crystal field by electrons in the 5s and 5p subshells [40]. A consequence is the splitting into manifolds in which the energy difference between different levels is relatively small ($\sim 10\,\mathrm{cm}^{-1}$). Because at room temperature the thermal energy $k_\mathrm{B}T$, where $k_\mathrm{B} = 1.38 \cdot 10^{-23}\,\mathrm{J/K}$ is the Boltzmann constant, corresponds to $200\,\mathrm{cm}^{-1}$, the thermal population of the manifolds, which follows a Boltzmann distribution $\propto \exp\left(E/k_\mathrm{B}T\right)$, plays a significant role [20]. The relevant pump and laser transition considered in this work take place between the ${}^5\mathrm{I}_8$ and the ${}^5\mathrm{I}_7$ manifold (see Figure 2.4), which results in a quasi-three-level nature of the laser medium. In the following section, the laser rate equations are derived for this kind of medium.

2.2.2 Laser Rate Equations

Laser rate equations allow modeling the temporal dynamics of the energy level populations. Typically, simplified laser rate equations are set up for a quasi-three-level laser, which consider only absorption as well as spontaneous and stimulated emission processes, and already provide a detailed understanding of the expected dynamics. More complex processes like multiphonon transitions or energy transfer processes involving higher lying manifolds are not considered. Figure 2.5(a) shows the relevant $^5I_8$ and $^5I_7$ manifolds with a population density of N_1 and N_2, respectively. Additionally, the pump and laser transitions with wavelengths of λ_p and λ_s are indicated. Figure 2.5(b) resembles Figure 2.3(b). However, the labeling of the energy levels and transitions is adapted to a quasi-three-level laser, emphasizing the thermal population of the manifolds. In contrast to a four-level laser, level $|1, i\rangle$ is thermally occupied, therefore as with the three-level laser, a threshold must be exceeded prior to laser operation. In addition, reabsorption at the laser wavelength is relevant in this type of laser. This usually requires the use of small mode diameters.

To set up the laser rate equations, all relevant processes that change the population of a level have to be considered. The lower and upper pump level are labeled with $|1, m\rangle$ and $|2, n\rangle$, respectively, and the lower and upper laser level are labeled with $|1, i\rangle$ and $|2, j\rangle$, respectively. The letters i, j, m, n are also used to label the respective transitions. The population of the upper manifold is increased by pumping the laser medium at a pump rate $W_p = W_{mn}$ and by reabsorption at the laser wavelength with a probability of W_{ij}. It is decreased by stimulated emission to the lower laser level with a probability W_{ji} and by spontaneous emission to the
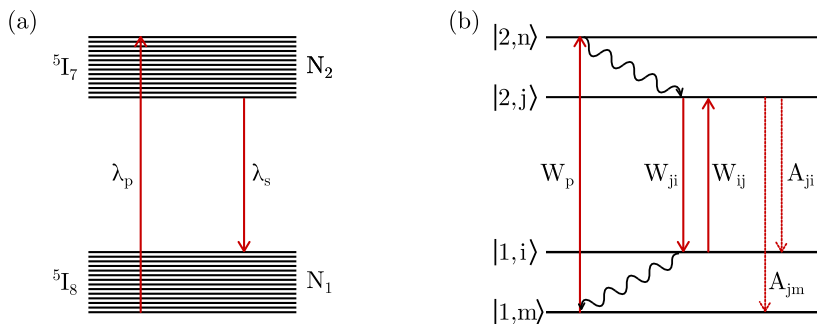

Figure 2.5: (a) Laser manifolds of a Ho^{3+}-doped laser crystal with the pump and laser transitions. (b) Energy levels and transitions in a quasi-three-level laser.

lower manifold with a rate A_{jm} and A_{ji}. The following equation describes the change in the population density of the upper manifold:

$$\frac{\partial N_{2j}}{\partial t} = W_\mathrm{p} N_{1m} + W_{ij} N_{1i} - (A_{jm} + A_{ji}) N_{2j} - W_{ji} N_{2j} \,. \tag{2.4}$$

The probabilities for stimulated emission and absorption are described by $W = \sigma I / E$ and the spontaneous emission rate is described by $A = \tau^{-1}$. τ is the lifetime of the upper manifold, I is the light intensity at the laser or pump wavelength, and E is the energy of a photon at the laser or pump wavelength. σ is the corresponding spectroscopic emission or absorption cross-section, which already includes the thermal population of the manifolds [20]. In this notation, it is not the specific energy levels but the entire manifold that is of interest, i.e. instead of considering the changes in population density of the levels $|2, j\rangle$ and $|2, n\rangle$, the change in population density of the entire manifold $|2\rangle$ is considered. Further, the following notation is used to specify the cross-sections: the subscripts e and a are used to label emission and absorption, respectively, and p and s are used to indicate the pump or laser wavelength. In this notation, the changes in the population density of the upper manifold N_2 and lower manifold N_1 averaged over the laser crystal axis are given by

$$\frac{\partial N_2}{\partial t} = \frac{\lambda_\mathrm{p}}{hc} I_\mathrm{p} \frac{\eta_\mathrm{abs}}{L} + \frac{\lambda_\mathrm{s}}{hc} I_\mathrm{s} (\sigma_\mathrm{as} N_1 - \sigma_\mathrm{es} N_2) - \frac{N_2}{\tau} \tag{2.5}$$

$$\frac{\partial N_1}{\partial t} = -\frac{\partial N_2}{\partial t} \,. \tag{2.6}$$

I_p is the pump intensity, η_abs is the pump absorption efficiency, and L is the crystal length. Because an inversion $\Delta N = N_2 - N_1$ is necessary for the operation of a laser, the change in the inversion is relevant and by subtracting Equation (2.5) from Equation (2.6), it is described by [38]

$$\frac{\partial \Delta N}{\partial t} = 2 \frac{\lambda_\mathrm{p}}{hc} I_\mathrm{p} \frac{\eta_\mathrm{abs}}{L} + c \left[(\sigma_\mathrm{as} - \sigma_\mathrm{es}) N - (\sigma_\mathrm{as} + \sigma_\mathrm{es}) \Delta N \right] \Phi - \frac{N + \Delta N}{\tau} \,. \tag{2.7}$$

$N = N_1 + N_2$ is the total population density of doping ions and $\Phi = \dfrac{\lambda_\mathrm{s}}{hc^2} I_\mathrm{s}$ is the photon density. In the cavity, the photon density is increased by stimulated emission and decreased by reabsorption, cavity losses, and output coupling. The change in photon density is described by [38]

$$\frac{\partial \Phi}{\partial t} = \frac{c}{2} \left[(\sigma_\mathrm{as} + \sigma_\mathrm{es}) \Delta N - (\sigma_\mathrm{as} - \sigma_\mathrm{es}) N \right] \Phi - \frac{\Phi}{\tau_\mathrm{c}} \,, \tag{2.8}$$

where τ_c is the cavity photon lifetime, which describes the time constant of cavity losses and output coupling. In stationary operation ($\frac{\partial \Delta N}{\partial t} = 0$ and $\frac{\partial \Phi}{\partial t} = 0$), Equations (2.7) and (2.8) have an analytical solution. When the pump intensity is not sufficiently high to compensate for the resonator losses, no laser field builds up, resulting in $\Phi = 0$. The solution to the rate equations is then given by [38]

$$\Delta N = 2\frac{\lambda_\text{p} \tau}{hc} I_\text{p} \frac{\eta_\text{abs}}{L} - N \, , \tag{2.9}$$

which reflects that states in the upper manifold are excited by pumping the laser medium during the upper level lifetime. As soon as the pump threshold is reached, the inversion stays constant, yielding the solution [38]

$$\Delta N = \Delta N_\text{th} = 2\frac{\lambda_\text{p} \tau}{hc} I_\text{th} \frac{\eta_\text{abs}}{L} - N \tag{2.10}$$

$$\Phi = \frac{\lambda_\text{p}}{hc^2} \frac{\eta_\text{abs}}{\ln G} \left(I_\text{p} - I_\text{th} \right) \, , \tag{2.11}$$

where I_th is the pump intensity that is required to reach the laser threshold. Overall, Equations (2.9)-(2.11) are summarized as follows: When the pump intensity of a quasi-three-level laser medium is increased, the inversion increases linearly at first while no photon field builds up because the overall cavity losses are too high. Above the pump threshold, the photon field increases linearly with increasing pump intensity while the inversion remains constant at its threshold value.

The laser rate equations (2.7) and (2.8) will again play a role for the Q-switching theory in Section 2.3 and for the fundamental behavior of an amplifier in Section 4.3.1.

2.2.3 Thermal Lensing

In bulk solid-state lasers, the term thermal lensing describes the lensing effect due to a lateral temperature gradient in the laser crystal. This effect is called the thermo-optic effect. The temperature gradient is accompanied by thermally induced birefringence due to the photoelastic effect and the bulging of the crystal end faces, which has an additional lensing effect. In this section, the heat generation mechanism is briefly discussed at first, followed by the derivation of the temperature profile in a cylindrical crystal for different pumping schemes. The thermo-optic

and photoelastic effect are then discussed and finally, end face bulging is described in more detail to derive the focal length of the thermal lens.

Heat Generation Mechanisms

When a laser crystal is pumped, heat is created in the crystal due to different contributions. In general, heat is generated by the emission of phonons. The following contributions lead to phonon emissions in the crystal:

1. Quantum defect between the pump wavelength λ_p and the laser wavelength λ_s: Phonon relaxation between the upper pump and laser level and between the lower laser and pump level contribute to the heat generation in the laser medium. A measure of this is the quantum defect $1 - \frac{\lambda_p}{\lambda_s}$ between the pump and the laser wavelength [42–44].

2. Quantum defect between the pump wavelength λ_p and the fluorescence wavelength λ_f: Next to the laser transition, fluorescence is present in a pumped crystal and consequently the quantum defect $1 - \frac{\lambda_p}{\lambda_f}$ between the pump and the fluorescence wavelength is another measure for the heat generation via phonon relaxations [42–44].

3. Multiphonon relaxation: Multiple phonons can be emitted to bridge the transition from a higher lying manifold to a manifold with a lower energy. However, this process is relatively unlikely, as several phonons are involved. For example, in YAG, the maximum phonon energy is $700\,\mathrm{cm}^{-1}$, therefore at least seven phonons would be required to bridge the energy gap between the $^5I_7$ and the $^5I_8$ level [20].

4. Upconversion: Upconversion is an interionic process that describes the energy transfer in which one ion transitions from a state with a lower energy to a state with a higher energy, facilitated by the energy release from another ion transitioning from a higher energy state to a state with a lower one. In holmium-doped solid-state lasers, typically the two ions are initially in the $^5I_7$ state and one ion transitions to the $^5I_8$ state while the other one is upconverted to the $^5I_5$ state. From the $^5I_5$ state, multiphonon relaxation into the lower lying manifolds creates additional heat in the crystal [45]. Because two ions are involved, the probability of this process increases with the doping concentration, especially when doping concentrations higher than $1\,\%$ are used [46, 47].

5. Background absorption due to crystal impurities: Impurities in the crystal lead to a background absorption at the pump, laser, or fluorescence wavelength [43]. If the absorbed energy is not released through radiative transitions, it is released by interactions with the crystal lattice through phonons, resulting in the generation of heat.

In the end, all these processes originate from the absorption of the pump light. Thus, the thermal power P_{therm}, which is created in the crystal, is expressed as

$$P_{\text{therm}} = \eta_{\text{th}} P_{\text{abs}} \,.$$ (2.12)

η_{th} is the fractional thermal loading and P_{abs} is the absorbed pump power [42, 44].

Temperature Distribution in the Crystal

The previously described heat generation mechanisms lead to a temperature distribution $T(\vec{r})$ in the laser crystal, which is derived by the steady-state heat equation [48]

$$\nabla \cdot (\lambda_{\text{th}}(T) \nabla T(\vec{r})) = -q(\vec{r}) \,.$$ (2.13)

$q(\vec{r})$ is the thermal power created at a position $\vec{r}$ in a unit volume of the crystal, leading to the temperature change. Because the laser crystals used in this thesis have a cylindrical shape with length L and radius R_0, the heat equation is solved in cylindrical coordinates. Under the simplifications that the thermal conductivity λ_{th} is temperature-independent and constant, the heat load $q(\vec{r}) = q = \dfrac{P_{\text{therm}}}{\pi R_0^2 L}$ is constant, and there is no heat transport along the axial direction, it transforms into [39]

$$\frac{\partial^2 T(r)}{\partial r^2} + \frac{1}{r} \frac{\partial T(r)}{\partial r} = -\frac{q}{\lambda_{\text{th}}} \,.$$ (2.14)

This equation is solved by using the ansatz of a parabolic temperature distribution and the boundary condition that the temperature at the rod surface is $T(R_0)$. It holds [39]

$$T(r) = T(R_0) + \frac{q}{4\lambda_{\text{th}}} (R_0^2 - r^2) \,.$$ (2.15)

However, a constant heat load would correspond to a uniform longitudinal pump distribution in the crystal, which would only be a good approximation in the case of flashlamp-pumping [49]. In this work, however, the crystals were end-pumped with a Gaussian beam with a $1/\text{e}^2$ beam
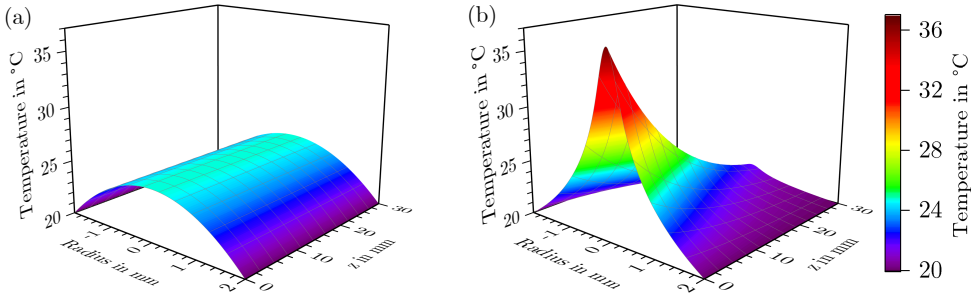
Figure 2.6: Exemplary temperature distribution in a cylindrical laser crystal assuming (a) a constant heat load and (b) a non-uniform pump distribution resulting from end-pumping.

radius ω_{p}. Due to the exponential axial absorption, Innocenzi et al. demonstrated that the temperature distribution for an end-pumping scheme is [50]

$$T(r, z) = T(R_0) + \frac{\alpha \eta_{\mathrm{th}} P_0}{4 \pi \lambda_{\mathrm{th}}} \mathrm{e}^{-\alpha z} \left[\ln \left(\frac{R_0^2}{r^2} \right) + E_1 \left(\frac{2 R_0^2}{\omega_{\mathrm{p}}^2} \right) - E_1 \left(\frac{2 r^2}{\omega_{\mathrm{p}}^2} \right) \right]. \tag{2.16}$$

α is the absorption coefficient and $P_0 = \dfrac{P_{\mathrm{abs}}}{1 - \mathrm{e}^{-\alpha L}}$ is the incident pump power. $E_1(x) = \int_x^\infty \mathrm{e}^{-t} t^{-1} \mathrm{d}t$ is the exponential integral function [51]. Figure 2.6 shows a comparison of the two temperature distributions. In the case of a constant heat load, the temperature does not change along the crystal axis and the maximum temperature is lower as compared to the case of Gaussian end-pumping. The temperature distribution in the case of Gaussian end-pumping is characterized by a high peak temperature at the front of the crystal and the temperature decreases while moving along the crystal axis.

A consequence of the temperature distribution are the thermo-optic effect, the photoelastic effect, and the bulging of the crystal end faces, which are discussed in the following sections.

Thermo-Optic Effect

The temperature distribution in the crystal directly leads to a change in refractive index $\Delta n(r)_{\mathrm{T}}$, which is known as the thermo-optic effect. In the case of a parabolic temperature distribution, it is given by [39]

$$\Delta n(r)_T = \frac{\partial n}{\partial T} \cdot (T(r) - T(0)) = -\frac{\eta_{\text{th}} P_{\text{abs}}}{4\lambda_{\text{th}} \pi R_0^2 L} \frac{\partial n}{\partial T} r^2 \,. \tag{2.17}$$

In the case of end-pumping with a Gaussian beam, however, the change in refractive index depends on the axial position and is given by

$$\Delta n(r,z)_T = -2\frac{\eta_{\text{th}} \alpha P_0}{4\lambda_{\text{th}} \pi \omega_{\text{p}}^2} e^{-\alpha z} \frac{\partial n}{\partial T} r^2 \,. \tag{2.18}$$

To derive this equation, the temperature distribution given in Equation (2.16) was developed into a power series and it was used that the rod radius is larger than the pump radius ($R_0 > \omega_{\text{p}}$), which is a good approximation for $r < \omega_{\text{p}}$ [50].

Photoelastic Effect

As a further consequence of the temperature distribution, the crystal expands thermally, which induces stress. This effect is called the photoelastic effect. The induced stress causes strain, which in turn changes the refractive index. Stress and strain are linked by Hooke's law [52]

$$\sigma_{ij} = c_{ijkl}\epsilon_{kl} \,, \tag{2.19}$$

where σ is the stress tensor, ϵ is the strain tensor, and c is the elasticity tensor. In the case of isotropic crystals, which is valid for YAG, symmetries reduce the number of elements. In this work, long and thin end-pumped crystals are considered. For these, the plane strain approximation is used in which $\epsilon_{zz} = \epsilon_{xz} = \epsilon_{yz} = 0$ holds. In this assumption, the axis along which the light propagates is long compared to the other dimensions of the crystal and only displacements parallel to the cross-section of the crystal are assumed [52]. Under the assumption of the parabolic temperature distribution, the stress components σ_r, σ_φ, and σ_z show a parabolic dependence of the radius as well [39]. The strains induced by these stresses lead to a change in the impermeability tensor [39]

$$\Delta B_{ij} = p_{ijkl}\epsilon_{kl} \,, \tag{2.20}$$

where p_{ijkl} are the elasto-optical coefficients. From the change in impermeability, a change in refractive index results. In the case of a cubic YAG crystal, the spherical optical indicatrix

transforms into an elliptical indicatrix under stress exposure. For the change of the refractive index in radial and tangential direction, respectively, it follows [39]

$$\Delta n(r)_{r,\varphi} = -\frac{1}{2} n_0^3 \Delta B_{r,\varphi} = -\frac{1}{2} n_0^3 \frac{\alpha_{\text{th}} q}{\lambda_{\text{th}}} C_{r,\varphi} r^2 \,, \tag{2.21}$$

where $C_{r,\varphi}$ are the photoelastic constants that depend on the elasto-optical coefficients [39]. The refractive index difference $\Delta n(r)_r - \Delta n(r)_\varphi$ indicates that thermally induced birefringence is present [39]. When a polarizer is included in a laser resonator, the thermally induced birefringence results in depolarization losses [44].

Bulging of the End Faces

An effect that further contributes to the formation of a thermal lens is the end face bulging. Because the end faces are not constrained, they elongate due to the internal stresses in the crystal. The elongation is expressed as

$$l(r) = l_0 + \alpha_{\text{th}} l_0 \left(T(r) - T(0) \right) \,, \tag{2.22}$$

where l_0 is the length of the elongation. From this, an end face curvature $R = -\left(\frac{\mathrm{d}l}{\mathrm{d}r} \right)^{-1}$ is calculated, resulting in a focal length of [53]

$$f_{\text{EF}} = \frac{R}{2(n_0 - 1)} = \frac{\lambda_{\text{th}}}{\alpha_{\text{th}} q(n_0 - 1) l_0} \,. \tag{2.23}$$

Total Focal Length of the Thermal Lens

Both the thermo-optic and the photoelastic effect cause a parabolic change in refractive index in the radial direction of the crystal, which induces a phase shift [50]

$$\Delta \phi(r) = \int_0^L k \Delta n(r) \mathrm{d}z = kL \left(\frac{q}{4\lambda_{\text{th}}} \frac{\partial n}{\partial T} + \frac{1}{2} n_0^3 \frac{\alpha_{\text{th}} q}{\lambda_{\text{th}}} C_{r,\varphi} \right) r^2 \tag{2.24}$$

on the light with wave number $k = 2\pi/\lambda$ that passes the laser crystal. Comparing this to the phase shift $\Delta \phi_f = \frac{kr^2}{2f}$ that light experiences when passing a thin lens [54], a focal length of the thermal lens [39]

$$f_n = \frac{\lambda_{\text{th}}}{qL} \left(\frac{1}{2} \frac{\partial n}{\partial T} + \alpha_{\text{th}} n_0^3 C_{r,\varphi} \right)^{-1} \qquad (2.25)$$

is concluded. In combination with the focusing effect due to the bulging of the end faces, a total thermal lens of [39]

$$f_{r,\varphi} = \left(\frac{1}{f_n} + \frac{1}{f_{\text{EF}}} \right)^{-1} = \frac{\lambda_{\text{th}}}{qL} \left(\frac{1}{2} \frac{\partial n}{\partial T} + \alpha_{\text{th}} n_0^3 C_{r,\varphi} + \frac{\alpha_{\text{th}}(n_0 - 1)l_0}{L} \right)^{-1} \qquad (2.26)$$

results. Because the focal length of the thermal lens is different for the radial and the tangential direction, the focal lengths are different for horizontally and vertically polarized light and they further depend on the position in the crystal. As a consequence, when the laser is operated with a linearly polarized output, the thermal lens leads to a bifocusing, which finally results in an astigmatic beam. For a YAG crystal, $f_\varphi / f_r = 1.2$ has been calculated [39]. In the case of Gaussian end-pumping, the parabolic temperature profile is only an approximation valid for $r < \omega_{\text{p}}$. For $r > \omega_{\text{p}}$, however, the temperature distribution and the resulting refractive index distribution are not parabolic anymore, which leads to higher-order terms in the thermal lens that cannot be compensated for. Finally, this leads to a degrading beam quality [55].

2.3 Generation of ns Pulses by Active Q-Switching

For many applications, laser pulses are required instead of a laser in CW operation, as for a short amount of time significantly higher intensities can be achieved due to the pulse dynamics. Depending on the required pulse length, different pulse generation mechanisms exist. For the generation of pulses in the ns regime, Q-switching is a suitable technique. A description of the active Q-switching process is given in Section 2.3.1. As in this thesis a highly repetitive Q-switched laser was investigated, characteristics of highly repetitive Q-switching are explained in Section 2.3.2. Section 2.3.3 describes the working principle of active Q-switching with an AOM.

2.3.1   Description of the Q-Switching Process

Q-switching is based on the modulation of cavity losses by switching the cavity between a low and a high quality factor Q. The Q-factor of a resonator is defined as

$$Q = 2\pi \frac{E_{st}}{E_d} \, ,$$

(2.27)

where E_{st} is the energy stored in the cavity and E_d is the dissipated energy per oscillation period [39]. For optical resonators, the Q-factor can be expressed as [39]

$$Q \approx 2\pi\nu_0 \frac{T_{rt}}{T_{OC} + \Lambda} \, ,$$

(2.28)

where ν_0 is the oscillation frequency and $T_{rt} = 2L/c$ is the resonator round-trip time. An increase in the cavity losses Λ therefore results in a lower Q-factor. In the first Q-switching phase, the resonator losses are kept at a high level such that the gain in the laser medium cannot compensate for the cavity losses. However, this time interval is used to store energy in the gain medium by optical pumping, therefore to create a high inversion. In the second Q-switching phase, the cavity losses are quickly reduced, allowing a photon field to build up inside the cavity in a short amount of time. The photon field depletes the inversion, thus limiting the further increase in the photon field. Consequently, a short pulse is generated. [38, 39]

In the following paragraphs, the Q-switching process is described by solving the rate equations introduced in Section 2.2.2 for the cavity states with a low and a high Q-factor.

1. Low Q-Factor

At a low Q-factor, the gain in the laser medium cannot compensate for the cavity losses. Thus, apart from spontaneous emission, no photon field is present in the resonator during the pump phase ($\Phi = 0$) and consequently the rate equation (2.7), describing the inversion in the laser medium, simplifies to [38]

$$\frac{\partial \Delta N}{\partial t} = R_p - \frac{N + \Delta N}{\tau} \, ,$$

(2.29)

where $R_\mathrm{p} = 2\dfrac{\lambda_\mathrm{p}}{hc} I_\mathrm{p} \dfrac{\eta_\mathrm{abs}}{L}$ is the pump rate. In this phase, the inversion builds up and is only decreased by losses due to spontaneous emission. The differential equation is solved by [38]

$$\Delta N(t) = R_\mathrm{p}\tau(1 - \mathrm{e}^{-t/\tau}) - N \,. \tag{2.30}$$

When $t \to \infty$, the inversion saturates to $\Delta N_\infty = R_\mathrm{p}\tau - N$. Consequently, when the pump phase is too long, the inversion saturates and the pumping process becomes inefficient.

2. High Q-Factor

A high Q-factor of the resonator is achieved by drastically decreasing the resonator losses. As a consequence, the photon field starts to build up from vacuum fluctuations, which trigger spontaneous emission. The inversion directly after the pump phase is the initial inversion ΔN_i. To calculate characteristic pulse parameters like the peak power, pulse width, and pulse energy, the rate equations (2.7) and (2.8) are considered neglecting spontaneous emission, as it is small compared to the photon field during the pulse. Thus, they are given by [38]

$$\frac{\partial \Delta N}{\partial t} = c\left[(\sigma_\mathrm{as} - \sigma_\mathrm{es})\,N - (\sigma_\mathrm{as} + \sigma_\mathrm{es})\,\Delta N\right]\Phi \tag{2.31}$$

$$\frac{\partial \Phi}{\partial t} = \frac{c}{2}\left(\sigma_\mathrm{as} + \sigma_\mathrm{es}\right)\left(\Delta N - \Delta N_\mathrm{th}\right)\Phi \,. \tag{2.32}$$

By dividing Equation (2.31) by Equation (2.32) and integrating the resulting equation, an approximate dependence between the photon field and the inversion during the pulse is analytically derived [38]:

$$2\Phi \approx \Delta N_\mathrm{i} - \Delta N + \left(\frac{\sigma_\mathrm{as} - \sigma_\mathrm{es}}{\sigma_\mathrm{as} + \sigma_\mathrm{es}}N - \Delta N_\mathrm{th}\right)\ln\left(\frac{\Delta N_\mathrm{i} - \frac{\sigma_\mathrm{as} - \sigma_\mathrm{es}}{\sigma_\mathrm{as} + \sigma_\mathrm{es}}N}{\Delta N - \frac{\sigma_\mathrm{as} - \sigma_\mathrm{es}}{\sigma_\mathrm{as} + \sigma_\mathrm{es}}N}\right) \,. \tag{2.33}$$

By introducing $\Delta N' = \Delta N - \dfrac{\sigma_\mathrm{as} - \sigma_\mathrm{es}}{\sigma_\mathrm{as} + \sigma_\mathrm{es}}N$ and exploiting that the photon field is zero when the inversion has reached its final value, from Equation (2.33) follows that [38]

$$\frac{\Delta N_\mathrm{f}'}{\Delta N_\mathrm{i}'} = 1 - \frac{1}{r}\ln\left(\frac{\Delta N_\mathrm{i}'}{\Delta N_\mathrm{f}'}\right) \,. \tag{2.34}$$

Furthermore, the pump parameter $r = \Delta N_\mathrm{i}'/\Delta N_\mathrm{th}' \approx P_\mathrm{p}/P_\mathrm{th}$ has been introduced. From Equation (2.34) follows that the Q-switching process depends on the initial inversion in the laser medium and the threshold of the laser medium, which contains the cavity parameters. [38]

The pulse peak power, pulse energy, and pulse duration are derived by using Equations (2.33) and (2.34). The photon field is amplified until the inversion has decreased to its threshold value, where the photon field reaches its maximum value. By substituting ΔN_th into Equation (2.33), the maximum photon field density $\hat{\Phi}$ is derived and the pulse peak power results [38]:

$$\hat{P} = \frac{h\nu}{\tau_\mathrm{c}}\hat{\Phi}V = \frac{r - 1 - \ln r}{2}\Delta N_\mathrm{th}'\frac{h\nu}{\tau_\mathrm{c}}V \,. \tag{2.35}$$

The peak power increases with an increasing difference between the initial and the threshold inversion and with a decreasing cavity photon lifetime. A high gain and a short resonator length contribute to a short cavity photon lifetime τ_c. The extracted energy of the pulse is given by

$$E_\mathrm{s} = \frac{1}{2}h\nu V\left(\Delta N_\mathrm{i} - \Delta N_\mathrm{f}\right) \tag{2.36}$$

The factor $\frac{1}{2}$ is introduced because each excitation is counted twice in the inversion ΔN. Assuming a temporal Gaussian pulse shape, the approximate pulse width is finally given by

$$t_\mathrm{p} = 2\sqrt{\frac{\ln(2)}{\pi}}\frac{E_\mathrm{s}}{\hat{P}} \approx 0.94\frac{E_\mathrm{s}}{\hat{P}} \,. \tag{2.37}$$

In the next paragraph, the time dependence of the photon field and the inversion are discussed.

Temporal Dynamics

As the dependence of photon field and inversion is known from Equation (2.33), the time dependence of the inversion and the photon field is calculated by substituting Φ by $\Phi(\Delta N)$ in Equation (2.31) and ΔN by $\Delta N(\Phi)$ in Equation (2.32), respectively. The solution to the resulting differential equations can be calculated numerically. [56]

The pulse build-up, however, can be derived analytically. This phase describes the phase until the photon field reaches the value of the photon field in CW operation. Because in Q-switched operation considerably higher values are expected from the peak photon field, it is assumed that,
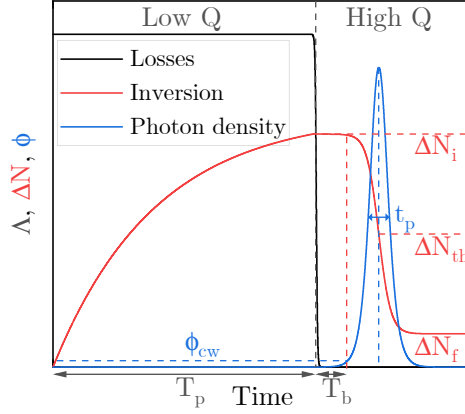
Figure 2.7: Temporal evolution of the cavity losses (black), the inversion in the laser medium (red), and the photon field (blue).

as long as the photon field is below its CW value, the inversion is not depleted ($\frac{\partial \Delta N}{\partial t} = 0$). With this approximation, the rate equation and its solution for the photon field are given by [38]

$$\frac{\partial \Phi}{\partial t} = \frac{1}{\tau_\text{c}}(r-1)\Phi \qquad \Rightarrow \qquad \Phi(t) = \Phi_0 \text{e}^{(r-1)\frac{t}{\tau_\text{c}}} . \tag{2.38}$$

Φ_0 is the noise photon density. Figure 2.7 shows the temporal evolution of the cavity losses, the inversion in the laser medium, and the photon field. During the pump phase T_p, the inversion builds up to its initial value ΔN_i. For reasons of simplicity, no pumping is assumed to be present in the high Q-factor phase. When the cavity losses are decreased, the pulse begins to grow exponentially from noise. The pulse-build up time T_b is defined as the time that the photon field needs to reach its CW value Φ_cw. Because the photon field is increasing, the inversion gets more and more depleted resulting in a decreasing gain. When the inversion falls below the threshold inversion ΔN_th, the photon field has reached its maximum value and starts to decrease due to resonator and output coupling losses. When the photon field has decreased to zero, a final inversion ΔN_f remains in the laser medium. [38]

2.3.2 Highly Repetitive Q-Switching

The description in Section 2.3.1 has so far only considered the generation of one pulse. When the losses are modulated with a repetition frequency ν_rep, pulses are generated repetitively. In

this regime, the final inversion after each pulse equals the initial inversion before the next pulse. Based on this consideration, the measurable pulse parameters depending on the repetition rate can be calculated. Two limiting cases are now considered.

In the case of low repetition rates, $\nu_{\text{rep}} \ll \tau^{-1}$ holds. For Ho^{3+}:YAG, τ^{-1} approximately equals 128 Hz. In this limit, the initial inversion $\Delta N_{\text{i}}'$ approximately equals the maximum inversion $\Delta N_{\infty}'$. As the initial inversion is constant in this case and the threshold inversion depends on the resonator geometry, a constant final inversion results in this case. Consequently, the pulse duration, the pulse energy, and the pulse peak power are constant as well. The average power

$$\langle P \rangle = E_{\text{s}} \nu_{\text{rep}} \tag{2.39}$$

increases linearly with increasing repetition rate. [38]

In the case of high repetition rates, $\nu_{\text{rep}} \gg \tau^{-1}$ holds. In this regime, the initial, threshold and final inversion are approximately equal considering that the maximum inversion is much larger. Furthermore, the average output power is constant ($\langle P \rangle \approx \text{const.}$), which is why this regime is called the quasi-continuous regime. Consequently, the pulse energy is $E_{\text{s}} \propto 1/\nu_{\text{rep}}$. The pulse width is given by [38]

$$t_{\text{p}} \propto \frac{\nu_{\text{rep}}}{\Delta N_{\infty}'} \, , \tag{2.40}$$

resulting in a pulse peak power of [38]

$$\hat{P} \approx \frac{E_{\text{s}}}{t_{\text{p}}} \propto \frac{\langle P \rangle \Delta N_{\infty}'}{\nu_{\text{rep}}^2} \, . \tag{2.41}$$

The limit of high repetition rates is investigated in this thesis.

2.3.3 Realization of Active Q-Switching with an AOM

Q-switching can be realized with active components like an AOM or electro-optic modulator (EOM) or passive components like saturable absorbers. In active Q-switching, the cavity losses are modulated actively, whereas with passive Q-switches, the switching is dependent on the photon field in the cavity [39]. In this thesis, active Q-switching was realized by using

an AOM. Compared to AOMs, EOMs exhibit a faster switching behavior, which may be a requirement for specific applications. However, high voltages must be applied to the EOMs to achieve the desired switching behavior, which requires careful handling. Q-switching with an AOM, on the other hand, is less complex in terms of the required driver, thus it is less space consuming, which can be a criterion for some applications.

The working principle of an AOM is based on the acousto-optic effect, which describes the modulation of the refractive index by an acoustic wave sent through the material. Typical acousto-optic materials are fused silica, lithium niobate (LiNbO$_3$), lead molybdate (PbMoO$_4$), and tellurium dioxide (TeO$_2$), which was used in this thesis [39]. The temporal modulation of cavity losses with an AOM is realized by periodically applying a radio frequency signal to a piezoelectric transducer, which generates the acoustic wave in the acousto-optic material. This acoustic wave causes a modulation of the refractive index along the traveling direction of the acoustic wave z, which is given by [39]

$$n(z,t) = n_0 + \Delta n_0 \sin\left(\omega_\mathrm{a} t - k_\mathrm{a} z\right) . \tag{2.42}$$

n_0 is the unperturbed refractive index of the acousto-optic material, Δn_0 is the amplitude of the refractive index modulation, ω_a is the angular frequency, and k_a is the wave vector of the acoustic
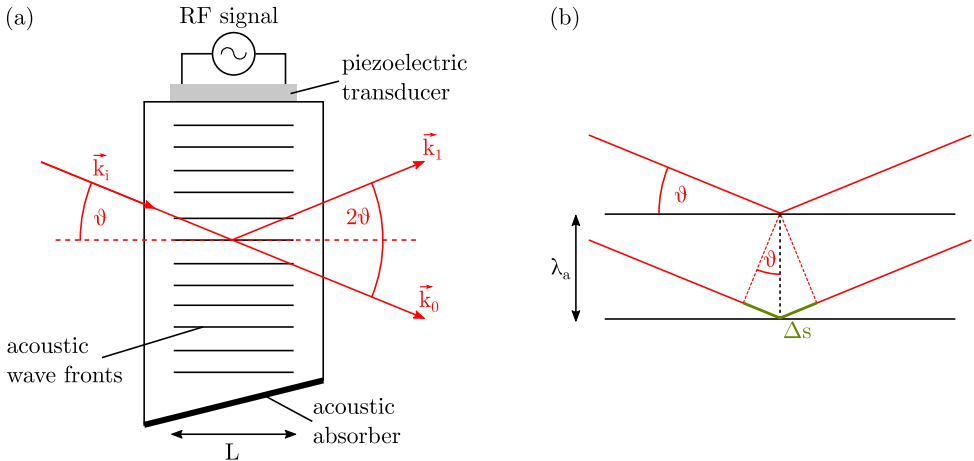

Figure 2.8: (a) Schematic representation of an AOM. An incident light ray is partially diffracted into the first diffraction order, which increases the cavity losses (adapted from [57]). (b) Reflection of a light wave at two successive wave fronts of the acoustic wave to derive the Bragg angle (adapted from [39]).

wave. The acoustic wave travels through the acousto-optic material with a sound velocity of $v_a = \omega_a/k_a = \lambda_a f_a$ until it is absorbed at the angled end surface. λ_a and f_a are the wavelength and frequency of the sound wave. Typical sound velocities are around 5 km/s. A schematic representation of an AOM is depicted in Figure 2.8(a). The acoustic wave spreads over a length of L. When a light ray with wavelength λ_s is incident on the AOM under an angle ϑ, it is partially diffracted at the diffraction grating created by the acoustic wave. The following equation applies to the ratio of the power of the diffracted beam P_1 and the power of the incident beam P_0 [39]:

$$\frac{P_1}{P_0} = \sin^2\left(L\frac{\pi}{\lambda_a}\Delta n_0\right) . \tag{2.43}$$

The amount of diffraction depends on the interaction length with the acoustic wave, the grating constant, as well as the strength of the refractive index modulation, which in turn depends on the material properties. In the Bragg regime, the angle of the first diffraction order is calculated by considering Figure 2.8(b). Constructive interference of two light rays that are reflected from two successive acoustic wave fronts is given when

$$\Delta s = 2\lambda_a \sin\vartheta \overset{!}{=} m\frac{\lambda_s}{n_0} \tag{2.44}$$

holds, where m is an integer. Consequently, the angle of the first diffraction order is approximately given by

$$\vartheta \approx \frac{\lambda_s}{2n_0\lambda_a} . \tag{2.45}$$

2.4 Nonlinear Conversion of the 2 μm Radiation

Q-switched lasers in the 2 μm range are suitable pump sources for OPOs in which the 2 μm light is down-converted to the 3–5 μm wavelength range. The conversion results from a nonlinear interaction between the incident laser field and a nonlinear crystal. The following sections provide an introduction on nonlinear optical interactions, starting from deriving the nonlinear electromagnetic wave equation in Section 2.4.1, followed by a description of difference frequency generation (DFG), which is the fundamental nonlinear process underlying OPOs, in Section 2.4.2. Angular phase matching as a requirement for the nonlinear conversion is

described subsequently in Section 2.4.3. Finally, Section 2.4.4 explains how OPOs differ from optical parametric generation (OPG) and optical parametric amplification (OPA) and Section 2.4.5 describes some limitations that result from using Gaussian beams instead of plane waves.

2.4.1 Nonlinear Wave Equation

Linear optical phenomena between light and a dielectric medium arise from a linear relation of an electric field and the polarization of the medium. When an electromagnetic wave (i.e. an oscillating electric field) with frequency ω

$$\vec{E}(\vec{r}, t) = \frac{1}{2}\vec{e}A(\vec{r}, t)\mathrm{e}^{i(kz-\omega t)} + c.c.,$$
(2.46)

which propagates along the z-axis, is incident on the medium, dipole moments are induced in the medium resulting in an electric polarization. Here, $\vec{e}$ is the polarization direction of the wave, $A(\vec{r}, t)$ is the complex amplitude, and k is the wave number. For small electric fields, the linear polarization in the frequency domain is given by

$$\vec{P}_{\mathrm{L}}(\vec{r}, \omega) = \epsilon_0 \chi^{(1)}(\omega)\vec{E}(\vec{r}, \omega),$$
(2.47)

where $\epsilon_0 = 8.85 \cdot 10^{-12}\,\mathrm{As/Vm}$ is the vacuum permittivity and $\chi^{(1)}$ is the linear electric susceptibility. For large electric fields, however, the relation between the polarization and the electric is field is no longer linear and higher order terms have to be considered. For the sake of clarity, the polarization, electric field, and electric susceptibilities are assumed to be scalar in the following equation

$$P(\vec{r}, \omega) = \epsilon_0 \left(\chi^{(1)}(\omega)E(\vec{r}, \omega) + \chi^{(2)}(\omega)E^2(\vec{r}, \omega) + \chi^{(3)}(\omega)E^3(\vec{r}, \omega) + ... \right)$$
(2.48)

$$= P_{\mathrm{L}}(\vec{r}, \omega) + P_{\mathrm{NL}}(\vec{r}, \omega).$$
(2.49)

When the vectorial character of the polarization and the electric field is considered, $\chi^{(n)}$ are susceptibility tensors of $(n+1)$-th order, which depend on the properties of the nonlinear material. The influence of the nonlinear polarization on the interaction between light with the medium is described by the nonlinear wave equation, which is derived from Maxwell's equations. In

an electrically neutral, nonconducting, isotropic, and homogeneous medium without magnetic dipoles, the nonlinear wave equation in the time domain is given by

$$\nabla^2 \vec{E}(\vec{r}, t) - \frac{1}{c^2} \frac{\partial^2}{\partial t^2} \vec{E}(\vec{r}, t) = \mu_0 \frac{\partial^2}{\partial t^2} \vec{P}(\vec{r}, t) \,, \tag{2.50}$$

where μ_0 is the vacuum permeability. By converting Equation (2.50) to the frequency domain and using Equations (2.49) and (2.47), the nonlinear wave equation is given by

$$\nabla^2 \vec{E}(\vec{r}, \omega) + \frac{\omega^2}{c^2} \left(1 + \chi^{(1)}(\omega) \right) \vec{E}(\vec{r}, \omega) = -\mu_0 \omega^2 \vec{P}_{\mathrm{NL}}(\vec{r}, \omega) \,. \tag{2.51}$$

Thus, the nonlinear polarization can be treated as perturbance term to the linear wave equation. Under the simplification that the electric field is an infinite plane wave and that the slowly varying envelope approximation is valid, Equation (2.51) is simplified and reduced to a differential equation for the complex amplitude of the electric field:

$$\frac{\partial}{\partial z} A(z, \omega) = \frac{i\omega}{2\epsilon_0 nc} \vec{e} \vec{P}_{\mathrm{NL}}(z, \omega) \mathrm{e}^{-ikz} \,. \tag{2.52}$$

This equation connects the nonlinear polarization with the complex amplitude of the electric field. [58–60]

2.4.2 Difference Frequency Generation

One example for a nonlinear process of second order is DFG. As this process is the underlying process of OPOs, it is discussed in more detail here. When two plane waves propagating with frequencies ω_1 and ω_2, wave vectors k_1 and k_2, complex amplitudes A_1 and A_2, and a propagation along the z-direction are incident on a nonlinear medium, the second order nonlinear polarization is given by [60]

$$P_{\mathrm{NL}}^{(2)}(z, t) = \frac{1}{4} \epsilon_0 \chi^{(2)} (A_1^2 \mathrm{e}^{2i(k_1 z - \omega_1 t)} + A_2^2 \mathrm{e}^{2i(k_2 z - \omega_2 t)} + 2A_1 A_2 \mathrm{e}^{i((k_1 + k_2)z - (\omega_1 + \omega_2)t)} \tag{2.53}$$

$$+ 2A_1 A_2^* \mathrm{e}^{i((k_1 - k_2)z - (\omega_1 - \omega_2)t)} + |A_1|^2 + |A_2|^2 + c.c.) \,. \tag{2.54}$$

The process defined by the first two terms is called second harmonic generation, the third term yields sum frequency generation, the last two terms yield optical rectification, and the fourth term defines the process of DFG. Therefore, when two waves with frequencies ω_1 and ω_2 with a high intensity are incident on a nonlinear medium, a light wave with a frequency $\omega_3 = \omega_1 - \omega_2$ can be created. Due to momentum conservation, it must further hold that $k_3 = k_1 - k_2$. The nonlinear polarization in the frequency domain is then given by [59]

$$P_{\mathrm{NL}}^{(2)}(z, \omega_3) = \epsilon_0 d_{\mathrm{eff}} \left(A_1(z, \omega_1) A_2^*(z, \omega_2) \mathrm{e}^{(i(k_1 - k_2)z)} + c.c. \right) , \tag{2.55}$$

where $d_{\mathrm{eff}} = 1/2\chi^{(2)}$ is the nonlinear coefficient. Inserting the nonlinear polarization into Equation (2.52) gives the coupled wave equations [59]

$$\frac{\partial}{\partial z} A_3(z, \omega_3) = \frac{i\omega_3 d_{\mathrm{eff}}}{n_3 c} A_1(z, \omega_1) A_2^*(z, \omega_2) \mathrm{e}^{i\Delta kz} \tag{2.56}$$

$$\frac{\partial}{\partial z} A_2(z, \omega_2) = \frac{i\omega_2 d_{\mathrm{eff}}}{n_2 c} A_1(z, \omega_1) A_3^*(z, \omega_2) \mathrm{e}^{i\Delta kz} \tag{2.57}$$

$$\frac{\partial}{\partial z} A_1(z, \omega_1) = \frac{i\omega_1 d_{\mathrm{eff}}}{n_1 c} A_2(z, \omega_1) A_3(z, \omega_2) \mathrm{e}^{-i\Delta kz} . \tag{2.58}$$

Illustratively, these equations describe the following: When an incident electric field, composed of the frequency components ω_1 and ω_2, creates a nonlinear polarization in the nonlinear medium, a wave with frequency ω_3 is created. Conversely, this wave creates a nonlinear polarization with the other two waves such that the other two frequency components are generated. $\Delta k = k_1 - k_2 - k_3$ is called the phase mismatch. Under the simplified assumption that the field amplitudes $A_1(z, \omega_1)$ and $A_2^*(z, \omega_2)$ are constant, Equation (2.56) is solved by integrating over the length of the crystal [59]:

$$A_3(z, \omega_3) = \frac{\omega_3 d_{\mathrm{eff}}}{n_3 c} \frac{\mathrm{e}^{i\Delta kz}}{\Delta k} . \tag{2.59}$$

The intensity of this wave after passing the crystal is then given by [59]

$$I_3 = \frac{1}{2} n_3 \epsilon_0 c |A_3(L, \omega_3)|^2 = \frac{8\pi^2 d_{\mathrm{eff}}^2 L^2 I_1 I_2}{\epsilon_0 n_1 n_2 n_3 c \lambda_3^2} \mathrm{sinc}^2 \left(\frac{\Delta k L}{2} \right) . \tag{2.60}$$

It becomes clear that an efficient conversion of ω_3 requires a large nonlinear coefficient d_{eff}, high intensities of the waves with ω_1 and ω_2, long interaction lengths, and a small phase mismatch. Figure 2.9(a) shows the intensity of the generated wave depending on the phase mismatch. The
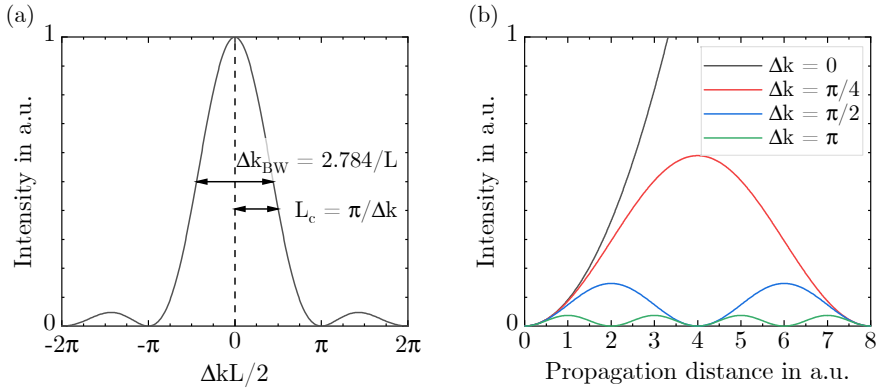
Figure 2.9: Intensity of a wave generated in a DFG process depending on (a) the phase mismatch $\Delta k L/2$ and (b) the propagation distance in the crystal for a fixed phase mismatch (adapted from [58]).

phase mismatch decreases the intensity of the generated wave. The phase matching bandwidth Δk_{BW} corresponds to the full width at half maximum (FWHM) of the intensity. The coherence length L_{c} is a measure of the distance at which the difference frequency is generated. In Figure 2.9(b), the intensity of the generated wave is shown depending on the propagation distance in the crystal. For perfect phase matching, the intensity increases parabolically with the propagation distance. For imperfect phase matching, the intensity oscillates with the propagation distance with a period of $2L_{\mathrm{c}}$. Therefore, the intensity of the generated wave increases up to the coherence length. When it propagates further, the intensity decreases because of backconversion into the pump waves. The larger the phase mismatch is, the smaller the coherence length and the length at which a conversion takes place without any backconversion. [58]

One method for achieving phase matching is angular phase matching, which is explained in the following section.

2.4.3   Angular Phase Matching

Angular phase matching exploits the birefringence of anisotropic media. In isotropic media, the refractive index is independent of the polarization and propagation direction of the incident wave in the medium. This does not apply to anisotropic media. Biaxial crystals are characterized by three distinct refractive indices ($n_x \neq n_y \neq n_z$). In this thesis, ZGP crystals were used for the nonlinear conversion. These crystals are uniaxial, thus they have one optical axis.

Light propagating along this axis experiences the same refractive index for both polarization directions. Here, $n_x = n_y \neq n_z$ holds. Waves polarized along x and y are called ordinary waves ($n_x = n_y = n_o$), waves polarized along z are called extraordinary waves ($n_z = n_e$). ZGP is a positive uniaxial material, thus $n_e > n_o$. For waves that propagate through the crystal under an angle ϑ with the optical axis, the refractive index is calculated by

$$\frac{1}{n_e(\vartheta)^2} = \frac{\cos^2 \vartheta}{n_o^2} + \frac{\sin^2 \vartheta}{n_e^2} \, . \tag{2.61}$$

This equation can be derived from the index ellipsoid depicted in Figure 2.10. [58, 59]

In the case of DFG, perfect phase matching requires

$$\Delta k = \frac{n_1 \omega_1}{c} - \frac{n_2 \omega_2}{c} - \frac{n_3 \omega_3}{c} = \frac{(n_1 - n_2)\omega_1}{c} - \frac{(n_3 - n_2)\omega_3}{c} = 0 \, . \tag{2.62}$$

In normally dispersive media, the refractive index increases with frequency, therefore this equation cannot be fulfilled. However, Equation (2.62) can be fulfilled in anisotropic media when ordinary and extraordinary waves are mixed. It is distinguished between type I and type II phase matching. In type I phase matching, the two waves with smaller frequencies have the same polarization, whereas in type II phase matching, the two waves with smaller frequencies have different polarizations. In the following, type I phase matching is considered for a positive uniaxial crystal, as this applies to ZGP in particular. In this configuration, the wave with ω_1 is
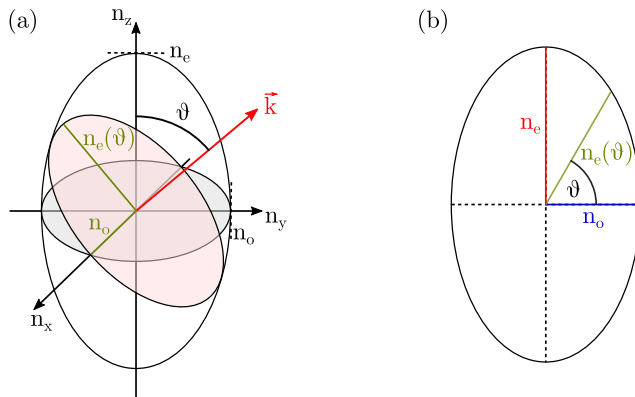

Figure 2.10: (a) Index ellipsoid of a positive uniaxial crystal. The optical axis is oriented parallel to the z-axis. (b) For a light beam that propagates with an angle ϑ with the z-axis, the electric field experiences refractive indices between n_o and $n_e(\vartheta)$, depending on the state of polarization (based on [41]).

an ordinary wave, whereas the waves with ω_2 and ω_3 are extraordinary waves. To fulfill the phase matching condition, the light needs to propagate through the crystal at an angle with the optical axis, therefore this method is called angular phase matching. The phase matching condition then is

$$\frac{n_\mathrm{o}(\lambda_1)}{\lambda_1} = \frac{n_\mathrm{e}(\vartheta, \lambda_2)}{\lambda_2} + \frac{n_\mathrm{e}(\vartheta, \lambda_3)}{\lambda_3} \,. \tag{2.63}$$

The refractive indices are described by the Sellmeier equations. Figure 2.11(a) illustrates the phase matching condition in the degenerate case where $\lambda_2 = \lambda_3 = 2\lambda_1$. With $\lambda_1 \approx 2\,\mu\mathrm{m}$, the condition is fulfilled because $n_\mathrm{e}(\vartheta_\mathrm{d}) < n_\mathrm{e}$. ϑ_d denotes the angle for which degenerate phase matching is fulfilled. Figure 2.11(b) illustrates the phase matching condition in the non-degenerate case. When two wavelengths are given, the third one is calculated by energy conservation. The phase matching angle ϑ_nd, which denotes the angle for which non-degenerate phase matching is fulfilled, can then be determined by solving Equation (2.63) numerically. Figure 2.12 shows the wavelengths λ_2 and λ_3 that fulfill the phase matching condition at a given angle. [59]

The effective nonlinearity d_eff is usually given in dependence on the crystal axis. When the crystal is tilted to the phase matching angle ϑ, for ZGP, the nonlinearity changes to [59]

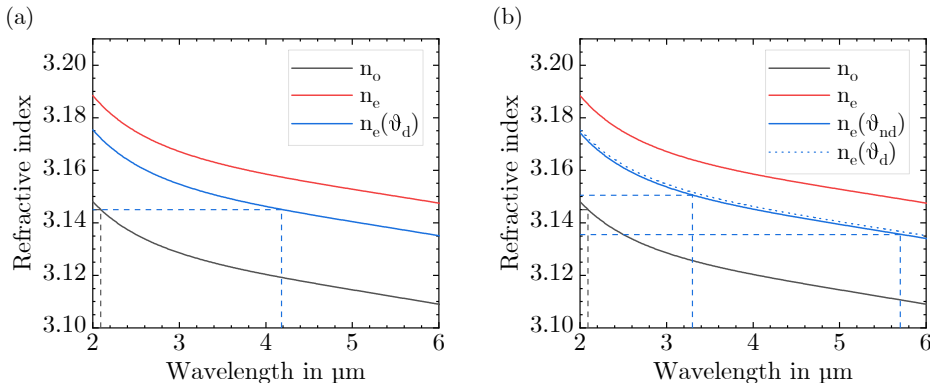$$d_\mathrm{eff} = d_{36} \cdot \sin(2\vartheta) \,. \tag{2.64}$$

Figure 2.11: Illustration of the phase matching condition in the (a) degenerate and (b) non-degenerate case. The refractive index data have been taken from [61].
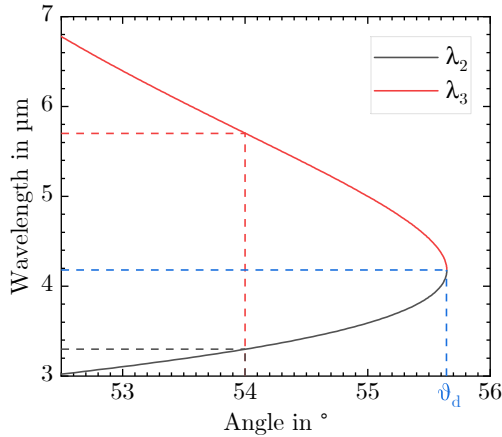
Figure 2.12: Wavelengths fulfilling the phase matching condition in dependence on the phase matching angle.

One alternative to angular phase matching is temperature phase matching, where the temperature dependence of the refractive index is used to achieve phase matching. Another common technique is quasi-phase matching, where a small phase mismatch is accepted but reversed by alternately stacking the same crystal with different crystal orientations. [58]

2.4.4 Optical Parametric Oscillators

OPOs are based on the principle of OPG. When a photon with frequency ω_p is incident on a nonlinear medium, it can spontaneously split into two lower frequency photons with frequencies ω_s and ω_i (see Figure 2.13(a)). In this process, no real excitation of the nonlinear medium is involved, the interaction takes place via a virtual state. Only photons that satisfy the phase matching condition are generated in this process. [58]

When both a pump and a signal wave are incident on a nonlinear medium, OPA can occur when the waves have suitable polarizations. In this process, the signal wave gets amplified and an idler wave is generated (see Figure 2.13(b)). Typically, the single-pass gain in this process is only weak. [58]

In OPOs, both of these processes take place. A nonlinear crystal is placed in between two parallel mirrors and is pumped with a frequency ω_p. At first, signal and idler photons are
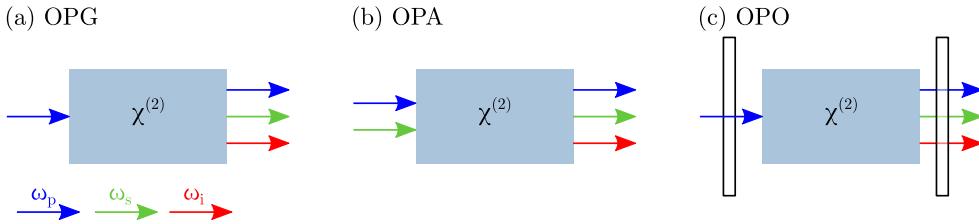
Figure 2.13: Comparison of the parametric processes (a) OPG, (b) OPA, and (c) OPO.

generated from OPG. Due to OPA, these photons are then amplified by passing the crystal multiple times. It must be distinguished between singly-resonant (SR) and doubly-resonant (DR) OPOs (SROPOs vs. DROPOs). In a SROPO, the mirrors are reflective for only the signal or idler wave, whereas in a DROPO, the mirrors are reflective for both the signal and the idler wavelength. [58]

In this thesis, DROPOs in a single-pass pump configuration are considered. In such a configuration, the generated signal and idler photons are only amplified when they propagate in the same direction as the pump photons due to the phase matching condition. As soon as the resonator losses are compensated by the single-pass gain, the threshold of the OPO is reached and the OPO starts to oscillate for higher pump powers. In ZGP OPOs, the threshold is typically in the kW regime. Therefore, these OPOs cannot be pumped with CW lasers, but have to be pumped with Q-switched lasers that deliver high peak powers. For temporal Gaussian pulses, only the part of the pulse, which is above the threshold, is converted in the nonlinear crystal. Therefore, short pulses are desirable because the rise-time until the threshold is reached is shorter. Furthermore, a tight focusing helps to maximize the intensity of the pump beam. However, this entails limitations which are discussed in the following section. [58]

2.4.5　Limitations Resulting From Real Optical Beams

In real media, OPOs experience some limitations, which have not been considered in Sections 2.4.1 to 2.4.4. Firstly, parasitic absorption reduces the conversion efficiency and heats the crystal, therefore creating a thermal lens, which strongly influences the resonator modes. Because the refractive index depends on the temperature, this can further change the phase matching condition slightly [58]. For ZGP, the absorption decreases with increasing pump

wavelengths [62]. Therefore, it is beneficial to tune the pump lasers to longer wavelengths, where the parasitic absorption is lower.

Furthermore, plane waves have been considered so far. However, a typical focused Gaussian beam has a finite divergence. Consequently, it can only be approximated as plane waves with different propagation directions in the proximity of the focus. This changes the phase matching condition as well. [58]

Another limitation arising in birefringent materials is the beam walk-off. For the extraordinary waves, the direction of energy transport and the propagation direction of the wave are not the same. As a consequence, the ordinary and extraordinary waves do not have a perfect overlap over the entire length of the nonlinear crystal limiting the conversion efficiency. The smaller the beam sizes in the crystal, the more severe is the effect of the walk-off of the beams. Consequently, a trade-off between a high pump intensity and a small walk-off has to be found. The walk-off is quantified by the walk-off angle ρ, which in ZGP is given by [59]

$$\tan \rho = \frac{n_e(\vartheta)^2}{2} \left(\frac{1}{n_e^2} - \frac{1}{n_o^2} \right) \sin(2\vartheta).$$ (2.65)

In the design of the OPO, these limitations have to be considered carefully. Furthermore, the damage threshold of the nonlinear crystals should not be exceeded, which is a further restrictive condition on the diameter of the pump beam. [58]

3 Theoretical and Experimental Methods

This chapter describes the theoretical and experimental methods used in this thesis in detail. As thermal effects in the laser crystal are central to laser operation and the resonator layout, theoretical and experimental approaches for the determination of the thermal lens are presented in Section 3.1. Section 3.2 discusses the measurement methods used in the laboratory and the exemplary characterization of a basic Ho^{3+}:YAG laser. In addition, qualitative measurements on the thermal blooming of the 1908 nm pump laser are shown.

3.1 Determination of the Thermal Lens

Matrix optics is an appropriate method for simulating the propagation of light through optical elements like free space, windows, lenses, or even a thermal lens, therefore it is introduced in Section 3.1.1. Following this, an analytical and a numerical approach to calculate the corresponding matrix of a thermal lens are presented and compared in Section 3.1.2. A facile numerical simulation tool used to design laser resonators is presented in Section 3.1.3. Finally, in Section 3.1.4, the thermal lens is determined experimentally.

3.1.1 Matrix Optics

Matrix optics is a method describing the evolution of light rays through optical elements. In this method, a light ray is represented by its offset $r(z)$ from the optical axis and the angle $\vartheta(z)$ with this axis [38]. Figure 3.1(a) schematically illustrates how a light ray with offset r_1 and angle ϑ_1
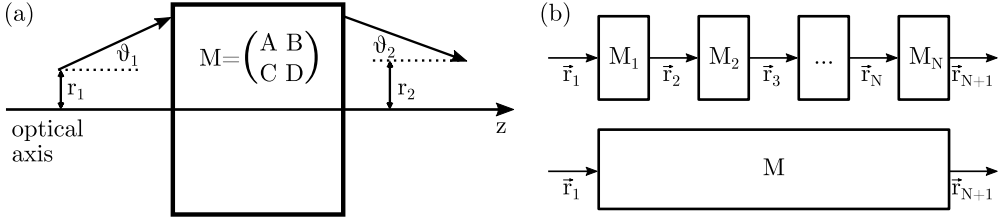
Figure 3.1: (a) Transformation of a light ray when passing an optical element described by the matrix M (based on [38, 63]). (b) Ray-transfer matrix of an optical system consisting of multiple elements (based on [54]).

transforms into a ray with offset r_2 and angle ϑ_2 when it passes an optical element described by the ray-transfer matrix M. Mathematically, this is described by [54]

$$\begin{pmatrix} r_2 \\ \vartheta_2 \end{pmatrix} = M \cdot \begin{pmatrix} r_1 \\ \vartheta_1 \end{pmatrix} = \begin{pmatrix} A & B \\ C & D \end{pmatrix} \cdot \begin{pmatrix} r_1 \\ \vartheta_1 \end{pmatrix} . \tag{3.1}$$

To calculate the propagation of a light ray through multiple optical elements described by the matrices M_1, M_2, ..., M_N, the total matrix of the optical system is determined by (see Figure 3.1(b)) [54]

$$M = M_N \cdot ... \cdot M_2 \cdot M_1 . \tag{3.2}$$

Although ray optics cannot be applied in general to calculate the evolution of laser beams due to their wave nature, an optical system can still be described by the same matrices as in the case of ray optics. Laser beams are typically described as Gaussian beams, where the field distribution is derived by solving the corresponding wave equation [64]

$$\nabla^2 \vec{E}(\vec{r}, t) = \frac{1}{c^2} \frac{\partial^2 \vec{E}(\vec{r}, t)}{\partial t^2} . \tag{3.3}$$

Under the assumptions that the electric field oscillates at a single frequency ν, the propagation direction is the z-direction, and the transverse field distribution is radially symmetric, the field distribution of a Gaussian beam is [38]

$$\vec{E}(r, z, t) = E_0 \vec{e} \frac{\omega_0}{\omega(z)} e^{-i\phi(z)} e^{-ik\frac{r^2}{2R(z)}} e^{-\frac{r^2}{\omega(z)^2}} e^{i(2\pi\nu t - kz)} . \tag{3.4}$$

E_0 is the field amplitude, $\vec{e}$ is the polarization direction, ω_0 is the beam radius at the waist, $\omega(z)$ is the beam radius, $\phi(z)$ is the Gouy phase shift, and $R(z)$ is the radius of curvature of the phase front at the position z. The beam radius and the phase front curvature of a Gaussian beam with wavelength λ are given by [63]

$$\omega(z) = \omega_0 \sqrt{1 + \left(\frac{z}{z_R}\right)^2} \tag{3.5}$$

$$R(z) = z + \frac{z_R^2}{z} . \tag{3.6}$$

$z_R = \frac{\pi \omega_0^2}{\lambda}$ is the Rayleigh length at which the beam area doubles. In order to apply matrix optics to Gaussian beams, the complex beam radius $q(z)$ is introduced [63]:

$$\frac{1}{q(z)} = \frac{1}{R(z)} - i \frac{\lambda}{\pi \omega(z)^2} . \tag{3.7}$$

When the incident Gaussian beam is described by the complex beam radius q_1 and the matrix of the optical element is given by the ABCD matrix M as defined in Equation (3.1), then the transmitted complex beam radius q_2 is [63]

$$q_2 = \frac{A q_1 + B}{C q_1 + D} . \tag{3.8}$$

This equation will be relevant for the modeling of the thermal lens with matrices in Section 3.1.2 and for the simulation tool introduced in Section 3.1.3.

3.1.2   Simulation Methods for Determining the Thermal Lens

To model the thermal lens, different approaches are possible. A radially and axially uniform pumping results in a parabolic temperature and refractive index profile as defined in Equation (2.17), and is described by a duct matrix, which is derived from the ray equation. To account for the exponential absorption in the case of end-pumping, the thermal lens can be modeled numerically with an infinitesimal duct matrix approach, which works for an arbitrary axial local pump absorption. In the special case of single-pass pumping, the ray equation is analytically solvable. These approaches are explained and compared in the following sections.

Derivation of the Duct Matrix by the Ray Equation

For the derivation of the duct matrix, the trajectory of the light in a medium with a varying refractive index must be calculated. Fermat's principle in the form

$$\delta \int_A^B n(\vec{r}) \mathrm{d}s = 0 \tag{3.9}$$

describes the variation of the optical path length between two points A and B [54]. From varying the path $\vec{r}(s)$, the ray equation is derived [54]:

$$\frac{\mathrm{d}}{\mathrm{d}s} \left(n(\vec{r}) \frac{\mathrm{d}\vec{r}}{\mathrm{d}s} \right) = \nabla n(\vec{r}) \tag{3.10}$$

As derived in Section 2.2.3, the refractive index profile is approximately parabolic and radially symmetric when a radially symmetric pump beam is used:

$$n(r, z) = n_0(z) - \frac{1}{2} n_2(z) r^2 \,. \tag{3.11}$$

$n_2(z)$ describes the change in refractive index due to the parabolic temperature profile in the crystal. In a paraxial approximation and by using $n(r, z)$, Equation (3.10) simplifies to [63]

$$\frac{\mathrm{d}}{\mathrm{d}z} \left(n_0(z) \frac{\mathrm{d}r}{\mathrm{d}z} \right) = \nabla n(r, z) \,. \tag{3.12}$$

When a uniform pumping scheme is assumed, there is no axial dependence of the refractive index resulting in [63]

$$\frac{\mathrm{d}^2 r(z)}{\mathrm{d}z^2} + \frac{n_2}{n_0} r(z) = \frac{\mathrm{d}^2 r(z)}{\mathrm{d}z^2} + \gamma^2 r(z) = 0 \,. \tag{3.13}$$

A uniform pumping scheme is considered a good assumption when the absorption length is considerably longer than the crystal length ($\alpha^{-1} \gg L$). The solution $r(z)$ to this differential equation is given by [63]

$$r(z) = r_0 \cos(\gamma z) + \frac{\mathrm{d}r_0}{\mathrm{d}z} \frac{1}{\gamma} \sin(\gamma z) \,, \tag{3.14}$$

where r_0 and $\frac{dr_0}{dz}$ are the initial position and slope of the ray. From $r(z)$ and its derivative $\frac{dr}{dz}$, the ABCD matrix of the simple quadratic duct with length z can be concluded [63]

$$M_{\text{duct}}(z) = \begin{pmatrix} \cos(\gamma z) & \frac{1}{n_0 \gamma} \sin(\gamma z) \\ -n_0 \gamma \sin(\gamma z) & \cos(\gamma z) \end{pmatrix} . \tag{3.15}$$

When a Gaussian beam passes a duct with a length L, it can be assigned the focal length

$$f = \frac{1}{n_2 L} \tag{3.16}$$

if it is long compared to the crystal length [38].

Numerical Approach for Arbitrary Axial Pump Distributions

To account for the exponential absorption in end-pumped crystals, an infinitesimal approach has to be chosen, which is based on the duct matrix derived in Equation (3.15). In the infinitesimal matrix approach, the crystal is divided into quadratic ducts with an infinitesimal length dz. Each duct has a radial parabolic refractive index profile, but to account for the exponential absorption of the pump light, n_2 is different for each duct and depends on the propagation distance z [65]:

$$n_2(z) = \frac{\xi \eta_{\text{th}}}{\pi \omega_{\text{p}}^2} \left| \frac{\partial P_{\text{abs}}}{\partial z} \right| . \tag{3.17}$$

Here, the material-dependent parameter $\xi = \frac{\partial n}{\partial T}(2\lambda_{\text{th}})^{-1}$ is introduced. In the case of Gaussian end-pumping, an additional factor of 2 would have to be considered as shown in Equation (2.18). However, this factor has been omitted due to disagreement with experimental data. The disagreement might result from pump saturation effects that are higher in the center of the Gaussian beam than in the wings, thus decreasing the heat generation in the beam center and flattening the radial temperature distribution in the center. Furthermore, in the temperature distribution introduced by Innocenzi [50], the lasing operation was disregarded, which considerably changes the heat generated in the laser crystal [44, 55, 66].

The infinitesimal duct matrix is given by [65]

$$M_{\mathrm{dz}}(z) = \begin{pmatrix} \cos(\gamma(z)\mathrm{d}z) & \frac{1}{n_0\gamma}\sin(\gamma(z)\mathrm{d}z) \\ -n_0\gamma(z)\sin(\gamma(z)\mathrm{d}z) & \cos(\gamma(z)\mathrm{d}z) \end{pmatrix} \approx \begin{pmatrix} 1 & \frac{\mathrm{d}z}{n_0} \\ -n_0\gamma(z)^2\mathrm{d}z & 1 \end{pmatrix}, \quad (3.18)$$

where $\gamma(z)^2 = \dfrac{n_2(z)}{n_0}$ and $\sin(x) \approx x$ and $\cos(x) \approx 1$ is used to take the infinitesimal nature of $\mathrm{d}z$ into account. The total ABCD matrix of the crystal is then calculated by multiplying all infinitesimal duct matrices as shown in Equation (3.2). This numerical approach allows for calculating the thermal lens that results from an arbitrary axial pump distribution.

Analytical Approach for Single-Pass Pumping

In the special case of a pump beam that passes the crystal once, an analytical solution to the ray equation exists, thus calculation time is saved. To derive this analytical solution in the case of single-pass pumping, the ray equation (3.13) needs to be solved for a z-dependent change in refractive index $n_2(z)$. By assuming an exponential absorption of the pump light, Equation (3.17) develops into

$$n_2(z) = \frac{\xi\eta_{\mathrm{th}}\alpha P_0}{\pi\omega_{\mathrm{p}}^2}\mathrm{e}^{-\alpha z} = n_{20}\mathrm{e}^{-\alpha z} . \tag{3.19}$$

The solution to Equation (3.12) is calculated with Mathematica and is given by

$$r(z) = r_0 A_0 + n_0\frac{\mathrm{d}r_0}{\mathrm{d}z}B_0 \quad \text{with} \tag{3.20}$$

$$A_0 = \frac{J_1(\zeta)Y_0\left(\zeta\sqrt{e^{-\alpha z}}\right) - Y_1(\zeta)J_0\left(\zeta\sqrt{e^{-\alpha z}}\right)}{J_1(\zeta)Y_0(\zeta) - J_0(\zeta)Y_1(\zeta)} \quad \text{and} \tag{3.21}$$

$$B_0 = \frac{1}{\sqrt{n_{20}n_0}}\frac{Y_0(\zeta)J_0\left(\zeta\sqrt{e^{-\alpha z}}\right) - J_0(\zeta)Y_0\left(\zeta\sqrt{e^{-\alpha z}}\right)}{J_1(\zeta)Y_0(\zeta) - J_0(\zeta)Y_1(\zeta)} \quad \text{and} \tag{3.22}$$

$$\zeta = \frac{2}{\alpha}\sqrt{\frac{n_{20}}{n_0}} . \tag{3.23}$$

J_n and Y_n ($n = 0, 1$) are Bessel functions of the first and second kind. By deriving this differential equation, the elements of the ABCD matrix M_{ana} are concluded in analogy to Equation (3.15). The matrix elements C_0 and D_0 are given by

$$C_0 = \sqrt{n_{20}n_0 e^{-\alpha z}} \frac{J_1(\zeta)Y_1\left(\zeta\sqrt{e^{-\alpha z}}\right) - Y_1(\zeta)J_1\left(\zeta\sqrt{e^{-\alpha z}}\right)}{J_1(\zeta)Y_0(\zeta) - J_0(\zeta)Y_1(\zeta)} \quad \text{and} \tag{3.24}$$

$$D_0 = \sqrt{n_{20}n_0 e^{-\alpha z}} \frac{1}{\sqrt{n_{20}n_0}} \frac{Y_0(\zeta)J_1\left(\zeta\sqrt{e^{-\alpha z}}\right) - J_0(\zeta)Y_1\left(\zeta\sqrt{e^{-\alpha z}}\right)}{J_1(\zeta)Y_0(\zeta) - J_0(\zeta)Y_1(\zeta)} \ . \tag{3.25}$$

Due to its analytical nature, the thermal lens calculation is considerably faster with this approach than with the numerical approach. However, Equation (3.12) cannot be solved analytically for arbitrary axial pump distributions. For example, the case of a double-pass pump light absorption is not accessible analytically. In this case, the numerical approach is required to model the thermal lens.

Comparison of the Three Approaches

The results obtained with the different approaches need to be compared to ensure the consistency of the analytical and numerical approach and to compare the extent to which the duct approach differs from the other two. The matrix elements are compared depending on the propagation distance through the thermal lens. The meaning of the individual matrix elements can be understood as follows: In Equation (3.1), two limiting cases can be considered, which are

1. r_1 arbitrary, $\vartheta = 0 \quad \Rightarrow \quad r_2 = Ar_1 \quad$ and $\quad \vartheta_2 = Cr_1$,   (3.26)

2. $r_1 = 0, \vartheta$ arbitrary $\quad \Rightarrow \quad r_2 = B\vartheta_1 \quad$ and $\quad \vartheta_2 = D\vartheta_1$ (3.27)

Thus, A describes the trajectory of the light ray through the thermal lens depending on the initial radial position. C contains the focusing information of the thermal lens because it yields the angle with the propagation axis depending on the initial position. From C, the focal length of the thermal lens can directly be concluded. In analogy to A, B describes the trajectory through the thermal lens entering in the center of the lens under an initial angle. D describes the change in the angle with the propagation axis compared to the initial angle.

Figure 3.2 shows the matrix elements plotted versus the axial position for the analytical approach for two sets of parameters. In both cases, a pump diameter of $\omega_\mathrm{p} = 250\,\mu\mathrm{m}$ is used. In case 1, an absorbed pump power of 45 W is assumed, whereas 22.5 W of absorbed pump power are assumed in case 2. Comparing case 1 and case 2 for the elements A, C, and D shows that the thermal lensing is half as strong in case 2 compared to case 1 because the change in the matrix
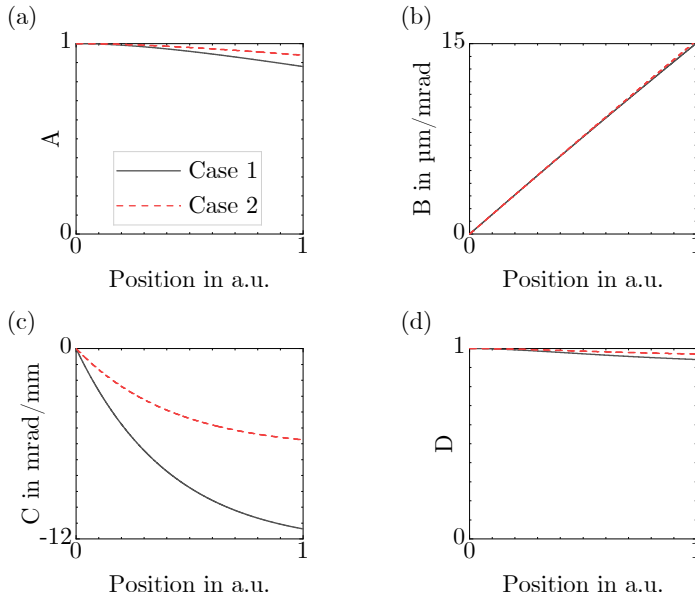
Figure 3.2: Development of the matrix elements calculated with the analytical approach over one crystal length for two cases. The parameters are $\xi = 5.09 \cdot 10^{-7}$ m/W [38], $\eta_{\mathrm{th}} = 10\,\%$, $\omega_{\mathrm{p}} = 250\,\mu$m. Case 1: $P_{\mathrm{abs}} = 45$ W (solid black line). Case 2: $P_{\mathrm{abs}} = 22.5$ W (dashed red line).

elements between the positions 0 and 1 amounts to half the value when case 2 and case 1 are compared. This is in accordance with the lower absorbed pump power. Furthermore, the main information of the thermal lensing is contained in the matrix elements A and C. Assuming an initial position $r_1 = 1$ mm and an initial angle of $\vartheta_1 = 1$ mrad for case 1, the change in trajectory resulting from matrix element A is approximately $100\,\mu$m, whereas it is $15\,\mu$m due to matrix element B. Thus, the influence of matrix element B is almost one order of magnitude smaller. The situation is similar for the elements C and D. The change in angle is approximately 11 mrad due to matrix element C, whereas it is 0.05 mrad due to matrix element D. Thus, C is the dominant parameter here.

Figure 3.3 shows a comparison of the duct, numerical, and analytical approach for the parameters assumed for case 1. Firstly, the numerical and analytical result yield the same matrix elements, whereas they differ from the duct approach, which is in accordance with the assumptions made in the calculations. The change in trajectory is stronger at the front of the crystal in the analytical approach due to the higher amount of absorbed pump light at the front of the crystal (see matrix
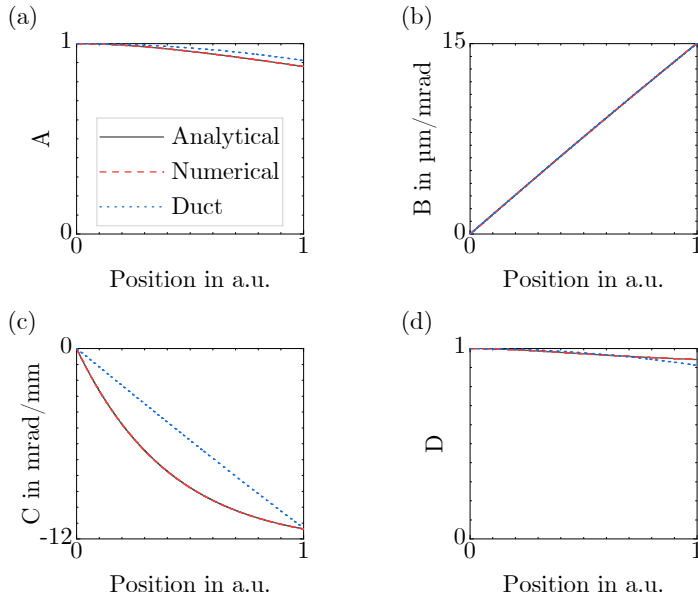
Figure 3.3: Development of the matrix elements calculated with the analytical (solid black line), numerical (dashed red line), and duct (dotted blue line) approach over one crystal length. The parameters are the same as in case 1.

element A). The change in the angle with the propagation axis is also stronger at the front of the crystal for the same reasoning (see matrix element C).

Figure 3.4 shows a comparison of the analytical and duct approach when a laser beam propagates through an optical element exhibiting thermal lensing. For the calculations, an absorbed pump power of $P_{abs} = 50\,\text{W}$ and a pump beam radius of $250\,\mu\text{m}$ are assumed. The Gaussian beam is incident on the thermal lens with its focus at the crystal front facet at a position of $0\,\text{cm}$. The plots show the propagation of this beam through and after the crystal. In analogy to Figure 3.3, the stronger bending of the beam at the front of the crystal results from the increased heat generation near the crystal front when the exponential absorption is considered in the analytical approach (red dashed curve).

These approaches are not only used to model the thermal lens but also to calculate mode sizes within laser resonators. For this purpose, a homemade numerical simulation tool is presented in the following section.
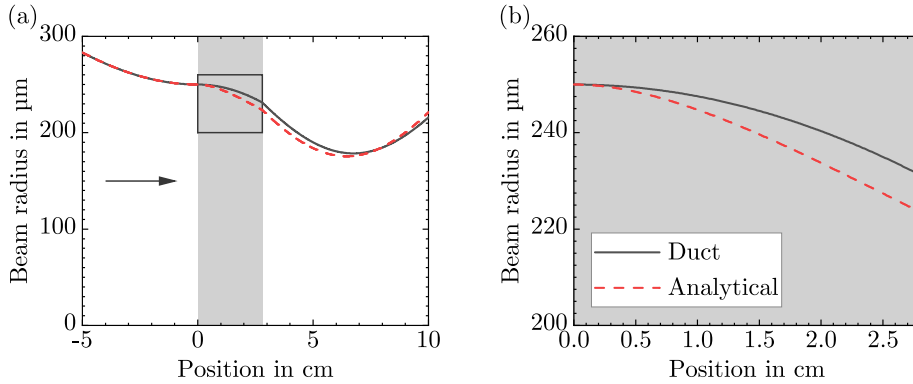
Figure 3.4: (a) Propagation of a Gaussian beam with a beam radius of 250 µm through a thermal lens modeled with the duct (black) and analytical (red) approach. The thermal lens is indicated by the grey rectangle. The arrow indicates the propagation direction of the beam. (b) Magnification of the indicated area in plot (a).

3.1.3   Numerical Simulation Tool for Designing Resonators

To optimize the laser resonators and establish a good overlap between pump and laser mode, a simulation of the resonator facilitates the choice of optics prior to an experimental investigation. For this purpose, a facile homemade simulation tool was developed, which assumes a linear resonator geometry terminated by an HR and OC mirror. The resonator includes optical elements such as lenses, mirrors, a crystal, and the propagation through materials with an arbitrary refractive index.

Figure 3.5 provides an overview over the steps required for the simulation. After defining the resonator, the ABCD matrix is calculated for each element in the resonator. The matrices for mirrors, lenses, and the propagation in a material with refractive index n are defined in [63]. Due to its high flexibility, the crystal matrix is modeled with the numerical approach presented in the Section 3.1.2. This tool is not limited to crystals with a homogeneous doping concentration, but also crystals with varying doping concentrations along the crystal axis can be modeled. From the ABCD matrices, the round-trip matrix M_{RT} of the resonator is calculated by multiplying all optical elements that are passed within one round-trip through the cavity [38]. With the
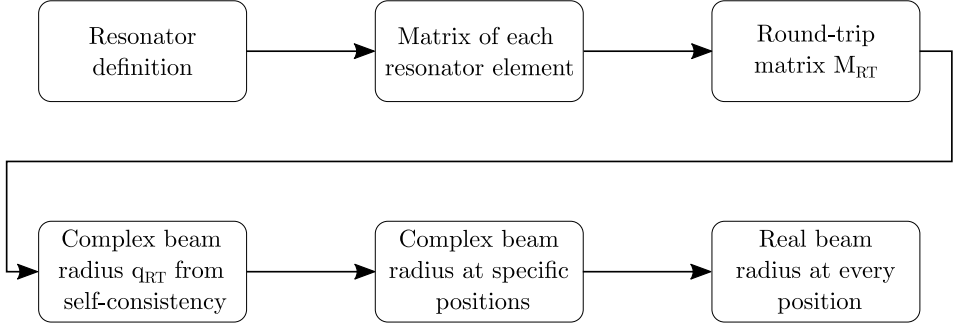
Figure 3.5: Flow chart of the numerical resonator simulation.

condition of self-consistency, the complex beam radius q_{RT} at the starting point of the round-trip is calculated by

$$q_{RT} = \frac{M_{RT,11}q_{RT} + M_{RT,12}}{M_{RT,21}q_{RT} + M_{RT,22}} \ .$$

(3.28)

q_{RT} is then propagated through the cavity by using Equation (3.8). From the complex beam radius at the beginning and at the end of each element, the real beam radius in that element is calculated by using the relations (3.5) and $z_R = \frac{\pi\omega_0^2}{\lambda} = \text{Im}(q)$.

The cavity can then be optimized with respect to mirror curvatures, element distances, and focal lengths of the lenses such that mode matching is established over a wide range of pump powers.

An exemplary resonator is simulated with the introduced simulation tool. A plane HR mirror and an OC with a radius of curvature of $R = 0.5\,\text{m}$ with a distance of $L = 12.5\,\text{cm}$ is assumed. Further, $\eta_{th} = 10\,\%$ and a pump beam diameter of $2\omega_p = 700\,\mu\text{m}$ is assumed. In a first step, the average mode size in the crystal and on the OC mirror is calculated (see Figure 3.6). The resulting resonator stability curves show a typical U-shape in accordance with the stability curves presented by Magni in 1987 [67]. At the intersections of the pump beam diameter with the average beam diameter in the crystal, the mode matching condition is fulfilled, which is a requirement for lasers with a high beam quality. In case of a larger pump than resonator mode diameter, especially at high pump powers, higher order modes with larger beam diameters can start to build up. This typically results in a decrease in beam quality. In the case of a smaller pump than resonator mode diameter, the wings of the resonator mode are outside of the gain volume, resulting in reabsorption of the laser mode and an inefficient operation. Furthermore, in
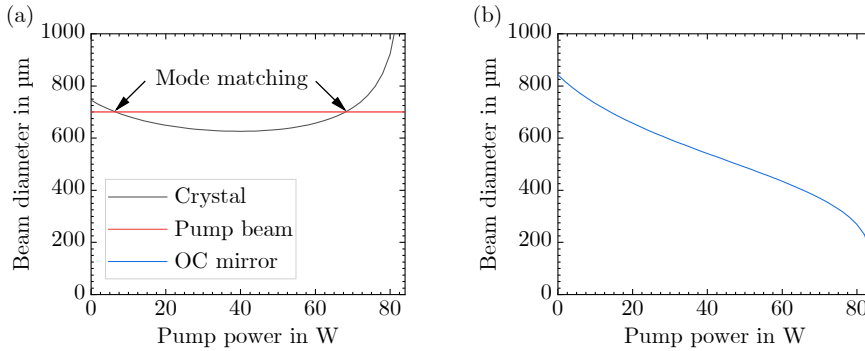
Figure 3.6: Mode size of (a) the resonator mode in the crystal (black) and the pump mode (red) and (b) the resonator mode size on the OC mirror (blue).
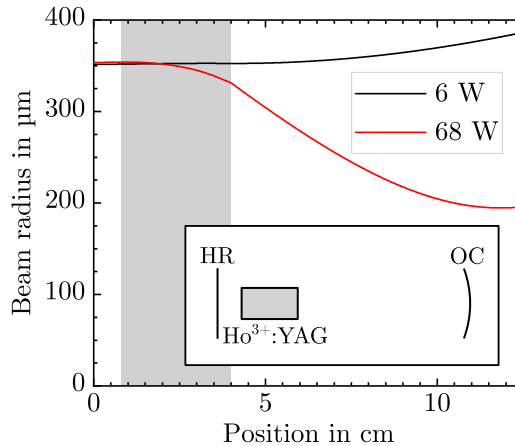

Figure 3.7: Mode size in the resonator at the mode matching points of 6 W (black) and 68 W (red) of pump power. The inset shows the simulated resonator.

this case the resonator is operated near its stability limit which may lead to an instable operation. The mode size inside the resonator is simulated for the mode matching points at 6 W and 68 W of pump power marked in Figure 3.6 (see Figure 3.7). While at 6 W of pump power the thermal lens is weak and the resonator is mainly stabilized by the curved OC mirror, the thermal lens is strongly focusing at 68 W.

For a precise modeling of the resonators, it is indispensible to estimate the focal length of thermal lens and the fractional thermal loading and calibrate the model against the experiment. Section 3.1.4 presents experimental approaches to determine the thermal lens.

3.1.4 Experimental Determination of the Thermal Lens

To select reasonable parameters for the simulation and design of the resonators, it is necessary to verify and calibrate the model. As the thermal lens parameters are critical and relatively uncertain, it is necessary to estimate the focal length of the thermal lens and the fractional thermal loading, for which a number of methods including geometrical methods, methods based on the cavity modes, and interferometric measurements exist [44]. In the following sections, the focal length of the thermal lens is estimated using two different methods. The first method is based on the resonator stability criterion in a plane-plane resonator. The second method uses the simulation approach presented in Section 3.1.3 in combination with beam diameter measurements outside the resonator. An interferometric thermal lens measurement will be presented in Section 4.2.5.

Estimation of Thermal Lens by Resonator Stability Criterion

As a resonator with a plane HR and OC mirror is located at the border of the stability zone [38], it becomes stable as soon as a weak focusing lens is introduced in the resonator. In Figure 3.8, this corresponds to the focal length f_1 (green arrow). On the other hand, when the focal length becomes shorter than the distance from the more distant mirror, the resonator becomes unstable (see red arrow in Figure 3.8). This criterion can be used to estimate an upper limit of the thermal focal length of the laser crystal with the following measurement: At a fixed resonator length L, the pump power is increased, which shortens the focal length of the thermal lens until the resonator becomes unstable. When the laser crystal is placed closely to one of the mirrors, the resonator length at the stability limit is an estimation of the thermal focal length at the respective absorbed pump power. Under the assumption that the fractional thermal loading is
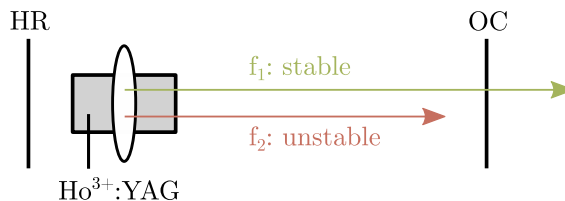

Figure 3.8: A plane-plane resonator is stable as long as the thermal focal length is longer than the distance of the thermal lens from the more distant mirror.
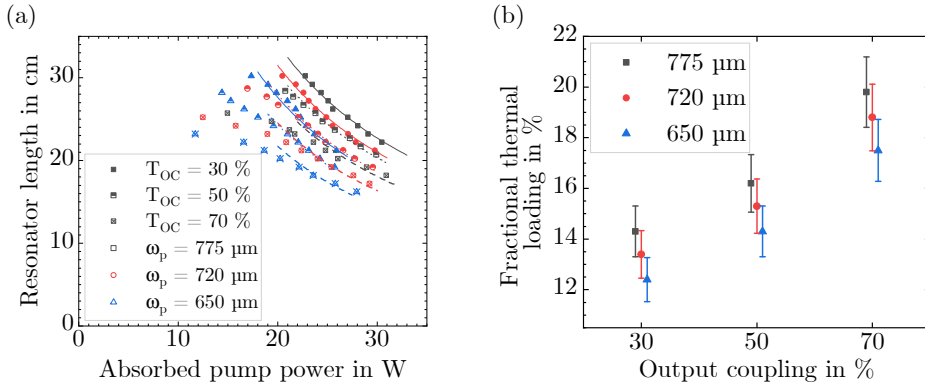
Figure 3.9: (a) Resonator length at the stability limit depending on the absorbed pump power for different configurations. The lines correspond to a fit performed by reproducing the experiment with the simulation tool. (b) Fractional thermal loading concluded from the measurement shown in (a). The small lateral offset between the data points was introduced for reasons of clarity.

constant during one measurement, $L \approx f_{th} \propto P_{abs}^{-1}$ holds. For the measurement, a Ho^{3+}:YAG crystal with a length of 26 mm and a doping concentration of 0.75 % was used.

Figure 3.9(a) shows the measured resonator length depending on the absorbed pump power for different configurations. In addition to different OC transmissions (solid symbols: $T_{OC} = 30\%$, half-solid symbols: $T_{OC} = 50\%$, crossed symbols: $T_{OC} = 70\%$), different pump diameters (black: $\omega_p = 775\,\mu m$, red: $\omega_p = 720\,\mu m$, blue: $\omega_p = 650\,\mu m$) were investigated. A higher OC transmission comes along with a shorter focal length of the thermal lens because the intensity of the intracavity laser field is lower which decreases the probability of stimulated emission and increases the influence of detrimental effects like upconversion, which lead to an additional heat generation. When the pump diameter is decreased, the thermal focal length becomes shorter, as a smaller pump diameter leads to a stronger local heating corresponding to a stronger refractive index variation and a stronger focusing effect. For the parameter sets with $T_{OC} = 30\%$ (solid symbols), the inverse proportionality of the resonator length with the absorbed pump power is confirmed by the experimental data. For the other OC transmissions, this proportionality can only be confirmed for some of the data points. On the one hand, this is attributed to an increasing alignment sensitivity when the OC transmission is increased, especially at long resonator lengths, which leads to an underestimated resonator length. On the other hand, the assumption of a constant fractional thermal loading may not be true as is shown in Figure 3.9(b). To determine the fractional thermal loading η_{th}, the homemade simulation tool

is used by numerically simulating the resonator length at which the resonator becomes unstable for a fixed pump power and fitting the data shown in Figure 3.9(a). Besides the increase in fractional thermal loading with an increasing output coupling, an increase in fractional thermal loading is also observed with an increasing pump beam diameter. The former observation might be explained by the lower intracavity laser field at a higher output coupling which decreases the probability for stimulated emission and increases the probability for upconversion and non-radiative processes. The latter observation might be explained by the larger absolute number of ions that can be excited to the upper manifold and thus contribute to detrimental non-radiative transitions. Overall, the fractional thermal loading is strongly dependent on the exact operation parameters and can only be roughly estimated to be around 10–20 %. Another restriction is further given by the measurement method. Because it uses the stability limit, the measurement is conducted for a weak laser operation. However, the fractional thermal loading differs with and without laser operation [42]. In laser operation, the fractional thermal loading is smaller due to an increased probability in stimulated emission.

Estimation of Thermal Lens by Mode Simulation

To determine the thermal lens in laser operation, the beam diameter of the laser mode is measured at different positions outside the cavity. By simulating the laser mode inside the resonator and propagating it outside of the resonator, the measured beam diameters are fit.
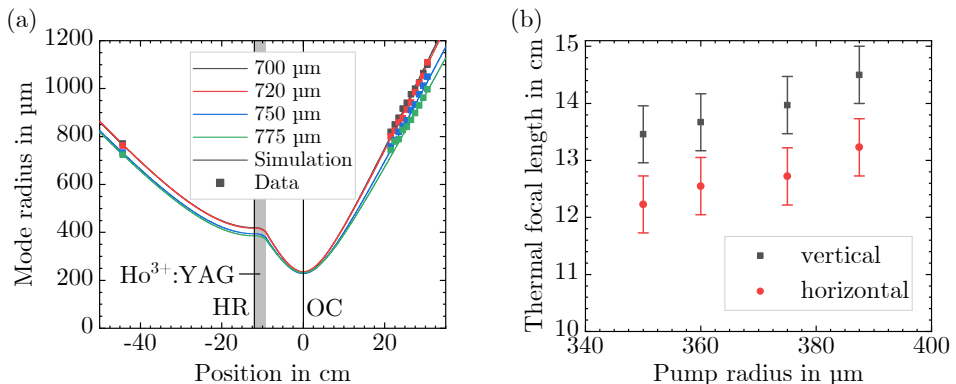

Figure 3.10: (a) Beam diameter measured outside the resonator and simulated mode fitting the data points for different pump diameters at a fixed pump power of 45 W. Data exemplarily shown for the vertical beam direction. (b) Focal length of the thermal lens for the vertical and horizontal beam direction concluded from the measurement shown in (a).

A 12 cm long plane-plane resonator was set up for the experiment. Figure 3.10(a) shows the data points and mode simulation for an OC transmission of 50 % and varying pump diameters between 700–775 μm for the vertical beam axis. From the simulated mode parameters, the thermal focal length is calculated (see Figure 3.10(b)). Thermal focal lengths around 12–15 cm were determined depending on the beam axis and pump diameter. In comparison with the measurement based on the resonator stability limit, these values are smaller because the measurement was conducted at a higher absorbed pump power of 44 W. As expected, an increase in the focal length with increasing pump diameter is observed. Furthermore, the focal length is longer for the vertical than for the horizontal beam axis by a factor of approximately 1.1. This results from the thermally induced bifocusing as explained in Section 2.2.3 and is in the expected order of magnitude.

3.2 Experimental Methods

In addition to the simulation methods, the experimental methods and measuring instruments are explained in Section 3.2.1. In Section 3.2.2, a basic Ho^{3+}:YAG resonator is characterized with the methods introduced before. Section 3.2.3 then focuses on the thermal blooming effect of the pump beam.

3.2.1 Measuring Instruments and Experimental Procedures

Parameters that are of particular interest for the characterization of a laser are its output power, beam profile and beam quality, pulse characteristics as well as its spectral output. The following section explains the working principle of the instruments needed to measure these parameters.

Laser Power: Thermopile Detectors

To measure the high average laser powers, a temperature measurement is carried out. Figure 3.11(a) depicts a schematic representation of a laser power detector. A sensor disc absorbs the incident laser light creating a radial heat flow. The sensor disc is surrounded by a thermopile consisting of a series of thermocouples. In a thermocouple, two electric conductors are
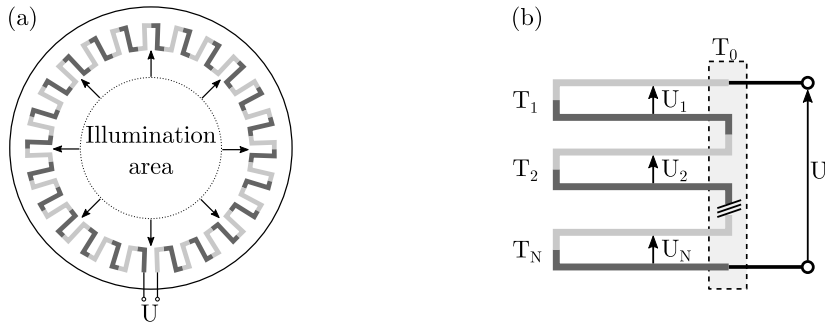
Figure 3.11: (a) Schematic representation of a thermal sensor. The illumination area is surrounded by a thermopile, which converts the heat created by the absorbed laser radiation into a voltage (based on [70]). (b) Working principle of a thermopile consisting of N thermocouples (based on [69]).

connected. When the contact point is at a different temperature than the end points of the conductors, a current is induced leading to a measurable voltage of

$$U_1 = \int_{T_0}^{T_1} S_{\mathrm{AB}}(T)\,\mathrm{d}T \tag{3.29}$$

between the end points [68]. T_0 is the temperature at the end points, T_1 is the temperature at the contact point, and $S_{\mathrm{AB}}(T)$ is the temperature-dependent relative Seebeck coefficient of the two materials. As in a thermopile multiple thermocouples are connected in series (see Figure 3.11(b)), the voltages of the individual thermocouples add up [69]. Consequently, the exact beam size and position on a power detector is not relevant because the entire illumation area is surrounded by a thermopile. Depending on the incident radiation, different types of absorber layers, e.g. surface or volume absorbers, are used. Due to the radial heat flow, the response time in such a detector depends on the size of the absorber. [70]

Depending on the laser power, different thermal sensors were used in this thesis: Ophir 2A-BB-9, Ophir 30A-BB-18, Ophir 30(150)A-SV-17, and Ophir FL400A-BB-50.

Laser Beam Profilers: Pyroelectric and Microbolometer Detectors

In addition to thermal detectors for measuring the laser power, sensors for measuring the laser beam profile are also based on thermal effects. Two main technologies are used to measure laser beam profiles in the 2 μm range. Pyroelectric detectors are based on the pyroelectric effect,

whereas microbolometers exploit the temperature dependence of the specific resistance [69]. In both cases, the incoming infrared radiation is absorbed resulting in a temperature increase of the sensor, which is converted into an electrical signal [69].

In pyroelectric sensors, a pyroelectric crystal is polarized due to the change in temperature. As a consequence, the surface of the crystal charges. By modulating the incoming radiation, the change in charge can be measured by two electrodes placed on the opposite sides of the pyroelectric crystal (see Figure 3.12(a)). In pyroelectric sensor arrays, the spatial resolution is limited by the heat conduction between the single elements [69]. A typical pyroelectric crystal is lithium tantalate (LiTaO$_3$), among others, and pixel sizes around 75 μm are commercially available [71, 72].

In bolometers, a temperature-dependent resistance is thermally isolated from a heat sink and a current flows through the sensor element. When it is irradiated, its specific resistance changes which leads to a change in voltage. In contrast to pyroelectric sensors, no modulation of the incoming infrared radiation is required. Microbolometers are based on micro-electromechanical systems (MEMS) reaching pixel sizes down to 17 μm. Typically, a vanadium dioxide (VO$_2$) bolometer is isolated from the silicon substrate by a MEMS bridge (see Figure 3.12(b)). On top of the substrate, the electrical read-out circuit and a reflective layer, which forms a $\lambda/4$-resonator
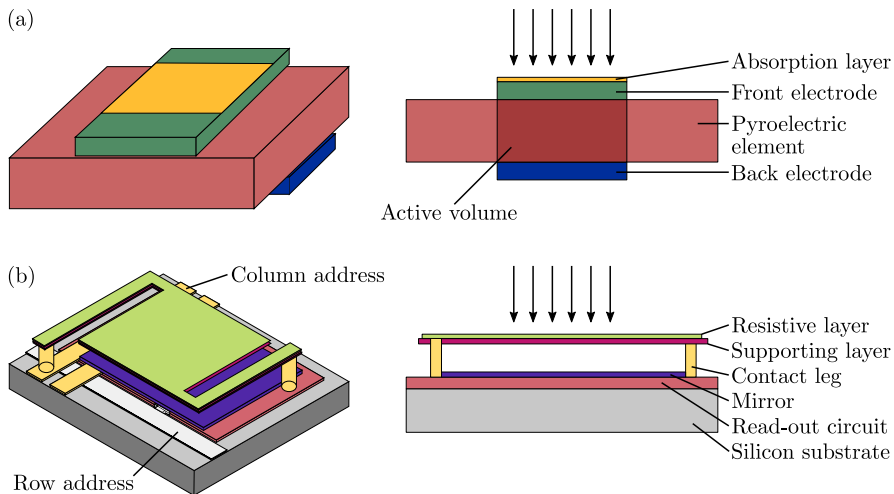

Figure 3.12: Schematic setup of (a) a pyroelectric sensor (based on [73]) and (b) a microbolometer sensor (based on [74, 75]).

with the bolometer layer to receive an optimized absorption, are located. The distance between the bolometer and the substrate is in the μm range. Thus, the microbolometer has to be encapsulated in a vacuum, as otherwise the surrounding gas would lead to heat conduction between the bolometer layer and the substrate. [76]

Detectors based on both technologies were used in this thesis. For practical purposes, the main difference lies in the pixel size. Assuming a minimum number of ten illuminated pixels for a reliable measurement, the measurable beam diameter is 800 μm with the pyroelectric sensor and 170 μm with the microbolometer sensor. The detectors were mainly used for monitoring the laser beam profile and determining the beam propagation factor.

To correctly determine the beam propagation factor of a laser beam as a measure for the beam quality, ISO 11146-1:2021 [77] has to be considered. To follow that, a focusing element with a focal length f is placed in the laser beam such that a beam waist is generated. The beam propagation factor M^2 is then determined by measuring the beam diameter at various positions along the beam propagation direction z and fitting the hyperbolic beam diameter given by

$$\omega(z) = \omega_0 \sqrt{1 + \left(\frac{(z - z_0)M^2\lambda}{\pi\omega_0^2}\right)^2}.$$ (3.30)

M^2 describes how close the laser beam approaches a diffraction-limited Gaussian beam, which is characterized by $M^2 = 1$ [78]. Thus, the parameter M^2 is a measure of how tightly a beam with a given divergence angle can be focused or vice versa how strong a beam with a given focus diverges. The beam diameter has to be measured at least at ten different positions, with one half of the measurement points lying within one Rayleigh length of the beam waist and the other half outside of two Rayleigh lengths of the beam waist. Some exemplary measurement planes are indicated as red dashed lines in Figure 3.13. The beam diameter is measured with an Ophir Pyrocam IIIHR (pyroelectric sensor) or a DataRay WinCamD-IR-BB (microbolometer sensor). In both cases, the $D4\sigma$ definition is used for the beam width. In this definition, the beam width is defined as four times the standard deviation of the intensity distribution of the beam, mathematically expressed as [77–79]

$$D4\sigma = 4\sqrt{\frac{\int_{-\infty}^{\infty}\int_{-\infty}^{\infty} I(x, y)(x - x_0)^2 \mathrm{d}x\mathrm{d}y}{\int_{-\infty}^{\infty}\int_{-\infty}^{\infty} I(x, y)\mathrm{d}x\mathrm{d}y}},$$ (3.31)
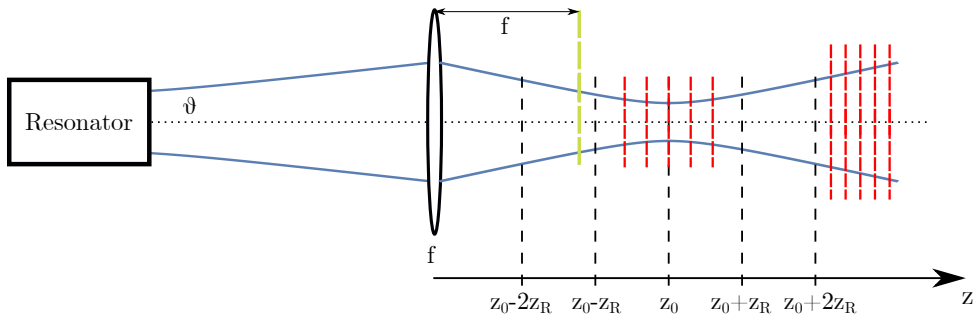
Figure 3.13: Schematic setup used for the determination of the beam propagation factor M^2.

where x_0 is the centroid of the distribution in x-direction. In case of a diffraction-limited beam, the $D4\sigma$ definition corresponds to the $1/e^2$ beam radius [79].

Another measurement for which the detectors are used is the determination of the angular pointing described in ISO 11670:2003 [80]. With this measurement, the beam angle with respect to the optical axis is determined by exploiting the fact that a focusing lens transforms the angle θ of the beam with the optical axis into an offset r on a detector. The detector is placed in the distance of the geometrical focal length of the lens f. The beam angle is then given by

$$\theta = \frac{r}{f} \, .$$

(3.32)

Pulse Characterization: PEM Detectors

To characterize the laser pulses, detectors based on the photoelectromagnetic (PEM) effect are used [81]. When light is incident onto a semiconductor material, it is absorbed according to the Beer-Lambert law, leading to a concentration gradient n of the generated electron-hole pairs, which is highest near the surface of the absorber. Thus, the charge carriers diffuse into the bulk of the material (see Figure 3.14(a)). When an external magnetic field is applied perpendicular to the incident light, electrons and holes are deflected to opposite sides of the semiconductor material (see Figure 3.14(b)). Consequently, an electric field builds up and a voltage, which depends on the intensity of the incident light, can be measured. [82–84]
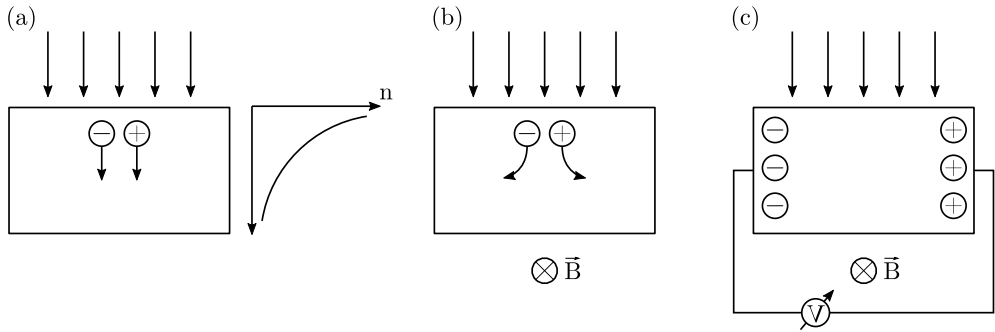
Figure 3.14: Qualitative explanation of the photoelectromagnetic effect (based on [83]). (a) Diffusion direction of electron-hole pairs due to the concentration gradient induced by light absorption. (b) In a magnetic field, electrons and holes are deflected in opposite directions. (c) Between the ends of the semiconductor, a voltage can be measured.

By connecting a PEM detector (VIGO HgCdTe (MCT) Photovoltaic Detector PEM-10.6) to an oscilloscope (Tektronix TBS2000B Digital Storage Oscilloscope), the pulse shapes of the incident laser pulses are measured. From the pulse shape, the pulse duration is determined numerically by calculating the standard deviation σ of the pulse distribution. The pulse duration Δt_p is then given by the FWHM of the distribution: $\Delta t_\mathrm{p} = 2\sqrt{2\ln 2}\sigma$. Together with a knowledge of the laser power and repetition rate, the pulse energy and pulse peak power can be deduced.

Spectral Characterization: Optical Spectrum Analyzer

To characterize the spectral output of the $2\,\mu\mathrm{m}$ laser source and the mid-wave infrared radiation, an optical spectrum analyzer (OSA) is used. The OSA used in this work is based on a Czerny-Turner spectrometer in which the diffracting element is a grating [85]. Figure 3.15 shows a schematic representation of a Czerny-Turner spectrometer. The light to be analyzed enters the OSA through the entrance slit, is collimated by a mirror, and illuminates a reflection grating. At the grating, the light is divided into its spectral components because the diffraction angle depends on the wavelength. A focusing mirror images the light onto the detector plane. Overall, the spectrum is thus spatially resolved. The exit slit in front of the detector ensures that only a limited spectral width is detected. By rotating the grating, different spectral components can be analyzed. [86]
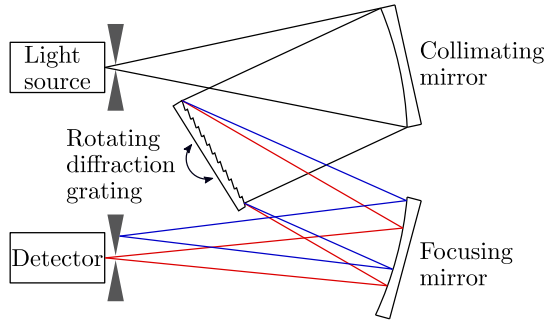
Figure 3.15: Schematic representation of a Czerny-Turner spectrometer (based on [75]).

In this work, a Yokogawa AQ6375B Optical Spectrum Analyzer was used. The maximum resolution of this device is specified to 0.05 nm [87].

3.2.2 Characterization of a Basic Ho^{3+}:YAG Laser Setup

In the following section, a basic Ho^{3+}:YAG resonator is described and characterized exemplarily. This is intended to provide a reference point for evaluating the improvements achieved through this work and to justify the choice of certain parameters.

The investigated resonator layout is depicted in Figure 3.16(a). The collimated output beam of a commercially available Tm^{3+}-doped fiber laser with a beam diameter of 5.5 mm is focused into the laser crystal with a beam diameter of 500–600 µm by a Galilean telescope consisting of the lenses L_1 and L_2 ($R < 0.5\%$ for 1850–2200 nm). The pump laser has a maximum output power of 106 W and emits with a beam propagation factor $M^2 < 1.1$ at 1907.6 nm. The $^5I_8 \rightarrow {}^5I_7$ transition is resonantly pumped by this wavelength [47, 88]. The input coupling is realized by an input coupling (IC) mirror ($R > 99.9\%$ for 1908 nm, $R > 99\%$ for the s-polarized 2090 nm light and $R < 2\%$ for the p-polarized 2090 nm light). Due to the high reflectivity of the IC mirror for the s-polarization of the 2090 nm light, high losses are introduced for this polarization ensuring a linearly p-polarized output. The Ho^{3+}:YAG crystal is 28 mm long and doped with 0.7 %, which means that 0.7 % of ytterbium ions of the host crystal have been replaced by Ho^{3+}-ions, to mitigate upconversion losses [46, 47]. It is mounted in a copper heat sink and water-cooled to 20 °C. The cavity is formed by a plane HR mirror ($R > 99.9\%$ for 1900–2100 nm) and a concave OC mirror with a radius of curvature of 0.3 m and the transmission of
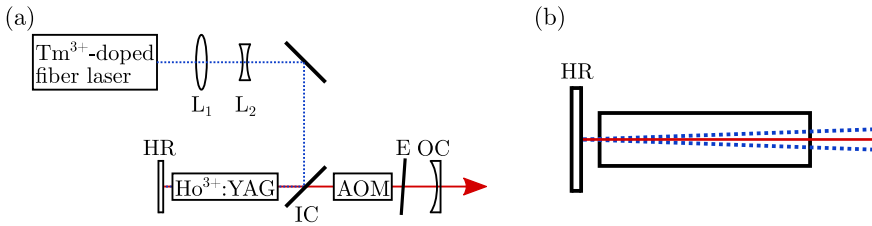
Figure 3.16: (a) Schematic setup of the reference resonator. (b) V-shaped pass of the pump beam through the laser crystal (dotted blue line).

the mirrors is varied from 30–70 %. The physical cavity length is 10 cm. The cavity is designed as short as the physical dimensions of the components allow to achieve short Q-switched pulses. In addition, a shorter cavity allows for a wider range of accepted thermal focal lengths. Because the HR mirror is highly reflective at the pump wavelength, the pump light passes the laser crystal twice resulting in an optimized absorption. However, the HR mirror is tilted by a small angle for the pump beam to avoid a direct back-reflection into the pump source. The back-reflected light is instead directed on a power meter by a scraper mirror ensuring the measurement of the residual pump power. Due to the angle of the HR mirror, the pump mode inside the laser crystal has a V-shape in the horizontal axis (see Figure 3.16(b)). To keep this effect small, the distance between the HR mirror and the Ho^{3+}:YAG crystal is minimized. In addition, the resonator contains an AOM for Q-switching, which is connected to its driver transmitting the modulation signal generated by an arbitrary function generator (Tektronix AFG31000 Series Arbitrary Function Generator). Furthermore, an 80 µm thick fused silica etalon allows the selection of the 2091 nm longitudinal line, which is the strongest emission line of Ho^{3+}:YAG, thus it ensures an efficient operation [89].

As the setup has been explained, the choice of OC mirror is now reasoned by simulating the mode diameter in the laser crystal for different conditions (see Figure 3.17). For all simulations, a fractional thermal loading of 12 % is assumed. At first, the pump diameter is fixed to 550 µm and the OC curvature is varied from 0.1 m up to a plane mirror corresponding to an infinite radius of curvature. Within this range of radii of curvature, the resonator is stable up to an absorbed pump power of 74 W. A smaller radius of curvature is equivalent to a smaller mode diameter in the crystal due to an increased focusing effect of the OC mirror. To obtain high output powers, the mode matching point with a higher pump power at the intersection of the pump diameter (dashed line) and the crystal mode diameter (solid lines) is of interest, as a mode matching of the pump and laser mode is essential for a laser with a high beam quality. For
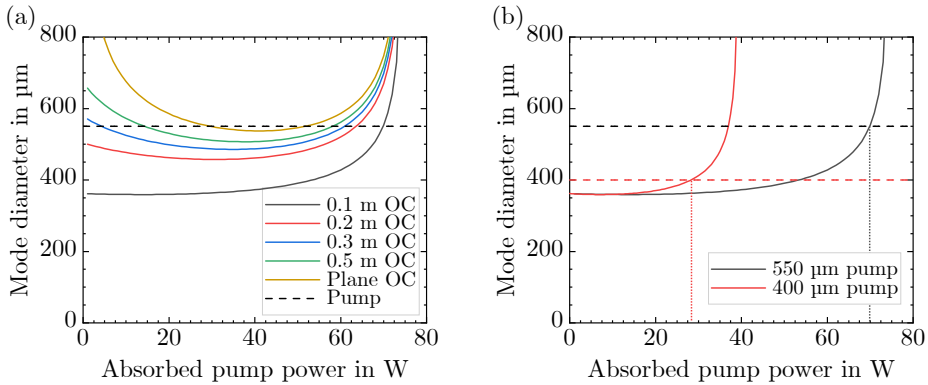
Figure 3.17: (a) Mode diameter in crystal depending on the absorbed pump power for different OC curvatures. The pump diameter is fixed to 550 μm (dashed line). (b) Mode diameter in crystal depending on the absorbed pump power for different pump diameters. For demonstration purposes, the OC curvature is fixed to 0.1 m.

a stronger curvature of the OC mirror, this mode matching point is at a higher pump power, therefore leading to an increased output power. However, this comes at the expense of an operation close to the stability limit which typically leads to fluctuations in the output power and beam quality. Therefore, such an operation mode should be avoided. On the other hand, if the pump diameter is adapted to the small mode resulting with the 0.1 m OC mirror, the stability limit drastically shifts to a lower pump power due to the increased thermal lensing (see red curve in Figure 3.17(b)). As a consequence, the expected output power is strongly reduced. It is therefore essential to select an OC mirror that matches the resonator length and pump diameter. Due to a compromise between the mode matching at a high power and an operation at a sufficient distance to the stability limit, an OC mirror with 0.3 m radius of curvature is selected.

The optimal OC reflectivity is determined experimentally by characterizing resonators with different OC reflectivities with respect to output power, pulse characteristics, and beam quality. Figure 3.18 shows the output power of the resonators with different OC transmissions depending on the pump power. The pump threshold increases with an increasing OC transmission, as this corresponds to a decreased intracavity laser field intensity. The slope efficiency is maximal for an OC transmission of 40 %, whereas the maximum output power of around 50 W is measured in the resonator with the 50 % transmission OC mirror. This is due to the overall lowest parasitic losses while absorbing the pump light efficiently at the same time. Figure 3.19(a) and Figure 3.19(b) shows the residual pump power and the depolarized power reflected from the
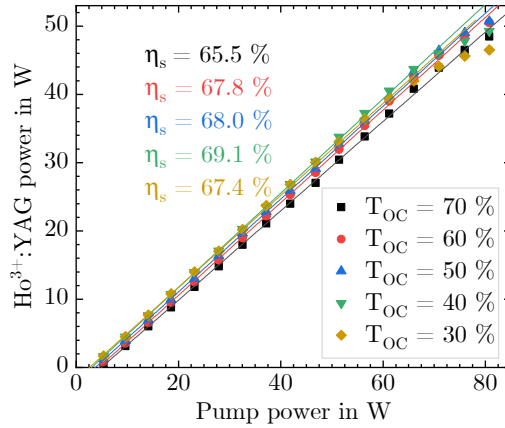
Figure 3.18: Ho^{3+}:YAG output power depending on pump power for different OC transmissions.
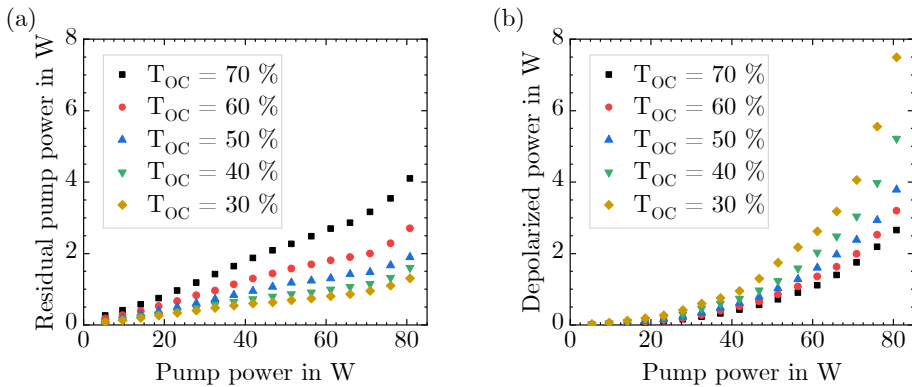

Figure 3.19: (a) Residual pump power and (b) depolarized power for different OC transmissions.

IC mirror, respectively, depending on the pump power. Because a lower OC transmission is equivalent to a higher intracavity laser intensity, the electrons are de-excited from the upper laser level by stimulated emission more efficiently. As a consequence from their transfer to the lower manifold, more pump photons can be absorbed, which leads to a reduced residual pump power. A further consequence of the high intracavity laser field is the increased depolarization loss. For the OC transmission of 50 %, both an efficient pump light absorption and an acceptable depolarization loss are ensured.

In Q-switched operation, the AOM is operated at 50 kHz. The pulse characteristics are determined by extracting 250 pulses from the oscilloscope connected to the PEM detector with a resolution of 1 ns. The maximum pulse energy of 0.9 mJ is achieved with the 50 % OC mirror (see Figure 3.20) for a pump power of 68 W. The pulse duration and the temporal pulse center, which is a measure for the pulse build-up time, in dependence on the pump power are shown in Figure 3.21. Both show the expected reciprocal relation with the pump power. The pulse duration is shortest for a low OC transmission, but it converges to 50 ns independent of the OC transmission at high pump powers. The same observation is made for the pulse center which
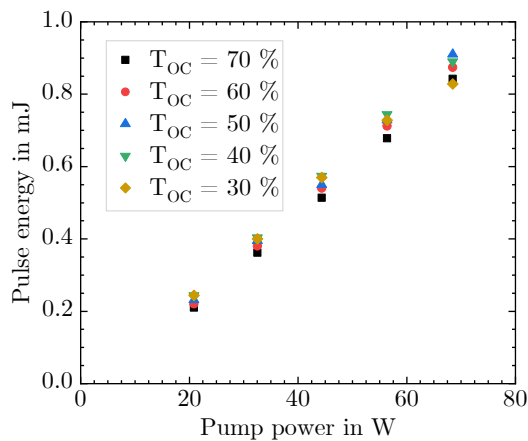

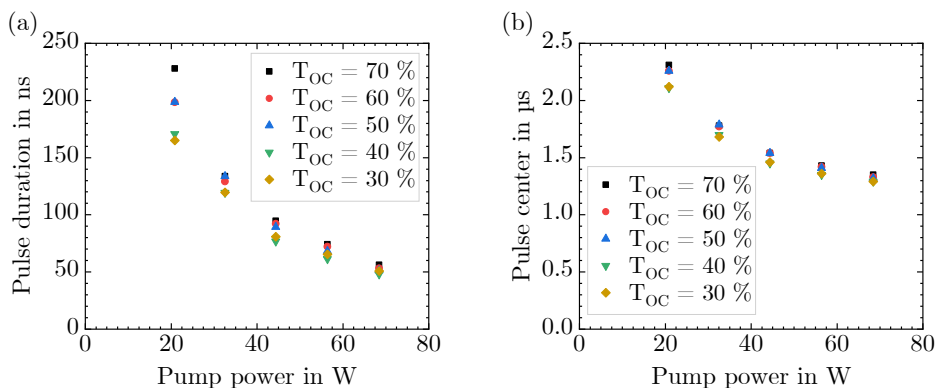Figure 3.20: Ho^{3+}:YAG pulse energy depending on pump power for different OC transmissions.

Figure 3.21: (a) Pulse duration and (b) temporal pulse center for different OC transmissions.

converges to approximately 1.4 µs at a high pump power. Here, the pulse center is the time that is measured for the pulses to reach the peak power from the moment that the Q-factor of the cavity is increased. Because the time required for the decay of the sound wave equals the time that the sound wave needs to travel from the ultrasonic transducer to the optical axis of the laser mode, the pulse center does not equal the pulse build-up time, but it does allow a comparison of the pulse build-up time at different pump powers.

Another important measure to evaluate the Q-switched output is the pulse stability. It is determined by calculating the root mean square (RMS) deviation of the pulse energy. A large pulse instability is typically associated with a large pulse jitter, which means that the pulses are not emitted at well-defined times. A high pulse stability is reached in the case when a good mode matching between pump and laser mode is established. Examples of instable and stable pulses are shown in Figure 3.22(a) and Figure 3.22(b), respectively. The pulses were recorded at a pump power of 44.4 W and 68.5 W in the resonator with the OC mirror with 50 % transmission. The instable pulses have an RMS energy deviation of 15.8 % and only show a small temporal overlap, whereas the stable pulses have an energy deviation of 1.7 % and further show a good temporal overlap. The instable pulses at 44.4 W of pump power are a consequence of a large mode mismatch of pump and laser mode. In contrast to this, the stable pulses at 68.5 W of pump power indicate a good mode matching, which is verified by a determination of the beam propagation factor (see Figure 3.23(a)). In both beam axes, the beam propagation factor is 1.12. The beam is further slightly astigmatic, which comes from
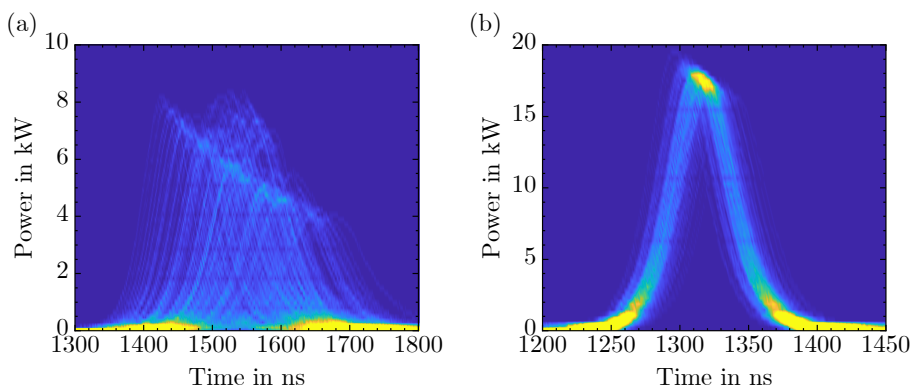

Figure 3.22: (a) Instable pulses recorded at a pump power of 44.4 W corresponding to an average pulse energy of 0.55 mJ. The RMS deviation is 15.8 %. (b) Stable pulses recorded at a pump power of 68.5 W corresponding to an average pulse energy of 0.91 mJ. The RMS deviation is 1.7 %.
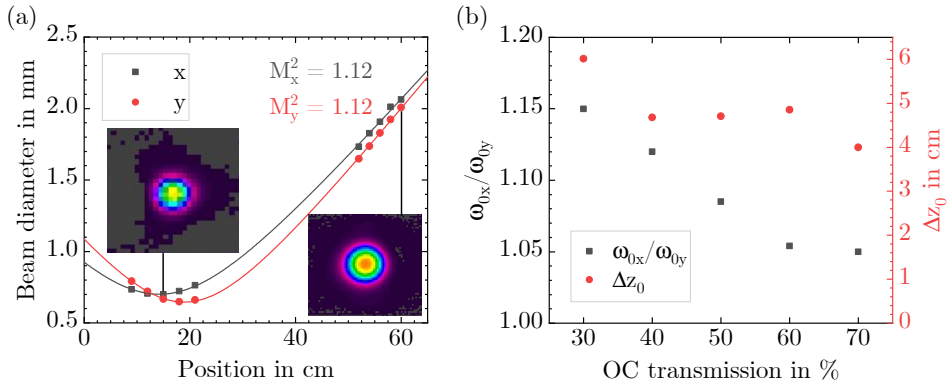
Figure 3.23: (a) Measurement of beam propagation factor with 50 % OC transmission at 68 W of pump power yielding 45 W of output power. (b) Quantification of astigmatism as a ratio of the beam waist diameters in the x- and y-direction and the difference of the beam waist positions. A higher OC transmission comes with a weaker astigmatism.

the thermally induced bifocusing of the laser crystal. Because the beam axis in which the beam is linearly polarized experiences the smaller focal length f_r, the stability limit is closer, which leads to a widening of the beam in this axis and explains the different beam diameters in the horizontal and vertical beam axis. The second contribution for the astigmatism results from the tilted 45° mirror. Tilted elements in resonators effectively have a different path length in the sagittal and tangential plane of the beam. Therefore, the effective resonator length is slightly different in both beam directions [90]. Especially when the resonator is operated near its stability limit, small deviations in the resonator length strongly influence the resonator mode sizes. The beam propagation factor was measured for the different OC transmissions at a pump power of 68.5 W and the astigmatism was quantified by calculating the ratio of the beam waist diameters in the vertical and horizontal beam axis and the difference of the beam waist positions. Although the fractional thermal loading was shown to increase for an increasing OC transmission in Figure 3.9, the trend is towards a weaker astigmatism when the OC transmission is increased. This might be explained by two contributions: Firstly, as the absorbed pump power decreases with an increasing OC transmission, the thermal lensing is weaker. Secondly, the number of cavity round-trips is reduced with an increasing OC transmission, thus the influence of the thermal lens is decreased.

Figure 3.24 shows the spectral output for different OC transmission. A shift towards a longer wavelength is observed when the OC transmission is reduced. This is in line with the results
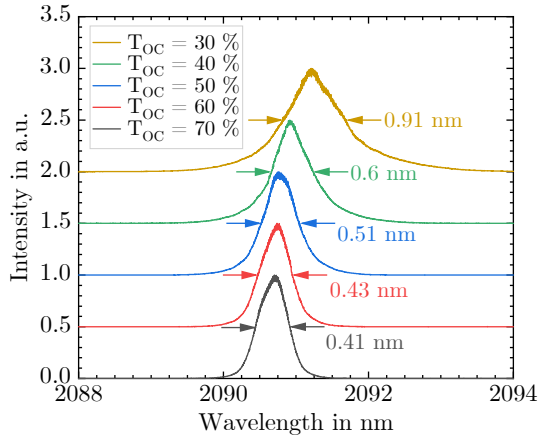
Figure 3.24: Spectral output depending on the transmission of the OC mirror.

obtained by Kwiatkowski et al. [91]. Additionally, a broadening of the spectrum with a higher OC reflectivity is observed as a result of the different manifold population densities and the resulting different gain cross-sections.

As a result of the previous investigations, the OC reflectivity is fixed to 50 % mainly due to the optimized output power that is achieved in this configuration.

3.2.3 Qualitative Assessment of Thermal Blooming of the 1908 nm Pump Beam

In this section, the influence of water vapor absorption of the 1908 nm pump beam on its beam propagation is qualitatively investigated. This effect is discussed here, as it is relevant for the explanation of observations described in Chapter 4 and 5.

When a laser beam propagates through a turbulent medium, it is distorted due to inhomogeneities in the refractive index of the medium [92]. In the case of a heat-induced turbulence, this effect is referred to as thermal blooming [92, 93]. In this work, the effect becomes relevant for the Tm^{3+}-doped fiber laser emitting at 1908 nm that is used to pump the Ho^{3+}:YAG laser crystal. Figure 3.25(a) and Figure 3.25(b) show the absorption coefficient of water vapor from 0–10 µm and around 1.908 µm, respectively. In addition, the spectral output of the
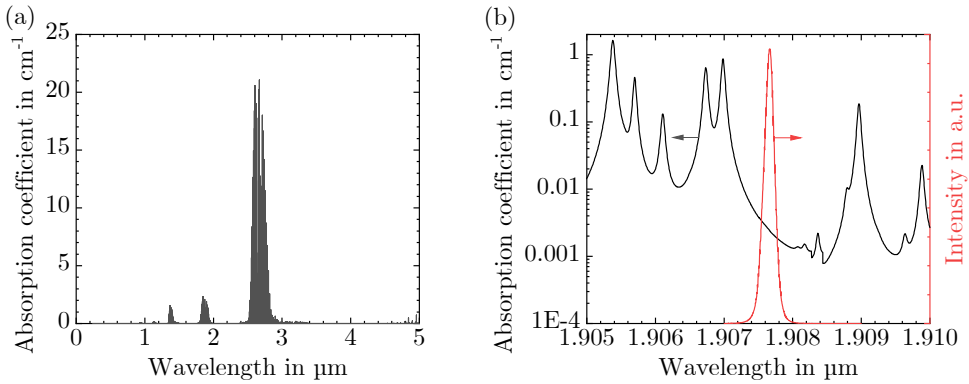
Figure 3.25: Absorption coefficient of water vapor obtained from the HITRAN database [94] and calculated with the HITRAN Application Programming Interface (HAPI) [95] from (a) 0–5 µm and (b) around 1908 nm.

Tm^{3+}-doped fiber laser cooled to 22 °C and emitting at 80 W is included in Figure 3.25(b). The line-by-line transition data was obtained from the *hi*gh-resolution *tran*smission molecular absorption (HITRAN) database [94]. To calculate the absorption coefficient from the line intensities, the HITRAN Application Programming Interface (HAPI) was used [95]. When a gas is exposed to pressure and temperature, the transition lines broaden homogeneously due to collisions of the molecules and inhomogeneously due to thermal movement of the molecules [63]. This is taken into account by assuming a Voigt profile for each of the lines [96]. Figure 3.25(b) shows the overlap of the spectral emission of the Tm^{3+}-doped fiber laser with the 1.907 µm absorption line. Thus, when the laser is propagated through undried air containing water vapor, it is partially absorbed. This leads to a heating of the air, which decreases the refractive index due to expansion and convection [92, 97]. As a consequence, the laser beam is defocused. Thermal blooming becomes especially critical when the laser intensity is high and the propagation length through the ambient air is long.

To observe this effect qualitatively, the output beam of the Tm^{3+}-doped fiber laser is focused by a lens with a focal length of $f = 57\,cm$ and is subsequently reflected by an HR mirror (see Figure 3.26). A small amount of light passes the HR mirror and propagates through the air with a negligible thermal blooming effect, as the air is not heated due to the low power of the beam. The part of the beam that is reflected from the HR mirror propagates through the ambient air with a high power resulting in the presence of the thermal blooming effect. The propagation distance for both beams is approximately 70 cm. For both beams, the divergence and beam propagation factor M^2 are measured to estimate the diameter in the beam waist. The
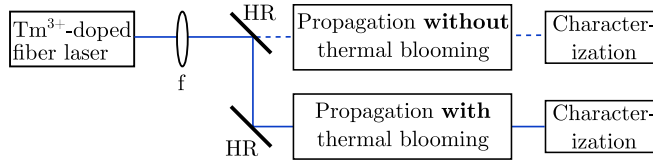
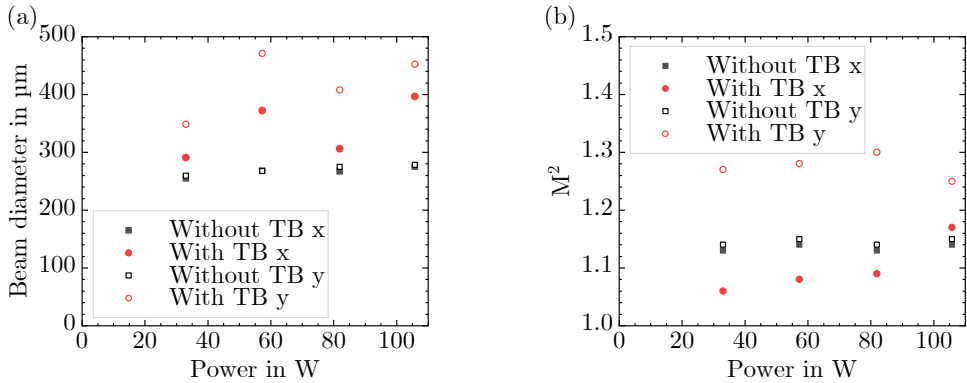Figure 3.26: Schematic setup to qualitatively measure the thermal blooming of the Tm^{3+} fiber laser.

Figure 3.27: (a) Beam waist diameter with and without thermal blooming (TB) depending on the power. (b) Beam propagation factor M^2 with and without thermal blooming depending on the pump power. x/y refers to the horizontal/vertical beam axis.

beam diameter of the thermally bloomed beam is expected to be larger due to the defocusing nature of thermal blooming in air. The measurement was conducted at an average temperature of $(23 \pm 1)\,°C$ and a relative humidity of $(49 \pm 3)\,\%$ corresponding to an absolute humidity of $(10 \pm 1)\,g/m^3$.

Figure 3.27(a) shows the beam waist diameter with and without thermal blooming for the horizontal (x) and vertical (y) beam axis. Without thermal blooming, the beam diameter is only slightly increasing with increasing power and it is about $270\,μm$ in diameter. With thermal blooming, an increase in beam diameter is observed in both beam axes, with the beam diameter in the vertical axis showing a stronger increase. Besides, a trend towards a stronger increase in beam diameter with increasing power is observed. This is explained by the increased heating of the air due to the higher laser intensity. The beam propagation factor without thermal blooming is around 1.15 in both beam axes and constant over power. Under the presence of thermal blooming, the beam propagation factor mainly increases in the vertical beam axis to a value of almost 1.3, whereas it is similar to the value without thermal blooming in the horizontal
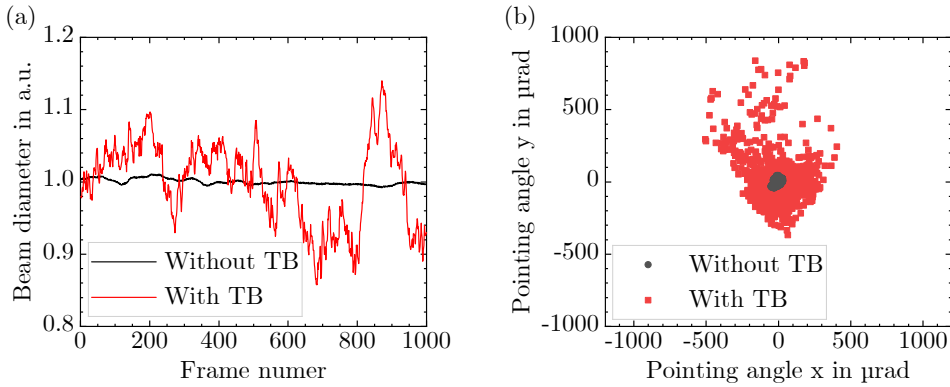
(a)

(b)

Figure 3.28: (a) Change in vertical beam diameter over time without (black) and with (red) thermal blooming (TB). (b) Pointing angle in the horizontal (x) and vertical (y) direction. Measurements conducted at a laser power of 106 W.

axis within the limits of measurement accuracy. The asymmetry in the horizontal and vertical direction results from a complex interplay of the heating of the air, the flow conditions near the optical table induced by the flow box, and the exact distribution of the water vapor concentration. The detailed description and investigation of these contributions would be beyond the scope of this thesis.

Next to the defocusing effect of thermal blooming, a further effect is observed: a considerable instability of the beam diameter and angular pointing over time. To observe this effect, the pyro-electric detector is positioned in the distance of the focal length of an $f = 23.6$ cm plano-convex lens and the beam diameter and beam centroid are measured over 1000 frames at the maximum laser power of 106 W. The maximum change in beam diameter is around 1 % without thermal blooming in both axes, whereas it is 10 % in the horizontal and 14 % in the vertical beam axis when thermal blooming is present (see Figure 3.28(a)). In this setup, a change in beam diameter on the detector corresponds to a change in divergence in front of the focusing lens which is in turn connected to a change in beam waist diameter. Figure 3.28(b) shows the beam centroid position on the detector converted into the pointing angle. Without thermal blooming, an average pointing angle of around 15 µrad is determined in all directions. With thermal blooming, the pointing angle is symmetric in the horizontal axis and takes a mean value of 100 µrad. In contrast to this, an asymmetry is observed in the vertical beam axis, where the average pointing angle in the negative direction is approximately 100 µrad, whereas it amounts to 160 µrad in the positive direction.
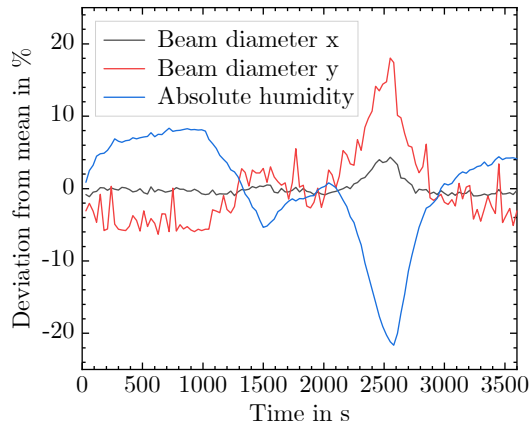
Figure 3.29: Beam diameter in the horizontal (x) (black line) and vertical (y) (red line) beam direction and the absolute ambient humidity (blue line) measured over a time of 1 h.

Thermal blooming has severe effects on the laser output of the Ho^{3+}:YAG laser, as it defines the pumped volume. This is especially problematic when the ambient conditions change through the use of air conditioning. Figure 3.29 shows the change in the far-field beam diameter of a Ho^{3+}:YAG laser operated at 50 W close to the resonator stability limit and the absolute humidity of the ambient air. The data show a negative correlation with a correlation factor of -0.8 between the absolute humidity and the horizontal beam diameter and a correlation factor of -0.93 between the absolute humidity and the vertical beam diameter. With a decrease in the absolute humidity, the thermal blooming decreases, which in turn reduces the pump beam diameter. As a consequence, the thermal lens becomes stronger, which shifts the operation point closer to the resonator stability limit, thus it results in an increased output beam diameter. Consequently, the experiments in this work were conducted at roughly constant humidity conditions to eliminate this effect.

In conclusion, this section has provided qualitative data on the thermal blooming of the Tm^{3+}-doped fiber laser in the laboratory environment. Both a defocusing of the beam as well as an increasingly unstable behavior over time has been observed.

4   Power Scaling of Ho^{3+}:YAG Resonators

In this chapter, two approaches for the power scaling of Ho^{3+}:YAG resonators with a near-diffraction-limited beam quality are presented. The power scaling capabilities by improving the thermal management inside the crystal are investigated in Section 4.2. Section 4.3 presents the power scaling in a MOPA system.

Section 4.2 is based on the results discussed in the publication:

4.1   Introduction

As a strategy for building crystal lasers with a diffraction-limited beam quality, end-pumping the laser rods is the most suitable pump geometry because this enables an optimal mode matching between the pump and the laser mode. However, a high beam quality requires the pump mode to be adapted to the laser mode, which typically results in small mode diameters, especially when compact designs are desired [39, 99, 100]. Due to the exponential absorption of the pump light, this leads to high peak temperatures that come along with thermally induced stress peaks near the front facet of the laser crystal [99]. In the worst case, crystal fracture is the consequence, but even when this limit is not reached, the thermally induced stresses lead to birefringence, thus a deterioration in beam quality and optical losses result [39, 101]. A solution for reducing the temperature peak at the crystal front, which has been proven to be useful, is the attachment of an

undoped end cap, fabricated from the same material as the crystal host material, to the front of the crystal by diffusion-bonding [39]. This results in an axial heat transport from the doped into the undoped region, therefore drastically reducing the peak temperature inside the crystal [99]. In addition, end face bulging is avoided [39]. Such composite crystals have widely been used for the power scaling of laser resonators in the last decades [102–105].

When this approach is thought further, an improved thermal management along the crystal axis cannot only be generated by attaching undoped end caps but also by the diffusion-bonding of differently doped crystal segments. By using increasingly doped crystal segments along the pump light direction, the pump light absorption is optimized, leading to a more uniform longitudinal temperature gradient. This results in a further peak temperature and stress reduction as compared to only attaching an undoped end cap [106]. This approach has been used in a wide variety of laser crystals including Nd^{3+}:YAG [32, 107, 108], Nd^{3+}:YVO$_4$ [109, 110], Nd^{3+}:YLF [111], Tm^{3+}:YAG [112], and Yb^{3+}:YAG [113] in recent years. In addition to an improved output power and slope efficiency, an improvement in the beam profile and beam quality was reported [32, 108, 112]. Furthermore, with a multi-segmented crystal a weaker thermal lensing effect was observed [109, 110]. Wilhelm et al. and Jiang et al. have also presented different optimization strategies for designing multi-segmented crystals [100, 111]. Besides multi-segmented crystals, some groups have researched on gradient-doped laser crystals, e.g. Nd^{3+}:YAG [114, 115], Nd^{3+}:YLF [116], and Cr^{2+}:ZnSe [117], which are intended to generate a constant absorption over the crystal length. However, the fabrication of gradient-doped crystals remains challenging [100, 111, 118].

The multi-segmented approach has so far not been used in Ho^{3+}:YAG lasers. Due to their efficient resonant pumping scheme and the resulting low quantum defect, the heat generation in Ho^{3+}:YAG lasers is low [119]. Therefore, it is unclear whether a multi-segmented crystal leads to a significant improvement of the laser performance. This question is addressed in Section 4.2.

Another approach for the power scaling of Ho^{3+}:YAG laser resonators with a diffraction-limited beam quality is the amplification in a single- or multi-stage amplifier system. With only an oscillator, the output power cannot be scaled infinitely, as thermal lensing and thermal distortions drastically increase at elevated pump powers resulting in a deterioration of the beam quality [120]. By adding an amplifier system, an output power scaling of the laser system is enabled while maintaining the beam quality, thus increasing the brightness of the laser source [39]. The preservation of the beam quality is explained by the lower influence of the

thermal lens in the amplifier crystal because it is only passed once, whereas it is passed multiple times in a resonator geometry [39, 121]. Additionally, no resonator stability criteria limit the achievable output power and the mode matching in an amplifier is uncritical, which enables to use a larger pump than laser beam diameter to mitigate thermal lens aberrations. In addition to the beam quality, the pulse width and repetition rate as well as the spectral width are mainly determined by the oscillator in a MOPA system [39, 121]. In contrast to this, the amplifier stage determines the output power and pulse energy [39]. Besides the power and energy scalability, a MOPA system offers further advantages. Firstly, the oscillator can be operated at a lower output power mitigating the risk of damaging intracavity optical components [122]. Secondly, when the Ho^{3+}:YAG source is used as pump source for an OPO, the resonator needs to be protected from back-reflections occuring at the OPO components, which cause instabilities [123]. Typically, Faraday isolators are used for this purpose. However, these components are power limited due to parasitic absorption [124]. Here, an amplifier system allows to scale the output power subsequent to the isolators. The disadvantages of a MOPA system are the increased complexity and the lower compactness compared to laser resonators.

MOPA approaches have already widely been used to increase the output power of Ho^{3+}:YAG lasers [30, 120, 125]. In 2018, Zhao et al. showed a two-stage amplifier system with an output power of 231 W [120]. Liu et al. reported a total output power of 332 W from a two-stage amplifier in 2021 [30]. In 2022, Mi et al. presented a 450 W Ho^{3+}:YAG MOPA system comprised of three amplifier stages and they further investigated the depolarization losses of the system [125]. In all these MOPA systems, the beam quality factor was well below $M^2 < 2$.

In Section 4.3, a single-stage Ho^{3+}:YAG amplifier is investigated. In distinction to already existing literature, the focus in this thesis is set to the investigation of the amplification behavior for different pump powers and the agreement with an appropriate physical model.

4.2   Resonator with a Segmented Laser Crystal

The following sections describe the design and characterization of the segmented crystal as well as its use in a laser resonator. At first, theoretical considerations concerning the design of a segmented crystal are presented in Section 4.2.1. This includes the calculation of the optimal longitudinal doping concentration. Section 4.2.2 shows the experimental characterization of the

designed segmented crystal. The cavity design in which both the segmented and a corresponding homogeneously doped crystal are compared and its optimization are presented in Section 4.2.3. In Section 4.2.4, details on the optimum resonator configurations with both laser crystals are given. For a further investigation of the crystals, an interferometric investigation of the thermal lens is presented in Section 4.2.5, which provides information on the radial temperature profile in the crystal. Information on the longitudinal temperature distribution is generated by a simulation based on a beam propagation method and the results are presented in Section 4.2.6. Finally, Section 4.2.7 explains the differences of the resonators with the two crystals by means of resonator stability criteria and discusses differences to existing literature. The investigation of the resonator with the segmented crystal is concluded with a summary in Section 4.2.8.

4.2.1   Theoretical Considerations on Segmented Crystals

In this section, the optimum longitudinal absorption coefficient required for a uniform pump light absorption over the length of the crystal is derived. The derivation is shown for single- and double-pass pumping and the results are compared to a conventional homogeneous doping concentration. Then, the absorption properties of a segmented crystal comprised of N increasingly doped segments are derived. Finally, the numerical approach used for the optimization of a segmented crystal with four segments is described.

Calculation of the Optimal Absorption Coefficient

The heat generated in the laser crystal depends on the absorbed pump power per unit length. Figure 4.1 schematically illustrates the absorption of light in a medium with width dz and
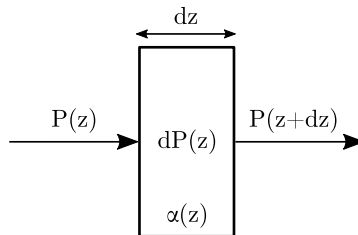

Figure 4.1: Derivation of absorbed power $-\mathrm{d}P(z)$ in a medium with absorption coefficient $\alpha(z)$.

absorption coefficient $\alpha(z)$ when the pump light passes the crystal in a single-pass. For the absorbed light $-\mathrm{d}P(z)$ in the medium, it holds:

$$-\mathrm{d}P(z) = -(P(z + \mathrm{d}z) - P(z)) = \alpha(z)P(z)\mathrm{d}z \,, \tag{4.1}$$

where $P(z)$ and $P(z + \mathrm{d}z)$ are the incident and transmitted pump power, respectively. This differential equation is solved by

$$P(z) = P_0 \exp\left(-\int_0^z \alpha(z')\mathrm{d}z'\right) \,. \tag{4.2}$$

Thus, in a single-pass of the pump light, the absorbed pump power per unit length is given by

$$P_{\mathrm{sp}}(z) = -\frac{\mathrm{d}P(z)}{\mathrm{d}z} = \alpha(z)P_0 \exp\left(-\int_0^z \alpha(z')\mathrm{d}z'\right) \,. \tag{4.3}$$

In the case of a homogeneously doped reference crystal with length L_0 and a constant absorption coefficient α_0, an absorbed pump power per unit length of

$$P_{\mathrm{hom,sp}}(z) = \alpha_0 P_0 \exp\left(-\alpha_0 z\right) \tag{4.4}$$

results. Provided that an axial heat transport is neglected, the generated heat and the temperature in the crystal are proportional to the absorbed pump power per unit length, therefore they follow this exponential decay as well. Consequently, a higher heat load results near the front facet of the crystal than at the end facet.

In the case of a single-pass pumping scheme, a homogeneous heat distribution is achieved with a longitudinally varying absorption coefficient $\alpha_{\mathrm{sp}}(z)$, which is derived by requiring that $P_{\mathrm{sp}}(z)$ is constant. From $P_{\mathrm{sp}}(z) \stackrel{!}{=} P_{\mathrm{sp}}(0)$, a differential equation results for the optimal absorption coefficient:

$$\frac{\mathrm{d}\alpha_{\mathrm{sp}}(z)}{\mathrm{d}z} = \alpha_{\mathrm{sp}}(z)^2 \quad \text{with} \tag{4.5}$$

$$\alpha_{\mathrm{sp}}(0) = \frac{1 - \exp(\alpha_0 L_0)}{L_0} \,. \tag{4.6}$$

The initial condition (4.6) is derived by requiring that the total absorption averaged over the crystal length in the homogeneously doped crystal is the same as the constant absorption in

the crystal with an optimal doping concentration. Solving Equation (4.5) with a separation of variables approach yields the optimal absorption coefficient [100]

$$\alpha_{\mathrm{sp}}(z) = \left(\frac{L_0}{1 - \mathrm{e}^{-\alpha_0 L_0}} - z \right)^{-1} . \tag{4.7}$$

The approach for calculating the optimal absorption coefficient in a double-pass pumping scheme, where the pump light is back-reflected after the first pump pass, is similar. Both the light passing the crystal in the forward direction as well as the back-reflected light contribute to the heat generation. Thus, in analogy to Equation (4.3), the absorbed power per unit length is described by

$$P_{\mathrm{dp}}(z) = \alpha(z)P_0 \left[\exp\left(-\int_0^z \alpha(z')\mathrm{d}z' \right) + \exp(-2\alpha_0 L_0) \exp\left(\int_0^z \alpha(z')\mathrm{d}z' \right) \right], \tag{4.8}$$

where the total absorption is assumed to be the same as that of the reference crystal after a double-pass of the pump light. From $P_{\mathrm{dp}}(z) \overset{!}{=} P_{\mathrm{dp}}(0)$, the differential equation for the optimal absorption coefficient $\alpha_{\mathrm{dp}}(z)$ is derived:

$$\frac{\mathrm{d}\alpha_{\mathrm{dp}}(z)}{\mathrm{d}z} = \alpha_{\mathrm{dp}}(z)^3 \frac{L_0}{\sinh(\alpha_0 L_0)} \sqrt{\left(\frac{\sinh(\alpha_0 L_0)}{\alpha_{\mathrm{dp}}(z)L_0} \right)^2 - 1} \quad \text{with} \tag{4.9}$$

$$\alpha_{\mathrm{dp}}(0) = \frac{\tanh(\alpha_0 L_0)}{L_0} . \tag{4.10}$$

This differential equation is solved analytically in Mathematica. Under the consideration that the absorption coefficient needs to be positive and monotonously increasing, the only physically meaningful solution is [100]

$$\alpha_{\mathrm{dp}}(z) = \sqrt{(L_0 - z)^2 + \frac{L_0{}^2}{\sinh^2(\alpha_0 L_0)}}^{\,-1} . \tag{4.11}$$

Figure 4.2 shows a comparison of the absorption coefficient of a homogeneously doped reference crystal (0.5 % doping concentration, 28 mm length) (black) and the corresponding optimal absorption coefficients in a single- (red) and double-pass (blue) configuration in comparison.

From the absorption coefficient, the absorbed power per unit length is calculated by Equation (4.3) and (4.8) for the single-pass $P_{\mathrm{opt,sp}}(z)$ and the double-pass case $P_{\mathrm{opt,dp}}(z)$. The
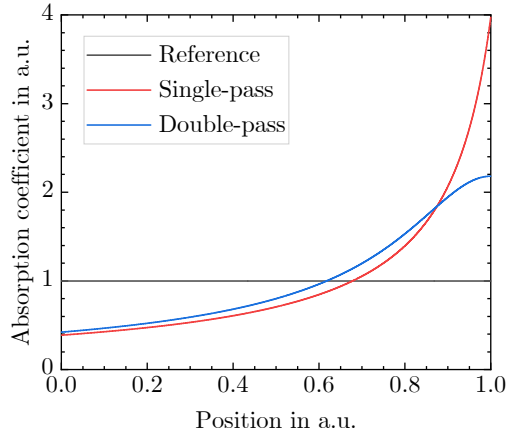
Figure 4.2: Optimal absorption coefficients for a laser crystal in a single- (red) and double-pass (blue) configuration. The absorption coefficient of the reference crystal is indicated in black.
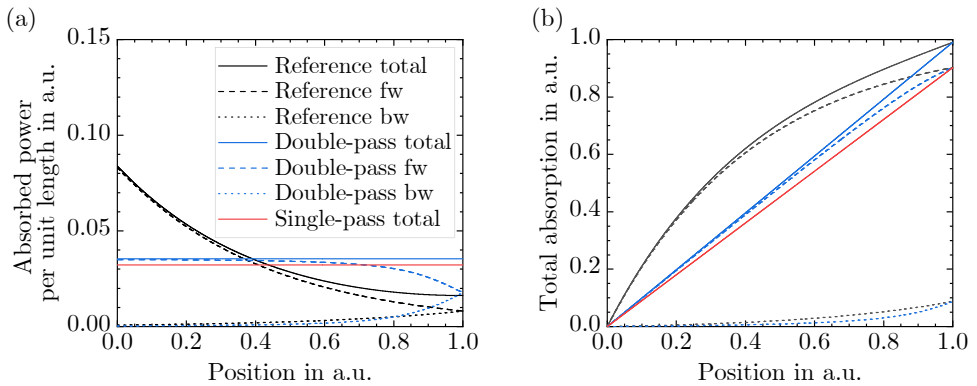

Figure 4.3: (a) Absorbed power per unit length and (b) total absorbed power in the forward and the backward direction in a crystal with optimal absorption coefficient (single-pass (red) and double-pass (blue)) in comparison to a crystal with homogeneous absorption coefficient (black). fw/bw refers to the forward and backward direction, respectively.

total absorbed power up to the position z in the crystal is calculated by integrating these equations along the crystal axis. The absorbed power per unit length and the total absorption are compared for the three cases in Figure 4.3(a) and Figure 4.3(b), respectively. In the case of the homogeneously doped crystal and the optimal double-pass case, the contributions to the total absorbed power are shown for the forward and the backward pass of the light. As designed, the optimal absorption coefficients generate a constant absorbed power per unit length. Because

in the double-pass case a greater amount of light is absorbed as compared to the single-pass case, the absorbed power per unit length is larger. The total absorption along the crystal axis increases linearly. In the single-pass case, 90 % of the light is absorbed, whereas this amounts to 99 % in the case of the double-pass.

One drawback behind this theoretical approach is the difficulty in growing a crystal with a specific longitudinal absorption coefficient [100, 111, 118]. However, the optimal absorption coefficient can be approached by diffusion-bonding several crystal segments with different lengths and absorption coefficients. The following section describes the absorption in the resulting segmented crystal mathematically.

Absorption in a Segmented Laser Crystal

A scheme of a homogeneously doped and a segmented crystal is depicted in Figure 4.4(a) and Figure 4.4(b), respectively. The homogeneously doped crystal has a constant longitudinal absorption coefficient α_0 and length L_0, whereas the segmented crystal is characterized by N segments with absorption coefficients α_i and lengths L_i ($i = 1, ..., N$). In analogy to Equation (4.8), the absorbed power per unit length can be considered in each segment in the forward and in the backward direction. In segment n ($L_1 + ... + L_{n-1} \leq z < L_1 + ... + L_n$), it holds for the forward and backward direction, respectively, that [100]

$$P_{\text{seg,fw}}(z) = \alpha_n P_0 \exp\left(-\sum_{i=1}^{n-1} \alpha_i L_i\right) \exp\left[-\alpha_n\left(z - \sum_{i=1}^{n-1} L_i\right)\right] \quad \text{and} \tag{4.12}$$

$$P_{\text{seg,bw}}(z) = \alpha_n P_0 \exp\left(-2\sum_{i=1}^{N} \alpha_i L_i\right) \exp\left(\sum_{i=1}^{n-1} \alpha_i L_i\right) \exp\left[\alpha_n\left(z - \sum_{i=1}^{n-1} L_i\right)\right]. \tag{4.13}$$

The single-pass case is directly described by Equation (4.12), whereas the total absorbed power per unit length in segment n in the double-pass case is described by

$$P_{\text{seg,dp}}(z) = P_{\text{seg,fw}}(z) + P_{\text{seg,bw}}(z) \tag{4.14}$$

$$= \alpha_n P_0 \cosh\left[\sum_{i=n}^{N} \alpha_i L_i - \alpha_n\left(z - \sum_{i=1}^{n-1} L_i\right)\right]. \tag{4.15}$$

To ensure the comparability between the segmented crystal and the homogeneously doped reference crystal, two boundary conditions are imposed. Firstly, the length of both crystals is set equal.
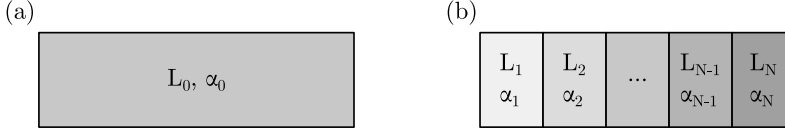
Figure 4.4: Scheme of (a) homogeneously doped crystal with constant absorption coefficient α_0 and length L_0 and (b) segmented crystal consisting of N segments with constant absorption coefficients α_i and lengths L_i.

Secondly, the absorption times length product must be equivalent, which leads to the same absorption after passing the entire crystal. These two conditions are mathematically formulated as

$$L_0 = \sum_{i=1}^{N} L_i \quad \text{and} \tag{4.16}$$

$$\alpha_0 L_0 = \sum_{i=1}^{N} \alpha_i L_i \, . \tag{4.17}$$

To generate a uniform heat distribution in the crystal, the absorbed power per unit length must be as homogeneous as possible, which is achieved by optimizing the segment lengths L_i and the absorption coefficients α_i. The following section describes different approaches for numerically optimizing the crystal segments.

Numerical Optimization of the Segmented Crystal

Overall, the optimization problem has $2N$ parameters and 2 boundary conditions, resulting in $2(N-1)$ degrees of freedom. Wilhelm et al. have described different optimization strategies, including approaching the optimal absorption coefficient by that of the segmented crystal, minimizing the variance of the resulting temperature distribution, and minimizing the peak temperatures of the distribution [100]. In all these approaches, the axial heat transport was neglected. Jiang et al. took this into consideration and optimized a segmented crystal based on minimizing the maximum tensile stress in the crystal [111]. The approach used in this thesis slightly differs from those presented by Wilhelm et al. It minimizes the difference between the absorbed power per unit length of the segmented crystal $P_{\text{seg}}(z)$ and the optimally doped crystal $P_{\text{opt}}(z) = P_{\text{opt}} = \text{const.}$. Mathematically, this is described by minimizing the function

$$f_1(\alpha_1, ..., \alpha_N, L_1, ..., L_N) = \int_0^L (P_{\text{seg}}(z) - P_{\text{opt}})^2 \mathrm{d}z \, . \tag{4.18}$$

In principle, this optimization could be performed for single-pass and double-pass pumping. However, for this work, only the case of double-pass pumping is optimized due to the resulting increased absorption efficiency. The optimization is implemented numerically. In addition, several constraints are imposed on the optimization. Firstly, the number of segments is fixed to $N = 4$ because only a small improvement was shown with each additional segment [126]. As the difficulty in the fabrication process also increases with each segment, a minimum number of segments should be aimed for from this point of view. Secondly, increasing doping concentrations over the length of the crystal are assumed as a logical consequence of the optimal doping concentration derived in the prior section. Thirdly, for three of the segments, already grown crystals should be used, which limits the available doping concentrations for these segments to 0.35 %, 0.7 %, 0.75 %, 0.9 %, and 1.1 %. In addition, the highest doping concentration is limited to 1.1 % to mitigate upconversion losses [47]. For the fourth segment, the position in the segmented crystal and the doping concentration could be chosen freely.

To evaluate the resulting segmented crystals, different criteria are considered:

1. Difference between the absorbed power per unit length of the segmented $P_{\text{seg}}(z)$ and the optimally doped crystal P_{opt} described by

$$f_1(\alpha_1, ..., \alpha_N, L_1, ..., L_N) = \int_0^L (P_{\text{seg}}(z) - P_{\text{opt}})^2 \mathrm{d}z \,. \tag{4.19}$$

2. Increase of total absorption along the segmented crystal compared to the optimum crystal described by

$$f_2(\alpha_1, ..., \alpha_N, L_1, ..., L_N) = \int_0^L \left(\int_0^z P_{\text{seg}}(z')\mathrm{d}z' - \int_0^z P_{\text{opt}}\mathrm{d}z' \right)^2 \mathrm{d}z \,. \tag{4.20}$$

3. Maximum absorbed power per unit length described by

$$f_3(\alpha_1, ..., \alpha_N, L_1, ..., L_N) = \max(P_{\text{seg}}(z)) \,. \tag{4.21}$$

These criteria should be minimized at the same time. The optimal crystal with a gradual doping concentration, the homogeneously doped crystal, and an optimized segmented crystal with four segments, which has been optimized without any restrictions regarding the doping concentrations, serve as a reference. The segment characteristics of the latter crystal are

given in Table 4.1. In addition to the numerical values of f_1, f_2, and f_3, the table shows the product of these three figures of merit normalized to this segmented crystal. Also, the reduction of the maximum crystal temperature ΔT_{max} with respect to the homogeneously doped crystal is given in Table 4.1. A peak temperature reduction of 46.3 % is achieved with the optimal crystal, whereas this amounts to 37.2 % in the freely optimized segmented crystal. Figure 4.5(a) shows the absorbed power per unit length of this crystal (blue) in

Table 4.1: Comparison of design and figures of merit for the reference crystals (optimum crystal with gradual doping concentration, homogeneously doped crystal, and segmented crystal optimized without constraints on the doping concentrations of the segments).

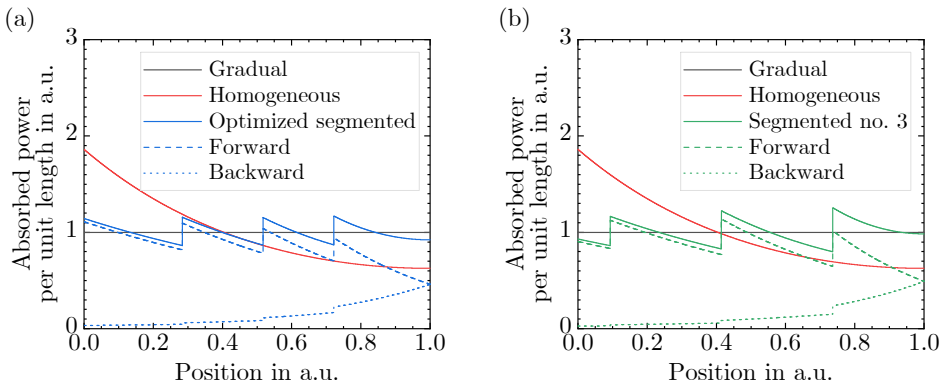| Crystal	f_1	f_2	f_3	$f_1 \cdot f_2 \cdot f_3$	ΔT_{max} in %
Optimum L = 28 mm Gradual doping	0	0	34.6	0	46.3
Homogeneous L = 28 mm D = 0.7 %	425.9	308.6	64.5	11145.7	0
Optimized segmented L = (7.9, 6.6, 5.7, 7.8) mm D = (0.43, 0.58, 0.77, 1.03) %	21.3	0.9	40.5	1.0	37.2

Figure 4.5: Absorbed power per unit length for the (a) segmented crystal optimized without constraints on the doping concentration (blue) and the (b) segmented crystal no. 3 optimized with three fixed doping concentrations (green). For comparison, the absorbed power per unit length is also shown for the gradually doped crystal (black) and the homogeneously doped crystal (red).

the forward (dashed), backward (dotted), and both (solid) directions in comparison with the optimum crystal (black) and the homogeneously doped crystal (red).

Based on the doping concentrations of the freely optimized segmented crystal, the doping concentration of the fourth segment is fixed to 1.1 %. Furthermore, the doping concentrations 0.7 % and 0.75 % are not used in a crystal at the same time due to the small difference in doping concentration. Under these constraints, five promising candidates for segmented crystals are given in Table 4.2. For crystal no. 1 and no. 2, the doping concentration of the first segment was unconstrained, and for the crystals no. 3, no. 4, and no. 5 the second segment was unconstrained. All candidates show a reduction of the peak temperature between 30 % and 34 % with respect to the homogeneously doped crystal. Because the segmented crystal no. 3 has the lowest figure of merit $f_1 \cdot f_2 \cdot f_3$, this crystal has been chosen for fabrication. Figure 4.5(b) shows the absorbed power per unit length for this crystal (green) in the forward (dashed), backward (dotted), and in both (solid) directions in comparison with the gradually doped crystal (black) and the homogeneously doped crystal (red). The absorption behavior is similar as with the freely optimized segmented crystal.

Table 4.2: Comparison of design and figures of merit for the numerically optimized segmented crystals with three fixed doping concentrations. The best figure of merit is achieved with crystal no. 3.

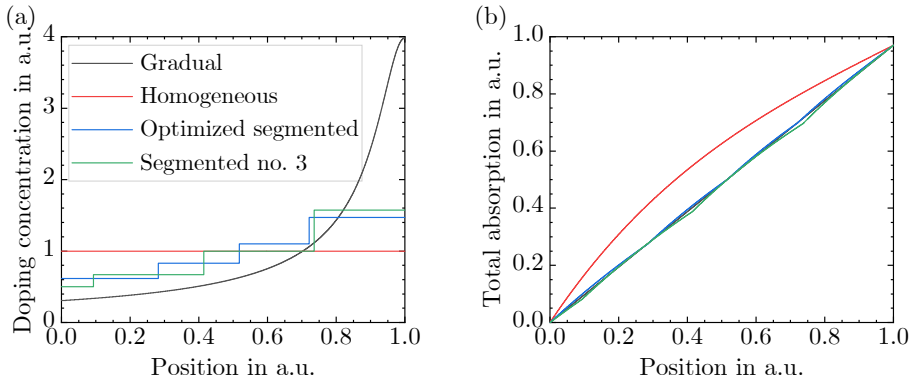| Crystal	f_1	f_2	f_3	$f_1 \cdot f_2 \cdot f_3$	ΔT_{max} in %
Segmented no. 1 L = (11.3, 7.2, 4.9, 4.6) mm D = (0.49, 0.7, 0.9, 1.1) %	32.9	1.5	42.7	2.8	33.8
Segmented no. 2 L = (12.4, 6.5, 4.7, 4.4) mm D = (0.46, 0.75, 0.9, 1.1) %	40.5	2.2	43.8	5.1	32.1
Segmented no. 3 L = (2.6, 9.0, 9.0, 7.4) mm D= (0.35, 0.47, 0.7, 1.1) %	41.0	1.1	43.5	2.7	32.6
Segmented no. 4 L = (4.7, 8.5, 7.5 7.3) mm D = (0.35, 0.5, 0.75, 1.1) %	41.5	4.1	43.3	9.6	32.8
Segmented no. 5 L = (5.3, 10.7, 6.9, 5.1) mm D = (0.35, 0.55, 0.9, 1.1) %	52.5	2.8	45.0	8.6	30.3

Figure 4.6: (a) Doping concentration and (b) total absorbed power along the crystal axis for the optimum (black), the homogeneously doped (red), the optimized segmented (blue), and the segmented crystal no. 3 (green) in comparison.

Figure 4.6(a) shows the doping concentration along the crystal axis for the gradually doped (black), the homogeneously doped (red), the freely optimized segmented (blue) and the segmented crystal no. 3 (green) in comparison. Both segmented crystals approach the gradual doping concentration equally well. Also, the total absorption along the crystal axis is similar for these two segmented crystals and both approach the linear increase of the optimum crystal well (see Figure 4.6(b)). Therefore, the imposed constraints on the doping concentration are considered to be acceptable.

The segmented crystal no. 3 was fabricated externally by diffusion-bonding the individual segments. For a successful bonding, a precise polishing of the segment end faces is required. After polishing, the two segments are optically contacted and thermally activated to recombine the dangling bonds of the segment end faces. [99]

4.2.2 Experimental Characterization of the Segmented Crystal

Prior to testing the fabricated segmented crystals in laser operation, it is characterized experimentally with different techniques. Firstly, it is optically inspected with visible light. Secondly, the absorption efficiency and the doping concentrations of the crystal segments are determined.

Inspection with Visible Light

To get an impression of the longitudinal absorption, both the homogeneously doped and the segmented crystal are illuminated with light from a helium-neon laser at 543 nm and an image is taken from the side. Because the incident light is absorbed by the doping ions, they also emit fluorescence. Consequently, a higher amount of fluorescence is expected near the front facet of the crystal in the homogeneously doped crystal due to the higher absorption according to the Beer-Lambert law. In contrast to this, a smoothed fluorescence is expected in the segmented crystal. By reversing the segmented crystal, an even higher fluorescence is expected near the front of the crystal. The images taken with a commercial CCD camera are shown in Figure 4.7. The crystals were illuminated with the helium-neon laser from the left side. The absorbing and thus fluorescing volume of the crystal can clearly be identified. Near the front facet of the homogeneously doped and the segmented crystal, a non-absorbing region is present, which results from the undoped end cap attached to both crystals. The images are analyzed quantitatively by initially converting it to grey scale values, which corresponds to the intensity of the fluorescence, and then by adding up all pixels in the radial direction. The fluorescence intensity depending on the longitudinal crystal position is shown in Figure 4.8(a). In the homogeneously doped crystal (black), a roughly exponential absorption of the pump light is observed. In the segmented crystal with the low doped segment oriented towards the light source (red), the fluorescence along the crystal axis is almost constant. The peak in fluorescence at a position of 0.75 results from scattering at the bonding surface. The segment boundaries can clearly be identified at the positions where the fluorescence shows sharp peaks. With the
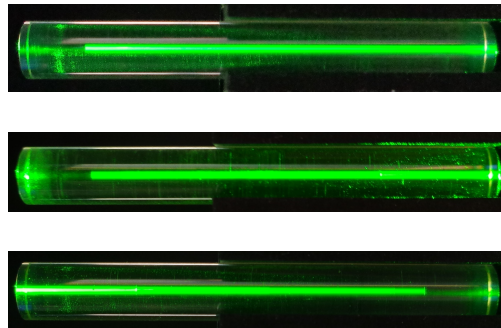

Figure 4.7: Images taken from the (a) homogeneously doped crystal, (b) segmented crystal oriented with the low doping concentration towards the light source, and (c) segmented crystal oriented with the high doping concentration towards the light source. The light from the helium-neon laser is incident from the left.
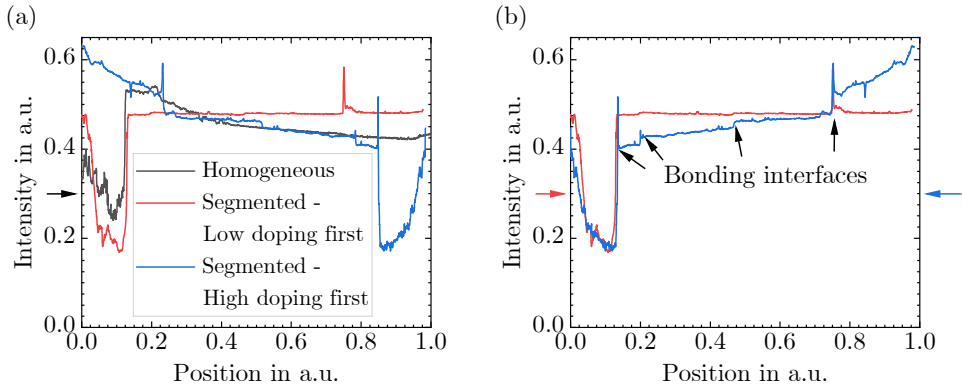
Figure 4.8: (a) Intensity of the 543 nm fluorescence depending on the longitudinal crystal position for the (a) homogeneously doped (black), segmented (red), and inverted segmented crystal (blue). The black arrow indicates the direction of illumination. (b) Fluorescence intensity of segmented (red) and inverted segmented (blue) crystal with opposite illumination directions (indicated by the red and blue arrow). From the measurement, the bonding interfaces can clearly be identified.

segmented crystal mounted in the reverse direction, the crystal segments can even be more clearly recognized. In comparison with the homogeneously doped crystal, the absorption in the first segment is even stronger. Figure 4.8(b) shows the same data as Figure 4.8(a), however only for the segmented crystal with reversed pumping directions. Therefore, the crystal orientation is the same, which allows to clearly identify the bonding interfaces.

With this simple approach, the proper fabrication of the segmented crystal is verified. Furthermore, the doping concentration of the crystals is measured by scanning them with a Tm^{3+}-doped fiber laser.

Measurement of Absorption Efficiency and Doping Concentration

For the measurement of the absorption efficiency and the longitudinal doping concentration of the homogeneously doped and the segmented crystal, both crystals are illuminated with a Tm^{3+}-doped fiber laser emitting at 1908 nm. The detailed setup is illustrated in Figure 4.9. To monitor the input power, the 1908 nm light is attenuated with a half-wave plate ($\lambda/2$) and a thin-film polarizer (TFP) and the s-polarized power reflected from the TFP is measured at the power meter P_1. The crystal is placed in the transmitting arm of the TFP and the transmitted power P_2 behind the crystal is measured. The transmitted power depending on the input power is shown
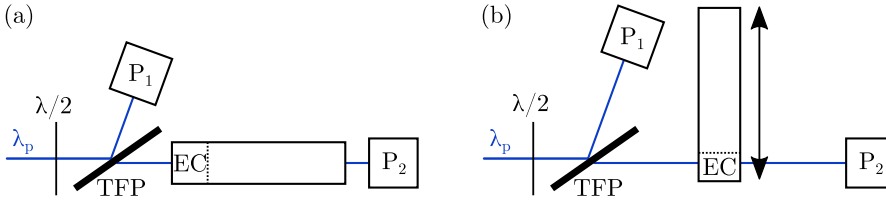
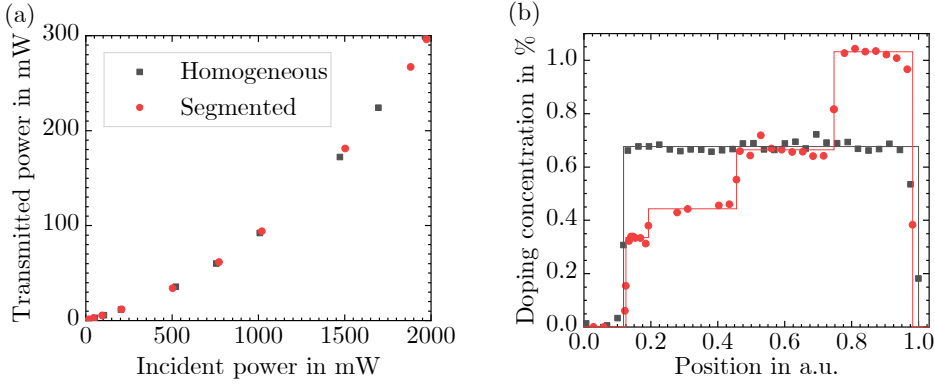Figure 4.9: Setup for measuring the (a) absorption efficiency and (b) longitudinal doping concentration.

Figure 4.10: Measurement of (a) transmitted power depending on the input power and (b) doping concentration along the crystal axis of the homogeneously doped (black) and segmented (red) crystal.

in Figure 4.10(a). For high incident powers, the transmitted power increases overproportionally. This results from a saturation of the absorption. To measure the doping concentration, the crystal is illuminated perpendicular to its crystal axis. In [114], the different path lengths when passing the circular cross-section of the rod, which result from the expanded laser beam, were shown to be negligible. Because of the cylindrical crystal shape, losses resulting from the Fresnel reflection at the curved surface are considered by a calibration of the measurement at the undoped end caps of the crystals. Therefore, the transmitted power P_2 behind the crystal is given by

$$P_2 = P_1 \cdot \frac{P_{2,E}}{P_{1,E}} \exp(-\alpha d), \qquad (4.22)$$

where $P_{1,E}$ and $P_{2,E}$ is the incident and transmitted power behind the undoped end cap and d is the diameter of the crystal. The doping concentrations along the crystal axis for both crystals are shown in Figure 4.10(b). In the case of the segmented crystal, the lower doping concentration with respect to the homogeneously doped crystal at the front facet and the higher

doping concentration at the end facet was confirmed. Also, the individual crystal segments can clearly be identified. Both the measured doping concentrations and the segment lengths are in accordance with the design of the segmented crystal.

Both crystals are then used in a compact resonator and their performance in laser operation is compared.

4.2.3   Cavity Design and Optimization

To compare the performance of both crystals in laser operation, a compact cavity delivering a good beam quality and high output power is designed. The design has been presented in detail in [127] and is based on the cavity design presented in Section 3.2.2. A schematic overview over the architecture is shown in Figure 4.11. In comparison to the setup presented in Section 3.2.2, it mainly differs in the HR mirror, which is convex in this setup. Furthermore, the cavity length is decreased to 9.8 cm. The radius of curvature of the HR mirror is optimized to get a high beam quality and a maximized output power. In addition, the pump diameter is adapted using an adjustable telescope to guarantee an optimal mode matching. Two goals are pursued with the optimization. Firstly, the output power of this compact single-end-pumped resonator is to be maximized. Secondly, differences between the homogeneously doped and the segmented crystal regarding the maximal achievable output shall be investigated.

The optimization procedure is as follows: For a fixed mirror configuration, the pump power is increased until the beam profile begins to deteriorate. At that point, the laser mode approaches the limit of the resonator stability zone and is larger than the pump mode. By increasing the pump beam diameter, a nearly diffraction-limited beam profile is restored. This is repeated until pulse instabilities are observed. At this point, the laser mode size varies strongly over the length
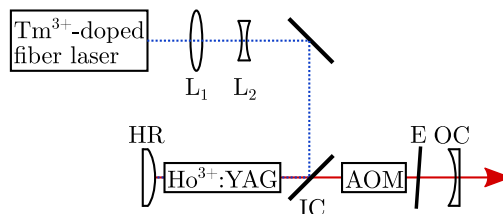

Figure 4.11: Schematic of the laser resonator used to investigate the homogeneously doped and the segmented crystals.

of the crystal such that mode matching cannot be achieved. Consequently, the maximum output power of this compact resonator is reached. This experiment is repeated for HR mirrors with radii of curvature R_c of -0.5 m, -0.4 m, -0.3 m and -0.25 m.

For a stronger radius of curvature, a higher output power is achieved. This results from the partial compensation of the thermal lens by the convex HR mirror [27]. Hence, a stronger curvature leads to a compensation of the thermal lens at higher powers, thus the pump power at which the resonator stability limit is reached increases. From this optimization, the optimum HR mirror with $R_c = -0.25$ m is determined, which generates the maximum pulse energy with the minimum pulse duration. This holds true for both crystals and a characterization of this configuration is presented for both crystals in the following section.

4.2.4   Experimental Characterization of the Cavity

Figure 4.12(a) shows the Ho^{3+}:YAG output power depending on the pump power for the homogeneously doped (black) and the segmented crystal (red). Both resonators exhibit high slope efficiencies of around 67 % and small pump thresholds of 3.7 W (homogeneously doped crystal) and 5.1 W (segmented crystal). The lower pump threshold in the case of the homogeneously doped crystal is assumed to result from the slightly lower pump beam diameter, which was set to achieve an optimal mode matching at the working point. In addition, potential upconversion in the highly doped segment of the segmented crystal might be a loss mechanism that increases the pump threshold. The maximum output powers, which are achieved with the two crystals, are 57.7 W (segmented crystal) and 62.4 W (homogeneously doped crystal). A detailed discussion and explanation of this observation will be given in Section 4.2.7. The beam propagation factor M^2 is also measured depending on the pump power. The according curves are included in Figure 4.12(a) for the vertical beam axis. In both resonators, the beam propagation factor is near-diffraction-limited for low pump powers and then deteriorates up to a pump power of approximately 60 W. When further increasing the pump power, an improvement in the beam propagation factor is observed. The cause for this lies in varying mode sizes of the pump and the resonator mode and the resulting mode (mis)match. A near-diffraction-limited beam propagation factor is reached for the homogeneously doped crystal for a pump power of 89 W, whereas for the segmented crystal a near diffraction-limited beam propagation factor is already achieved for a pump power of 82 W. Similar to the power curves, a shift to higher pump powers is observed for the homogeneously doped crystal as well. A more detailed analysis for the
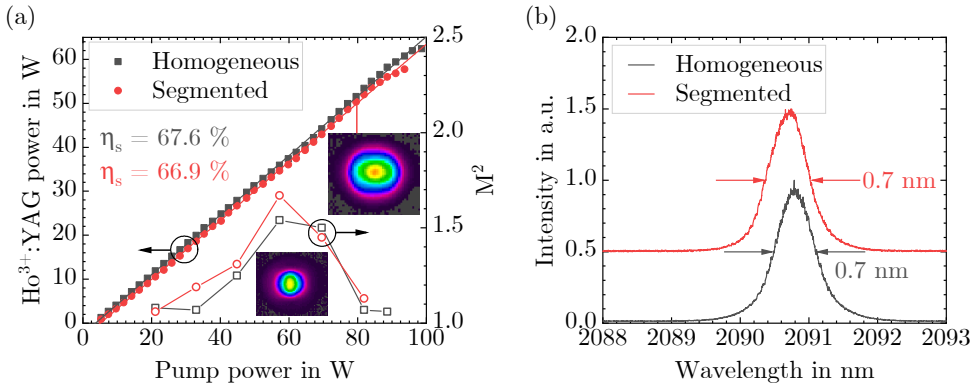
Figure 4.12: (a) Output power and beam propagation factor of the resonators with the homogeneously doped (black) and the segmented crystal (red) in comparison. (b) Spectral output of the homogeneously doped (black) and the segmented crystal (red).

course of the beam propagation factor will also be presented in Section 4.2.7. The emission wavelength for both resonators is shown in Figure 4.12(b). Both show a linewidth of 0.7 nm and a center wavelength of 2090.8 nm. Besides that, no additional peaks in the spectrum of the segmented crystal indicate parasitic interferences inside the resonator, thus the high quality of the bonding interfaces can be concluded.

Figure 4.13(a) shows the residual pump power and Figure 4.13(b) shows the depolarized power resulting from the thermally induced birefringence in the crystal. The increased residual pump light in the case of the segmented crystal might result from two contributions: Firstly, the segmented crystal contains one low doped segment in which the absorption is likely to saturate. Secondly, the increased absorption in the case of the homogeneously doped crystal might result from an improved mode matching, as in this case excited states are efficiently de-excited and therefore available to absorb photons again. The depolarized power is slightly smaller for the segmented crystal. This probably results from the more steady temperature distribution and the resulting smaller thermal stresses. However, this only holds true up to a pump power of 87 W because the resonator was optimized for a pump power of 82 W.

Due to a stable operation during Q-switching at 89 W (homogeneously doped crystal) and 82 W (segmented crystal), measurements of the beam propagation factor are shown exemplarily in these working points in Figure 4.14(a) and Figure 4.14 (b). An output power of 57.6 W and 51.9 W, respectively, was measured. In comparison with the basic resonator presented
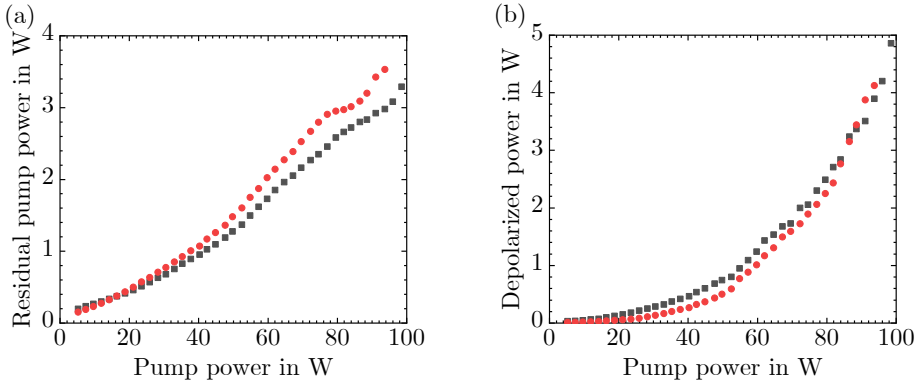
Figure 4.13: (a) Residual and (b) depolarized power depending on the pump power for the homogeneously doped (black) and the segmented crystal (red) in comparison.
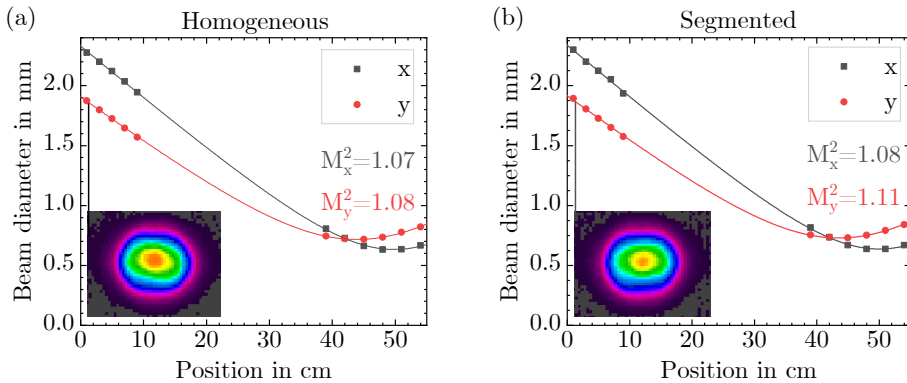

Figure 4.14: Beam propagation factor measurements for (a) the homogeneously doped and (b) the segmented crystal at pump powers of 89 W and 82 W, respectively.

in Section 3.2.2, which delivered an output power of 45 W, this corresponds to an increase in output power of 28 %. In both cases, the beam propagation factor is around 1.1 in both beam axes. Additionally, the beam diameters evolve equivalently along the beam caustic for both crystals, which indicates that the mode evolves similarly inside the resonator. The disadvantage of this high-power resonator is that it results in an astigmatic beam as can clearly be seen from both beam caustics.

In Q-switched operation, pulses with a maximum energy of 1.14 mJ and a minimum pulse duration of 40 ns are generated for the homogeneously doped crystal at a repetition rate of
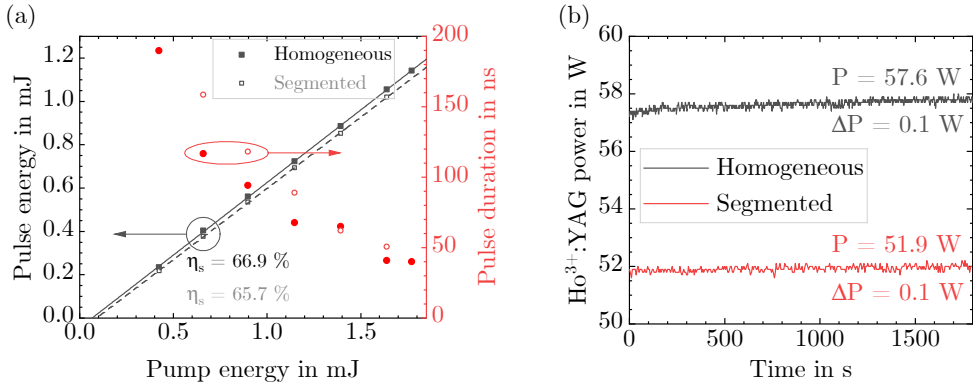
Figure 4.15: (a) Pulse energy (black) and pulse duration (red) depending on the pump energy for the homogeneously doped (filled symbols) and the segmented crystal (open symbols) in comparison. (b) Power stability measurement over 30 min for the homogeneously doped (black) and the segmented (red) crystal at the working points.

50 kHz (see Figure 4.15(a)). The slope efficiency is similar as in CW operation. As has been expected from CW operation, a slightly lower maximum pulse energy (1.04 mJ) and a longer minimum pulse duration (50 ns) is measured for the segmented crystal. The lower energy results from the lower output power at the working point. The cause for the longer pulse duration is believed to be the larger pump beam diameter that is needed to achieve mode matched operation and results in a slightly lower inversion. A theoretical explanation for this observation will be given in Section 4.2.7. Figure 4.15(b) shows a measurement of the average output power over a time of 30 min for the resonators with both crystals at their respective working points. In both cases, a stable operation is achieved and the standard deviation is only 0.1 W.

To summarize, both in CW as well as in Q-switched operation, the homogeneously doped crystal and the segmented crystal show a similar behavior, although a slightly higher output power, higher pulse energies, and shorter pulse durations are achieved with the homogeneously doped crystal.

To rule out the possibility that the poorer performance of the segmented crystal is due to losses at the bonding surfaces, the resonator losses are determined by performing a Caird analysis in both cases [128]. In a Caird analysis, the slope efficiency of a resonator is determined for different

OC mirror transmissions T_{OC} to deduce the resonator losses by the following calculation: From the theoretical slope efficiency [38]

$$\eta_s = \frac{\lambda_p}{\lambda_s} \frac{-\ln(1 - T_{OC})}{2\ln G} \eta_{abs},$$ (4.23)

a linear relation between the inverse slope efficiency with respect to the absorbed pump power $\eta_{s,abs}^{-1}$ and $(-\ln(1 - T_{OC}))^{-1}$ can be derived:

$$\frac{1}{\eta_{s,abs}} = \frac{1}{\eta_{s,0}} (-\ln(1 - \Lambda))(-\ln(1 - T_{OC}))^{-1} + \frac{1}{\eta_{s,0}} \quad \text{with} \quad \eta_{s,0} = \frac{\lambda_p}{\lambda_s} \eta_{mode}.$$ (4.24)

η_{mode} includes the impact of the specific cavity design on the efficiency. Figure 4.16 shows the output power depending on the pump power for different OC mirror transmissions for the resonator with the segmented crystal. By determining the slope efficiency depending on T_{OC} and using Equation (4.24), the Caird plots, shown in Figure 4.17(a) for the homogeneously doped crystal and in Figure 4.17(b) for the segmented crystal, are generated. The resonator losses Λ and the intrinsic slope efficiency $\eta_{s,0}$ can be determined by performing a linear fit to the Caird plots. The resonator losses are around 2 % for both the homogeneously doped and the segmented crystal. The intrinsic slope efficiency is 1 % higher in the resonator with the homogeneously doped crystal and amounts to 70.8 %. These similar results for both crystals
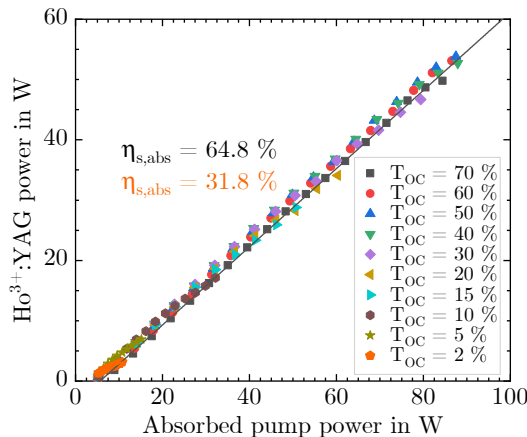

Figure 4.16: Ho^{3+}:YAG output power of the resonator with the segmented crystal with respect to the absorbed pump power for different OC mirror transmissions. The slope efficiency is exemplarily given for $T_{OC} = 70\%$ (black) and $T_{OC} = 2\%$ (orange).
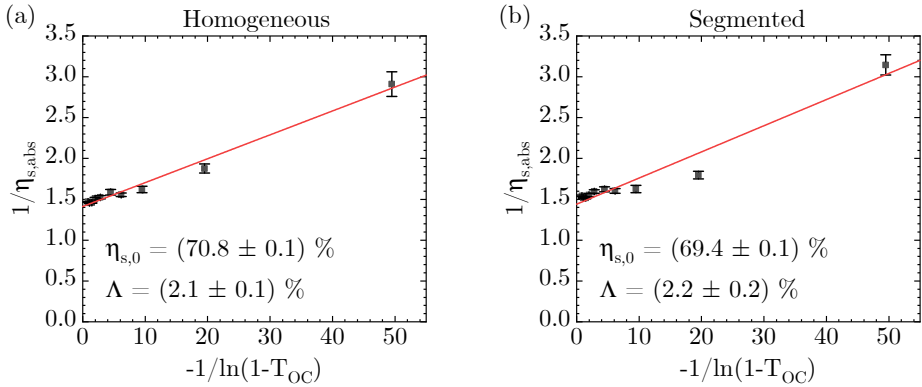
Figure 4.17: Caird analyses of the resonators with the (a) homogeneously doped and (b) segmented crystal.

indicate that the segmented crystal does not introduce considerable losses to argue that the approximately 10 % lower output power could be attributed to these.

To get a deeper understanding of the differences between the two crystals, an interferometer is set up to determine the radial temperature profiles in the crystals, which contribute to thermal lensing.

4.2.5   Investigation of Thermal Lensing in Laser Operation

Experimental Setup of Interferometer

The interferometer setup is depicted in Figure 4.18. Light from a helium-neon laser with a wavelength of $\lambda_{\mathrm{HN}} = 633\,\mathrm{nm}$ is polarized and shaped with a two-lens telescope such that a focus is created in the distance of the focal length of the resonator HR mirror. This ensures roughly planar wave fronts directly behind the HR mirror. Furthermore, the waist size and the resulting beam divergence are aligned such that a beam diameter of approximately 5 mm is generated at the resonator HR mirror to illuminate the entire crystal cross-section. In front of the HR mirror, a polarizing beam splitter (PBS) and a quarter-wave plate ($\lambda/4$) under 45° are inserted such that the light is circularly polarized. The laser crystal directly behind the HR mirror is not anti-reflective (AR) coated for λ_{HN}. Consequently, the incident light is partially reflected from the first surface of the crystal, generating the reference wave. The transmitted wave passes
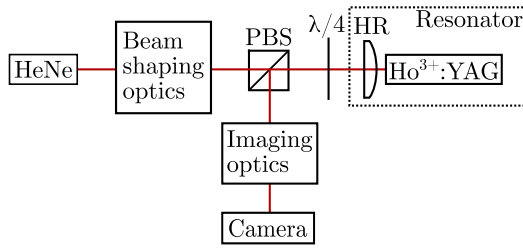
Figure 4.18: Interferometer setup for thermal lens investigation.

through the crystal and is partially reflected at the second surface of the crystal, generating the test wave. Both waves then pass the quarter-wave plate again resulting in a polarization state perpendicular to the initial polarization state. Both beams are therefore reflected at the PBS. Spatial filtering with an aperture inserted in the distance of the focal length of the HR mirror ensures the separation of undesired reflections from the HR mirror and the desired reflections from the Ho^{3+}:YAG crystal. A plano-convex lens with a focal length of $f = 30\,\text{cm}$ images the crystal onto a CCD camera.

The interference pattern is generated due to an optical path difference (OPD) between the reference and the test wave. Because the test wave passes the laser crystal twice, the OPD is given by

$$\text{OPD}(r) = 2n(r)L\,. \qquad (4.25)$$

Here, $n(r)$ is the refractive index of the laser crystal, which varies radially due to the pump light absorption, and L is the length of the crystal. With this approach, the radial profile of the refractive index averaged over the length of the crystal can be investigated. As explained in Chapter 2, both the change in refractive index due to the thermo-optic effect as well as the change in refractive index due to the photoelastic effect contribute to $n(r)$. Because a significant contribution to the refractive index variation in YAG results from the thermo-optic effect [53], it is assumed to be the only contribution to the formation of the interference pattern and is used to estimate the radial temperature distribution. A further effect that is imaged in the interference patterns is the bulging of the end faces. However, this effect is assumed to be small as well and is therefore neglected in the evaluation of the interference patterns. Overall, the main goal is to estimate the order of magnitude of the temperature and to compare the segmented crystal with the homogeneously doped crystal, which is possible by the described

assumptions. The OPD between two interference fringes equals the illumination wavelength λ_{HN}. Consequently, from Equation (4.25), the refractive index difference Δn between two interference fringes

$$\Delta n = \frac{\lambda_{HN}}{2L} \tag{4.26}$$

is concluded. The temperature difference ΔT between two interference fringes is calculated from Δn by using the thermo-optic coefficient $\mathrm{d}n/\mathrm{d}T = 9.9 \cdot 10^{-6}\,\mathrm{K}^{-1}$ of YAG [55] and is given by

$$\Delta T = \frac{\Delta n}{\mathrm{d}n/\mathrm{d}T} \approx 1\,\mathrm{K}\,. \tag{4.27}$$

Evaluation of Interferometer Images

Figure 4.19 shows interferograms recorded for increasing pump powers (from left to right) and for the homogeneously doped (top row) and the segmented (bottom row) crystal. Because an increasing pump power increases the heat generation in the crystals, the number of interference fringes increases as well. Both the homogeneously doped and the segmented crystal show a similar number of interference fringes indicating a similar temperature inside the crystal. Temperature profiles with respect to the edges of the crystals are extracted in the x- and y-direction from the interferograms by locating the positions of the interference maxima and
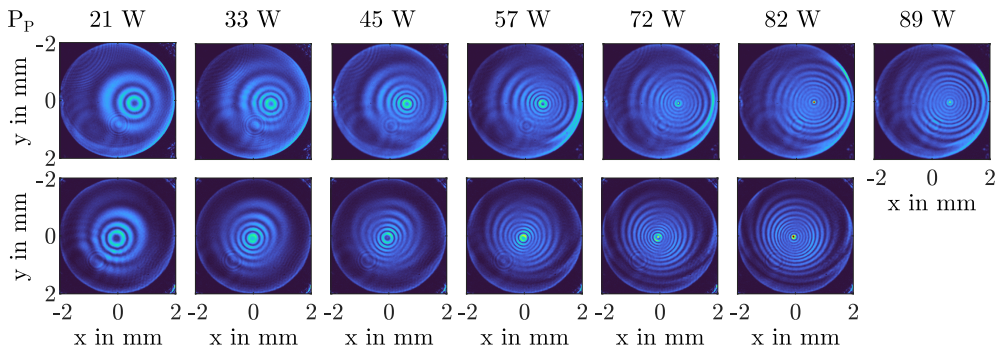

Figure 4.19: Interferograms for homogeneously doped (top row) and segmented (bottom row) crystal for increasing pump powers. With an increasing pump power, the distance of the interference fringes decreases and more fringes become visible which indicates a stronger thermal lensing.

minima. The data is used to fit the radial temperature distribution for Gaussian end-pumped crystals derived by Innocenzi [50]

$$T(r) = A \cdot \left[\ln\left(\frac{b^2}{r^2}\right) - E_1\left(\frac{2r^2}{\omega_\mathrm{p}^2}\right) \right] . \qquad (4.28)$$

A is a measure for the peak temperature, b is the distance of the peak of the distribution to the edge of the crystal, and ω_p is the pump radius. Because the interferograms are non-centrosymmetric, the function has been adapted to take this into account. Figure 4.20 exemplarily shows the resulting temperature distributions for the homogeneously doped (top row) and the segmented (bottom row) crystal for the x- (left) and y-direction (right) and for a pump power of 21 W (see Figure 4.20(a)) and 89 W (see Figure 4.20(b)). In the working points, the maximum temperature difference with respect to the edge of the crystal is 12.7 K for the homogeneously doped and 13.5 K for the segmented crystals. At the lower pump power of 21 W, this temperature difference is considerably lower and amounts to 3.5 K in the case of the homogeneously doped crystal and 4.6 K in the case of the segmented crystal.
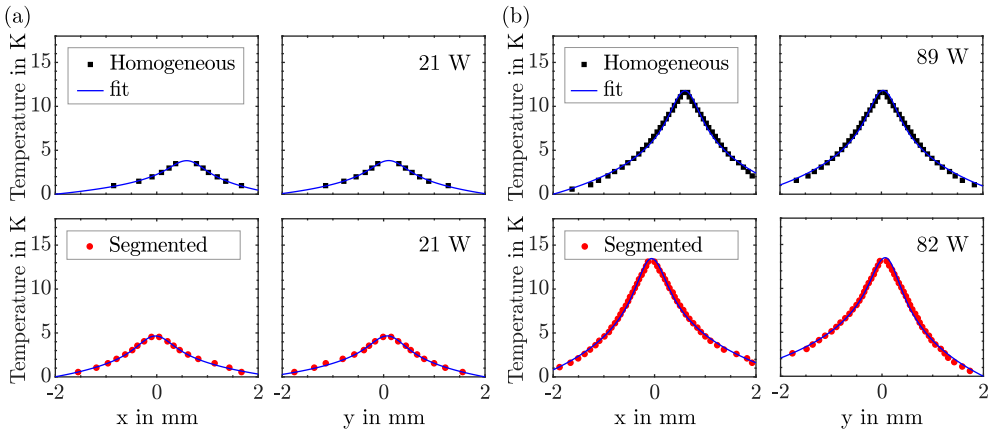

Figure 4.20: Temperature profiles with respect to the crystal edge temperature in the x- (left) and the y-direction (right) extracted from the interferograms at a pump power of (a) 21 W and (b) 89 W and 82 W for the homogeneously doped (top row) and segmented crystal (bottom row), respectively.

From the temperature profiles, the focal length of the thermal lens can be estimated. Two considerations are taken into account here. Firstly, the OPD of a thin spherical lens with focal length f is given by [104]

$$\mathrm{OPD}_{\mathrm{lens}} = \mathrm{OPD}_0 - \frac{r^2}{2f} \, . \tag{4.29}$$

Secondly, the temperature distribution in Equation (4.28) can be approximated to

$$T(r) \approx A \left[\Gamma + \ln \left(\frac{2b^2}{\omega_{\mathrm{p}}^2} \right) \right] - \frac{2A}{\omega_{\mathrm{p}}^2} r^2 \tag{4.30}$$

for $r < \omega_{\mathrm{p}}$. Here, $\Gamma \approx 0.577$ is Euler's constant. By comparing the OPD resulting from this temperature difference with the OPD of a thin spherical lens, the focal length f_{th} of the thermal lens can be determined:

$$f_{\mathrm{th}} = \frac{\omega_{\mathrm{p}}^2}{4A \cdot \mathrm{d}n/\mathrm{d}T \cdot L} \, . \tag{4.31}$$

Figure 4.21(a) and Figure 4.21(b) show the derived focal lengths for the homogeneously doped and the segmented crystal, respectively. Both focal lengths are in a similar range. For the fits, a decrease in the pump beam radius with increasing pump power was taken into account. The thermal focal length is on the order of 5–15 cm, which is in line with the measurements presented
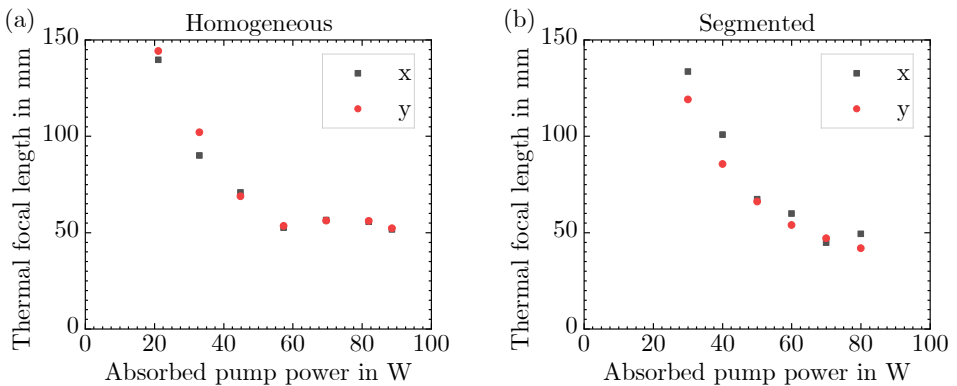

Figure 4.21: Focal lengths of the thermal lens derived from the fits according to Innocenzi of the temperature profiles for the (a) homogeneously doped and (b) segmented crystal.

in Section 3.1.4. In comparison to the prior measurement, the shorter focal lengths at high pump powers result from the smaller pump diameter used in this measurement. Considering the rough approximation that only the thermo-optic effect contributed to the formation of refractive index distribution, these results have given a good insight into the radial temperature profile in the crystals and the longitudinally averaged temperature in the crystal.

To get an understanding of the longitudinal temperature distribution, a simulation is used and the results are presented in the following section.

4.2.6   Longitudinal Temperature Profiles

The simulation is based on a split-step beam propagation method and was presented by Rupp et al. in 2022 [129]. In this simulation, an electromagnetic field is propagated and transformed by the laser crystal and other optical elements in the cavity. In the laser crystal, a temperature distribution develops due to the absorption and gain dynamics. The temperature distribution is calculated numerically by a 3-dimensional finite difference method, therefore thermal lensing effects are taken into account in this model.

Figure 4.22 shows a comparison of the simulated and experimental power curves for the homogeneously doped crystal. With 72 %, the slope efficiency of the simulated power curve
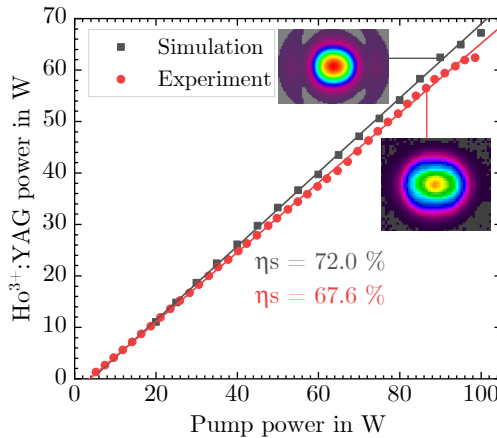

Figure 4.22: Comparison of Ho^{3+}:YAG output power of the experiment and the simulation for the homogeneously doped crystal.
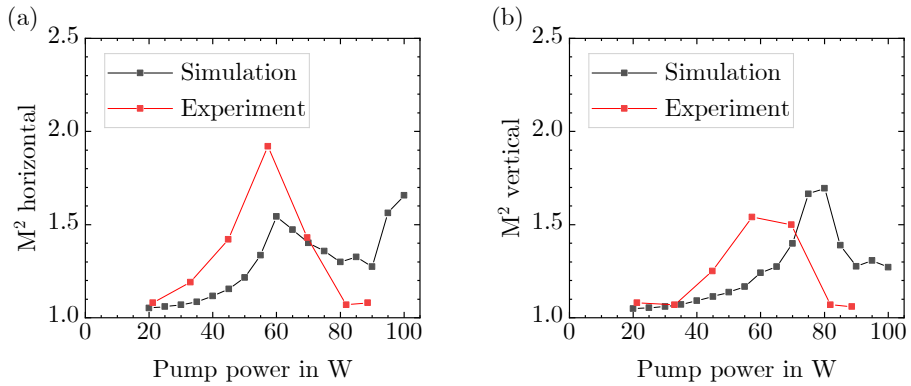
Figure 4.23: Comparison of (a) horizontal and (b) vertical beam propagation factors in the simulation (black) and the experiment (red).

is slightly higher than that of the experimentally measured power curve. Also, a slightly higher maximum output power of 67 W is simulated. Deviations in this comparison can result from discrepancies in the simulation input parameters, which are hard to predict perfectly. Figure 4.23(a) and Figure 4.23(b) show the beam propagation factors parallel and perpendicular to the optical table, respectively, which are similar in the simulation and the experiment. In the horizontal direction, the beam propagation factor deteriorates up to a pump power of 60 W followed by an improvement of the beam propagation factor in both cases. In the vertical direction of the simulation, the beam propagation factor deteriorates up to a slightly higher power compared to the experiment. However, for pump powers around 90 W, both beam propagation factors improve. Because the simulation has emulated the basic behavior of the experimental observations, the simulated temperature in the crystal should also provide insight about the temperature in the crystal in the experiment.

Figure 4.24 shows the simulated longitudinal on-axis temperature distribution for three crystals. This includes the homogeneously doped crystal (black), the segmented crystal as used in the experiment (red), and an optimized segmented crystal (blue). The pump light is incident onto the crystals from the left side. For the homogeneously doped crystal, the highest peak temperature and largest temperature gradient are observed, which is in accordance with the expectations. The strong increase in the temperature near the crystal front facet results from an effective axial heat transport into the undoped YAG end cap. The segmented crystal shows a smaller temperature gradient and also a smaller peak temperature. In contrast to the homogeneously doped crystal, the highest temperature is not reached at the front but rather at the end of the crystal. The center
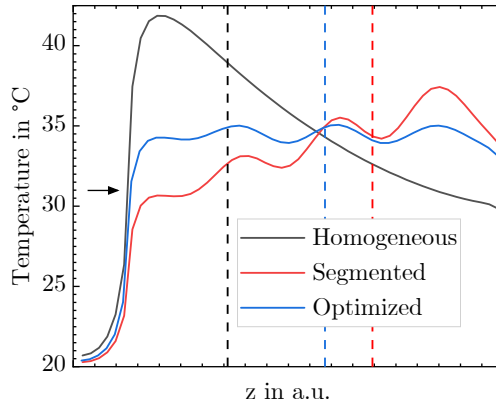
Figure 4.24: Simulated longitudinal temperature distribution in a homogeneously doped (black), segmented (red), and optimized segmented (blue) crystal. The pump light direction is indicated by the arrow. The dashed lines indicate the effective position of the thermal lens when it is approximated as a thin lens.

of the temperature distribution is a measure of the effective position of the thermal lens, the impact of which is discussed in the following section. Due to the temperature peak at the front of the crystal in the homogeneously doped crystal, the effective position of the thermal lens is close to the front of the crystal, whereas it tends to be at the end of the segmented crystal. Additionally, a crystal is optimized with the simulation such that a roughly constant on-axis temperature is generated. This crystal has equally long segments with doping concentrations of 0.55 %, 0.65 %, 0.75 %, and 0.85 %. With this crystal, the thermal lens is effectively positioned in between those of the homogeneously doped and the segmented crystal. Despite having the lowest peak temperature, an improvement in output power or beam quality is not observed in the simulations as well. The reason for this probably lies in the comparatively low peak temperature of a maximum of just over 40 °C. In contrast to this, the thermal fracture limit in YAG is approximately 200 W/cm [38], which is only approached for far higher pump powers and temperatures. In previous results from segmented Nd^{3+}-doped crystals, considerably higher pump powers were used, resulting in a significantly higher maximum temperature in the crystals [106]. Additionally, those lasers were not optimized for an operation with a good beam quality but for an operation with the highest possible output power. As a consequence, a segmented crystal does not seem to offer any advantages in a low power regime where a good beam quality can still be achieved.

In the following section, a closer look is taken at the resonator stability criteria to further explain the outperformance of the homogeneously doped over the segmented crystal.

4.2.7 Discussion

The superior performance of the homogeneously doped over the segmented crystal is explained by considering the specific effective position of the thermal lens in the resonator in combination with resonator stability criteria. A simple resonator with two plane cavity end mirrors with a distance L including a thermal lens with focal length f, which is approximated by a thin lens, is depicted in Figure 4.25. The distance between the thin lens and the HR mirror is denoted by d. This resonator has two stability regions: $\frac{d(L-d)}{L} < f < d$ and $f > L - d$. For the pump powers used in our experiments, an operation in the second stability region results. Therefore, when the distance between the HR mirror and the thin lens decreases, a longer focal length is required to remain within the stability region. As for YAG the focal length of the thermal lens decreases with an increase of the pump power, only lower pump powers are allowed when the thermal lens moves away from the center of the resonator. In the homogeneously doped crystal, a larger portion of the pump light is absorbed at the front of the crystal compared to the segmented crystal. Because both crystals are pumped from the center of the resonator, the effective position of the thermal lens in the segmented crystal is closer to the HR mirror and consequently only lower pump powers are allowed to remain in the stability region. Conversely, higher output powers are achievable with the homogeneously doped crystal. Additionally, a smaller distance from the HR relates to an increased intrinsic resonator mode diameter. This explains the larger pump diameter, which is necessary for a mode matched operation of the segmented crystal, and the resulting longer pulse duration.

To further verify this hypothesis, another resonator is set up in which the pump scheme is reversed. Instead of pumping the crystals from the center of the resonator, they are pumped through a plane HR mirror, which is highly transmissive for the pump wavelength and the crystals are oriented with their end caps facing the pump beam (see Figure 4.26(a)). As a
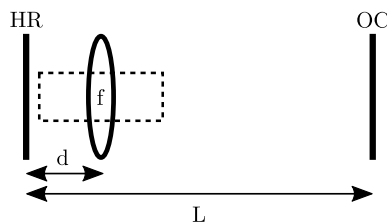

Figure 4.25: Simple plane-plane resonator of length L with a thermal lens f located at a distance of d from the HR mirror.
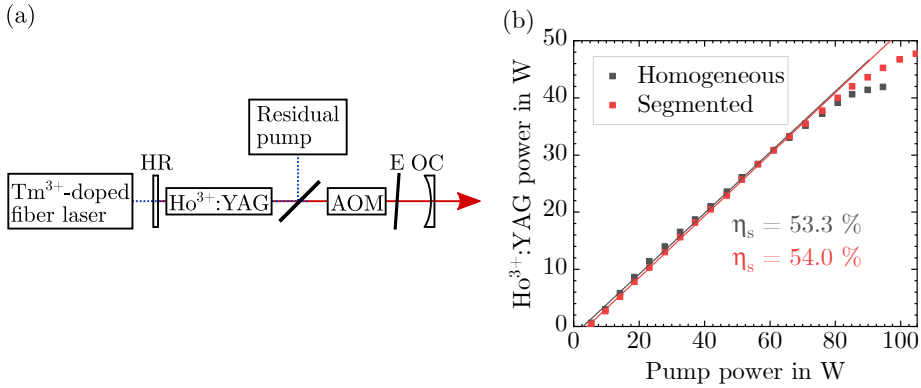
(a)

(b)

Figure 4.26: (a) Schematic representation of a resonator with a reversed pumping scheme. (b) Ho^{3+}:YAG output power with respect to the pump power for the homogeneously doped (black) and the segmented (red) crystal in the resonator with the reversed pumping scheme.

consequence, the thermal lens of the homogeneously doped crystal is effectively closer to the HR mirror in this pumping scheme, and the thermal lens of the segmented crystal is effectively closer to the center of the resonator. Therefore, the segmented crystal is expected to show a superior performance. As a consequence of pumping through the HR mirror, only a single-pass of the pump light is possible. This leads to a lower slope efficiency and a higher pump threshold, but has no impact on the effect that is to be investigated. Other than this and the plane HR mirror, the setup corresponds to the one presented in Section 4.2.4. Figure 4.26(b) shows the resulting power curves for the homogeneously doped and the segmented crystal. Due to the single-pass of the pump light, the slope efficiency is around 54 %. However, with the segmented crystal, a higher output power and a higher slope efficiency are achieved due to the improved effective position of the thermal lens inside the resonator, which confirms the expectation.

In addition to the different performance of the crystals, a strong pump power dependence of the beam propagation factor M^2 was observed for both crystals in Section 4.2.4. To explain this, the mode diameter ω_c in the crystal (black) depending on the pump power is calculated with the simulation tool described in Section 3.1.3. For the simulation, a pump diameter of 550 µm and a heat efficiency factor of 12 % is assumed. Figure 4.27 shows the simulated mode diameter in the crystal and the pump beam diameter depending on the pump power. In the experiments, the pump beam diameter ω_p (red) decreased linearly with increasing pump power. However, this is an undesired property of the commercial collimator of the Tm^{3+}-doped fiber laser. A beam propagation factor of $M^2 \approx 1$ is usually achieved when $\omega_c \approx \omega_p$ holds. This is the case for
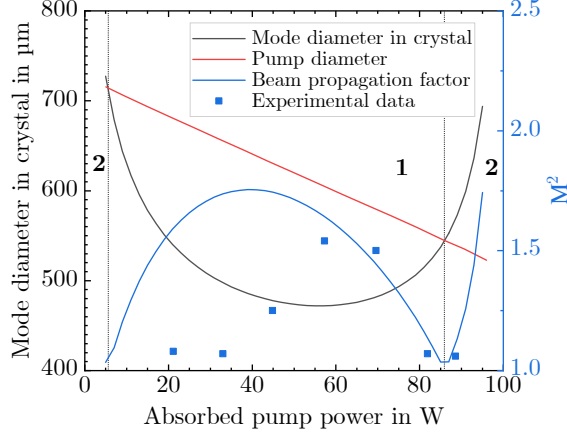
Figure 4.27: Simulated mode diameter in the crystal (black) and experimentally determined pump beam diameter (red) depending on the absorbed pump power. From the mode mismatch, a value for the beam propagation factor (blue) is estimated. The experimental data from Figure 4.12 is included for comparison (blue squares).

$P_{abs} \approx 5\,\text{W}$ and $P_{abs} \approx 86\,\text{W}$. The region for which $\omega_c < \omega_p$ holds, is labeled with region 1, whereas in region 2 $\omega_c > \omega_p$ holds. In both regions, a mode mismatch is present, which results in a deterioration of the beam propagation factor. In region 1, the beam propagation factor can be approximated as [130]

$$M^2 \approx \left(\frac{\omega_p}{\omega_c}\right)^2. \tag{4.32}$$

Under the assumption that the mode mismatch causes the deterioration of the beam propagation in region 2 as well, it is estimated as

$$M^2 \approx \left(\frac{\omega_c}{\omega_p}\right)^2. \tag{4.33}$$

This can be explained as follows: When the pump diameter is smaller than the laser mode diameter in the crystal, the laser can only emit in the pumped region. This leads to a diffraction-limited beam quality at low pump powers. At high pump powers, however, reabsorption of the laser mode in the unpumped region leads to a deterioration of the beam quality. In region 1 where the laser mode in the crystal is smaller than the pump mode, higher order modes can establish. However, this only occurs when the gain is high enough, which is not considered in this depiction. From the experimental data (blue squares), it can be concluded that the gain is not high enough

to excite higher order modes for pump powers lower than 40 W because a diffraction-limited beam quality was measured. This is why the beam quality is actually better than expected from the theoretical consideration (blue curve) in this graph. For pump powers higher than 40 W, an excitation of higher order modes occurs and the beam propagation factor derived from the resonator mode size shows a good agreement with the experimentally measured values.

4.2.8 Summary

To summarize, a segmented crystal with four segments was designed and theoretically compared to an optimally doped crystal with the aim to generate a more homogeneous longitudinal temperature distribution in the laser crystal. In comparison with already existing literature, a modified approach for the optimization of the crystal was presented. The fabricated segmented crystal was investigated by an optical inspection and by different absorption measurements. To investigate this crystal in laser operation and to compare it with a homogeneously doped reference crystal, a compact cavity was designed and characterized. In the experiments, the homogeneously doped crystal showed an approximately 10 % higher output power and 20 % shorter pulses. Both laser crystals were operated stable over half an hour with a near-diffraction-limited beam propagation factor of $M^2 \approx 1.1$. A Caird analysis showed similar resonator losses around 2 % in both resonators. Thus, the poorer performance of the segmented crystal could not be explained by losses at the multiple bonding interfaces. An interferometric thermal lens investigation yielded a similar average crystal temperature and thermal focal length. A simulation based on a split-step beam propagation method was in good agreement with the experimental data and the simulated longitudinal temperature profile yielded a different effective position of the thermal lens when it was approximated as a thin lens. This insight lead to the hypothesis that the superior performance of the homogeneously doped crystal is explained by a more centered effective position of the thermal lens in the resonator, resulting in a wider resonator stability range, which in turn allows for higher output powers. By reversing the direction of the pump light, a higher output power was measured with the segmented crystal confirming this hypothesis. In comparison with existing literature that showed an improved performance with a segmented crystal, the peak temperatures in the Ho^{3+}:YAG crystals were considerably lower, which is a further reason why an improvement with the segmented crystal could not be observed.

4.3 Amplifier Setup

In the following sections, a single-stage Ho^{3+}:YAG MOPA system is discussed. Section 4.3.1 presents a theoretical model to describe the amplifier characteristics. The design of the amplifier stage is described in Section 4.3.2. The output characteristics of the MOPA system as well as the comparison with the theoretical model are shown in Section 4.3.3. The section closes with a short summary in Section 4.3.5.

4.3.1 Theoretical Considerations

To understand the amplification behavior, similar rate equations to those presented in Section 2.2.2 are considered. In the following section, the notation from Section 2.2.2 is used. When the amplifier crystal is pumped, an inversion is created. When a photon field consisting of photons with a suitable wavelength passes the inverted medium, it is amplified provided that the pump threshold is exceeded. The amplification of the photon field Φ at the signal wavelength λ_s over the crystal length is depicted in Figure 4.28. When an infinitesimally thin element $\mathrm{d}z$ of the crystal is passed, the change in the photon field is given by [54]

$$\mathrm{d}\Phi = \Phi \left(\sigma_{\mathrm{es}} N_2 - \sigma_{\mathrm{as}} N_1 \right) \mathrm{d}z = \Phi \gamma \mathrm{d}z \,, \tag{4.34}$$

where γ is the gain coefficient. The solution to this differential equation is given by

$$\Phi(z) = \Phi_0 \exp(\gamma z) \tag{4.35}$$

yielding an exponential increase in the photon field when passing the amplifier crystal. The rate equations are in principal the same as in Equation (2.5) and (2.6). When the pump rate R is
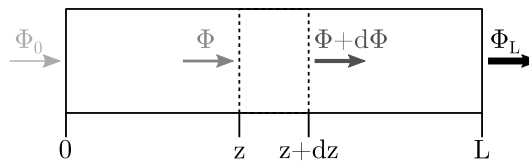

Figure 4.28: Schematic representation of pumped amplifier crystal including the change in photon density Φ over the length of the crystal (based on [54]).

expressed as $R = \Phi_p \left(\sigma_{ap} N_1 - \sigma_{ep} N_2 \right)$, where Φ_p is the photon density at the pump wavelength λ_p, a differential equation results for the inversion ΔN:

$$\frac{\partial \Delta N}{\partial t} = N \left(\Phi_p \left(\sigma_{ap} - \sigma_{ep} \right) - \Phi \left(\sigma_{es} - \sigma_{as} \right) - \frac{1}{\tau} \right)$$
$$- \Delta N \left(\Phi_p \left(\sigma_{ap} + \sigma_{ep} \right) + \Phi \left(\sigma_{as} + \sigma_{es} \right) + \frac{1}{\tau} \right) . \tag{4.36}$$

Therefore, under equilibrium conditions, the inversion is given by

$$\Delta N = N \frac{\left(\Phi_p \left(\sigma_{ap} - \sigma_{ep} \right) - \Phi \left(\sigma_{es} - \sigma_{as} \right) - \frac{1}{\tau} \right)}{\left(\Phi_p \left(\sigma_{ap} + \sigma_{ep} \right) + \Phi \left(\sigma_{as} + \sigma_{es} \right) + \frac{1}{\tau} \right)} \tag{4.37}$$

With this, the gain coefficient can be expressed as

$$\gamma = \frac{\gamma_0}{1 + \frac{\Phi}{\Phi_s}} \tag{4.38}$$

$$\text{with} \quad \gamma_0 = N \frac{\Phi_p \left(\sigma_{es} \sigma_{ap} - \sigma_{as} \sigma_{ep} \right) - \frac{\sigma_{as}}{\tau}}{\Phi_p \left(\sigma_{ap} + \sigma_{ep} \right) + \frac{1}{\tau}} \tag{4.39}$$

$$\text{and} \quad \Phi_s = \Phi_p \frac{\sigma_{ap} + \sigma_{ep}}{\sigma_{as} + \sigma_{es}} + \frac{1}{\tau \left(\sigma_{as} + \sigma_{es} \right)} , \tag{4.40}$$

where γ_0 and Φ_s are the small-signal gain coefficient and the saturation photon density, respectively [54]. The small-signal gain indicates which gain a small signal experiences when it passes the amplifier crystal. In this case, the inversion is high enough to provide for enough states in the upper laser level such that all incoming photons are amplified by stimulated emission. When a larger photon density is incident on the laser crystal, the gain saturates due to the limited amount of upper level states. The saturation photon density is a measure of the photon density which decreases the gain coefficient to half the small-signal gain [54]. With $P = \frac{hc}{\lambda} \pi \omega^2 \Phi$, the saturation photon density can be converted to the saturation power

$$P_s = P_p \frac{\omega_s^2}{\omega_p^2} \frac{\lambda_p}{\lambda_s} \frac{\sigma_{ap} + \sigma_{ep}}{\sigma_{as} + \sigma_{es}} + \frac{\frac{hc}{\lambda_s} \pi \omega_s^2}{\tau \left(\sigma_{as} + \sigma_{es} \right)} , \tag{4.41}$$

where ω_p and ω_s are the beam diameters of the pump and the signal beam, respectively. From Equation (4.38) - (4.41), the following observations are made:

1. Firstly, when the amplifier crystal is unpumped ($\Phi_p = 0$), the small-signal gain coefficient is $\gamma_0 = -N \sigma_{as}$. In this case, the signal is absorbed by the amplifier crystal. Therefore,

from measuring the absorption of the signal light in an unpumped crystal, the experimental and theoretical small-signal gain coefficient can be compared.

2. Secondly, in an unpumped amplifier crystal, the saturation photon density is $\Phi_{s,0} = \dfrac{1}{\tau \left(\sigma_{as} + \sigma_{es}\right)}$, which corresponds to the spectroscopic saturation flux density.

3. Thirdly, in the limit of large pump photon densities, the small-signal gain coefficient is constant and only depends on the material parameters:
$\gamma_{0,max} = N \dfrac{\sigma_{es}\sigma_{ap} - \sigma_{as}\sigma_{ep}}{\sigma_{ap} + \sigma_{ep}}$.

4. The saturation power increases linearly with the pump power. This will be investigated in Section 4.3.3 in particular by measuring gain curves for varying pump powers.

It should be noted at this point that the model is greatly simplified compared to the experiment. For example, neither the longitudinal nor the transverse intensity distribution of the pump or laser mode are taken into account.

4.3.2 Design of Amplifier Stage

To investigate the optical gain properties of a Ho^{3+}:YAG amplifier, a similar resonator to the one presented in Section 4.2.4 is used. A schematic representation of the entire setup is depicted in Figure 4.29. In contrast to the previously presented resonator, the HR mirror is replaced by one with a radius of curvature of -0.15 m to further shift the output power to a higher level. Subsequent to the resonator, a variable attenuator consisting of a half-wave plate and a TFP is used to control the signal input power for the amplifier stage. A Galilean telescope (lenses L_6 and L_7) focuses the signal beam to a $1/e^2$ beam diameter of $\omega_s = 570\,\mu m$ into the center of the amplifier crystal. As amplifying medium, two $0.75\,\%$ doped Ho^{3+}:YAG crystals with a total length of 52 mm are used. To pump the amplifier crystals, a second 100 W Tm^{3+}-doped fiber laser is focused by a three-lens telescope (L_3, L_4, and L_5) to a beam waist diameter of $\omega_p = 600\,\mu m$. To investigate different amplifier pumping schemes, the unpolarized output of the Tm^{3+}-doped fiber laser is approximately split in half by a TFP. An attenuator is installed in each pump arm to control the input pump power. The combining of the pump and the signal beam into the amplifier crystals is realized by a dichroic IC mirror ($R > 99.9\,\%$ for 1980 nm, $R > 99\,\%$ for the s-polarized 2090 nm light and $R < 2\,\%$ for the p-polarized 2090 nm light). While a co-pumping scheme is generated when the pump and the signal light pass the amplifier
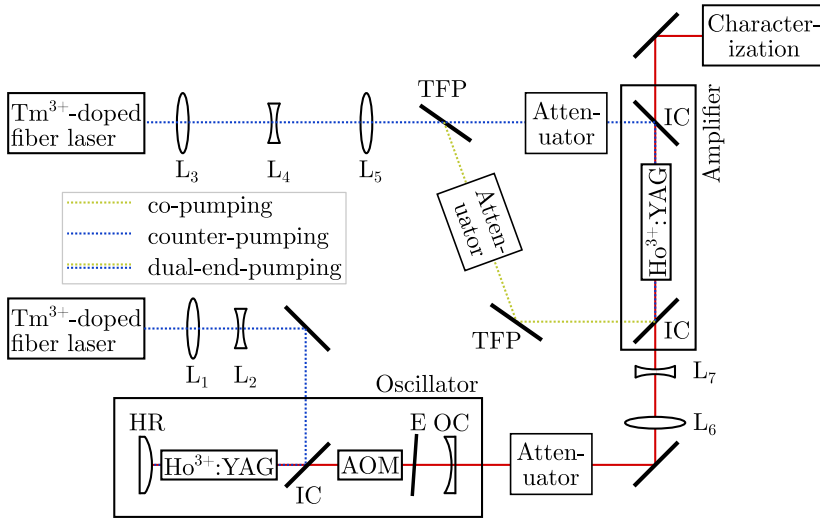
Figure 4.29: Schematic representation of the MOPA setup including both the oscillator and the amplifier stage.

crystals in the same direction, a counter-pumping scheme is realized when the pump light passes the amplifier crystal in the opposite direction compared to the 2090 nm signal light. A dual-end-pumping scheme results when co- and counter-pumping are combined.

4.3.3 Characterization of Ho^{3+}:YAG Amplifier

Due to the improved resonator, some important characteristics are briefly summarized in the following. A maximum output power of 65.7 W is measured with a slope efficiency of 63.4 % (see Figure 4.30(a)). Beam propagation factors of $M^2 = 1.14$ and $M^2 = 1.05$ are measured in the horizontal (x) and vertical (y) beam direction at an output power of 61.8 W, which is therefore set as the working point (see Figure 4.30(b)). Figure 4.30(c) shows the power stability measured over half an hour. The standard deviation is 0.1 W confirming the stable operation. At 50 kHz repetition rate, Q-switched pulses with 33 ns pulse duration, a pulse energy of 1.24 mJ, and a pulse peak power of 38 kW are measured (see Figure 4.30(d)).

Figure 4.31 shows the amplifier output power depending on the pump power for the co-, counter-, and dual-end-pumping scheme. While the highest slope efficiency of 69.9 % is achieved in the co-pumping scheme, the slope efficiency of the counter-pumping scheme amounts to 59.8 %.
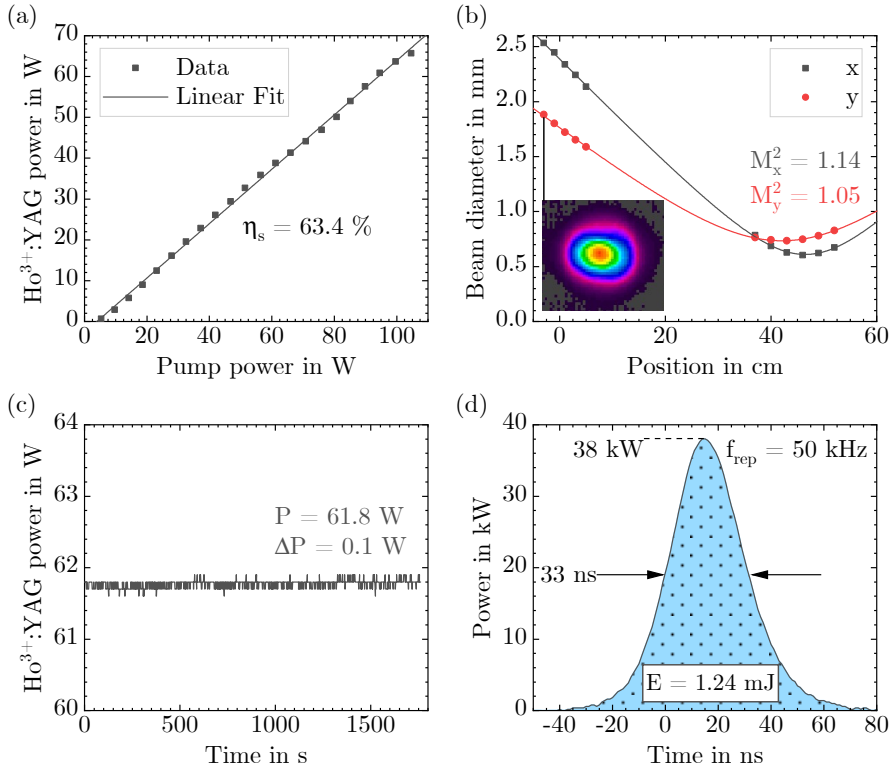
Figure 4.30: Characteristics of the modified oscillator. (a) Ho^{3+}:YAG output power depending on pump power. (b) Beam propagation factor measured at 62 W of output power. (c) Power stability measurement over 30 min. (d) Exemplary output pulse reaching a peak power of 38 kW.

The slope efficiency of the dual-end-pumping scheme (65.6 %) is in between these values. The split of the pump power at the TFP limits the available pump power to around 50 W for the co- and counter-pumping direction. In the dual-end-pumping scheme, the entire available pump power of 101 W is available. The superior performance of the co-pumping scheme might be explained by the longitudinal distribution of the signal and the inversion making up the specific longitudinal gain distribution. Overall, the gain distribution results from a complex interplay of pump and signal mode, but the following considerations are intended to approximate the problem. Firstly, due to gain saturation effects and the increasing signal along the crystal axis, the gain coefficient decreases with the propagation of the signal through the crystal. Secondly, the distribution of the inversion along the crystal axis strongly depends on the chosen pumping scheme. In the co-pumping scheme, the inversion is highest at the front of the crystal due to the
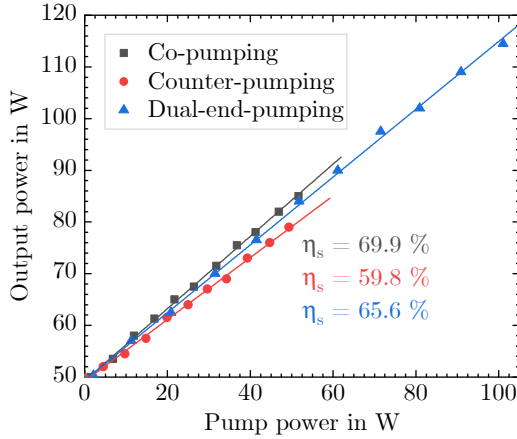
Figure 4.31: Amplifier output power depending on the input power with a fixed signal power of 62 W for different pumping schemes.

exponential absorption of the pump light, resulting in the highest gain coefficient at this position. In contrast to this, the gain coefficient is highest at the end of the crystal in the counter-pumping scheme. In the dual-end-pumping scheme, the inversion is comparably homogeneous over the length of the crystal. Thus, the first effect is dominant in this case. For this setup, the gain distribution leading to a maximum total gain results for the co-pumping scheme. However, due to the highest available pump power in the dual-end-pumping scheme, this configuration is characterized in more detail in the following paragraph.

Figure 4.32 shows the amplifier output power and the depolarized power depending on the pump power for the dual-end-pumping scheme. Due to a slightly improved alignment in comparison with the power curve presented in Figure 4.31, a slightly higher slope efficiency of 67.5 % and a maximum output power of 122 W is measured when the incoming signal power is set to 62 W. A pump threshold of 11 W is determined. Below this pump power, the inversion in the amplifier crystal is not high enough to compensate for the reabsorption losses of the signal beam. At the highest output power, the depolarized power is below 2 W corresponding to a value of $< 1\,\%$. From the linearity of the power curve, the pump power limitation of the setup is concluded. Thus, a further power scaling might be achieved with a higher available pump power. The beam propagation factor is measured to be around $M^2 \approx 1.2$, which is only a small deterioration in comparison with the oscillator beam propagation factor (see Figure 4.32(b)). The measurement of the power stability is shown in Figure 4.32(c). In comparison with the oscillator power
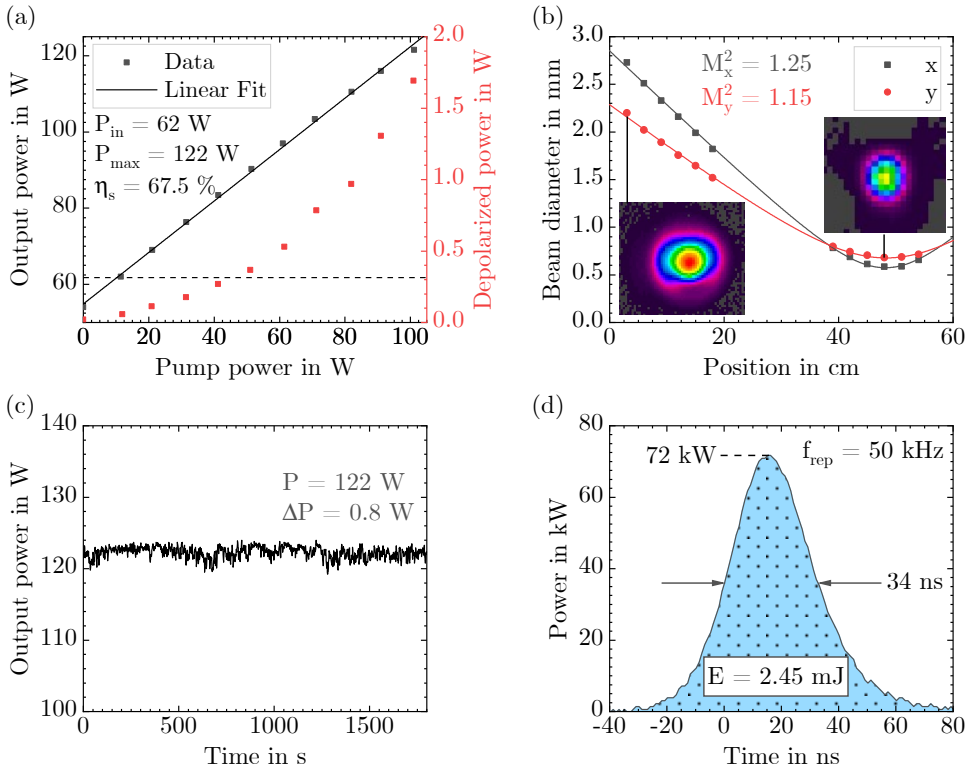
Figure 4.32: Characteristics of the amplifier output. (a) Output power depending on pump power. (b) Beam quality measured at 122 W of output power. (c) Power stability over 30 min. (d) Exemplary output pulse reaching a peak power of 72 kW.

stability, the standard deviation of the output power increases to 0.8 W. The higher instability might result from instabilities of the amplifier pump laser due to thermal blooming, as the propagation path was considerably longer compared to that of the oscillator pump beam. At the maximum output power, pulses with an energy of 2.45 mJ, a pulse duration of 34 ns, and a pulse peak power of 72 kW are measured, which is almost twice as much as was measured for the oscillator pulses. Therefore, the gain at maximum pump and signal power is approximately $G = 2$. A more detailed analysis of the optical gain depending on the pump and signal power is discussed in the following paragraph.

At first, the gain coefficient of the signal beam when passing the unpumped amplifier crystals is determined. It is calculated by

$$\gamma = \frac{1}{L} \ln \left(\frac{P_{\text{out}}}{P_{\text{in}}} \right) , \tag{4.42}$$

where P_{in} is the incident signal power and P_{out} is the power measured behind the amplifier crystals with a total length L. The gain coefficient depending on the incident signal power is shown in Figure 4.33(a). The attenuation is reflected in the negative value of the gain coefficient. In addition to the measured data, the plot includes the theoretically expected gain coefficient calculated from the material parameters $N = 1.04 \cdot 10^{26}\,\text{m}^{-3}$ and $\sigma_{\text{as}} = 0.21 \cdot 10^{-24}\,\text{m}^2$ [20] resulting in a theoretical small-signal gain coefficient of $\gamma_{0,\text{theo}} = -21.5\,\text{m}^{-1}$. By performing the fit given in Equation (4.38), the small-signal gain is experimentally determined to $\gamma_{0,\text{exp}} = -15.9\,\text{m}^{-1}$. The 26 % deviation from the theoretical expectation might result from uncertainties in the power measurement and the crystal doping concentration. In addition to the small-signal gain coefficient, the saturation power is determined from the fit and it amounts to 4.9 W, whereas the theoretically expected value is 2.2 W. Figure 4.33(b) shows the gain coefficient for the amplifier crystals pumped with powers between 20 W and 101 W. For an increasing pump power, an increase in the gain coefficient is observed and for an increasing signal power, the gain coefficient is reduced. This is in accordance with the expectation from the theoretical model. For the higher pump powers, the small-signal gain coefficient approximately amounts to 0.45 cm^{-1}, which corresponds to a total gain factor of 10.4 over the entire crystal. For the
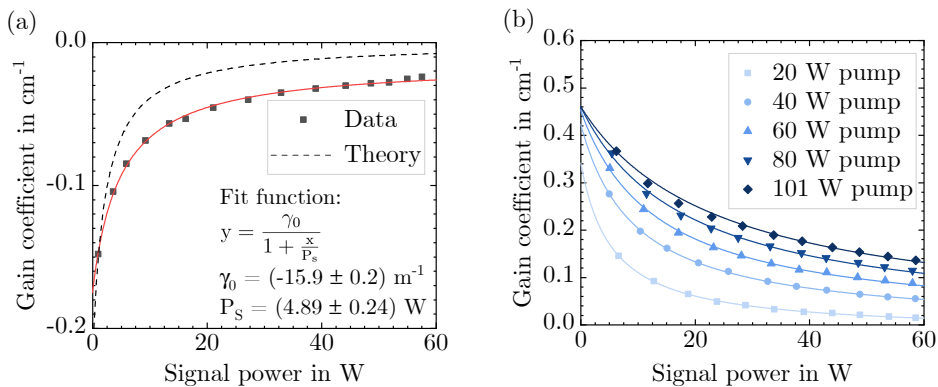

Figure 4.33: Gain coefficient for (a) an unpumped crystal and (b) a crystal pumped with increasing powers between 20 W and 100 W.
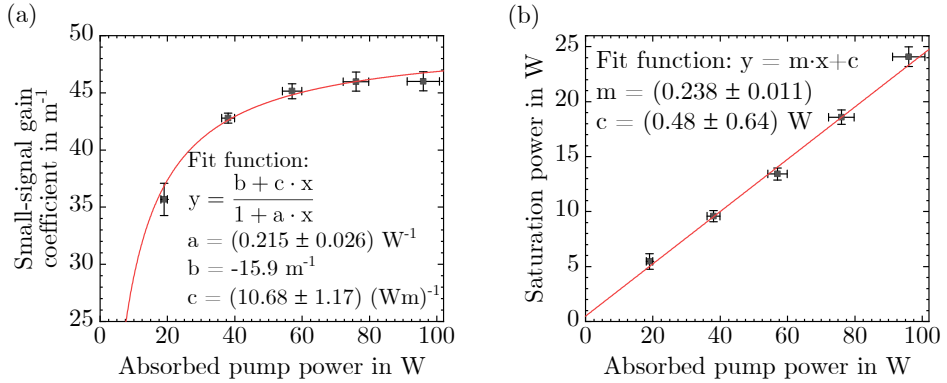
Figure 4.34: (a) Small-signal gain coefficient and (b) saturation power depending on the absorbed pump power. Both parameters show the expected qualitative behavior.

maximum pump power of 101 W and the maximum signal power of 60 W, the gain coefficient is $0.13 \, \text{cm}^{-1}$, resulting in a gain of 2. From the fit parameters, the small-signal gain coefficient and the saturation power is determined for each pump power. Figure 4.34(a) and Figure 4.34(b) show the small-signal gain coefficient and the saturation power, respectively, as a function of the absorbed pump power. The absorption efficiency is estimated to be 95 %. The fit function and fit parameters are given in the inset of the respective plots. For the fit of the small-signal gain coefficient, the fit parameter b is set to the value that was determined from Figure 4.33(a). From the theoretical model and the material parameters $\sigma_{es} = 1.2 \cdot 10^{-24} \, \text{m}^2$, $\sigma_{ap} = 1.2 \cdot 10^{-24} \, \text{m}^2$, and $\sigma_{ep} = 0.77 \cdot 10^{-24} \, \text{m}^2$ [20], the maximum small-signal gain coefficient in the limit of infinitely high pump powers is determined to be $\gamma_{0,\text{max,exp}} = (50 \pm 8) \, \text{m}^{-1}$, whereas from the model a value of $\gamma_{0,\text{max,theo}} = 67.6 \, \text{m}^{-1}$ was expected. This corresponds to a deviation of 26 % of the experimental from the theoretical value. The saturation power increases linearly with the absorbed pump power as expected from the theoretical model (see Figure 4.34(b)). From the fit, the spectroscopic saturation power is determined to be 0.5 W. The theoretically expected slope amounts to $m_{\text{theo}} = 1.17$, whereas the value of the experimentally determined slope is $m_{\text{exp}} = 0.24$.

Overall, the small-signal gain coefficient and the saturation power show the expected dependence on the pump power, although the experimentally determined values differ from the theoretical ones. This might result from the deviations of the experiment from the simplified model. Further deviations arise due to measurement uncertainties in the input and output power and the beam diameters of the pump and signal mode. Further, an increase in the pump beam diameter with a higher pump power due to thermal blooming effects cannot be ruled out.

4.3.4 Discussion

Finally, the results obtained here are compared with findings from the literature. Table 4.3 shows the results obtained from three published Ho^{3+}:YAG amplifier systems in comparison with this work. P_{in} denotes the signal input power to the amplifier stage, $P_{p,max}$ denotes the maximum pump power, and P_{max} refers to the maximum signal output power. The results obtained in all works are in a similar range. Typical slope efficiencies are around 70 % and optical-to-optical conversion efficiencies (OOCEs) are around 60 %. In addition to the efficiencies, the gain factors are comparable as well, especially when the parameters from the model presented in this work are used to estimate the gain factors at the corresponding pump and signal powers from the references [30, 120, 125]. For a pump power of 140 W and a signal power of 55.1 W as has been shown by Zhao et al. [120], the model predicts a gain factor of 2.6, for a pump power of 165 W and a signal power of 90 W as has been shown by Liu et al. [30], the model predicts a gain factor of 2.1, and for a pump power of 145 W and a signal power of 81.8 W as has been shown by Mi et al. [125], the model predicts a gain factor of 2.1. As the gain properties of the amplifier presented in this work and the literature results are comparable, the higher overall output power that was presented in the literature is attributed to the higher available pump power in these works. This indicates that a further power scaling is achievable when higher pump powers are available.

4.3.5 Summary

To summarize, a single-stage Ho^{3+}:YAG amplifier was investigated in terms of the output beam and the optical gain characteristics. At first, a theoretical model was derived to describe the gain characteristics starting from the rate equations. Under equilibrium conditions, a saturation of the

Table 4.3: Comparison of published Ho^{3+}:YAG amplifier system with the results obtained in this thesis.

Reference	Year	P_{in} in W	η_s in %	OOCE in %	G at $P_{p,max}$	P_{max} in W
[120]	2018	55.1 W	66.1	60.6	2.5 at 140 W	140
[30]	2021	90 W	73.6	65.9	2.2 at 165 W	201
[125]	2022	81.8 W	68.8	57.6	2.0 at 145 W	165
This work	2024	61.8 W	67.5	59.6	2.0 at 101 W	122

gain coefficient and a linear increase of the saturation power with the pump power were predicted. For the experiments, the oscillator design was slightly improved compared to the one presented in Section 4.2.4 by using an HR mirror with a smaller radius of curvature. The amplifier stage was further designed such that a co-, counter-, and dual-end-pumping scheme could be investigated within the same setup. These pumping schemes mainly differed in the longitudinal gain distribution that developed in the amplifying medium. Although the highest slope efficiency of 69.9 % was achieved in the co-pumping scheme, it was limited in pump power, thus the dual-end-pumping scheme was characterized in detail. A maximum output power of 122 W was measured with a beam propagation factor of $M^2 \approx 1.2$. Therefore, the preservation of the beam propagation factor in an amplifier was confirmed. From the linear course of the power curve, a pump power limitation was concluded, thus further power scaling is possible when a pump source with a higher output power is used. The Q-switched pulses were amplified to a pulse energy of 2.45 mJ and had a pulse peak power of 72 kW. The gain coefficients were measured for an unpumped amplifier crystal and for an amplifier crystal pumped with different pump powers. As predicted from the theoretical model, the saturation of the gain coefficient could be measured in both cases. Furthermore, the small-signal gain coefficient and the saturation power showed the expected qualitative behavior. Further scaling of the pump power seems possible, as the output power was limited by the available pump power.

5   Ho^{3+}:YAG Resonators with Increased Mechanical Stability

In this chapter, the mechanical stability of Ho^{3+}:YAG resonators is investigated. The resonator end mirrors are replaced by Porro prisms, which retro-reflect the incident light in one axis, therefore leading to an angular stabilization of the laser mode. Section 5.1 gives an overview over the existing research on Porro prism based laser resonators. In Section 5.2, a theoretical background is provided to understand the working principle of a Porro prism and its special characteristics. The Porro prisms are experimentally characterized in Section 5.3. Different cavities with Porro prisms are presented in Section 5.4. In Section 5.5, the obtained results are analyzed and discussed. Section 5.6 summarizes the chapter.

This chapter is based on the results discussed in the publication:

<u>K. Goth</u>, M. Griesbeck, M. Eitner, H. Büker, M. Eichhorn, and C. Kieleck, "Alignment-insensitive end-pumped continuous-wave crossed-Porro prism Ho^{3+}:YAG laser," *Optics Letters*, vol. 47, no. 13, p. 3143, 2022. DOI: 10.1364/OL.459892.

5.1   Introduction

For lasers that are intended to be operated in harsh environments, resulting in considerable mechanical vibrations, an alignment-insensitive resonator design is a requirement. Resonator designs that are distinguished by a high misalignment tolerance often use prisms as cavity end reflectors, e.g. right angle cones [132, 133], corner cube prisms [134–136], or Porro prisms [33, 137, 138]. Especially resonators with two crossed Porro prisms based on Nd^{3+}:YAG crystals have been used in applications like laser rangefinders [139–141], laser

designators [139, 142, 143], and for space applications [144–147] in the last decades. Research on both the characteristics of Porro resonators as well as on the characteristic properties of Porro prisms has been presented. In 1980, See has thoroughly described a Porro resonator, has investigated the impact of different angles enclosed by the two Porro apexes on the alignment stability, and has shown the overall increased alignment stability in a Porro resonator by a factor of 30 [33]. Lee and Leung have investigated the beam pointing [148] and lateral displacement [149] of the output beam from a misaligned Porro resonator as well as the alignment tolerance of such a resonator [150], both theoretically and experimentally. In addition, higher-order resonator modes developing in Porro resonators have been discussed in detail by Litvin et al. [151] and Burger et al. [152]. Next to Porro resonators, the physical properties of Porro prisms were investigated including their polarization properties [153, 154] and losses at the apex [151, 155]. In particular, Richards has introduced a zero phase shift (ZPS) Porro prism [156–158], which enables a depolarization compensation of the thermally-induced birefringence in the laser crystal [157].

Many of these Nd^{3+}:YAG lasers have been operated in a low-repetition-rate regime between 1–20 Hz with pulse energies of some tens of mJ resulting in average output powers below 1 W [141, 144, 147, 159]. In this operational regime, thermal lensing effects are weak, facilitating the resonator design. Lasers with average output powers of some Watts were also realized in a crossed-Porro design. However, these laser exhibited a multi-mode transverse mode structure resulting in high beam propagation factors [143, 145, 160].

In contrast to the four-level laser material Nd^{3+}:YAG, the quasi-three-level nature of Ho^{3+}:YAG imposes constraints on the resonator design due to reabsorption losses at the laser wavelength. These constraints are further exacerbated when a laser source with a near-diffraction-limited beam quality is required, as here an excellent overlap of the pump and the laser mode has to be established. Alignment-insensitive Ho^{3+}:YAG lasers with a near-diffraction-limited beam quality based on corner cube prisms have been presented by Wang et al. in 2018 [161] and by Yan et al. in 2023 [162]. However, they were operated at low average powers around 1 W.

In this thesis, the principle of a crossed-Porro resonator is applied to a Ho^{3+}:YAG laser for the first time. In distinction to already existing literature, the investigated lasers are designed to operate at a high average power and with an excellent beam quality, which implies the use of small pump diameters resulting in strong thermal lensing.

5.2   Theoretical Considerations on Porro Prisms

In Section 5.2.1, the working principle of a Porro prism and the resulting alignment insensitivity, when it is used in a laser resonator, is explained. Section 5.2.2 presents a calculation of the losses resulting from the prism apex, which is not infinitely sharp. The angular spectrum of the incident light beam as a loss mechanism is derived in Section 5.2.3. The polarization properties of the prisms are calculated with the Jones matrix formalism in Section 5.2.4 and the resulting possibility of depolarization compensation in a laser resonator is presented in Section 5.2.5.

5.2.1   Functional Principle of Porro Prisms

A Porro prism is a right-angled prism in which the beam is incident through the hypotenuse side face as indicated in Figure 5.1(a). Because the beam is totally internally reflected from the two prism side faces and the angle between the side faces is 90°, the beam reflected from the prism is antiparallel to the incident beam. This works both for beams that are incident onto the prism perpendicularly as well as under an angle (see Figure 5.1(b)). However, for obliquely incident beams, the reflective property only works in an angular range defined by the condition for the two total internal reflections (TIRs). A simple geometric consideration yields that the angular range $|\alpha_{\mathrm{TIR}}|$ is given by

$$|\alpha_{\mathrm{TIR}}| \leq \frac{\pi}{4} - \arcsin\left(\frac{n_1}{n_2}\right) , \qquad (5.1)$$
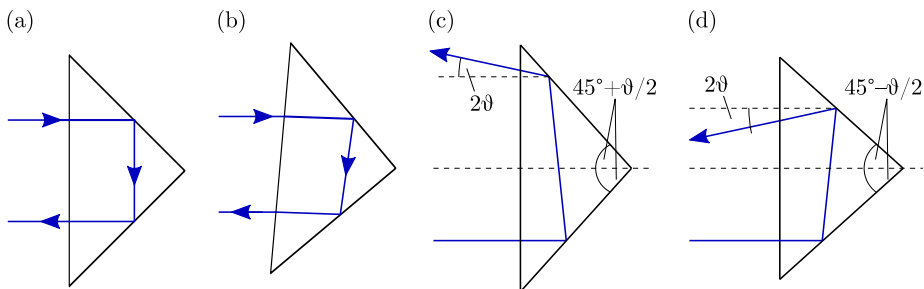

Figure 5.1: Reflection from a Porro prism when the beam is incident (a) perpendicular and (b) under an angle and when the Porro prism has an apex angle (c) larger and (d) smaller than 90° by ϑ.
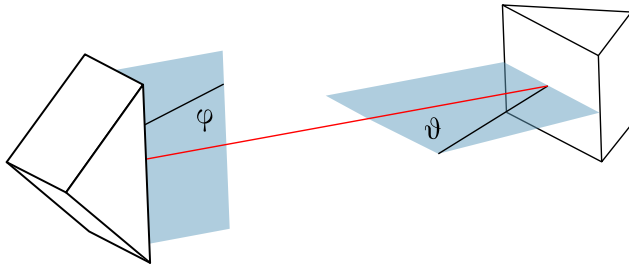
Figure 5.2: Working principle of a crossed-Porro cavity. The prism on the left/right side stabilizes the laser mode angle in the vertical/horizontal plane. φ/ϑ denotes the angle around which the left/right prism can be tilted while preserving its retro-reflective property.

where n_1 and n_2 are the refractive index of air and the prism material, respectively. When the incident and reflected beam shown in Figure 5.1(a) and Figure 5.1(b) are considered as the envelope of a Gaussian beam, the retro-reflection of a beam centered on the apex becomes clear. A crucial property of the Porro prism is the 90° angle of the apex. When the apex angle deviates from the 90° angle by ϑ, an angle of 2ϑ between the incident and reflected beam results. The direction of deviation depends on the apex angle being smaller or larger than 90° (see Figure 5.1(c) and Figure 5.1(d)).

When two prisms are used on the opposite sides of a resonator with their apexes aligned perpendicular to each other, then each prism stabilizes one beam axis due to its retro-reflective property (see Figure 5.2). The angle enclosed by the apexes can in principle take values between 0–90°, but the configuration with the highest alignment stability is reached for an angle of 90° [33, 163]. In addition to the alignment stability, the angle can also have an impact on the beam propagation factor and in resonators operated on higher order modes, the highest beam quality was simulated for an angle of 90° [164].

5.2.2 Calculation of Apex Losses

For an efficient retro-reflection, the apex of the prism must be as sharp as possible. In the vicinity of the apex, the side faces are not well defined resulting in a breakdown of the TIR. Consequently, the fraction of the light beam that overlaps with the apex is diffracted at the apex, therefore it is lost for the reflection. To approximate the losses which are expected from the apex, it is assumed to be rectangular in Figure 5.3.
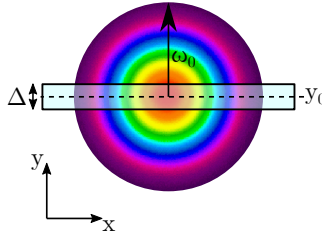
Figure 5.3: Calculation of losses for a Gaussian beam with beam radius ω_0 at the apex, which is depicted as a rectangle having a width Δ and a shift y_0 with respect to the beam center.

By calculating the overlap integral of the incident Gaussian beam with the rectangular area, the apex losses can be estimated. The intensity distribution of a Gaussian beam with peak intensity I_0 and beam diameter ω_0 is given by

$$I(x,y) = I_0 \exp\left(-2\frac{x^2 + y^2}{\omega_0^2}\right) . \tag{5.2}$$

Depending on the apex width Δ, the shift y_0 with respect to the center of the beam and the beam diameter, the losses are given by

$$\Lambda(\omega_0, \Delta, y_0) = \frac{\int_{y_0-\Delta/2}^{y_0+\Delta/2}\int_{-\infty}^{\infty} I(x,y)\mathrm{d}x\mathrm{d}y}{\int_{-\infty}^{\infty}\int_{-\infty}^{\infty} I(x,y)\mathrm{d}x\mathrm{d}y} = \frac{1}{2}\left(\mathrm{Erf}\left(\frac{2y_0+\Delta}{\sqrt{2}\omega_0}\right) - \mathrm{Erf}\left(\frac{2y_0-\Delta}{\sqrt{2}\omega_0}\right)\right) . \tag{5.3}$$

Typical values for the apex sharpness are around 5 μm [39]. As typical beam diameters are in the range of several hundred μm, the approximation $\Delta \ll \omega_0$ can be used. In this case, the losses are approximated as

$$\Lambda(\omega_0, \Delta, y_0) \approx \frac{\sqrt{2}\Delta}{\sqrt{\pi}\omega_0} \exp\left(-\frac{2y_0^2}{\omega_0^2}\right) . \tag{5.4}$$

As can intuitively be expected, the losses get larger when the apex width increases, the beam diameter decreases, and when the beam is centered on the apex. The apex losses will be determined experimentally in Section 5.3.

5.2.3 Influence of Angular Spectrum on TIR Range

The angular range for which the condition for both TIRs on the prism side faces is fulfilled only holds true for geometrical optics, where light is considered as a ray with a specific propagation direction. In the angular spectrum representation, a Gaussian beam is described as a superposition of plane waves with different propagation directions [165]. According to Equation (3.4), the electric field distribution describing a Gaussian beam in the beam waist is given by

$$E(x, y) = E_0 \exp\left(-\frac{x^2 + y^2}{\omega_0^2}\right) . \tag{5.5}$$

By applying a Fourier transform on the electric field distribution, the angular distribution is derived [51, 165]:

$$\hat{E}(\theta_x, \theta_y) = \int_{-\infty}^{\infty} \int_{-\infty}^{\infty} E(x, y) \exp\left(-i(k_x x + k_y y)\right) \mathrm{d}x \mathrm{d}y \tag{5.6}$$

$$= E_0 \pi \omega_0^2 \exp\left(-\frac{\omega_0^2 k^2}{4}(\theta_x^2 + \theta_y^2)\right) , \tag{5.7}$$

where θ_x and θ_y are the angles of the x- and y-component of the wave vector, k_x and k_y, with the z-axis, respectively. The intensity distribution is given by $\hat{I}(\theta_x, \theta_y) \propto \hat{E}(\theta_x, \theta_y)^2$. Figure 5.4(a) shows the intensity distribution of the angular spectrum in one dimension for different beam diameters. For a stronger beam focusing, the width of the angular spectrum increases. As a consequence, the angular range, for which both TIRs work, is reduced when a Gaussian beam with a wider angular spectrum is incident onto the prism. The losses Λ expected from the angular spectrum distribution of the Gaussian beam, when the prism is tilted by an angle β, is calculated by

$$\Lambda(\beta) = 1 - \int_{-(\alpha_{\mathrm{TIR}}-\beta)}^{\alpha_{\mathrm{TIR}}-\beta} \int_{-\infty}^{\infty} \hat{I}(\theta_x, \theta_y) \mathrm{d}\theta_x \theta_y \Big/ \int_{-\infty}^{\infty} \int_{-\infty}^{\infty} \hat{I}(\theta_x, \theta_y) \mathrm{d}\theta_x \theta_y \tag{5.8}$$

$$= 1 - \mathrm{Erf}\left(\frac{\sqrt{2}\pi\omega_0}{\lambda}\left(\alpha_{\mathrm{TIR}} - \beta\right)\right) . \tag{5.9}$$

In this equation, the integration only has to be performed in one axis, as the prism is tilted around the respective axis. Figure 5.4(b) shows the losses depending on the tilt angle of the
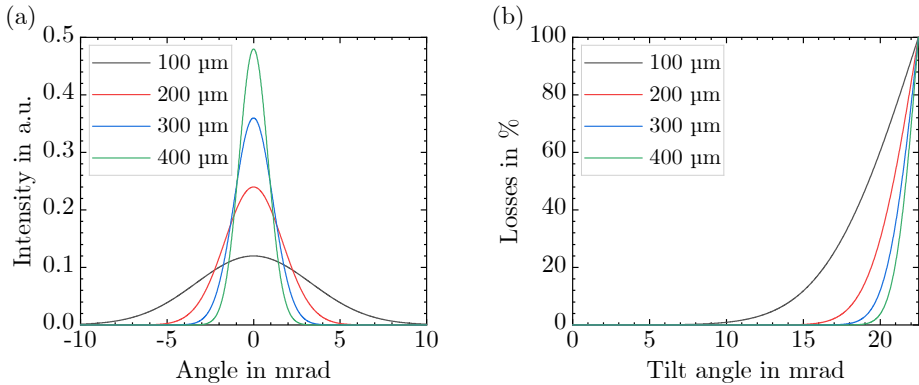
Figure 5.4: (a) Angular spectrum and (b) prism losses depending on the tilt angle for Gaussian beams focused to 100 μm (black), 200 μm (red), 300 μm (blue), and 400 μm (green).

prism for different diameters of the Gaussian beam. A smaller beam waist diameter results in a larger angular spectrum and increased losses at a given prism tilt angle.

5.2.4 Polarization Effects in Porro Prisms

TIR results in different phase shifts depending on the state of polarization [153]. Because the reflective property of Porro prisms is based on two TIRs, incident mixed polarization states experience different phase delays in the two intrinsic axes of the prism. This changes the polarization state of the reflected light beam compared to that of the incident light beam. The polarization properties of the Porro prisms play a crucial role in the output coupling of the light from the resonator. Two output coupling schemes can be distinguished, which both involve a TFP. Firstly, by rotating the prism apex, the intrinsic polarization axes of the prism are rotated, which results in a modified polarization state of the light reflected by the prism. As a consequence, the output coupling at the TFP is changed [138, 151]. A disadvantage of this method is that it is not possible to use the cross-Porro configuration with the highest alignment stability. Secondly, as an alternative to rotating the prism, the polarization state of the incident light can be altered by a wave plate [159, 166, 167].

A mathematical tool for calculating the effect of a system of optical elements on a polarization state is the Jones matrix formalism [64]. In the Jones matrix formalism, the polarization states of the light are described by vectors, which indicate the oscillation direction of the electric

Table 5.1: Vectors and matrices in the Jones matrix formalism describing different polarization states and optical elements, respectively [64].

Polarization state/Optical element	Symbol	Jones vector
Horizontal polarization	E_H	$\begin{pmatrix} 1 \\ 0 \end{pmatrix}$
Vertical polarization	E_V	$\begin{pmatrix} 0 \\ 1 \end{pmatrix}$
Mirror	M_M	$\begin{pmatrix} 1 & 0 \\ 0 & -1 \end{pmatrix}$
Quarter-wave plate (fast axis horizontal)	$M_{\lambda/4}$	$e^{-\frac{i\pi}{4}} \begin{pmatrix} 1 & 0 \\ 0 & i \end{pmatrix}$
Half-wave plate (fast axis horizontal)	$M_{\lambda/2}$	$e^{-\frac{i\pi}{2}} \begin{pmatrix} 1 & 0 \\ 0 & -1 \end{pmatrix}$
Polarizer (axis of transmission horizontal)	M_{PH}	$\begin{pmatrix} 1 & 0 \\ 0 & 0 \end{pmatrix}$
Porro prism (apex horizontal)	M_{Porro}	$\begin{pmatrix} e^{-i\phi} & 0 \\ 0 & e^{-i\chi} \end{pmatrix}$
ZPS Porro prism (apex horizontal)	$M_{Porro,ZPS}$	$\begin{pmatrix} 1 & 0 \\ 0 & 1 \end{pmatrix}$

field, and phase shifts, which are introduced by the optical elements, are described by matrices. Similar to the matrix optics formalism introduced in Section 3.1.1, by multiplying all Jones matrices from an optical system, the polarization state of the light, which is transmitted through the optical system, can be calculated. The polarization states and matrices of specific optical elements, which are relevant in the following investigations, are given in Table 5.1. Jones matrices for two types of Porro prisms are also included. M_{Porro} describes the phase delay of a classical Porro prism as shown in Figure 5.1. $M_{Porro,ZPS}$ is the Jones matrix of a Porro prism that does not introduce a phase delay between two perpendicular polarization states. Details on this type of Porro prism have been described in [156] and [158]. To derive these two matrices, the phase delay in the case of a single TIR is required. The phase delay $\phi(\alpha)$ for the s-polarization and $\chi(\alpha)$ for the p-polarization are given by [153]

$$\tan\left(\frac{\phi(\alpha)}{2}\right) = \frac{\sqrt{n^2 \sin^2 \alpha - 1}}{n \cos \alpha} \tag{5.10}$$

$$\tan\left(\frac{\chi(\alpha)}{2}\right) = n^2 \tan\left(\frac{\phi(\alpha)}{2}\right) , \tag{5.11}$$

where n is the refractive index of the prism and α is the angle of incidence. Consequently, the Jones matrix for one TIR is given by

$$\begin{pmatrix} e^{-i\chi(\alpha)} & 0 \\ 0 & e^{-i\phi(\alpha)} \end{pmatrix} . \tag{5.12}$$

For a Porro prism aligned with a horizontal apex and tilted by an angle of ϑ around its apex, the angle of incidence on the upper side face is $\alpha_1 = 45° - \vartheta$ and the angle of incidence on the lower side face $\alpha_2 = 45° + \vartheta$ (see Figure 5.5). These angles have to carefully be considered in the calculation of the phase shift of the Porro prism. When a horizontally polarized beam (in the laboratory system) is incident onto this prism, the beam is s-polarized with respect to the side faces of the prisms and as a consequence experiences the phase delay $\phi(\alpha)$. Under this consideration, the Jones matrix for a Porro prism with horizontal apex can easily be determined by multiplying the according Jones matrices for the two TIRs on the prism side faces:

$$\begin{aligned} M_{\text{Porro}} &= \begin{pmatrix} e^{-i\phi(\alpha_2)} & 0 \\ 0 & e^{-i\chi(\alpha_2)} \end{pmatrix} \cdot \begin{pmatrix} e^{-i\phi(\alpha_1)} & 0 \\ 0 & e^{-i\chi(\alpha_1)} \end{pmatrix} \\ &= \begin{pmatrix} e^{-i(\phi(\alpha_1)+\phi(\alpha_2))} & 0 \\ 0 & e^{-i(\chi(\alpha_1)+\chi(\alpha_2))} \end{pmatrix} . \end{aligned} \tag{5.13}$$
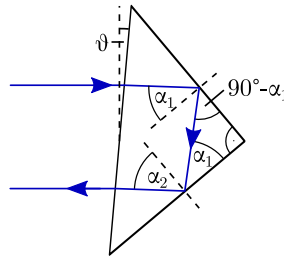

Figure 5.5: Porro prism with horizontal apex tilted by an angle ϑ around its apex. The indicated angles α_1 and α_2 are relevant to correctly determine the phase delay introduced by TIR.

In a ZPS Porro, the beam experiences two further TIRs from a surface which is aligned such that s- and p-polarization change their roles, therefore the phase delay between the two perpendicular polarization directions cancels.

When an optical element with the Jones matrix M_J is rotated around the optical axis by an angle of β, the Jones matrix for the rotated optical element $M_J(\beta)$ is given by

$$M_J(\beta) = R(\beta)M_J R(-\beta) \quad \text{with} \quad R(\beta) = \begin{pmatrix} \cos(\beta) & -\sin(\beta) \\ \sin(\beta) & \cos(\beta) \end{pmatrix}. \tag{5.14}$$

To derive the wave plate angle, which is necessary to achieve a certain output coupling, the following situation is considered (see Figure 5.6(a)): A light beam with arbitrary polarization E_{in} passes a TFP with horizontal transmission axis, a wave plate rotated by an angle of α, is then reflected by a Porro prism with vertical apex, and passes the wave plate again. The resulting elliptic polarization is then split at the TFP. Mathematically, the transmitted, E_T, and reflected, E_R, proportion through the TFP are given by

$$E_T = M_{\text{PH}} M_{\lambda/n}(-\alpha) M_{\text{Porro}}\left(\frac{\pi}{2}\right) M_{\lambda/n}(\alpha) M_{\text{PH}} E_{\text{in}} \tag{5.15}$$

$$E_R = 1 - E_T. \tag{5.16}$$

Here, $n = 2, 4$ refers to a half-wave or quarter-wave plate, respectively. The calculation is performed in the coordinate system of the incident beam. Figure 5.6(b) depicts the fast axis (FA) of the wave plate regarding to the beam propagation direction. Due to the choice of coordinate system, the wave plate angle changes to $-\alpha$ for the backward pass of the wave plate. Figure 5.7(a) and Figure 5.7(b) show the s- and p-polarized fraction that is reflected and
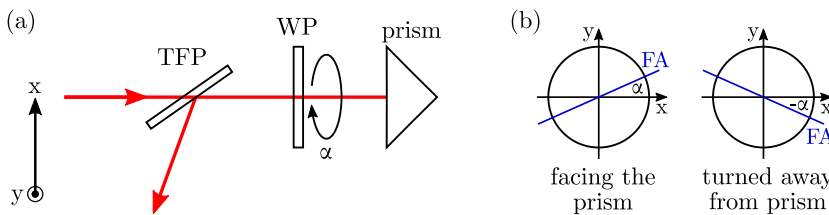

Figure 5.6: (a) Setup for measuring the polarization properties of the reflected beam when rotating the wave plate. The prism apex is vertical. (b) Determination of fast axis (FA) angle of the wave plate when the coordinate system of the incident beam is used.
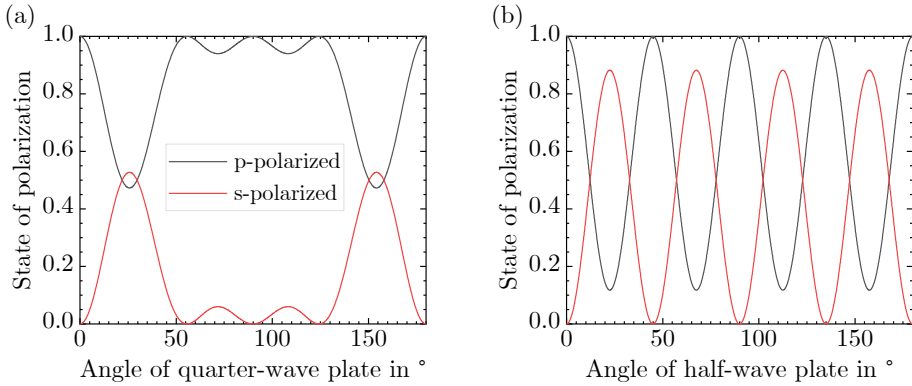
Figure 5.7: Calculated output state of polarization when rotating (a) the quarter-wave plate and (b) the half-wave plate in the setup shown in Figure 5.6.

transmitted at the TFP, when a quarter-wave plate and a half-wave plate is rotated, respectively. Considering the combination of TFP, quarter-wave plate, and Porro prism as output coupling unit of a resonator, an output coupling up to 52 % is realizable. With a half-wave plate, an output coupling between 0–88 % is possible.

5.2.5   Depolarization Compensation with Porro Prisms

Due to the thermally induced birefringence in the Ho^{3+}:YAG crystal, depolarization losses occur when the laser is operated at a linear polarization. In addition to losses, the thermally induced birefringence is also the cause of an astigmatic output beam. In combination with a wave plate, Porro prisms are suitable for compensating this depolarization due to the image rotation in the prism. In analogy to Section 5.2.4, this effect can be considered mathematically with Jones matrices. For the calculation, the situation shown in Figure 5.8(a) is taken into account. An initially p-polarized beam first passes a pumped laser crystal that introduces a phase delay, therefore resulting in depolarization. Then, a wave plate and a Porro prism with horizontal apex is double-passed. Finally, the crystal is passed again. In a system in which depolarization losses are compensated for, the final state of polarization is either the same as the initial state of polarization or it has the perpendicular state of polarization. In a cylindrical laser crystal, the eigensystem of the thermally induced birefringence is formed in the radial and tangential direction, thus it depends on the radial position r and the polar angle ϕ. In the Jones matrix formalism,
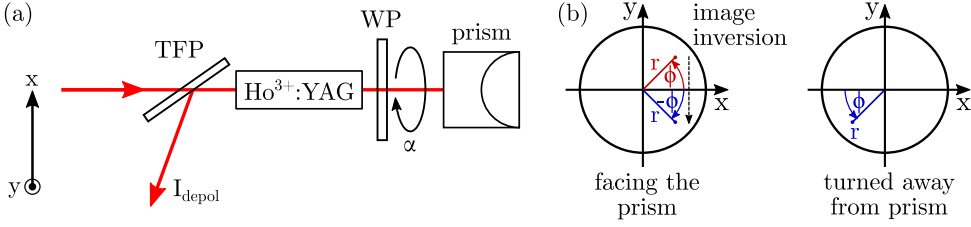
Figure 5.8: (a) Setup for evaluating the depolarization losses for different cases. (b) Determination of the polar angle of the crystal when the coordinate system of the beam is used. The first pass of the crystal is indicated by the red arrow, the image inversion is indicated by the dashed arrow, and the second pass of the crystal is indicated by the blue arrow.

the crystal is described as a phase plate that introduces a phase delay δ depending on the radial position r and the angle ϕ. Therefore, the Jones matrix for such a crystal is written as [157]

$$M_{\mathrm{c}}\left(\delta, \phi\right) = R(\phi) \begin{pmatrix} \mathrm{e}^{i\delta/2} & 0 \\ 0 & \mathrm{e}^{-i\delta/2} \end{pmatrix} R(-\phi)\,. \tag{5.17}$$

The Jones matrix of the optical system shown in Figure 5.8(a) is then given by

$$M_{\mathrm{J}}(\alpha) = M_{\mathrm{c}}\left(\delta, \phi\right) M_{\lambda/n}(-\alpha) M_{\mathrm{Porro}} M_{\lambda/n}(\alpha) M_{\mathrm{c}}\left(\delta, \phi\right)\,. \tag{5.18}$$

The angle ϕ in the second pass of the crystal (first matrix) is positive because the Porro prism introduces an image inversion on the beam (see Figure 5.8(b)). If a mirror was used instead of the prism, the negative angle ϕ would have to be considered. When the incident beam is horizontally polarized, the depolarized electric field is calculated by

$$E_{\mathrm{depol}} = M_{\mathrm{PH}}\left(\frac{\pi}{2}\right) M_{\mathrm{J}}(\alpha) E_{\mathrm{H}}\,. \tag{5.19}$$

By squaring the depolarized electric field, a measure for the depolarized intensity is calculated. Some combinations of wave plate and mirror or ZPS Porro prism and the resulting depolarized intensity are given in Table 5.2. The simple right-angled Porro prism is not included, as a complicated numerical expression results from the calculation. The combinations 1, 3, and 5 yield the same depolarization loss, which results from the simultaneous image inversion and change of position in the crystal when the Porro prism is used. The loss is decreased for the combinations 2 and 4 when a quarter-wave plate is included under an angle of 0°. Figure 5.9 shows the depolarization loss as a function of the polar angle of the crystal. For

Table 5.2: Different combinations of wave plate and mirror/ZPS Porro prism and the resulting depolarized intensity.

Number	Combination	Depolarized intensity
1	Mirror without wave plate	$I_1 \propto \sin^2(\delta)\sin^2(2\phi)$
2	Mirror with $\lambda/4$ (0°)	$I_2 \propto \sin^4(\delta/2)\sin^2(4\phi)$
3	ZPS Porro prism without wave plate	$I_3 \propto \sin^2(\delta)\sin^2(2\phi) = I_1$
4	ZPS Porro prism with $\lambda/4$ (0°)	$I_4 \propto \sin^4(\delta/2)\sin^2(4\phi) = I_2$
5	ZPS Porro prism with $\lambda/4$ (45°)	$I_5 \propto \sin^2(\delta)\sin^2(2\phi) = I_1$
6	ZPS Porro prism with $\lambda/2$ (22.5°)	$I_6 \propto 1$

the calculation of the curves, a radially-independent phase delay of $\delta = 0.5$ was assumed[1]. Additionally, the curves are depicted depending on the position in a crystal with radius 1. The combinations 1, 3, and 5 are represented by the black curve and the combinations 2 and 4 are represented by the red curve, which shows a considerably reduced depolarization. The course of the black curve can be explained as follows: For positions on the horizontal and vertical crystal axes ($\phi = 0, \pi/2, \pi, 3\pi/2$), the initial horizontal polarization is in the eigensystem of the crystal, thus no depolarized component is generated. However, on the diagonal axes ($\phi = \pi/4, 3\pi/4, 5\pi/4, 7\pi/4$), an initial horizontal polarization splits in the eigensystem of the crystal, which is diagonal in this case. Therefore, both components experience different phase delays in the crystal, resulting in an elliptic polarization after the second crystal pass, which leads to a depolarized component. When a quarter-wave plate under an angle of 0° is inserted between the crystal and the mirror (red curve), the argumentation remains the same for the horizontal and vertical axis. For the diagonal axes, however, the quarter-wave plate has an angle of 45° with respect to the resulting diagonal polarization. Therefore, in a double-pass of the quarter-wave plate, the polarization state is rotated by 90° and the radial and tangential polarization state change their roles. Consequently, in the second pass of the crystal, each component experiences the phase delay, which the other component has experienced in the first crystal pass. Thus, there is no phase delay between the components and the initial horizontal polarization is restored, which is why there is no depolarization loss in this case. A reduction in depolarization is also achieved with the simple Porro prisms, both without wave plate (blue) and with a quarter-wave plate under 0° (green). A complete depolarization compensation can be

---

[1] In Section 5.4.4, the experimental value is shown to be smaller but for the purpose of improving the visibility, the value was enhanced.
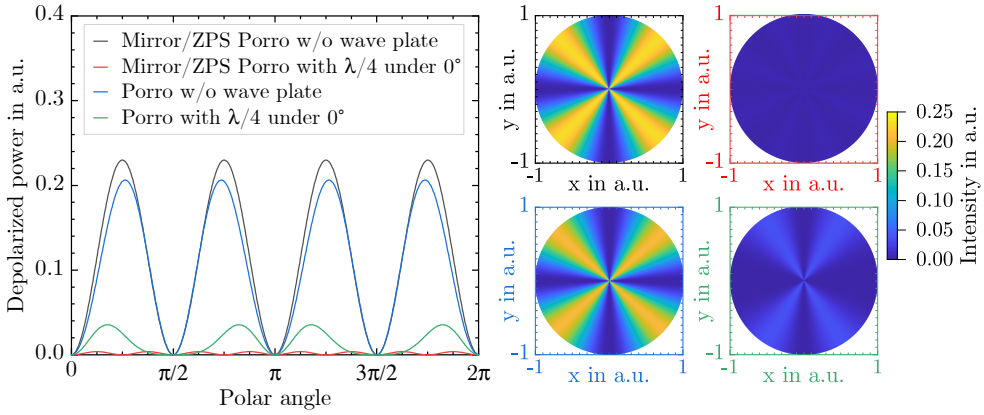
Figure 5.9: Depolarization losses for different combinations of mirror or Porro prism and wave plate depending on the polar angle ϕ in the crystal. For the calculation, a phase delay of $\delta = 0.5$ and an initial horizontal polarization was assumed. The labeling of the curves is given in the legend. For illustration purposes, the depolarized intensity is also shown as a function of the position in a crystal with radius 1. Here, the colors of the axes correspond to the colors of the respective curves.

achieved when the ZPS Porro is used in combination with a half-wave plate under 22.5°. In fact, the light is perpendicularly polarized with respect to the incident light after passing the crystal for the second time. However, this effect cannot be exploited in a simple linear cavity but only in a more complex polarization flip cavity. This cavity will be presented in Section 5.4.4.

5.3 Experimental Characterization of the Porro Prisms

At first, the Porro prisms are investigated with a light microscope in Section 5.3.1. Following this, the prism apexes are characterized regarding their width and angle in Sections 5.3.2 and 5.3.3. Finally, the polarization properties of the prisms are measured in Section 5.3.4.

5.3.1 Light Microscopic Investigation

For the assessment of the quality of the prism apexes, they are investigated with a microscope (Zeiss Axio Vert.A1 MAT) under a fivefold magnification. Figure 5.10 shows two exemplary images of the apexes of two prisms. The upper image shows a 1.06 mm wide defect
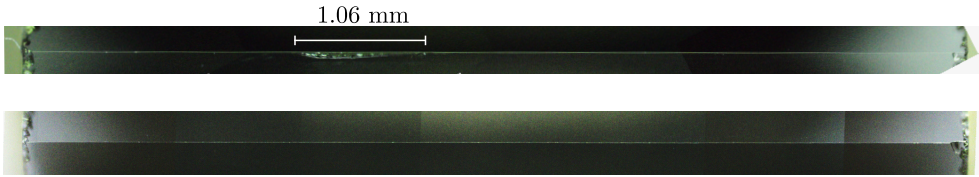
1.06 mm

Figure 5.10: Microscopic investigation of two Porro prisms in comparison. Top: The apex shows a large defect with a length of 1.06 mm. Bottom: Defect-free apex of an apex with a high quality.

at the apex, which is large considering that typical beam diameters are below 1 mm. The lower image shows the apex of a prism without any defects. Based on these images, a first qualitative assessment of the prism apexes was performed. To determine the apex width quantitatively, the apexes are investigated with a Ho^{3+}:YAG laser.

5.3.2 Apex Width

The experiment is based on a measurement of the reflected power by a prism as shown in Figure 5.11(a). For this purpose, the Porro prism is illuminated with a 2090 nm Ho^{3+}:YAG laser with a power of P_0 and a beam diameter ω_0 at the prism apex. The apex of the prism is aligned under a small angle to measure the reflected power P_R. The losses are then given by

$$\Lambda = 1 - \frac{P_R}{P_0} \, . \tag{5.20}$$

Based on Equation (5.4), the losses are measured for a varying apex position in the incident laser beam by scanning the apex vertically through the beam (see Figure 5.11(b)) and along the apex axis to investigate its homogeneity (see Figure 5.11(c)). Additionally, the apex is investigated for different beam diameters (see Figure 5.11(d)). Figure 5.12(a) shows the losses depending on the offset between prism apex and beam center for the prisms that have already been investigated under the light microscope. The prism apexes were illuminated with a beam diameter of approximately 600 μm. By fitting Equation (5.4) to the data, the apex width of Porro prism 1 is determined to be (30.0 ± 0.3) μm and for Porro prism 2, it amounts to (20.0 ± 0.6) μm. These values show the differences in apex sharpness between different prisms. To obtain low losses when the prisms are used in a resonator, those with the lowest apex widths should be preferred. Figure 5.12(b) shows the apex width for different types of prisms. Porro prism A (black) refers to Porro prisms with a round aperture. During the further course of the thesis, optimized
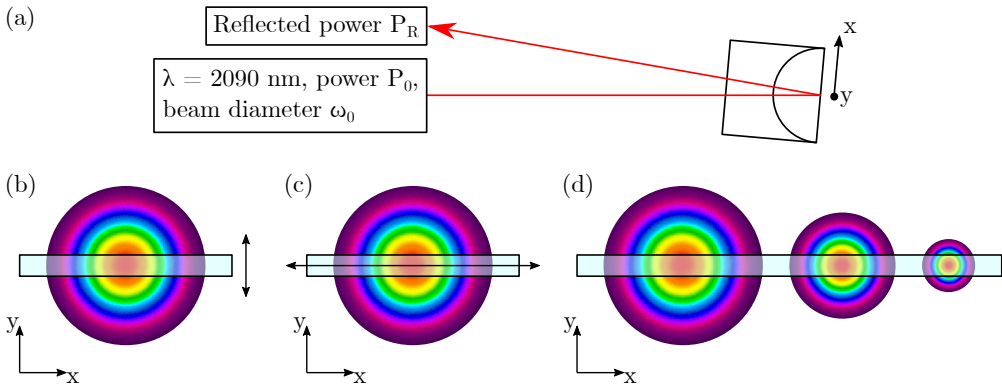
Figure 5.11: (a) Determination of apex sharpness by measuring the reflected power from a prism. (b) Movement of apex perpendicular to the apex. (c) Movement of apex along its axis. (d) Investigation of reflected power for different beam diameters.
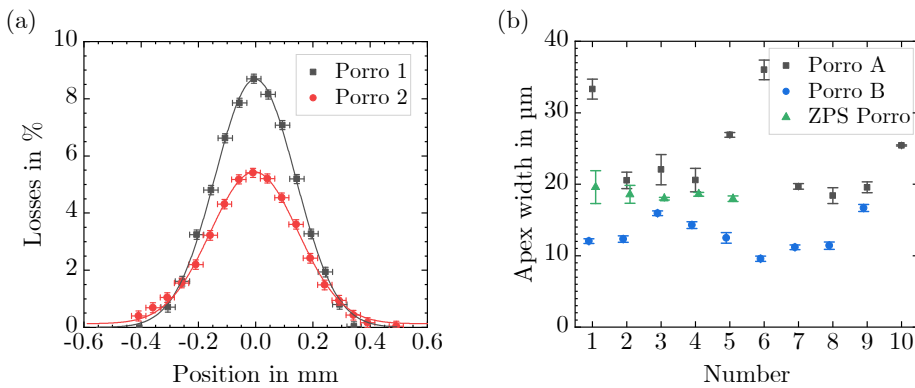

Figure 5.12: (a) Scan of the prisms vertical to their apex axes. (b) Apex width for different types of prisms.

prisms with a rectangular aperture were characterized (Porro prism B (blue)). In addition, the apex width of five ZPS Porro prisms (green) was measured. The quality of Porro prisms A strongly varies depending on the sample. Porro prisms B have on average the lowest apex width. The apex widths of the ZPS Porro prisms are on the order of the best prisms of Porro prisms A. The different apex widths will become relevant in Section 5.4. Figure 5.13(a) shows two exemplary scans along the apex axis. Porro prism 2 (red) shows a homogeneous apex with losses around 5 %, whereas Porro prism 1 (black) shows strongly varying losses around 10 % to 35 %. These high losses are due to the defect that has already been visible in the microscopic image. Figure 5.13(b) shows the apex losses of these two prisms depending on
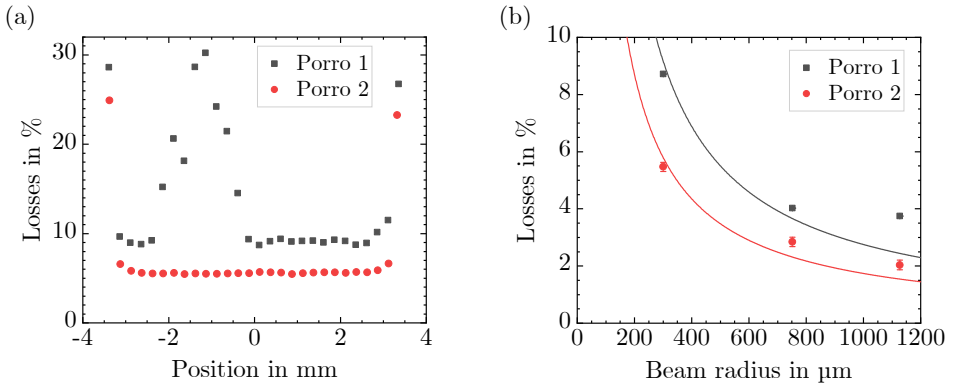
Figure 5.13: (a) Scan of the prisms parallel to their apex axes. (b) Losses at apex depending on beam diameter.

the beam diameter. With an increasing beam diameter, the losses decrease as expected from Equation (5.4). However, for the larger beam diameters, the losses are higher than expected from the model. Here, a further loss mechanism could result from a greater amount of defects or imperfections at the apex or the prism itself when a larger area is illuminated. In addition, the modeling of the apex as a rectangular loss window is a rough approximation and a further refinement of the model might yield a better fit with the experimental data. Overall, due to the observed loss mechanisms, the demand for an increased alignment tolerance is therefore associated with precisely manufactured optics, which can be a challenge.

5.3.3 Apex Angle

The apex angle of the prism is a crucial property because an apex angle unequal to $90°$ results in a widening of the incident beam. It is measured similar to the pointing stability measurement introduced in Section 3.2.1, thus an angular offset α is translated into a local offset r in the focal distance f of the lens. The setup consists of a collimated laser beam with a wavelength of $2.09\,\mu m$ and a diameter of $1.2\,mm$, which passes a TFP and a half-wave plate aligned under an angle of $22.5°$ and illuminates the prism under investigation (see Figure 5.14(a)). The beam is reflected from a Porro prism with a horizontally aligned apex and passes the half-wave plate again resulting in a large amount of the light to be perpendicularly polarized with the incident light, thus it is reflected from the TFP. After passing a lens with a focal length of $f \approx 40\,cm$, it is detected by a beam profiler. As the beam profiler must be positioned precisely in the distance

of the geometrical focal length of the lens to measure the smallest possible angle between two beams, its alignment is described in the following section.

Alignment and Calibration of the Setup

For the alignment, the prism is illuminated at two different vertical positions of the upper side face. The inset of Figure 5.14(a) indicates the resulting offset of the reflected beam when the prism is moved vertically. Because these two parallel beams are focused to the same spot in the distance of the geometrical focal length of the lens, this indicates the target position for the detector plane of the beam profiler. Figure 5.15(a) shows the centroid position of the two beams over 1000 frames after the alignment of the beam profiler. The offset of the beams in the vertical direction (perpendicular to the apex) is $10\,\mu$m. The expansion of the centroid positions is attributed to the intrinsic beam pointing of the laser source. Its standard deviation amounts to $20\,\mu$m. With a maximum error estimation, the total error on the offset is estimated to be $30\,\mu$m, corresponding to an angular offset of $75\,\mu$rad, thus it sets a limit to the minimum measurable angle between two beams. As in the measurement the lower and upper side face of the prism are illuminated one after the other, an angle of 4ϑ is measured between the beams when the angular
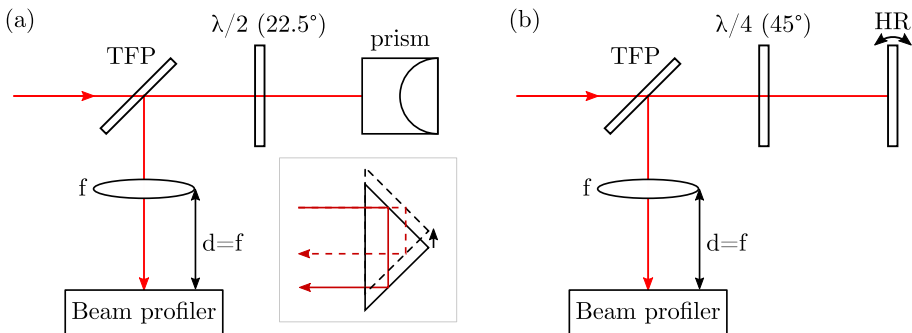

Figure 5.14: (a) Setup to measure the apex angle. The inset depicts the vertical shift of the prism to illuminate two spots on the upper side face, thus to create two parallel beams with an offset, which are used for the alignment of the beam profiler. (b) Setup to calculate the relation between the offset of two beams on the beam profiler and their enclosed angle in front of the lens.
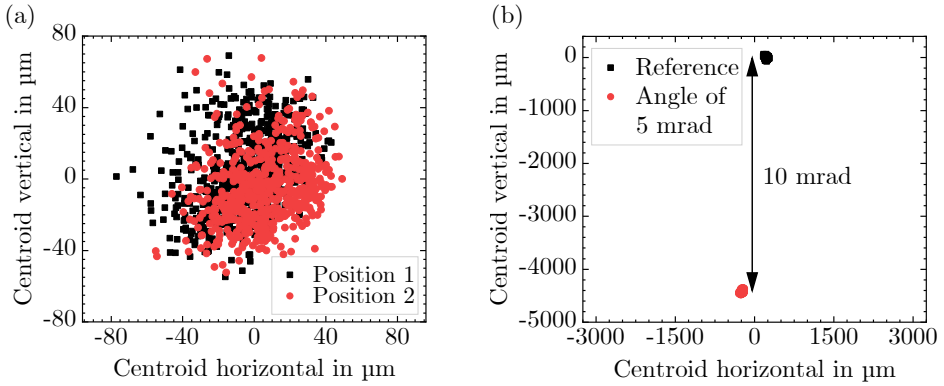
Figure 5.15: (a) Centroid position of two parallel reflected beams with an offset after the alignment of the beam profiler. (b) Calibration by measuring the centroid position of two tilted beams with an angle of 10 mrad.

deviation of the apex from 90° amounts to ϑ (in analogy to Figure 5.1(c)). Due to the refraction at the prism front face, the error on the apex angle measurement amounts to

$$\vartheta = \frac{75\,\mu\text{rad}}{4n} = 13\,\mu\text{rad} \,\widehat{=}\, 3'' \,, \tag{5.21}$$

where n is the refractive index of the prism.

To calibrate the setup, a mirror is placed at the position of the prism, rotated by a defined angle, and the offset between the two beams on the beam profiler is measured. Figure 5.15(b) shows the distance of $r = 4426\,\mu\text{m}$ of the two spots when the beams enclose an angle of approximately 10 mrad.

Measurement of Apex Angle for Different Prisms

To measure the apex angle, the lower side face is always illuminated before the upper one. This procedure allows to conclude if the measured angular deviation results from an angle larger or smaller than 90°. Table 5.3 gives an overview over the investigated prisms and the measured apex angles. In addition, Figure 5.16 shows the two beam positions on the beam profiler. Prisms no. 1 and 2 were measured as a reference because the deviations from the 90° angle were known from the manufacturer. The measured apex angle deviations are in good agreement with the values provided by the manufacturer. Like prism no. 1, prism no. 3 has a small angular deviation

Table 5.3: Exemplary prisms for which the apex angle deviation was measured.

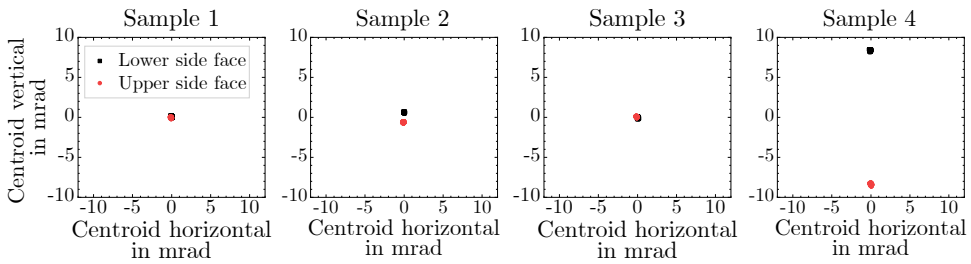| No.	Type	Specification	Apex angle deviation
1	ZPS Porro	Specified with 0.1″	$(3 \pm 3)''$
2	Porro	Specified with 39″	$(44 \pm 3)''$
3	Porro	-	$(-4 \pm 3)''$
4	Porro attached to Ho^{3+}:YAG crystal	-	$(601 \pm 3)''$

Figure 5.16: Centroid positions of the two beams reflected from the lower (black) and upper (red) side face on the beam profiler.
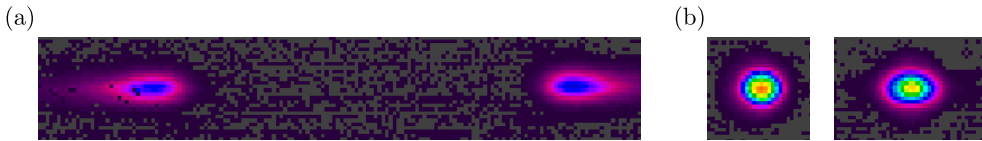

Figure 5.17: Reflected beam profiles from an imperfect apex angle. Note that the images are rotated by 90° with respect to the measurement. (a) Beam profile when the apex of prism no. 4 is illuminated resulting in a split beam. (b) Beam profile when only a side face of prism no. 2 is illuminated (left) and when the apex is illuminated (right), which results in a widening of the beam.

on the order of the measurement accuracy, thus the apex is of high quality. This prism will be used in the resonator presented in Section 5.4.2. Prism no. 4 is an example of a prism with a large angular error. When its apex is illuminated, the reflected beam is split (see Figure 5.17(a)). When the apex of prism no. 2 is illuminated, only a widening of the beam is observed (see Figure 5.17(b)). When this prism is used in a laser resonator, the angular error has a drastic effect on the resulting laser output.
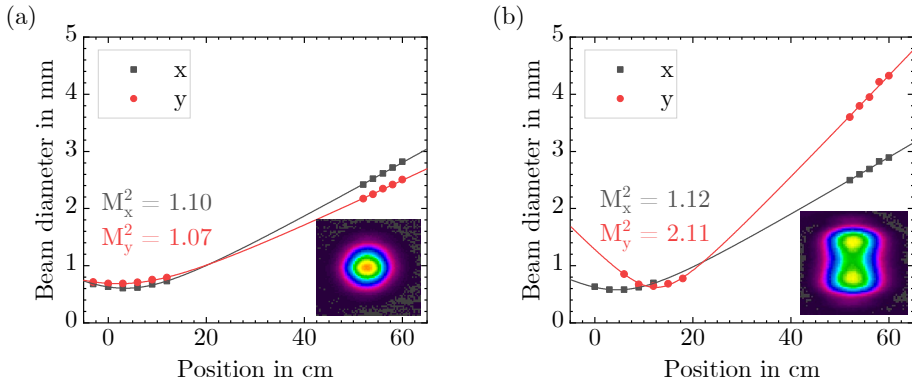
Figure 5.18: Measurement of beam propagation factor of a resonator with a Porro prism with (a) an apex angle of 90°
and (b) an apex angle deviating from 90°.

Comparison of Prisms with Different Apex Angles in Laser Operation

To investigate this effect, the beam quality of a linear resonator with prism no. 2 and 3 instead
of the OC mirror is determined. Figure 5.18 shows the measurement of the beam propagation
factor. A near-diffraction-limited beam quality and a round output beam profile is measured
when the prism with a 90° apex angle is used. In contrast to this, when a prism with an angular
deviation is inserted in the resonator, a drastic decrease in the beam quality is observed in the
axis perpendicular to the apex. In the beam profile, this manifests itself in a widening of the
beam profile. This once again emphasizes the importance of a high-quality apex angle.

5.3.4 Measurement of Polarization Properties

To experimentally verify the unique polarization properties of the Porro prisms, a similar setup
compared to the setup in Figure 5.6(a) is used. To ensure a loss-minimized measurement, the
prism is illuminated on one side face resulting in an offset of the reflected beam. The incident
s-polarized 2090 nm light passes a quarter- or half-wave plate, is reflected at the prism, passes
the wave plate again, and is analyzed depending on the wave plate angle. The resulting curves
are shown in Figure 5.19(a)-(d). In Figure 5.19(a) and Figure 5.19(b), the state of polarization
of a Porro prism with a quarter-wave plate and a half-wave plate, respectively, is analyzed.
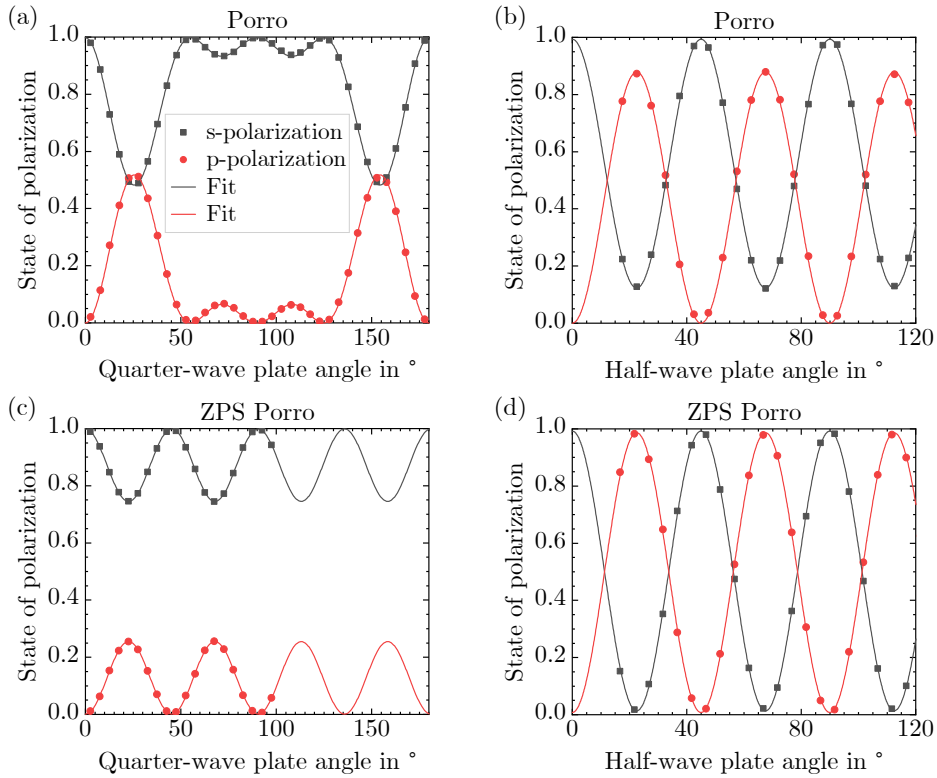
Figure 5.19: State of polarization when linearly polarized light passes a quarter-wave (left) or half-wave (right) plate, is reflected from a Porro (top) or ZPS Porro (bottom), and passes the wave plate again.

In Figure 5.19(c) and Figure 5.19(d), the state of polarization of a ZPS Porro prism with a quarter-wave plate and a half-wave plate, respectively, is analyzed. In all cases, an excellent agreement with the theoretical Jones model is confirmed.

5.4 Porro Prism Resonators

In this section, four Porro prism resonators are presented. The compact linear Porro prism resonator in Section 5.4.1 shows the limited power scaling capabilities of a simple linear resonator design with two crossed Porro prisms. A telescopic resonator design suggested to overcome these limitations is presented in Section 5.4.2. In addition, the alignment sensitivity is compared with that of a conventional resonator using mirrors as cavity end reflectors. A

length-optimized one-sided linear Porro prism resonator based on the resonator presented in Section 3.2.2 is characterized in Section 5.4.3. Section 5.4.4 addresses the depolarization compensation with a Porro prism resonator.

5.4.1 Compact Linear Porro Prism Resonator

In analogy to the previously presented resonators of this thesis, a similar linear cavity is used as a first Porro resonator attempt. The setup is depicted in Figure 5.20. The pump light is shaped by an afocal telescope, consisting of the lenses L_1, L_2, and L_3, and focused into the Ho^{3+}:YAG crystal with a pump beam diameter of 730 µm. In addition to the typical cavity end mirrors, two AR coated Porro prisms (P_1 and P_2) are used with their apexes aligned perpendicular to each other. As both prisms are HR, the output coupling is realized with a combination of a wave plate and a TFP. In this setup, the approximately polarizing properties of the IC mirror are used for this purpose. The wave plate (WP) is rotated such that an output coupling of 50 % results. To achieve this in the resonator with two cavity end mirrors, a quarter-wave plate is aligned under an angle of 22.5°. For the resonator with two Porro prisms, a half-wave plate is used under an angle of 12.2° determined by the Jones matrix calculations in Section 5.2.4. The total physical cavity length of the resonator is 13.3 cm.

Four configurations are investigated: a resonator with two end mirrors as a reference, one resonator with only prism P_1 and one with only prism P_2, and a resonator with both Porro prisms. Figure 5.21 shows the output power of these resonators with respect to the incident pump power. The mirror resonator has a slope efficiency of 60.8 %, which is lower than in the basic resonator presented in Section 3.2.2 because the pump beam diameter was chosen to be
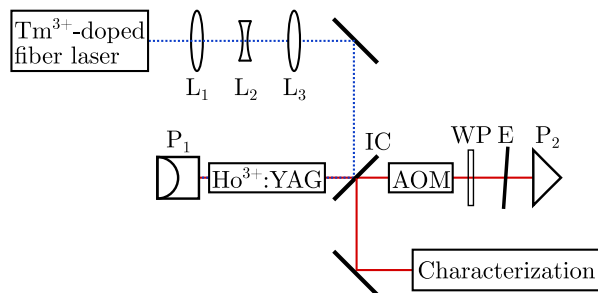

Figure 5.20: Setup of a simple linear Porro prism resonator. The abbreviations are explained in the text.
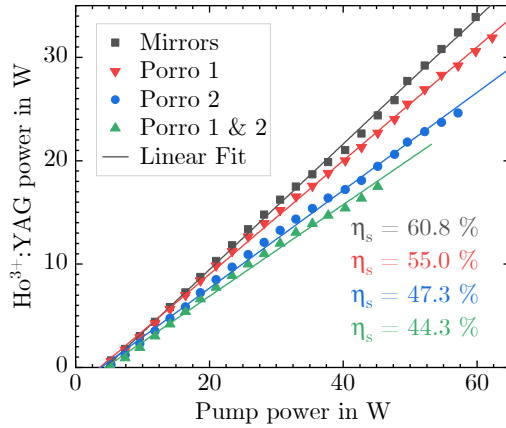
Figure 5.21: Ho^{3+}:YAG power depending on pump power for a resonator with two mirrors (black), Porro P_1 (red), Porro P_2 (red), and both Porro prisms (green).

larger in this setup with the idea of having a larger beam diameter at prism P_1, thus limiting the losses at this prism. When prism P_1 replaces the cavity end mirror close to the laser crystal, the slope efficiency decreases to 55.0 %, which is explained by the apex losses of this prism, which amount to 7 %. In this configuration, a maximum output power of 31.9 W is measured. When only prism P_2 is inserted instead of the respective mirror, the slope efficiency drops to 47.3 % corresponding to 18 % losses at this prism apex because of the smaller mode diameter at prism P_2 due to the focusing effect of the thermal lens. In the resonator with both prisms, the slope efficiency is further reduced to 44.3 %. In addition, an instable operation is observed for output powers above 17.5 W, which manifests itself in fluctuations of the beam profile and output power. As a consequence, the drastic losses at the apex of P_2 and the fluctuations in the resonator with both prisms hinder a power scaling in this simple linear resonator. To decrease the apex losses at prism P_2, a telescopic resonator is designed.

5.4.2 Telescopic Linear Porro Prism Resonator

The telescopic Porro resonator is presented in detail in [168]. An intracavity telescope (L_4 and L_5) with a magnification of $M = 5$ is inserted into the resonator to increase the mode size on prism P_2, thus to decrease the losses at this apex. Figure 5.22 shows a schematic representation of this resonator. In addition, a TFP specified for 2090 nm is inserted to ensure an optimal
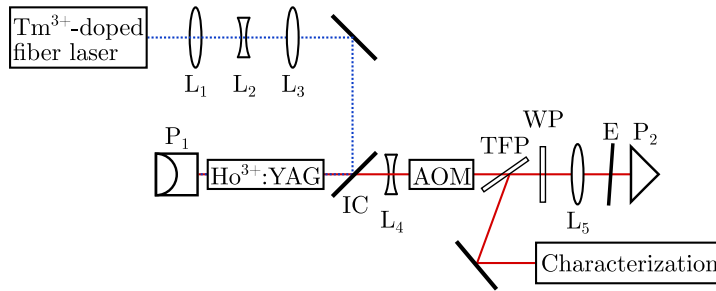
Figure 5.22: Schematic representation of telescopic Porro resonator architecture.
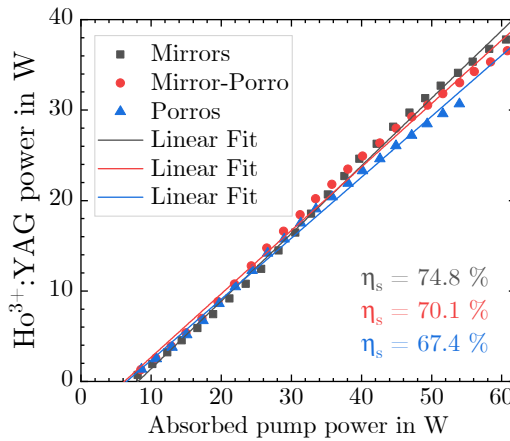
Figure 5.23: Comparison of Ho^{3+}:YAG output power depending on absorbed pump power for the three investigated telescopic resonators.

output coupling. Due to the additional optical elements, the total physical cavity length amounts to 21.4 cm.

In similarity with the previously investigated Porro resonator, this resonator is investigated in different configurations: Firstly, the resonator is set up with two HR mirrors (mirror resonator). Secondly, prism P_2 is inserted into the resonator (mirror-Porro resonator) to verify if the increased mode diameter leads to the desired loss reduction. Thirdly, the resonator with both Porro prisms is investigated (Porro resonator). The resonators are investigated regarding their output power and slope efficiency, beam quality, and angular alignment sensitivity. The power curves of the resonators are shown in Figure 5.23. All resonators have high slope efficiencies above 67 %. The mirror resonator has the highest slope efficiency of 74.8 %. Because each of

the prisms introduces small losses at the apex, the slope efficiencies in the mirror-Porro resonator and the Porro resonator decrease to 70.1 % and 67.4 %, respectively. This corresponds to prism losses of 4.5 % at prism P_2 and 2.8 % at prism P_1. This confirms that the intracavity telescope reduces the losses at prism P_2 due to an increased mode diameter.

The highest output power of 37.8 W is reached in the mirror resonator. In the Porro resonator, the maximum output power decreases to 30.7 W which is limited by the previously observed temporal instabilities in the output power and in the beam profile, in particular in the axis perpendicular to the apex of P_2. These instabilities are explained with fluctuations in the thermal lens, which might result from instabilities in the pump beam due to thermal blooming. As a consequence, the laser mode is moved perpendicular to the apex of prism P_2, which leads to an offset of the laser mode when it is reflected from the prism. This in turn changes the laser mode size in the crystal. Also, the resonator losses are reduced. Both effects result in a change of the gain properties of the crystal which, again, modifies the thermal lens.

Figure 5.24(a) and Figure 5.24(b) show the residual pump and depolarized power for all resonators. The resonators containing at least one prism show a higher absorption efficiency than the mirror resonator. The depolarized power is equal for the mirror and the mirror-Porro resonator up to an absorbed pump power of 45 W. Above this pump power, the depolarized power increases stronger for the mirror-Porro resonator due to the instabilities described before. The depolarized power in the Porro resonator is lower than for the other resonators because the
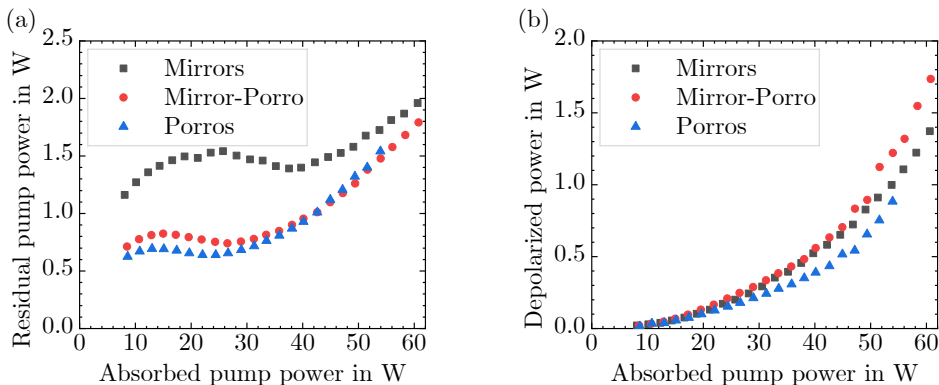

Figure 5.24: (a) Residual pump power and (b) depolarized pump power in the mirror and Porro resonators.
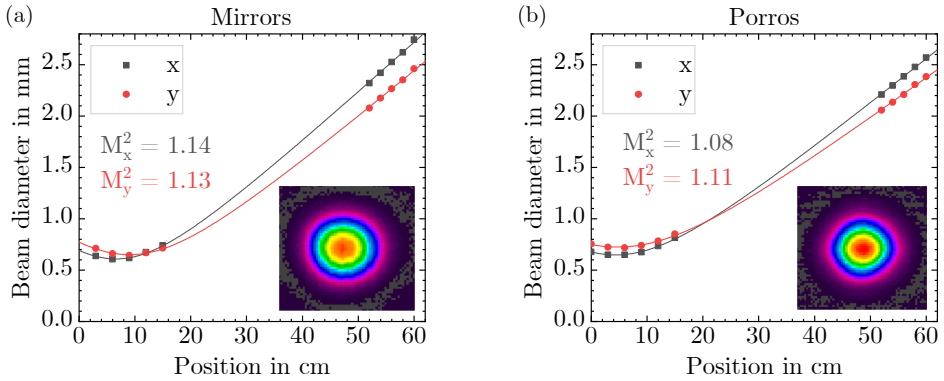
Figure 5.25: Measurements of beam propagation factor in (a) the mirror and (b) the Porro resonator.

Porro prism P_1 next to the crystal inverts the image of the laser mode. Therefore, the thermally induced birefringence in the crystal is partially compensated [157].

Measurements of the beam propagation factor in the mirror resonator and the Porro resonator at a pump power of 49.5 W reveal an excellent beam quality in both cases (see Figure 5.25 (a) and Figure 5.25(b), respectively). An output power of 30.8 W and 27.8 W was measured for the mirror and the Porro resonator, respectively. Both measurements include an image of the beam profile in the far field, which is similar for both resonators. For the mirror resonator, a beam quality factor of 1.14 in the x-direction and 1.13 in the y-direction was measured. For the Porro resonator, a slightly better beam quality of 1.08 in the x- and 1.11 in the y-direction was determined. The excellent beam quality shows that a good mode matching between pump and laser mode was generated. In addition to the improved beam quality of the Porro resonator, a slightly smaller astigmatism is observed, which results from the reduced birefringence in the Porro resonator.

To verify whether the alignment sensitivity of the Porro resonator is improved with respect to the mirror resonator, the mirrors and prisms are tilted and the resulting output power is measured. Figure 5.26 shows the normalized output power for the mirror (black) and Porro resonator (blue) when prism P_2 or the corresponding mirror is tilted. In Figure 5.26(a), the tilt axis is parallel to the apex (insensitive axis), whereas it is perpendicular to the apex in Figure 5.26(b) (sensitive axis). The alignment sensitivity is defined as tilt angle at which the normalized power equals 0.9 [159]. When prism P_2 is tilted around its insensitive axis, the alignment stability is ± 20 mrad. Within this angular range, only small changes in output power
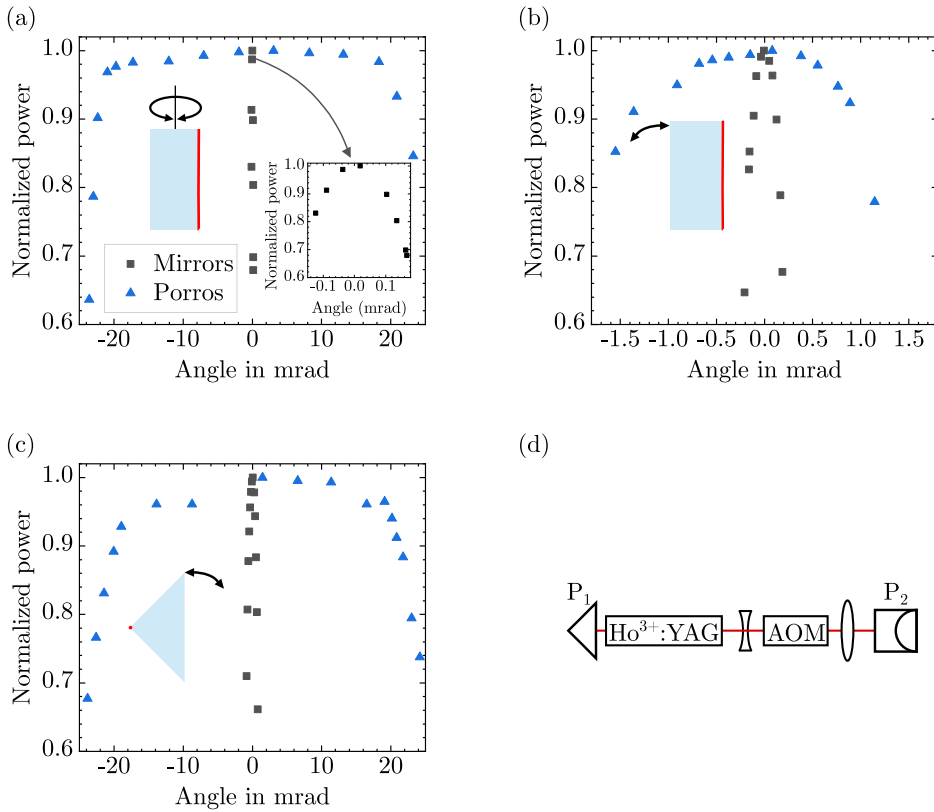
Figure 5.26: Determination of alignment sensitivity when (a) prism P_2 is rotated around its insensitive axis, (b) prism P_2 is rotated around its sensitive axis, and (c) prism P_1 is rotated around its insensitive axis. (d) Simplified side view of the telescopic Porro prism resonator to facilitate understanding (a)-(c).

are detected. This results from the retro-reflective property of the prism, which leads to an unchanged resonator mode. Considering the refractive index of the prisms, the TIR angle is 44.1 degree, thus an angular stability range of ± 22.2 mrad is expected. For tilt angles larger than 20 mrad, a drop in output power is expected and also observed in the experiment due to a breakdown of TIR. The angular spectrum of the Gaussian beam (see Section 5.2.3) leads to a flattened drop of the output power. For the mirror resonator, a drastically lower alignment sensitivity of 0.1 mrad is determined. The overall low stability is attributed to the use of the intracavity telescope. The cause for this are non-parallel mirrors, which lead to a decreasing overlap of pump and laser mode when the mirror is tilted. Overall, the Porro resonator has a 200 times higher alignment tolerance in this axis. Similar to this, when prism P_1 next to the

crystal is tilted around its insensitive axis, the alignment stability is above 20 mrad as well (see Figure 5.26(c)). However, the alignment sensitivity of the mirror resonator is 0.5 mrad in this case due to a smaller distance of the mirror from the pumped region. This results in an improved stability for the Porro resonator by a factor of 40.

When prism P_2 is tilted around its sensitive axis, an alignment sensitivity of 1 mrad is measured for the Porro resonator, whereas it is 0.1 mrad for the mirror resonator (see Figure 5.26(b)). Here, tilting the prism changes the position of the laser mode inside the cavity. However, the angular range of the opposite prism compensates for the angular change of the laser mode. The drop in output power results from a decreasing overlap of pump and laser mode with increasing tilt angle, therefore it is less sharp than for the tilt around the insensitive axis.

After the assessment of the alignment sensitivity, the focus is now directed towards the laser properties in Q-switched operation. When the Porro resonator is operated at a pulse repetition rate of 50 kHz, pulses with an energy up to 0.51 mJ and a minimum pulse duration of 170 ns are measured (see Figure 5.27(a)). This corresponds to a pulse peak power of 3 kW. Figure 5.27(b) shows the pulse energy and pulse duration depending on the pump energy. Like in CW operation, the pulse energy depends linearly on the pump energy. The slope efficiency is 53.9 %. This lower value compared to CW operation results from the fact that the linear fit has only been performed for the higher pump energies, where the local slope efficiency is slightly lower. In this range, pulse durations between 220 ns and 170 ns are measured. However, large pulse-to-pulse fluctuations around 10 % are observed in the Porro resonator. These might be a consequence of
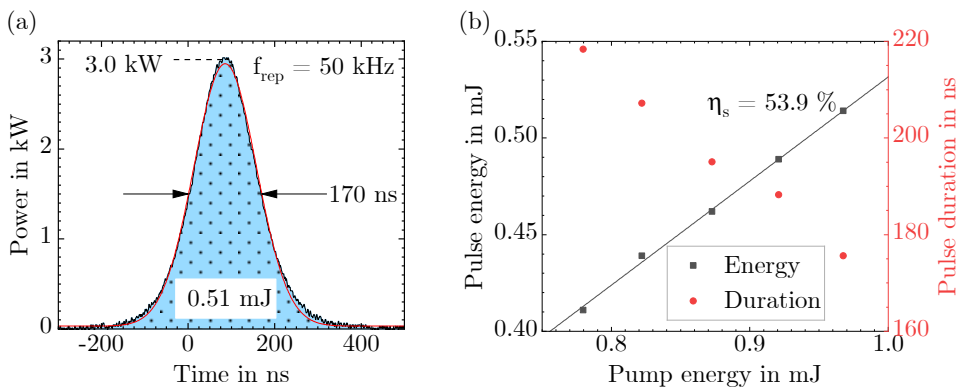

Figure 5.27: (a) Temporal shape of a Porro resonator pulse. (b) Pulse energy and pulse duration depending on pump energy.

the apex losses that effectively lead to a spatial loss distribution of the resonator, thus influencing the gain distribution in the crystal. Further, by changing the gain profile, the observed beam profile fluctuations contribute to the pulse instabilities as well.

To conclude, this telescopic Porro resonator showed a significantly higher alignment tolerance compared to the mirror resonator. Due to the comparatively large pump beam diameter in the crystal and the long cavity, pulse durations above 170 ns were measured. Besides, the pulses showed considerable pulse-to-pulse fluctuations. The output power scaling was mainly limited by fluctuations in the beam profile.

To rule out that the beam profile fluctuations are connected to losses at the prism apexes, the Porro prisms A, which were used up to this point, are replaced by the Porro prisms B shown to have a smaller apex width in Figure 5.12(b). In addition, the pump diameter is decreased to 500–600 μm to increase the inversion and to generate shorter pulses, and the intracavity telescoped is adapted to have a magnification of $M \approx 6$ to have a similar mode diameter on prism P_2 as in the previously presented telescopic resonator. Figure 5.28(a) shows the Ho^{3+}:YAG output power depending on the absorbed pump power for this resonator with both Porro prisms A and B. The power curves have almost the same slope efficiency and the course is similar, thus the sharper apexes with fewer losses do not improve the performance of the laser. At an output power of 28.5 W, 0.57 mJ pulses with a pulse duration of 124 ns were measured. This is almost 30 % shorter than in the previously presented telescopic resonator. Above this
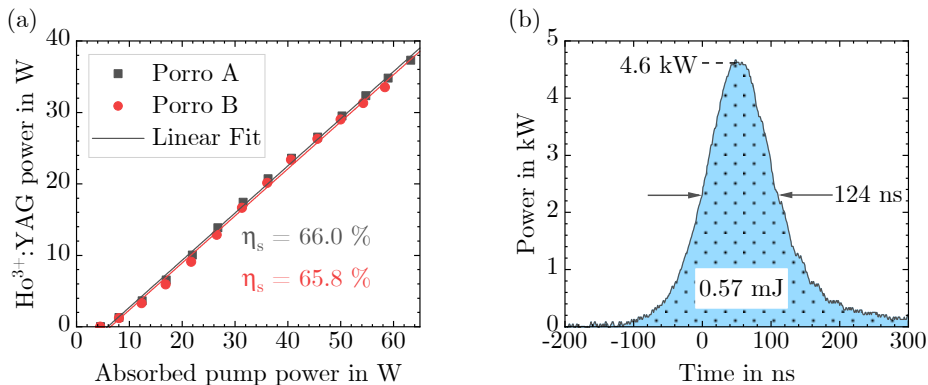

Figure 5.28: (a) Comparison of Ho^{3+}:YAG output power depending on absorbed pump power for a telescopic resonator with Porro prisms A with a round aperture and Porro prisms B with a rectangular aperture. (b) Exemplary temporal pulse shape at 28.5 W output power.
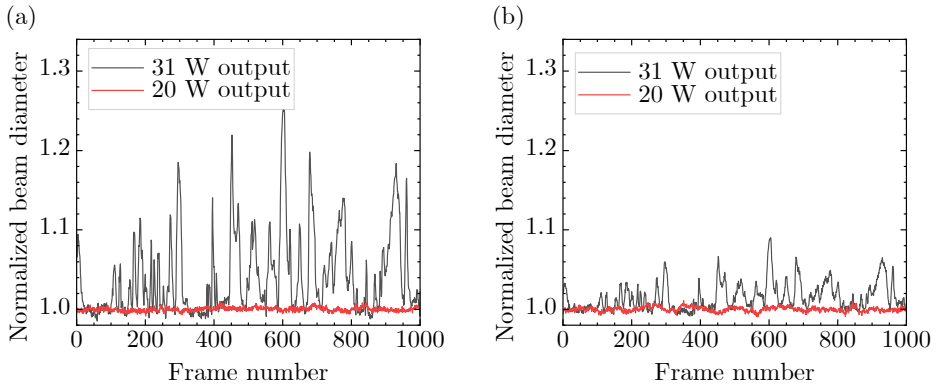
Figure 5.29: Beam fluctuations along (a) the horizontal beam direction and (b) the vertical beam direction for an output power of 20 W (red) and 31 W (black) in comparison.

output power, fluctuations in the beam profile are apparent in both resonators. Thus, they cannot be attributed to the apex losses. To illustrate the flucuations in the beam profile, Figure 5.29(a) and Figure 5.29(b) compare the normalized output beam profile in the horizontal and vertical direction, respectively, at an output power of 20 W, where a stable beam profile was measured and at 31 W of output power, where strong instabilities were observed. The instabilities are apparent in both beam axes, although they are stronger in the horizontal direction (perpendicular to P_2) because of the longer distance to the thermal lens. This leaves the hypothesis that they are caused by thermal blooming effects from the pump laser, which moves the pumped region from the ideal position determined by the intersection of the two apexes.

To achieve a further decrease in pulse length, a shorter cavity is realized by removing the intracavity telescope and by replacing the output coupling unit by a 50 % OC mirror.

5.4.3 Length-Optimized One-Sided Linear Porro Resonator

Figure 5.30 depicts the setup of the length-optimized Porro resonator. Similar to an undoped end cap, the Porro prism is directly attached to a 0.75 % doped 26 mm long Ho^{3+}:YAG crystal (named Porro crystal). Other than that, the setup equals the one presented in Section 3.2.2. Figure 5.31(a) shows the output power of the length-optimized Porro resonator (red) and the reference mirror resonator in which the Porro crystal is replaced by a conventional crystal and an HR mirror (black), depending on the pump power. Both resonators are operated with high
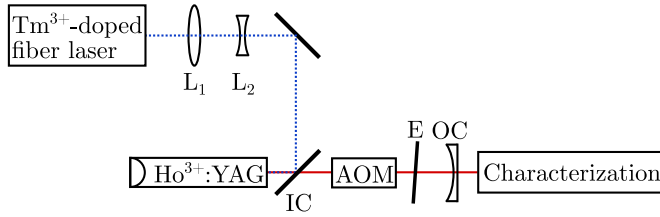
Figure 5.30: Schematic representation of Porro crystal setup.
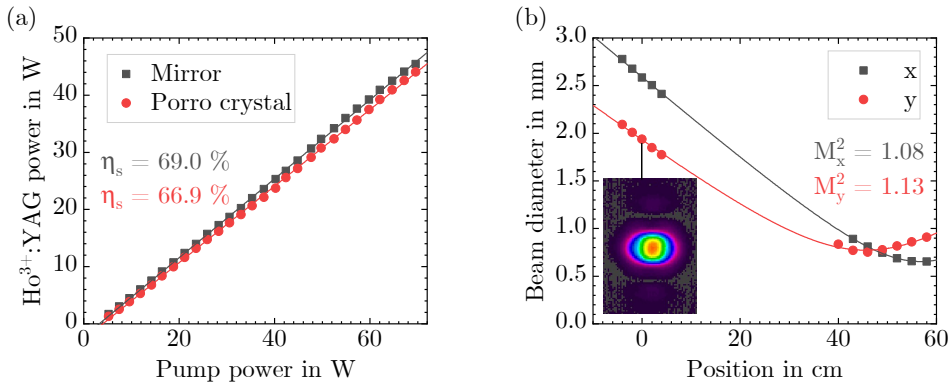
Figure 5.31: (a) Ho^{3+}:YAG output power of resonator with a plane HR mirror and the Porro crystal depending on the pump power. (b) Beam quality measurement of Porro crystal resonator at an output power of 34.8 W in Q-switched operation.

slope efficiencies of 69 % for the mirror and 66.9 % for the Porro resonator. The Porro resonator can be operated with a maximum output power of 44 W at a pump power of 69.6 W. Because an operation with a good beam quality is desired, the working point of this resonator is chosen to be at a pump power of 57 W corresponding to an output power of 35.6 W. For this working point, a beam quality measurement is shown in Figure 5.31(b). In the x-direction, a beam propagation factor of 1.13, and in the y-direction, a beam propagation factor of 1.08 is determined. The inset shows the beam profile of the output beam revealing a diffraction like pattern, which might result from the apex losses. In Q-switched operation, pulses with an energy of up to 0.8 mJ and a minimum pulse duration of 55 ns are measured (see Figure 5.32(a)) both resulting from the decrease in the cavity length. The slope efficiency of 67.5 % is similar to the value measured in CW operation. An exemplary pulse shape at the working point is shown in Figure 5.32(b). With a pulse energy of 0.7 mJ, a pulse peak power of 12.3 kW is achieved, which is more than
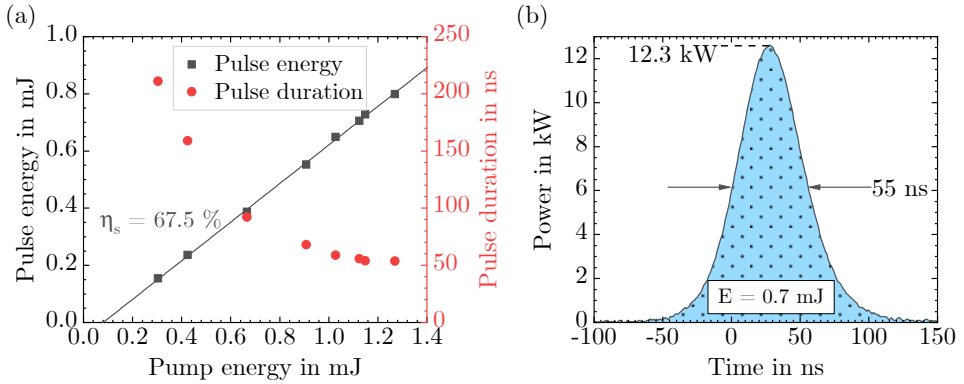
Figure 5.32: (a) Pulse energy and pulse duration depending on the pump energy. (b) Temporal evolution of pulse profile with Porro crystal.
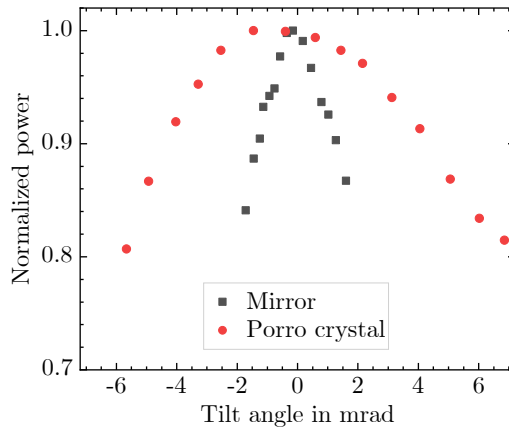
Figure 5.33: Angular stability when OC mirror opposite of the Porro crystal is tilted.

twice as high as in the telescopic Porro resonator. In addition, the RMS energy stability is 1.8 %, which is considerably lower than in the telescopic resonator design.

In accordance with Section 5.4.2, the alignment stability is determined by measuring the normalized output power depending on the tilt angle of the OC mirror (see Figure 5.33). Because the prism is attached to the Ho^{3+}:YAG crystal, the influence of a prism tilt cannot be measured. However, the opposite OC mirror is tilted around the axis in which the prism has its insensitive axis and should provide for an angular stabilization. With the mirror resonator,

an alignment stability of 1.25 mrad is measured, whereas it is improved to 4.4 mrad in the Porro resonator. Thus the stabilizing effect is already observed in a resonator with only one Porro prism. However, this comparatively small improvement in alignment tolerance is attributed to the significantly higher alignment tolerance of the mirror resonator investigated in this section (1.25 mrad) compared to that the telescopic mirror resonator (0.1 mrad). A more detailed discussion of this will be presented in Section 5.5.

5.4.4   Polarization Flip Cavity with Porro Prism

Many of the so far investigated resonators created an astigmatic output. A polarization flip cavity involving a ZPS Porro prism is one concept for its reduction. Figure 5.34(a) depicts the setup of such a polarization flip cavity. It differs from the previously presented length-optimized cavity mainly in two points. Firstly, a conventional 0.7 % doped Ho^{3+}:YAG crystal with an HR coating for the 1908 nm pump light is used to minimize the V-shape of the pump beam. Secondly, either a quarter-wave plate and an HR mirror or a half-wave plate and a ZPS Porro prism with horizontal apex are used to decrease the depolarization losses and to reduce the astigmatism of the output beam. Both combinations are investigated in this section. Because the polarization is rotated by 90° after a double-pass of the crystal, the half-wave plate and the ZPS Porro (see Table 5.2), it is reflected from the IC mirror, and an HR mirror with the same radius of curvature as the OC mirror and the same distance to the crystal reflects it back for another passage of the crystal, half-wave plate, and ZPS Porro prism.

Figure 5.34(b) illustrates the polarization flip after double-passing the crystal, the half-wave plate, and the Porro prism. Initially, the laser mode is horizontally polarized (black dashed arrow). When it passes the crystal for the first time, it experiences a delay with respect to the radial and tangential eigensystem of the crystal depending on the radial position (red dashed arrow). The half-wave plate under 22.5° with the Porro apex flips the polarization components (blue-dashed arrow) around its fast axis (green solid line). The ZPS Porro prism flips the polarization around its apex without introducing a further phase delay on one of the components (blue solid arrow). Then each polarization component is rotated around the fast axis of the half-wave plate again (red solid arrow). When the resulting polarization components then pass the crystal, the component that has experienced the radial phase delay in the first pass now experiences the tangential phase delay and vice versa. Thus, in total both components experience the same phase delay and are rotated by 90° resulting in the polarization flip (black
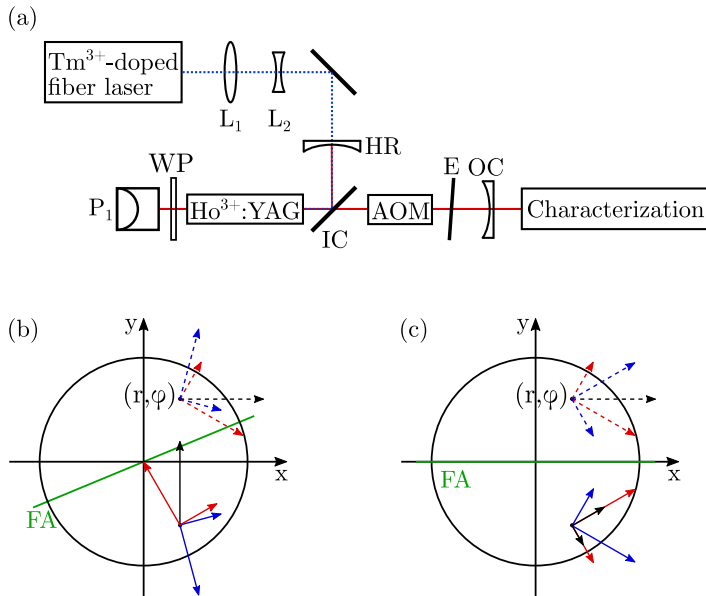
Figure 5.34: (a) Schematic setup of the polarization flip cavity intended to reduce the astigmatism. (b) Change in the state of polarization when the incident horizontally polarized light (black dashed) passes the crystal (red-dashed), a half-wave plate under 22.5° (blue dashed), is flipped at the horizontally aligned prism apex (blue solid), and passes the half-wave plate (red solid) and the crystal (black solid) again. The final polarization is flipped with respect to the initial one and linear. (c) Change in the polarization when passing the same components with the difference that the half-wave plate is aligned under 0°. In this situation, the final polarization is not flipped and is in general elliptical. For the sake of clarity, the size of the black arrows was reduced.

arrow). In analogy to this, Figure 5.34(c) shows the development of the polarization for a half-wave plate that has an angle of 0° with the Porro apex. Here, the polarization is not flipped, thus no depolarization compensation is generated.

In the first investigated configuration, an HR mirror and a quarter-wave plate at an angle of 0° are used, which aims for decreasing the depolarization losses. To measure the depolarization losses, the curved HR mirror is slightly tilted and the reflected power is measured. Figure 5.35(a) shows the power curves without a quarter-wave plate and with a quarter-wave plate under 0°. In both cases, the slope efficiency over the entire range of pump powers is 71 %. However, the local slope efficiency is 46.2 % without the quarter-wave plate and 63.0 % with the quarter-wave plate for high pump powers between 60–80 W. The reason for this is the depolarized power, which is considerably decreased at high pump powers with the quarter-wave plate. This allows a 2 W higher output power of 51.9 W at the maximum pump power. When the wave plate is
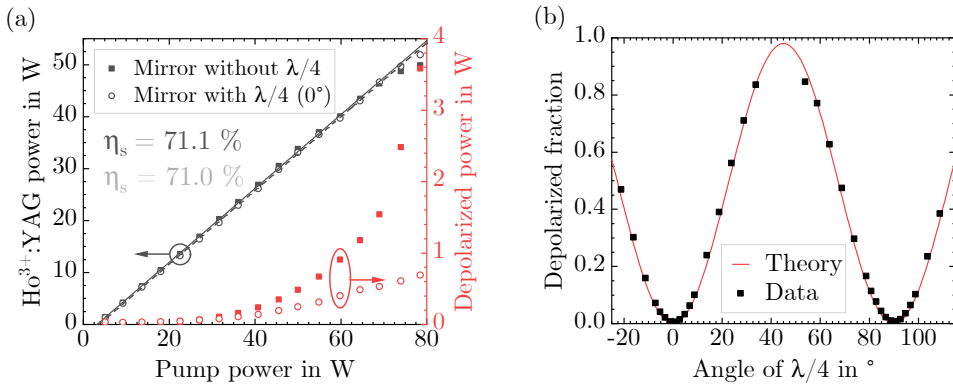
Figure 5.35: (a) Ho^{3+}:YAG output power and depolarized power in the linear cavity without (filled symbols) and with quarter-wave plate under 0° (open symbols). (b) Depolarized fraction depending on angle of quarter-wave plate.

rotated, the depolarized fraction increases until it reaches its maximum value at an angle of 45° (see Figure 5.35(b)). A good agreement with the theoretical curve is achieved when a phase delay of $\delta = 0.2$ averaged over the crystal radius is assumed.

Secondly, the resonator including a ZPS Porro prism is considered. A linear configuration without half-wave plate and a misaligned curved HR mirror is compared to the polarization flip cavity with a half-wave plate under 22.5° and the curved HR mirror aligned with the cavity mode. The corresponding power curves are shown in Figure 5.36. As expected, the linear cavity has a slightly lower slope efficiency than the linear cavity with the mirror. The slope efficiency is reduced further in the polarization flip cavity, which might be caused by the fourfold pass of the laser medium resulting in changed gain properties.

In addition, the beam propagation factor was measured at a pump power of 62 W for the linear cavity and 60 W for the polarization flip cavity (see Figure 5.37(a) and Figure 5.37(b)), which is similar in both configurations. Although the beam profile in the polarization flip cavity shows a halo around the main beam, the astigmatism is reduced, which proves the intended working principle of this setup experimentally.

Due to instable pulses observed in Q-switched operation, the presented Porro prism based resonators are not suitable for generating ns pulses and in the consequence, it cannot be used to pump an OPO. To pump the OPO, which will be investigated in Chapter 6, the Ho^{3+}:YAG laser presented in Chapter 4 will be used.
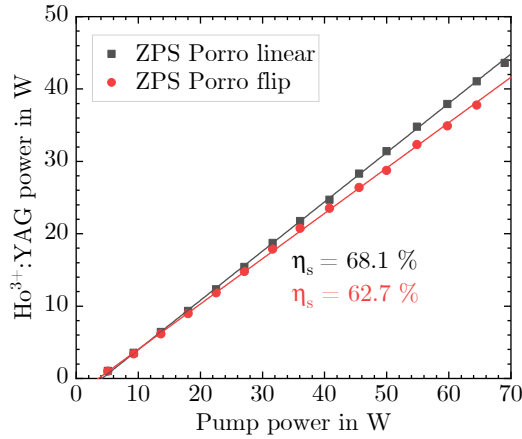
Figure 5.36: Ho^{3+}:YAG output power for the linear cavity with ZPS Porro (black) and the polarization flip cavity (red) in comparison.
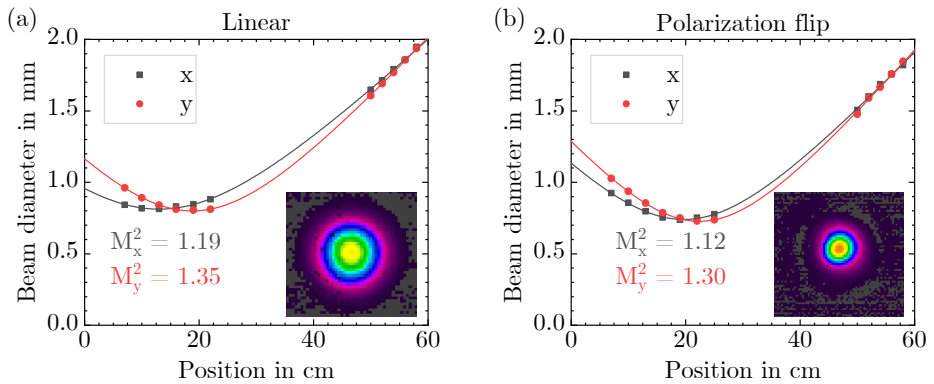
Figure 5.37: Measurement of beam propagation factor in the (a) linear cavity and the (b) polarization flip cavity.

5.5 Discussion

Finally, the results are discussed and compared to prior literature results. The small mode diameters resulting from the requirement for a good beam quality in the linear resonator lead to high losses and a limited power scaling capability. A telescopic resonator design offers a solution to this issue, but it comes at the cost of an inherently low alignment tolerance, which was 0.1 mrad in the telescopic resonator investigated in this thesis. The low alignment tolerance

arises due to the intracavity lenses as the lenses amplify any misalignment introduced by one of the resonator end mirrors. As a result, a significantly higher alignment tolerance is observed when prisms are used. This is particularly evident in the investigation of the angular tolerance in the resonator with the Porro crystal, which is only larger by a factor of three, thus it is a comparatively small improvement. Among other things, this is due to the large (compared to the telescopic design) alignment tolerance of the compact mirror resonator of 1.25 mrad. Therefore, for the design of a resonator with a high alignment tolerance, a telescopic design has only limited suitability. A further difficulty in optimizing Porro resonators arises from the fixed apexes, which require a stable position of the pump mode. Due to the presence of thermal blooming effects, this has not been guaranteed at high pump powers. Thus, further effort must be taken to find optimal operation conditions for Porro resonators with Ho^{3+}:YAG crystals. Nevertheless, the obtained results stand out in comparison with the existing literature. In comparison with prior research on Nd^{3+}:YAG based Porro prism resonators, the investigated resonators in this thesis were operated at significantly higher powers and with an excellent beam quality. For example, Winker et al. presented a multi-mode crossed-Porro prism resonator with a pulse energy of 220 mJ operating at 20.16 Hz, which corresponds to an average output power of 4.4 W, in 2004 [145]. In 2015, Yang et al. showed 93 mJ pulses at 20 Hz repetition rate, corresponding to an average output power of 1.9 W, with a beam propagation factor $M^2 < 2.5$ [160]. Huang et al. measured pulses with an energy of 196 mJ at 10 Hz repetition and with a beam propagation factor of $M^2 < 11$, which corresponds to an average power of 2 W [143]. Besides, alignment-insensitive resonators based on Ho^{3+}:YAG were limited in average output power as well. In 2018, Wang et al. presented a Q-switched Ho^{3+}:YAG laser with an output pulse energy of 2.18 mJ at 1 kHz repetition rate, corresponding to an average output power of 2.8 W. They measured a near-diffraction-limited beam propagation factor of $M^2 = 1.3$ [161]. A similar setup was presented by Yan et al. in 2023. They measured 6.8 mJ pulses at 100 Hz repetition rate, corresponding to an average output power of 0.68 W. In contrast to these results, this thesis shows that a significant average power scaling up to 28.5 W is possible with a near-diffraction-limited beam quality in Ho^{3+}:YAG Porro prism based resonators. Overall, resonators based on Porro prisms are suitable to increase the mechanical stability, although further research must be done to eliminate fluctuations in the beam profile, output power, and in the pulsed output.

5.6   Summary

To summarize, different resonators based on Porro prisms were investigated focusing on their mechanical stability and power and energy scalability. At first, the Porro prisms were theoretically and experimentally analyzed regarding properties connected to their apex as well as their polarization properties. A result of these investigations was that a sharp prism apex is essential to minimize losses and that the apex angle should not deviate from 90°, as this results in a widening of the beam. Subsequently, different Porro resonators were investigated. At first, a simple linear crossed-Porro cavity was investigated. Due to the small beam diameter and the associated losses, especially at the prism on the opposite side of the crystal, a drastic decrease in slope efficiency was observed compared to a conventional mirror resonator, thus the output power could not be scaled above 20 W. To enable a further power scaling, a telescopic resonator design was implemented, which enlarged the laser mode on the critical prism P_2. This enabled reducing the drop in slope efficiency and allowed an output power scaling up to 27.8 W with an excellent beam quality. In addition, the significantly higher alignment tolerance of the Porro resonator as compared to the mirror resonator was shown. Nevertheless, two issues remained. Firstly, at an elevated output power beam profile fluctuations limited the further output power scaling. These were finally attributed to the thermal blooming of the pump beam. Secondly, the pulse duration was longer than 100 ns, resulting in low peak powers, and large pulse-to-pulse fluctuations, which were attributed to the spatially modulated loss and gain profile, were observed. Therefore, such a laser would not be suitable to pump an OPO. With a more compact setup with only one Porro prism and a conventional 50 % OC mirror, the pulse length could be reduced to 55 ns while the increased alignment stability was also partially maintained. Finally, with a polarization flip cavity based on a ZPS Porro prism, a reduction in astigmatism could be shown.

6 Nonlinear Conversion of 2.09 µm Ho^{3+}:YAG Pulses

This chapter discusses the use of the Ho^{3+}:YAG laser from Section 4.2.4 to pump an OPO with ZGP as nonlinear material. After an introduction focusing on ways to generate light in the MWIR region in Section 6.1, theoretical considerations concerning the mode sizes in OPOs are shown in Section 6.2. The experimental setup is described in Section 6.3. It is characterized in Section 6.4 followed by a discussion of the results in comparison with the existing literature in Section 6.5. Finally, Section 6.6 summarizes the chapter.

This chapter is based on the results discussed in the publication:

6.1 Introduction

MWIR coherent light can be generated by a wide variety of methods. A requirement for direct laser sources in this wavelength range is a low phonon energy of the host material. Otherwise, in materials with high-phonon energies, the probability of bridging the laser transition by multi-phonon relaxation is high, leading to short upper laser level lifetimes and nonradiative decay [170, 171]. However, low phonon energies typically come with a low thermal conductivity and low damage threshold, which limits power scaling [172].

Suitable direct emitters in the MWIR region are rare-earth-doped fluoride fiber lasers or transition-metal-doped crystal lasers. Fluoride fiber lasers doped with Er^{3+} [173, 174], Ho^{3+} [175, 176], or Dy^{3+} [177] together cover the 3–4 μm region. Output powers of some tens of Watts have been shown in these fiber lasers. Transition-metal-doped crystal lasers like Cr^{2+}:ZnSe [178] or Fe^{2+}:ZnSe [179] are broadly tunable between 2–3.5 μm and 3.7–5.1 μm, respectively. These lasers have been operated either at high power or at high pulse energies. In addition, quantum cascade lasers are tunable emitters in the 3–300 μm range which can be realized by engineering the semiconductor layer structure [180–182]. Nevertheless, the simultaneous pulse energy and average power scalability remains a challenge in all of these lasers.

The power and energy scaling becomes possible by nonlinear conversion like DFG and OPOs. Widely used nonlinear crystals are periodically poled lithium niobate (PPLN) and potassium titanyl phosphate (KTP), which are transparent up to around 4 μm [184, 185]. In many OPOs, these crystals are pumped by a 1 μm or 1.5–1.6 μm laser, thus generating a signal beam in the near infrared region and an idler beam in the MWIR region [186–189]. When instead a 2 μm pump source is used, energy conservation yields that both the signal and the idler band are in the MWIR region. Pumping a PPLN OPO with a 2 μm laser has been shown, but parasitic absorption of the generated idler wave starting at 4 μm limits the efficiency [190, 191]. More suitable nonlinear crystals for pump wavelengths longer than 2 μm, which are transparent over the entire 3–5 μm range, are ZGP, cadmium silicon phosphide (CSP), orientation-patterned
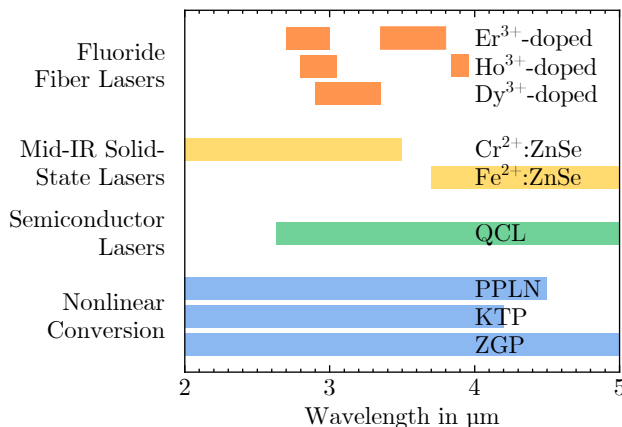

Figure 6.1: Overview over coherent sources emitting in the MWIR region (similar to [183], based on [13, 173–179, 181, 182, 184, 185]).

gallium arseninde (OP-GaAs), and orientation-patterned gallium phosphide (OP-GaP) [13]. Among these, ZGP has the most mature fabrication process and, in addition, a high nonlinear coefficient ($d_{36} = 75\,\mathrm{pm\,V^{-1}}$) and a high thermal conductivity [13]. An overview of the discussed MWIR sources and the wavelength range that they cover is shown in Figure 6.1.

OPOs based on ZGP crystals have been extensively studied in the last 25 years. In addition to different resonator geometries like linear, ring, and image rotation cavities [30, 121, 130, 192], the power scaling through multiple-stage optical parametric amplifiers was investigated [30, 193]. Linear OPO cavities stand out due to their low complexity and compact design. Up to 38 W of MWIR output power has been demonstrated [194]. However, this architecture requires using a Faraday isolator between the pump source and the OPO to protect the pump laser from back-reflections of the OPO components. More complex ring resonators can be operated without an isolation stage, thus enabling the power scaling of the MWIR output. An MWIR output power of 78 W was demonstrated from a ZGP ring OPO [30]. However, the degradation of the beam quality with increasing pump powers remains a challenge in either design. A solution to this issue is offered by image-rotating resonators, which improve the beam quality by generating a highly symmetric output beam through the suppression of higher order modes, but such designs are highly complex [121, 194, 195]. A less complex solution is the mode matching of pump and resonator modes by the inclusion of a negative lens in the cavity as has been shown in ring OPOs [193]. Because there is a lack of research on this design in a linear OPO cavity, it is investigated in this thesis.

6.2 Theoretical Considerations on OPO Resonator Mode Sizes

In similarity to laser resonators, one factor that determines the beam quality in an OPO is the mode matching of the pump and the resonator modes. The mode size simulation presented in Section 3.1.3 is therefore adapted to simulate a simple linear ZGP OPO and to evaluate the change in the signal mode diameter depending on the variation of different parameters. For the simulation, the 20 mm long nonlinear crystal is modeled as a material with a constant refractive index and the thermal lens is assumed to be a thin lens with focal length f_{th} positioned at one third of the crystal. The influence of gain guiding effects on the resonator mode size is neglected. Gain guiding effectively narrows the beam in the direction of the conversion due to a higher gain level at the beam center, where the intensity is higher [196]. The cavity with a length L is built
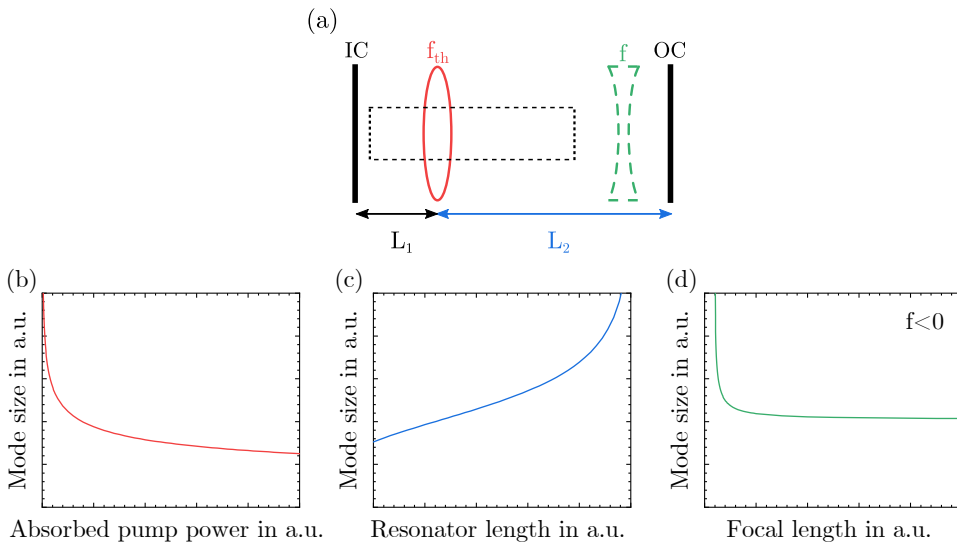
Figure 6.2: (a) Schematic depiction of the simulated plane-plane resonator. (b)-(d) Diameter of signal mode size in the nonlinear crystal depending on (b) the absorbed pump power (thermal lens), (c) the resonator length, and (d) the focal length of the negative lens.

by a planar IC and OC mirror. Additionally, a negative lens with a focal length f can be inserted. The distance between the thermal lens and the IC and OC mirror is denoted with L_1 and L_2, respectively. This simple cavity is depicted in Figure 6.2(a). The focal length of the thermal lens, the resonator length, and the focal length of the negative lens are varied one after the other and the mode diameter of the signal mode in the crystal is simulated. Figure 6.2(b) shows the mode size depending on the absorbed pump power for a 22 mm long resonator. With a larger amount of absorbed pump power, the thermal focal length and the signal mode size decrease. Due to the short resonator length, the minimum mode diameter is around 220 µm. As typical pump diameters are larger than 400 µm to stay above the damage threshold of the nonlinear crystal, the mode mismatch in such a short cavity directly becomes apparent. Additionally, as the mode diameter decreases with an increasing pump power, a deterioration of the beam propagation factor with higher pump and output powers is expected. Consequently, to improve the beam propagation factor, the OPO mode diameter must be adapted to the pump diameter by either increasing the resonator length (see Figure 6.2(c)) or by inserting a negative lens (see Figure 6.2(d)). The resonator length can in principle be increased until the distance of one of the resonator mirrors from the thermal lens is longer than the thermal focal length, as this results in an unstable cavity. However, because there are CO_2 absorption lines in the 3–5 µm

range [94], increasing the resonator length might lead to a decrease in the stability of the OPO output. When a negative lens is inserted in the resonator, this problem is mitigated because the lens material fills the air gap. For short focal lengths of the negative lens, the OPO mode size is large and it decreases for longer focal lengths. However, the range of focal lengths over which the OPO mode changes is small, thus requiring a careful experimental optimization of the negative lens.

In the following experiments, the focus is on investigating the beam propagation factor when the pump power and resonator length are varied. In addition, the influence of different diverging lenses on the beam propagation factor and output power is investigated.

6.3   Experimental Setup of ZGP OPO

The experimental setup is depicted in Figure 6.3. Due to its short pulses and high average power, the laser described in Section 4.2.4 is used as a pump source. Its output power is attenuated to 40 W by a TFP and a half-wave plate to stay below the damage thresholds of the subsequent Faraday isolators, which are necessary to protect the pump source from back-reflections of the OPO components. The isolators each consist of a commercially available Faraday rotator and a TFP, and for an optimum isolation, two of them are used. A second variable attenuator controls the pump power into the nonlinear crystal. The collimated pump beam is then shaped by a Galilean telescope to different pump beam diameters in the nonlinear crystal. They are chosen such that the typical damage threshold of the ZGP crystal, which is around $1\text{--}2\,\mathrm{J\,cm^{-2}}$, is not exceeded [197, 198]. Finally, a half-wave plate rotates the incident p- to s-polarization to fulfill the phase matching condition. The OPO is doubly-resonant and built by an IC mirror, the 6 mm x 6 mm x 20 mm nonlinear ZGP crystal cut to 55.5°, an optional diverging lens, and a plane-parallel OC mirror ($R < 1\,\%$ at 2.09 µm, $R = 50\,\%$ at 3–5 µm). Two different IC mirrors are used. For the optimization of pump parameters in Section 6.4.2, a plane-parallel
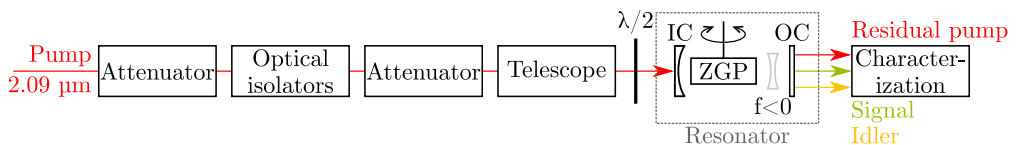

Figure 6.3: Schematic setup of pump beam shaping and OPO.

mirror ($R < 5\,\%$ at 1.85–2.2 μm and $R \geq 99.9\,\%$ at 3–5 μm) is used. However, due to the observation of detrimental thermal effects in this mirror, a plano-concave mirror ($R < 0.2\,\%$ at 2.09 μm and $R > 98\,\%$ at 2.5–5 μm) with a radius of curvature of 0.1 m is used in the subsequent optimization of the resonator with the diverging lens in Section 6.4.3. The AR coated (AR for 2–2.2 μm and 3.5–4.8 μm) ZGP crystal is water-cooled to 20 °C in a copper heat sink. To achieve angular phase matching, a rotation of the crystal around its vertical axis is enabled. Three AR coated diverging CaF$_2$ lenses with focal lengths of -0.1 m, -0.08 m, and -0.05 m are investigated. The physical lengths of the investigated cavities are 22 mm and 33 mm.

6.4   Experimental Characterization

At first, the pump source is investigated with a focus on tuning the repetition rate in Section 6.4.1. Then, optimum pump beam parameters are determined in Section 6.4.2. Finally, the influence of an intracavity lens on the beam propagation factor is investigated in Section 6.4.3.

6.4.1   Characterization of Pump Source

The resonator presented in Section 4.2.4 has so far only been operated at 50 kHz. By tuning the repetition rate, the pulse energy and pulse duration change. Thus, depending on the application, a suitable repetition rate can be chosen. Figure 6.4(a) shows the pulse energy and the pulse duration when the repetition rate is tuned from 25 kHz to 100 kHz in 5 kHz steps and the laser is operated at a fixed pump power of 89 W. The pulse duration increases linearly from 20 ns to 78 ns when increasing the repetition rate, and the pulse energy decreases from 2.2 mJ to 0.6 mJ and follows a hyperbolic curve. The temporal evolution of a Q-switched pulse at 25 kHz repetition rate is shown in Figure 6.4(b). The pulse duration of 20 ns and the pulse energy of 2.2 mJ result in a pulse peak power of 108 kW. As in ZGP OPOs a pump threshold in the kW regime has to be overcome prior to the conversion, it is favorable to work with high-peak-power pulses. For pumping the OPO, the pump power is limited to an average power of 34 W due to the damage thresholds of and losses at the optical isolators. This results in a maximum available pulse energy of 1.36 mJ with a maximum pulse peak power of 68 kW.
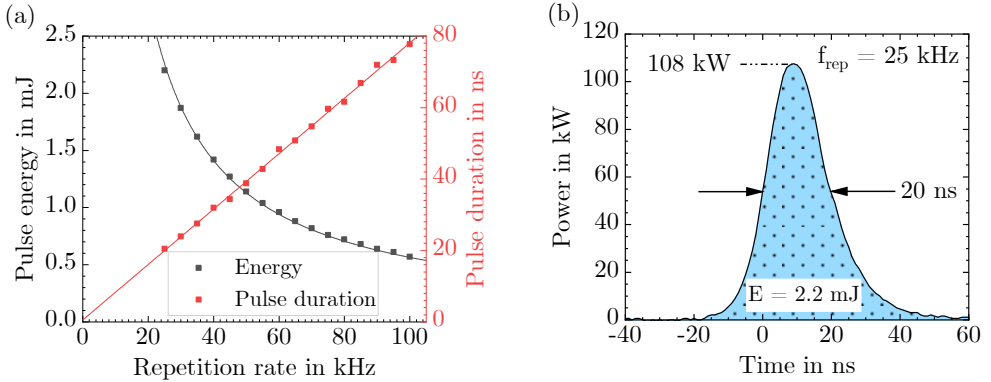
Figure 6.4: (a) Pulse energy and pulse duration depending on the repetition rate. (b) Temporal evolution of a Q-switched pulse at a repetition rate of 25 kHz at a pump power of 89 W.

6.4.2 Characterization of ZGP OPO for Different Pump Parameters

At first, the 22 mm long plane-parallel ZGP OPO cavity is investigated for different pump beam characteristics. The output power is investigated for different pump repetition rates of 25 kHz, 35 kHz, and 55 kHz. Besides that, different pump diameters of 400 μm, 500 μm, and 600 μm are investigated. In all experiments, the maximum pump fluence was limited to 1 J cm^{-2} to stay below the damage threshold of the nonlinear crystal. Thus, when both a low repetition rate and a small pump diameter are used, the incident pump power is limited to fulfill this condition. Therefore, the maximum available pump power can only be used in the combinations 25 kHz and 600 μm (black), 35 kHz and 500 μm (green), and 55 kHz and 400 μm (yellow). The resulting output power curves (see Figure 6.5) are discussed from different perspectives:

1. Same fluence (black, green, and yellow data points):

   Due to the longer pulse length at a higher repetition rate, the pump threshold increases with an increasing repetition rate because the proportion of the pulse that is below the conversion threshold is larger. All curves show a rollover at high pump powers, which is most severe for the smallest pump diameter (yellow). This is not expected from the theory on OPOs. The rollover might result from thermal effects in the IC mirror. When a smaller pump diameter is used, this leads to a higher temperature when the same amount

of pump light is absorbed. This could explain the strongest rollover in the configuration with the smallest pump diameter.

2. Same repetition rate (black, red, and blue data points):
At the same repetition rate, the pump threshold fluence is reached at a lower pump power when the beam diameter is smaller, which is confirmed by the experiments. In addition, the slope efficiency should increase at a higher pump fluence, which is, however, not observed in the experiments. Instead, a decreasing slope efficiency is measured with a smaller pump diameter. This might again result from the stronger local heating of the IC mirror.

3. Same pump diameter (blue, purple, and yellow data points):
Due to the higher pump energy at a lower repetition rate, the observed pump threshold is lowest for the lowest repetition rate, which is in line with the expectations. Additionally, among these configurations, the highest slope efficiency is reached with the lowest repetition rate.

Overall, the highest slope efficiency of 46.6 % and the highest maximum output power of 10.7 W is measured in the configuration with a repetition rate of 25 kHz and a pump diameter of 600 μm.
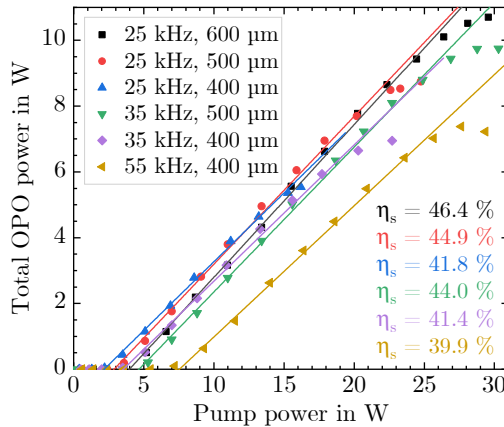
Figure 6.5: Total OPO output power as a function of the pump power. The pump source is operated at different repetition rates and focused to different pump diameters.

Two conclusions can be drawn from these experiments. Due to the highest available pulse energy, the pulse repetition rate is fixed at 25 kHz for the following experiments. Because of the observed thermal effects in the IC mirror, a different mirror is used in the following experiment.

6.4.3 Characterization of ZGP OPO with Diverging Lens

To improve the beam quality of the OPO, a resonator including a diverging lens is investigated. In contrast to the previous experiments, the IC mirror is plano-concave with a radius of curvature of 0.1 m. As a consequence, the intrinsic resonator mode is further decreased, which is unfavorable from a mode matching point of view. In addition, the $1/e^2$ pump diameter is aligned to 760 µm to remain below the damage threshold of the IC mirror, thus limiting the fluence to $0.6\,\mathrm{J\,cm^{-2}}$ at the maximum pump power. Five OPO configurations are investigated: a 22 mm long cavity and a 33 mm long cavity without additional negative lens, and a 33 mm long cavity with a −0.1 m, −0.08 m, and −0.05 m negative lens. Figure 6.6 shows the total signal and idler output power depending on the $\mathrm{Ho^{3+}}$:YAG pump power for these configurations. The 22 mm long cavity (black) has the lowest pump threshold of 3.2 W and reaches a maximum output of around 14 W. Increasing the resonator length to 33 mm (red) leads to an increase in the pump threshold because the rise time of the OPO is increased as a consequence of the decreased number of cavity round-trips. The maximum output power is around 14 W as well. When the intracavity lenses are inserted one after the other, the pump threshold increases further, which is
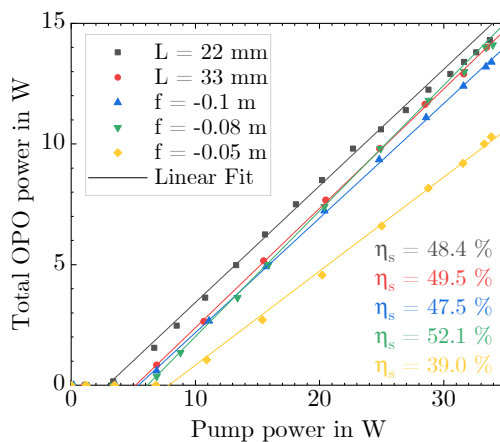
Figure 6.6: Total signal and idler output power depending on the pump power for different cavity configurations.
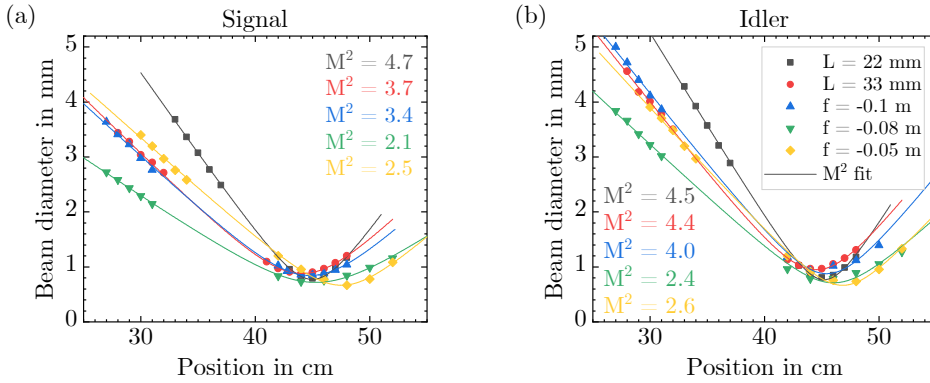
Figure 6.7: Measurements of the beam propagation factor of the vertical beam axis for the different cavity configurations for (a) the signal and (b) the idler light.

explained by the increasing OPO mode size, thus requiring a stronger refractive power of the thermal lens to obtain the same OPO fluence. In the resonators with the −0.1 m lens (blue) and the −0.08 m lens (green), a maximum output power of 13.4 W and 14.1 W is measured. Only the −0.05 m lens (yellow) has a drastically lowered slope efficiency of 39 % and a lower maximum output power of around 10 W as compared to the other configurations. This is attributed to an increase in the intrinsic OPO mode that does not match the pump diameter.

Differences in the output beam are not only observed regarding the output power but also regarding the beam propagation factor. Figure 6.7(a) and Figure 6.7(b) show the beam propagation factor for all configurations measured at the maximum pump power of 34 W for the signal and the idler beam, respectively. For the measurement, the signal and the idler beam are separated by a dichroic filter. The beam propagation is only shown for the vertical beam axis as an example. Due to the increase in the intrinsic mode size when the resonator length is increased and when a negative lens is inserted, the mode overlap with the pump mode is improved. Consequently, a smaller beam propagation factor is measured. This is valid for both the signal and the idler beam. The deterioration of the beam propagation factor with the −0.05 m lens is attributed to an increase of the intrinsic mode size exceeding that of the pump beam.

Overall, the highest slope efficiency of 52.1 % and the best beam propagation factor are measured in the resonator with the −0.08 m lens. Therefore, this cavity is looked into in more detail. Figure 6.8(a) shows the output power and beam propagation factor of the signal beam for the
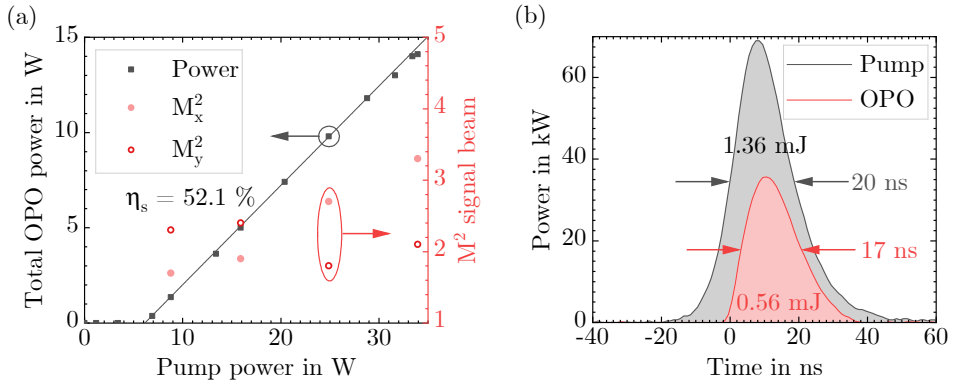
Figure 6.8: (a) Total OPO output power and beam propagation factor of the signal beam depending on the pump power. (b) Temporal pulse shape of the input pump pulse and the output OPO pulse.

horizontal (x) and vertical (y) beam axis depending on the pump power. A pump threshold of 6.2 W is determined, corresponding to a fluence of 0.11 J cm^{-2}. At the maximum pump power, a conversion efficiency of 41.5 % is determined. A deterioration in the beam propagation factor is observed with an increasing pump power, resulting from the increasing refractive power of the thermal lens, which decreases the intrinsic OPO mode size. The beam propagation factors in the horizontal and vertical beam axis are different, which is attributed to the astigmatic pump beam. Figure 6.8(b) shows the temporal pulse profile of an exemplary input pump pulse and the output OPO pulse. An OPO pulse energy of 0.56 mJ and a pulse duration of 17 ns are measured. The shorter pulse duration compared to the input pulse duration results from the high OPO threshold intensity that has to be overcome before the conversion starts. The RMS pulse stability is measured to be 2.3 % for the OPO pulses, which is slightly larger than the pump pulse stability of 1.3 %.

Figure 6.9(a) and Figure 6.9(b) show the beam propagation factors measured at the maximum output power of 14.1 W for the signal and the idler beam, respectively. For the signal beam, a beam propagation factor of 3.2/2.1 and for the idler beam, a beam propagation factor of 3.6/2.4 is measured in the horizontal/vertical beam direction, respectively. This is a significant improvement to the beam propagation factors that were measured in the 22 mm long cavity (signal: 6.6/4.7, idler: 6.3/4.5 in the horizontal/vertical beam axis) and the 33 mm long cavity (signal: 5.6/3.7, idler: 6.0/4.4 in the horizontal/vertical beam axis) without additional lens. It proves the working principle of the mode adaptation by using a negative lens.
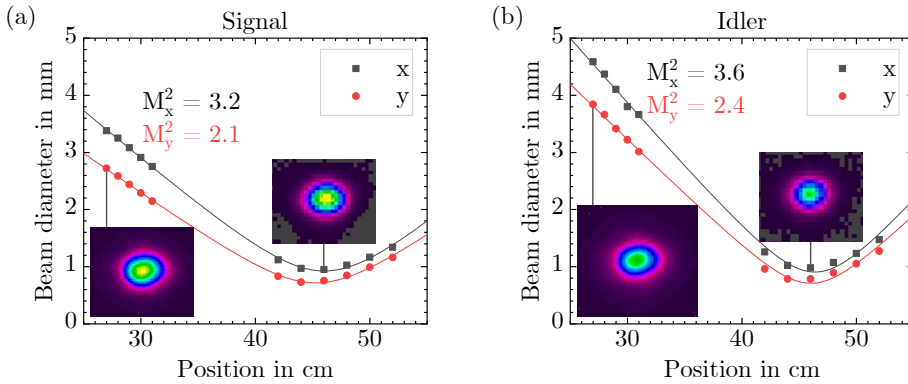
Figure 6.9: Measurements of the beam propagation factor for the maximum OPO output power for (a) the signal and (b) the idler light in the configuration with the −0.08 m lens.

6.5 Discussion

Finally, the obtained results are discussed in relation to the existing literature with a focus on the conversion efficiencies and the achieved beam quality. Typical conversion efficiencies for 2 μm pumped linear ZGP OPOs are around 50–60 %. In 2000, Budni et al. presented a Ho^{3+}:YAG-pumped ZGP OPO with a maximum output power of 4.2 W, corresponding to 0.42 mJ of pulse energy, with a conversion efficiency of 54 % [119]. In 2009, Elder et al. showed 12.6 W, 0.5 mJ MWIR pulses with 52 % conversion efficiency while the maximum pump fluence was 0.55 J cm^{-2} [192]. With a higher pump fluence of around 2.3 J cm^{-2}, Hemming et al. presented 24.2 W of ZGP output power in a walk-off compensated geometry with 62 % conversion efficiency [88]. With a pump fluence of 1.4 J cm^{-2}, Medina et al. further showed 38 W of average power with a conversion efficiency of 57 %, which is the maximum average power obtained from a linear ZGP OPO to date [194]. In 2017, Wang et al. [199] used a similar pump fluence in their experiments and demonstrated the highest conversion efficiency of 75.7 %. In contrast to the other presented works, they operated the pump source in a low-repetition-rate regime of 5 Hz with a maximum energy of 25 mJ, thus limiting thermal lensing in the ZGP crystal due to the low average power. However, pumping the OPO at a high pump energy and with a comparably large pump diameter came at the expense of a beam propagation factor around 10. In contrast to this, a lower conversion efficiency of 40 % was measured by Antipov et al., who pumped the OPO with a fluence of 0.4 J cm^{-2} and measured an output power of 10 W [200]. Considering these results, a high pump fluence plays a key role in generating a high conversion
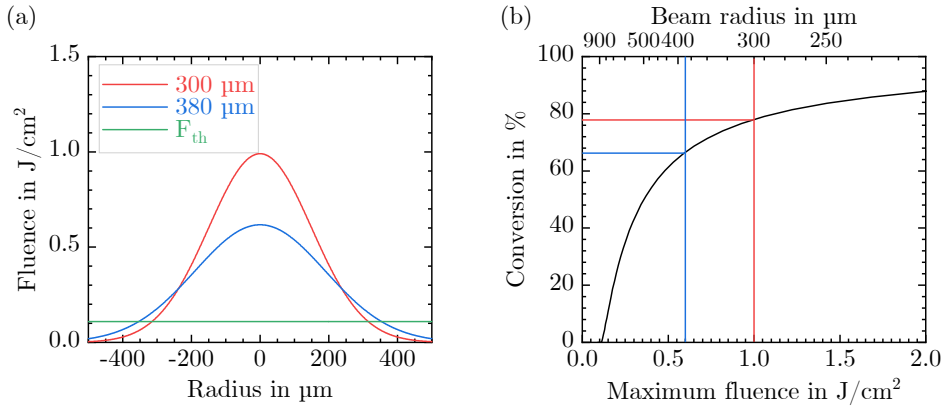
Figure 6.10: (a) Pump fluence over a Gaussian beam with a pulse energy of 1.36 mJ focused to a beam radius of 300 μm (red) and 380 μm (blue) in comparison to the measured pump threshold fluence of 0.11 J cm^{-2} (green). (b) Converted fraction of the Gaussian cross-section depending on the maximum fluence and pump beam radius.

efficiency with an OPO [192]. Figure 6.10(a) illustrates this in more detail. It shows the pump fluence at the maximum pump energy of 1.36 mJ over the cross-section of a Gaussian beam focused to a $1/e^2$ beam radius of 300 μm (red curve) and 380 μm (blue curve). The smaller pump beam generates a maximum fluence of 1 J cm^{-2}, whereas the larger beam generates a maximum fluence of 0.6 J cm^{-2}. From the experiments in Section 6.4.3, a threshold fluence of 0.11 J cm^{-2} was determined (green line). Only the part of the beam that is above the threshold is converted. The conversion, depending on the maximum fluence and beam radius, is shown in Figure 6.10(b). As a result, approximately 10 % more pump light is convertable when the incident pump fluence is 1 J cm^{-2} compared to a fluence of 0.6 J cm^{-2}. Thus, a higher conversion efficiency than 41.5 % is expected from the OPO presented in Section 6.4.3 if a higher pump fluence could be used. Then, the performance would reach similar conversion efficiencies as obtained by other research groups. Besides the pump fluence, further factors influencing the conversion efficiency are the following: Firstly, backconversion of the generated signal and idler beam in OPOs with a high gain reduces the conversion efficiency, but it was not investigated in the context of this work [201]. Secondly, short pump pulses limit the conversion efficiency due to the finite pulse build-up time in the OPO [201]. However, as the pulse peak power was shown to increase with a decreasing pulse length, the 20 ns pulse duration was accepted as a trade-off. Thirdly, an improvement in the conversion efficiency could be achieved for a length-matched laser and OPO resonator, which was also beyond the scope of this thesis [202].

Concerning the deterioration of the beam propagation factor at elevated pump and output powers, which many researchers have reported [88, 194], a solution to this issue is offered in this thesis. The beam propagation factors shown by Elder et al. ($M^2 \approx 2.7$ at 12.6 W of output power) [192], by Hemming et al. ($M^2 \approx 3.1$ at 24.2 W of output power) [88], or by Medina et al. ($M^2 \approx 2.2$ at 38 W of output power) [194] were better than those measured in this thesis for a simple linear OPO. Without the additional lens, a beam propagation factor of around $M^2 \approx 5$ was determined at 14.1 W of output power in the 33 mm long cavity, which is higher than in the other reported works. This is attributed to the large pump diameter used in this work and the astigmatic pump beam, which complicates having planar phase fronts in both beam axes. Furthermore, parasitic absorption in the ZGP crystal might influence the beam propagation factor, as it decreases the resonator mode size. The parasitic absorption depends on the crystal quality, thus it can vary between different crystals [203]. However, this was not investigated further in this thesis, as a large variety of ZGP crystals was not available. In addition, the backconversion of the pump beam deteriorates the beam quality [201].

However, this work proves that a beam quality improvement is possible by improving the mode matching properties between the OPO mode and the pump mode by an additional negative lens in the cavity. To compare the different OPO resonators regarding their total output power P_OPO and beam propagation factor at the same time, the brightness [164]

$$B = \frac{P_\mathrm{OPO}}{M_x^2 M_y^2 \lambda^2} \tag{6.1}$$

is calculated. For a rough estimate, the wavelength of degeneracy $\lambda = 2\lambda_\mathrm{p}$ and the geometric mean of the signal and idler M^2 value are used. Under these assumptions, brightness values between 99–144 kW mm^{-2} sr^{-1} were shown in the past [88, 119, 192, 194]. A summary of the published data and the calculated brightness is given in Table 6.1[1]. The optimum resonator with the −0.08 m lens has a brightness of 106 kW mm^{-2} sr^{-1}. From this point of view, it is comparable to the OPOs presented by Medina et al. [194, 203] and Elder et al. [192].

---

[1] The published data by Medina et al. indicate a remarkably high brightness of 460 kW mm^{-2} sr^{-1} (see row 4 in Table 6.1). However, when extracting the data from this publication and determining the beam propagation factor, a significantly higher beam propagation factor results from our calculations (see italicized row 5 in Table 6.1). Thus, it is believed that the high brightness value results from a calculation error in their published beam propagation factor. With the corrected values, a brightness of 101 kW mm^{-2} sr^{-1} results, which is also in line with results obtained by other research groups.

Table 6.1: Comparison of total OPO output power, beam propagation factors (published values), and calculated brightness values for some literature publications and this work. If specified in the publication, the beam propagation factor is included for both beam axes.

Reference	Year	λ_p in nm	P_{OPO} in W	M^2 signal	M^2 idler	B in $\frac{kW}{mm^2\,sr}$
[119]	2000	2090	4.2	1.2	1.5	134
[192]	2009	2100	12.6	2.2/3.1	2.1/3.6	99
[88]	2013	2090	24.2	3.1	3.1	144
[194]	2021	2065	38	2.2/2.3	2.1/2.2	460
[194]	*2021*	*2065*	*38*	*4.6/5.1*	*4.2/4.9*	*101*[1]
This work	2024	2090	14.1	3.2/2.1	3.6/2.4	106

To conclude, the strategy presented in this thesis can be especially useful in lasers that are operated in a high-energy regime, thus requiring large pump beam diameters due to the damage threshold of the nonlinear crystal, which inevitably leads to a large mode mismatch between the pump and the OPO modes.

6.6 Summary

To summarize, different OPO cavities were investigated concerning the optimum pump beam parameters and the beam quality improvement by the insertion of an additional negative lens. The pump beam was tuned to a repetition rate of 25 kHz leading to a minimum pulse duration of 20 ns and 2.2 mJ pulse energy with a peak power of 108 kW before the optical isolators (1.36 mJ pulses with 68 kW of peak power after the optical isolators). The insertion of a negative lens was motivated by geometric mode size considerations similar to those presented for the Ho^{3+}:YAG resonator in Sections 3.1.3 and 4.2.7. As the thermal lensing of the ZGP crystal decreases the mode size in the typically short OPO cavities to a beam diameter of around 220 μm, both an increase in the resonator length as well as an insertion of a negative lens can increase the OPO mode size, thus adapting it to the typically larger pump mode. In the experiments, the significant improvement of the beam propagation factor for both an increase in the resonator length and the insertion of a well-optimized negative lens was shown. By inserting a −0.08 m lens in the cavity, the beam propagation factor was improved to 3.2/2.1 (3.6/2.4) for the signal (idler) beam

in the horizontal/vertical beam axis, whereas a beam propagation factor of 6.6/4.7 (6.3/4.5) was measured without the additional lens. To explain the low conversion efficiency compared to the results obtained by other research groups, the pump fluence was compared for different pump beam diameters and an increase in the conversion was calculated for a higher pump fluence due to the proportion of the pump beam that is above the threshold fluence. In the optimized cavity, a maximum OPO average output power of 14.1 W, corresponding to 0.56 mJ pulses with a peak power of 36 kW, was measured.

7 Conclusion and Outlook

This thesis deals with the exploration and optimization of holmium-doped yttrium aluminum garnet (Ho^{3+}:YAG) resonators regarding their achievable output power with a near-diffraction-limited beam quality as well as their mechanical stability. In addition, the application of a Ho^{3+}:YAG laser for pumping an optical parametric oscillator (OPO) is investigated with a focus on improving the OPO resonator design to achieve an enhanced beam quality.

In preparation on the intended investigations, a simple ABCD matrix based simulation tool for designing laser resonators is presented. Furthermore, detrimental thermal blooming effects of the Tm^{3+}-fiber laser pump source, which influence the performance of the Ho^{3+}:YAG lasers, are qualitatively investigated. The following section summarizes the main findings of this thesis.

Firstly, two approaches for the power scaling of Ho^{3+}:YAG resonators are presented. The first approach investigates the temperature management in the laser crystal by comparing a homogeneously doped crystal with a crystal comprised of increasingly doped segments. Such a segmented Ho^{3+}:YAG crystal is investigated in this thesis for the first time. It is intended to create a more homogeneous pump light absorption resulting in a more homogeneous temperature distribution, thus reducing thermal stresses and enabling power scaling. After the presentation of a numerical approach to optimize the segment lengths and doping concentrations, the fabricated segmented crystal is characterized confirming the successful implementation of the design and the resulting smoothed longitudinal absorption when it is inspected with visible light. To compare the homogeneously doped and the segmented crystal, a cavity is optimized with a focus on achieving the maximum output power with a near-diffraction-limited beam quality. In this cavity, an average output power of 57.6 W with a stable Q-switched operation is measured with the homogeneously doped crystal, whereas the average output power of the segmented crystal

is limited to 51.9 W. In both cases, a beam propagation factor of $M^2 \approx 1.1$ is determined. To explore the outperformance of the homogeneously doped over the segmented crystal, both crystals are investigated interferometrically during laser operation. For both crystals, the maximum averaged longitudinal temperature as well as the focal length of the thermal lens are in a similar region. With a homemade simulation [129], the longitudinal temperature profile in the crystals is derived and it confirms the decreased maximum temperature for the segmented crystal. Additionally, it clarifies the different effective positions of the thermal lens inside the homogeneously doped and segmented crystal. Based on this, a resonator stability theory explains the outperformance of the homogeneously doped over the segmented crystal in the investigated resonator design. The discrepancy between prior literature results, which have indicated a higher achievable output power with the segmented crystal, are explained by the significantly higher peak temperatures in the crystals in those works. When an output beam with a high beam quality is desired, a careful matching of pump and laser mode is essential and this inevitably results in a limited output power. In combination with the excellent thermo-optical properties of Ho^{3+}:YAG, this limits the maximum temperature inside the laser crystal, therefore the segmented crystal cannot exploit its advantages at currently available pump powers.

Besides the temperature management in the laser crystal, the power scaling in a master oscillator power amplifier (MOPA) system is investigated. This power scaling approach is especially useful when a high beam quality is desired, as the beam quality is determined by the oscillator and preserved by the amplifier. In contrast to the existing literature, the amplifier is investigated with a focus on different pumping schemes and the optical gain properties. The maximum slope efficiency of 69.9 % is measured in the pump scheme where pump and laser mode propagate in the same direction, whereas the maximum average output power of 122 W is measured in the dual-end-pumping scheme due to the design of the experiment. The optical gain is investigated for varying pump and signal powers and a maximum gain of 2 is determined at the maximum signal and pump power. The small-signal gain coefficient and the saturation power are in qualitative agreement with the presented amplifier theory.

Secondly, the mechanical stability is investigated in Porro prism based resonator designs. This thesis presents Porro resonators with the quasi-three-level laser material Ho^{3+}:YAG for the first time. As a Porro prism is retro-reflective in one axis over an angular range determined by total internal reflection (TIR), two crossed Porro prisms stabilize the laser mode in both beam axes when they replace the typical resonator end mirrors. This results in a robust and alignment-

insensitive resonator. After exploring unique properties of these prisms theoretically, they are characterized experimentally regarding their apex quality and polarization properties. For the use in a laser resonator, a precise 90° apex angle as well as a maximum apex sharpness are essential. Different Porro resonators including either one or two Porro prisms are investigated regarding their power scaling, alignment stability, and pulse characteristics. A simple linear cavity confirms the relevance of the apex sharpness, as an imperfect apex increases the cavity losses, which directly translates into a drastically lowered slope efficiency, especially when the mode size on the prisms is small. To decrease the losses, a telescopic resonator design is suggested in which the laser is operated stable at an average power of 27.8 W, which, to the best of our knowledge, is the highest average output power shown in a Porro prism based resonator. Scaling the output power is further limited by fluctuations in the beam profile and output power, which are attributed to thermal blooming effects of the pump beam. The telescopic resonator shows a significantly increased alignment tolerance, which is up to a factor of 200 higher than in the same resonator with mirrors as end reflectors. One drawback of the presented design are the long pulse durations in the 100–200 ns range and the corresponding low pulse peak powers, which do not allow using this laser as a pump source for OPOs. A solution to this issue is offered by a more compact linear resonator built by a Porro crystal and a conventional output coupling mirror, reaching shorter pulse durations around 55 ns, a pulse energy of 0.7 mJ, and a pulse peak power of 12 kW. The use of one Porro prism allows for a partially increased alignment stability in this design. Finally, as in all presented lasers the thermally induced birefringence leads to an astigmatic beam, a polarization flip cavity is presented, which is able to reduce the astigmatism by exploiting the unique polarization properties of a zero phase shift Porro prism.

Thirdly, a zinc germanium phosphide (ZGP) OPO is pumped by a Ho^{3+}:YAG source to present an application of Ho^{3+}:YAG lasers. The OPO resonator is examined primarily in terms of improving the beam quality. Initially, considerations on the mode sizes in OPOs are presented depending on the thermal lens of the nonlinear crystal, the resonator length, and the influence of an additional negative lens. By tuning the pump source to a repetition rate of 25 kHz, 20 ns pulses with 108 kW of peak power are generated, which is far above the threshold for the nonlinear conversion. In the experiments, the influence of the resonator length and a diverging lens in the cavity are systematically investigated regarding the achievable output power and beam quality. In the optimum configuration including a −0.08 m lens, an average output power of 14.1 W is achieved with a conversion efficiency of 41.5 % and an averaged beam propagation factor of $M^2 \approx 2.8$. Although other works in the literature have shown a higher output

power and conversion efficiency, the novel approach of including a diverging lens in a linear OPO cavity, which is presented in this thesis, significantly improves the beam quality due to an improved mode matching of the pump and the OPO mode sizes.

From the investigations presented in this thesis, the following conclusions are drawn for the future optimization of Ho^{3+}:YAG lasers.

Power Scaling of Ho^{3+}:YAG Resonators

For the future power scaling of Ho^{3+}:YAG resonators, two cases are distinguished. For applications that require a high output power but have no specific demands on the beam quality, a segmented Ho^{3+}:YAG crystal can pave the way for the power scaling, as it reduces the maximum longitudinal temperature. However, exploiting the advantages of a segmented crystal requires pump sources with a higher pump power than currently available. In addition to power scaling, the segmented crystal can particularly be useful to optimally shape the resonator mode due to the shifted effective position of the thermal lens in comparison with the homogeneously doped crystal. For laser applications with high requirements regarding the beam quality, the power scaling should be implemented with a MOPA system, as this decouples the beam quality, which is determined by the oscillator, and the output power, which is controlled by the amplifier. Because many of the MOPA systems published in the literature are space consuming, future work should focus on designing more compact MOPA systems.

Mechanical Stability of Ho^{3+}:YAG Resonators

Future investigations on mechanically stable Ho^{3+}:YAG resonators can extend into the research on Porro prism based resonators. However, the investigations in this thesis indicate that this approach is more promising in an operation regime of lower output power to limit thermal lensing and thermal blooming effects, thus allowing to avoid a telescopic resonator design, which itself is intrinsically alignment sensitive. Overall, the operation of a Porro prism based Ho^{3+}:YAG resonator in a low-repetition-rate, high-pulse-energy regime should be considered in detail.

Nonlinear Conversion of 2.09 µm Ho^{3+}:YAG Pulses

Future work includes the optimization of ZGP OPOs regarding their output power and beam quality to increase the brightness of the coherent source. In similarity to the power scaling approach of Ho^{3+}:YAG resonators, a MOPA system is a suitable approach to achieve both a high beam quality and a high output power. This requires the systematic design of an OPO resonator with an excellent beam quality, where the optimization approach presented in this thesis should be included. In similarity to the power scaling of Ho^{3+}:YAG lasers, the power scaling should then be implemented in an optical parametric amplifier. To achieve a maximum output power, such a nonlinear conversion MOPA system should be combined with a Ho^{3+}:YAG MOPA system.

References

[1] T. H. Maiman, "Stimulated Optical Radiation in Ruby," *Nature*, vol. 187, no. 4736, p. 493, 1960. DOI: 10.1038/187493a0.

[2] Y. Guo *et al.*, "24.6 kW near diffraction limit quasi-continuous-wave Nd:YAG slab laser based on a stable-unstable hybrid cavity," *Opt. Lett.*, vol. 45, no. 5, p. 1136, 2020. DOI: 10.1364/OL.385387.

[3] G. D. Gautam and A. K. Pandey, "Pulsed Nd:YAG laser beam drilling: A review," *Opt. Laser Technol.*, vol. 100, p. 183, 2018. DOI: 10.1016/j.optlastec.2017.09.054.

[4] R. S. Sharma and P. Molian, "Weldability of advanced high strength steels using an Yb:YAG disk laser," *J. Mater. Process. Technol.*, vol. 211, no. 11, p. 1888, 2011. DOI: 10.1016/j.jmatprotec.2011.06.009.

[5] A. Sharma and V. Yadava, "Experimental analysis of Nd-YAG laser cutting of sheet materials - A review," *Opt. Laser Technol.*, vol. 98, p. 264, 2018. DOI: 10.1016/j.optlastec.2017.08.002.

[6] C. Leone, S. Genna, G. Caprino, and I. De Iorio, "AISI 304 stainless steel marking by a Q-switched diode pumped Nd:YAG laser," *J. Mater. Process. Technol.*, vol. 210, no. 10, p. 1297, 2010. DOI: 10.1016/j.jmatprotec.2010.03.018.

[7] C. Romano, G. Ritt, M. Henrichsen, M. Eichhorn, and C. Kieleck, "Investigation of the polymer material perforation time: Comparison between two fiber laser wavelengths," *Journal of Polymer Research*, vol. 31, no. 2, p. 51, 2024. DOI: 10.1007/s10965-024-03885-w.

[8] K. Scholle, S. Lamrini, P. Koopmann, and P. Fuhrberg, "2 μm Laser Sources and Their Possible Applications," in *Frontiers in Guided Wave Optics and Optoelectronics*, IntechOpen, 2010. DOI: 10.5772/39538.

[9]   T. J. Carrig, "Novel pulsed solid state sources for laser remote sensing," in *Solid State Laser Technologies and Femtosecond Phenomena*, vol. 5620, SPIE, 2004, p. 187. DOI: 10.1117/12.581962.

[10]   B. Göhler *et al.*, "Gated viewing at 2.09 μm laser wavelength: experimental system assessment and comparison to 1.57 μm," in *Electro-Optical and Infrared Systems: Technology and Applications XX*, vol. 12737, SPIE, 2023, p. 127370C. DOI: 10.1117/12.2684727.

[11]   O. Steinvall, R. Persson, F. Berglund, O. K. S. Gustafsson, and F. Gustafsson, "Using an eyesafe military laser range finder for atmospheric sensing," in *Laser Radar Technology and Applications XIX and Atmospheric Propagation XI*, vol. 9080, SPIE, 2014, p. 90800W. DOI: 10.1117/12.2049044.

[12]   "PHOTONIC FRONTIERS: EYE-SAFE LASERS - Retina-safe wavelengths benefit open-air applications." (2008), [Online]. Available: https://www.laserfocusworld.com/test-measurement/research/article/16555076/photonic-frontiers-eye-safe-lasers-retina-safe-wavelengths-benefit-open-air-applications (visited on 03/01/2024).

[13]   P. G. Schunemann, K. T. Zawilski, L. A. Pomeranz, D. J. Creeden, and P. A. Budni, "Advances in nonlinear optical crystals for mid-infrared coherent sources," *J. Opt. Soc. Am. B*, vol. 33, no. 11, p. D36, 2016. DOI: 10.1364/JOSAB.33.000D36.

[14]   M. Vainio and L. Halonen, "Mid-infrared optical parametric oscillators and frequency combs for molecular spectroscopy," *Phys. Chem. Chem. Phys.*, vol. 18, no. 6, p. 4266, 2016.

[15]   I. Elder, "Performance requirements for countermeasures lasers," in *Technologies for Optical Countermeasures VII*, vol. 7836, SPIE, 2010, p. 783605. DOI: 10.1117/12.868323.

[16]   K. Zou *et al.*, "High-capacity free-space optical communications using wavelength- and mode-division-multiplexing in the mid-infrared region," *Nature Communications*, vol. 13, no. 1, p. 7662, 2022. DOI: 10.1038/s41467-022-35327-w.

[17]   "Atmospheric transmission." (2024), [Online]. Available: https://about.ifa.hawaii.edu/ukirt/calibration-and-standards/astronomical-utilities/transmission-and-extinction/atmospheric-transmission/ (visited on 02/28/2024).

[18]   R. L. Aggarwal, D. J. Ripin, J. R. Ochoa, and T. Y. Fan, "Thermo-optic properties of laser crystals in the 100-300 K temperature range: $Y_3Al_5O_{12}$ (YAG), $YAlO_3$ (YALO) and $LiYF_4$ (YLF)," in *Solid State Lasers XIV: Technology and Devices*, vol. 5707, SPIE, 2005, p. 165. DOI: 10.1117/12.601635.

[19]   S. R. Bowman and B. J. Feldman, "Demonstration and analysis of a holmium quasi-two-level laser," in *Solid State Lasers III*, vol. 1627, SPIE, 1992, p. 46. DOI: 10.1117/12.60183.

[20]   M. Eichhorn, "Quasi-three-level solid-state lasers in the near and mid infrared based on trivalent rare earth ions," *Appl. Phys. B*, vol. 93, no. 2, p. 269, 2008. DOI: 10.1007/s00340-008-3214-0.

[21]   L. F. Johnson, J. E. Geusic, and L. G. Van Uitert, "Coherent oscillations from Tm^{3+}, Ho^{3+}, Yb^{3+} and Er^{3+} ions in yttrium aluminum garnet," *Appl. Phys. Lett.*, vol. 7, no. 5, p. 127, 1965. DOI: 10.1063/1.1754339.

[22]   O. L. Antipov, N. G. Zakharov, M. Fedorov, N. M. Shakhova, N. N. Prodanets, L. B. Snopova, V. V. Sharkov, and R. Sroka, "Cutting effects induced by 2 µm laser radiation of cw Tm:YLF and cw and Q-switched Ho:YAG lasers on ex-vivo tissue," *Med. Laser Appl.*, vol. 26, no. 2, p. 67, 2011. DOI: 10.1016/j.mla.2011.02.004.

[23]   T. Y. Fan, G. Huber, R. L. Byer, and P. Mitzscherlich, "Continuous-wave operation at 2.1 µm of a diode-laser-pumped, Tm-sensitized $Ho:Y_3Al_5O_{12}$ laser at 300 K," *Opt. Lett.*, vol. 12, no. 9, p. 678, 1987. DOI: 10.1364/OL.12.000678.

[24]   X. Mu, H. E. Meissner, and H. C. Lee, "Thulium fiber laser 4-pass end-pumped high efficiency 2.09-µm Ho:YAG laser," in *2009 Conference on Lasers and Electro-Optics and 2009 Conference on Quantum electronics and Laser Science Conference*, IEEE, 2009, p. 1.

[25]   W. C. Yao, E. H. Li, Y. J. Shen, C. Y. Ren, Y. G. Zhao, D. Y. Tang, and D. Y. Shen, "A 142 W Ho:YAG laser single-end-pumped by a Tm-doped fiber laser at 1931 nm," *Las. Phys. Lett.*, vol. 16, no. 11, p. 115001, 2019. DOI: 10.1088/1612-202x/ab459d.

[26]   X. M. Duan, Y. J. Shen, B. Q. Yao, and Y. Z. Wang, "146.4 W end-pumped Ho:YAG slab laser with two crystals," *Quantum Electron.*, vol. 48, no. 8, p. 691, 2018. DOI: 10.1070/QEL16717.

[27]   E. Lippert, H. Fonnum, G. Arisholm, and K. Stenersen, "A 22-watt mid-infrared optical parametric oscillator with V-shaped 3-mirror ring resonator," *Opt. Express*, vol. 18, no. 25, p. 26475, 2010. DOI: 10.1364/OE.18.026475.

[28] Y.-J. Shen, B.-Q. Yao, X.-M. Duan, T.-Y. Dai, Y.-L. Ju, and Y.-Z. Wang, "Resonantly pumped high efficiency Ho:YAG laser," *Appl. Opt.*, vol. 51, no. 33, p. 7887, 2012. DOI: 10.1364/AO.51.007887.

[29] X. M. Duan, Y. J. Shen, B. Q. Yao, and Y. Z. Wang, "A 106W Q-switched Ho:YAG laser with single crystal," *Optik*, vol. 169, p. 224, 2018. DOI: 10.1016/j.ijleo.2018.05.094.

[30] G. Liu *et al.*, "161 W middle infrared ZnGeP$_2$ MOPA system pumped by 300 W-class Ho:YAG MOPA system," *Opt. Lett.*, vol. 46, no. 1, p. 82, 2021. DOI: 10.1364/OL.413755.

[31] M. Ganija, K. Boyd, and J. Munch, "High-Power Q-Switched Near Infrared Cryogenic Lasers," in *2023 Conference on Lasers and Electro-Optics Europe & European Quantum Electronics Conference (CLEO/Europe-EQEC)*, IEEE, 2023, p. 1. DOI: 10.1109/CLEO/Europe-EQEC57999.2023.10231721.

[32] R. Wilhelm, D. Freiburg, M. Frede, D. Kracht, and C. Fallnich, "Design and comparison of composite rod crystals for power scaling of diode end-pumped Nd:YAG lasers," *Opt. Express*, vol. 17, no. 10, p. 8229, 2009. DOI: 10.1364/OE.17.008229.

[33] B. A. See, K. Fueloep, and R. Seymour, "An assessment of the crossed Porro prism resonator," *Technical Memorandum ERL-0162-TM*, 1980.

[34] R. G. Gould *et al.*, "The LASER, light amplification by stimulated emission of radiation," in *The Ann Arbor conference on optical pumping, the University of Michigan*, vol. 15, 1959, p. 92.

[35] A. L. Schawlow and C. H. Townes, "Infrared and Optical Masers," *Phys. Rev.*, vol. 112, no. 6, p. 1940, 1958. DOI: 10.1103/PhysRev.112.1940.

[36] J. P. Gordon, H. J. Zeiger, and C. H. Townes, "Molecular Microwave Oscillator and New Hyperfine Structure in the Microwave Spectrum of NH$_3$," *Phys. Rev.*, vol. 95, no. 1, p. 282, 1954. DOI: 10.1103/PhysRev.95.282.

[37] A. Einstein, "Zur Quantentheorie der Strahlung," *Physikalische Zeitschrift*, vol. 18, p. 121, 1917.

[38] M. Eichhorn, *Laser Physics: From Principles to Practical Work in the Lab*, 1st ed. Springer, 2014. DOI: 10.1007/978-3-319-05128-4.

[39] W. Koechner, *Solid-state laser engineering*, 2nd ed. Springer, 2013. DOI: 10.1007/978-3-662-14219-6.

[40]   I. T. Sorokina and K. L. Vodopyanov, *Solid-State Mid-Infrared Laser Sources*, 1st ed. Springer, 2003, p. 262. DOI: 10.1007/3-540-36491-9.

[41]   W. Demtröder, *Experimentalphysik 3: Atome, Moleküle und Festkörper*, 5th ed. Springer-Verlag, 2016. DOI: 10.1007/978-3-662-49094-5.

[42]   T. Fan, "Heat generation in Nd:YAG and Yb:YAG," *IEEE J. Quantum Electron.*, vol. 29, no. 6, p. 1457, 1993. DOI: 10.1109/3.234394.

[43]   M. Eichhorn, "Theoretical and experimental investigation on an Er^{3+}:YAG solid-state heat-capacity laser," in *Laser Technology for Defense and Security V*, vol. 7325, SPIE, 2009, p. 732502. DOI: 10.1117/12.816598.

[44]   S. Chénais, F. Druon, S. Forget, F. Balembois, and P. Georges, "On thermal effects in solid-state lasers: The case of ytterbium-doped materials," *Prog. Quantum Electron.*, vol. 30, no. 4, p. 89, 2006. DOI: 10.1016/j.pquantelec.2006.12.001.

[45]   N. P. Barnes, B. M. Walsh, and E. D. Filer, "Ho:Ho upconversion: applications to Ho lasers," *J. Opt. Soc. Am. B*, vol. 20, no. 6, p. 1212, 2003. DOI: 10.1364/JOSAB.20.001212.

[46]   S. R. Bowman, J. E. Tucker, and S. Kirkpatrick, "Progress in the modeling of migration limited energy transfer in laser materials," in *Advanced Solid State Lasers*, Optica Publishing Group, 1998, p. CS22. DOI: 10.1364/ASSL.1998.CS22.

[47]   E. Lippert, S. Nicolas, G. Arisholm, K. Stenersen, and G. Rustad, "Midinfrared laser source with high power and beam quality," *Appl. Opt.*, vol. 45, no. 16, p. 3839, 2006. DOI: 10.1364/AO.45.003839.

[48]   H. D. Baehr and K. Stephan, *Wärme- und Stoffübertragung*, 10th ed. Springer Vieweg, 2019. DOI: 10.1007/978-3-662-58441-5.

[49]   U. O. Farrukh, A. M. Buoncristiani, and C. E. Byvik, "An analysis of the temperature distribution in finite solid-state laser rods," *IEEE J. Quantum Electron.*, vol. 24, no. 11, p. 2253, 1988. DOI: 10.1109/3.8568.

[50]   M. E. Innocenzi, H. T. Yura, C. L. Fincher, and R. A. Fields, "Thermal modeling of continuous-wave end-pumped solid-state lasers," *Appl. Phys. Lett.*, vol. 56, no. 19, p. 1831, 1990. DOI: 10.1063/1.103083.

[51]   M. Abramowitz and I. A. Stegun, *Handbook of Mathematical Functions with Formulas, Graphs, and Mathematical Tables. National Bureau of Standards Applied Mathematics Series 55. Tenth Printing.* ERIC, 1972.

[52]   S. P. Timoshenko and J. N. Goodier, *Theory of elasticity*, 2nd ed. McGraw-Hill Book Company, Inc., 1951.

[53]   W. Koechner, "Thermal Lensing in a Nd:YAG Laser Rod," *Appl. Opt.*, vol. 9, no. 11, p. 2548, 1970. DOI: 10.1364/AO.9.002548.

[54]   B. E. A. Saleh and M. C. Teich, *Fundamentals of Photonics*, 3rd ed. Wiley, 2019. DOI: 10.1002/0471213748.

[55]   W. A. Clarkson, "Thermal effects and their mitigation in end-pumped solid-state lasers," *J. Phys. D: Appl. Phys.*, vol. 34, no. 16, p. 2381, 2001. DOI: 10.1088/0022-3727/34/16/302.

[56]   W. G. Wagner and B. A. Lengyel, "Evolution of the Giant Pulse in a Laser," *J. Appl. Phys.*, vol. 34, no. 7, p. 2040, 1963. DOI: 10.1063/1.1729732.

[57]   "Acousto-optic Modulators." (2023), [Online]. Available: https://www.fiberoptics4sale.com/blogs/wave-optics/acousto-optic-modulators (visited on 12/12/2023).

[58]   R. L. Sutherland, *Handbook of Nonlinear Optics*, 2nd ed. CRC press, 2003. DOI: 10.1201/9780203912539.

[59]   P. E. Powers, *Field Guide to Nonlinear Optics*. SPIE Press, 2013, vol. FG29. DOI: 10.1117/3.1002081.

[60]   R. W. Boyd, *Nonlinear Optics*, 3rd ed. Elsevier, Academic Press, 2008.

[61]   D. E. Zelmon, E. A. Hanning, and P. G. Schunemann, "Refractive-index measurements and Sellmeier coefficients for zinc germanium phosphide from 2 to 9 μm with implications for phase matching in optical frequency-conversion devices," *J. Opt. Soc. Am. B*, vol. 18, no. 9, p. 1307, 2001. DOI: 10.1364/JOSAB.18.001307.

[62]   L. A. Pomeranz, P. G. Schunemann, D. J. Magarrell, J. C. McCarthy, K. T. Zawilski, and D. E. Zelmon, "1-micron-pumped OPO based on orientation-patterned GaP," in *Nonlinear Frequency Generation and Conversion: Materials, Devices, and Applications XIV*, vol. 9347, SPIE, 2015, p. 93470K. DOI: 10.1117/12.2080876.

[63]   A. E. Siegman, *Lasers*. Oxford University Press, 1986.

[64]   E. Hecht and K. Lippert, *Optik*, 7th ed. De Gruyter, 2018. DOI: 10.1515/9783110526653.

[65]   M. Eichhorn, "Thermal lens effects in an Er^{3+}:YAG laser with crystalline fiber geometry," *Appl. Phys. B*, vol. 94, no. 3, p. 451, 2009. DOI: 10.1007/s00340-008-3292-z.

[66] M. Pollnau, P. J. Hardman, M. A. Kern, W. A. Clarkson, and D. C. Hanna, "Upconversion-induced heat generation and thermal lensing in Nd:YLF and Nd:YAG," *Phys. Rev. B*, vol. 58, no. 24, p. 16076, 1998. DOI: 10.1103/PhysRevB.58.16076.

[67] V. Magni, "Multielement stable resonators containing a variable lens," *J. Opt. Soc. Am. A*, vol. 4, no. 10, p. 1962, 1987. DOI: 10.1364/JOSAA.4.001962.

[68] E. Hering and G. Schönfelder, Eds., *Sensoren in Wissenschaft und Technik*, 3rd ed. Springer Vieweg Wiesbaden, 2023. DOI: 10.1007/978-3-658-39491-2.

[69] F. Bernhard, *Handbuch der Technischen Temperaturmessung*, 2nd ed. Springer-Verlag, 2014. DOI: 10.1007/978-3-642-24506-0.

[70] "Introduction to Laser Power Sensors." (2023), [Online]. Available: https://www.ophiropt.com/de/t/laser-power-sensors-introduction (visited on 12/22/2023).

[71] "Pyroelectric Technology in Laser Sensors and Beam Analyzers." (2023), [Online]. Available: https://www.ophiropt.com/de/n/pyroelectric-technology (visited on 12/29/2023).

[72] *Pyroelectric Array Cameras*, Ophir Optronics Solutions Ltd, 2023.

[73] D. Shvedov, V. Norkus, and G. Gerlach, "Beschleunigungsempfindlichkeit pyroelektrischer Sensoren (Acceleration Sensitivity of Pyroelectric Infrared Detectors)," *tm - Technisches Messen*, vol. 73, no. 2, p. 78, 2006. DOI: 10.1524/teme.2006.73.2.90.

[74] H. Budzier and G. Gerlach, *Thermal Infrared Sensors: Theory, Optimisation and Practice*, 1st ed. John Wiley & Sons, 2011. DOI: 10.1002/9780470976913.

[75] M. Löffler-Mang, H. Naumann, and G. Schröder, *Handbuch Bauelemente der Optik: Grundlagen, Werkstoffe, Geräte, Messtechnik*, 8th ed. Carl Hanser Verlag GmbH Co KG, 2020.

[76] H.-R. Tränkler and L. Reindl, Eds., *Sensortechnik*, 2nd ed. Springer Vieweg Berlin, Heidelberg, 2014. DOI: 10.1007/978-3-642-29942-1.

[77] "Laser und Laseranlagen – Prüfverfahren für Laserstrahlabmessungen, Divergenzwinkel und Beugungsmaßzahlen – Teil 1: Stigmatische und einfach astigmatische Strahlen," DIN Deutsches Institut für Normung e. V., DIN EN ISO 11146-1:2021-11, 2021. DOI: 10.31030/3258715.

[78] A. E. Siegman, "How to (Maybe) Measure Laser Beam Quality," in *Diode Pumped Solid State Lasers: Applications and Issues*, Optica Publishing Group, 1998, p. MQ1. DOI: 10.1364/DLAI.1998.MQ1.

[79]   *BeamGage®User Guide*, Ophir-Spiricon, LLC, 2019.

[80]   "Laser und Laseranlagen - Prüfverfahren für Laserstrahlparameter - Strahllagestabilität," DIN Deutsches Institut für Normung e. V., DIN EN ISO 11670:2003, 2003. DOI: 10.31030/9446092.

[81]   *PEM series HgCdTe detectors datasheet*, VIGO System S.A., 2020.

[82]   I. K. Kikoin and S. D. Lazarev, "Photoelectromagnetic effect," *Sov. Phys. Usp.*, vol. 21, no. 4, p. 297, 1978. DOI: 10.1070/PU1978v021n04ABEH005538.

[83]   M. Nowak, "Photoelectromagnetic effect in semiconductors and its applications," *Prog. Quantum Electron.*, vol. 11, no. 3-4, p. 205, 1987. DOI: 10.1016/0079-6727(87)90001-2.

[84]   R. Savkina and O. Smirnov, "Photoconductive and Photovoltaic IR Detectors," in *Handbook of II-VI Semiconductor-Based Sensors and Radiation Detectors: Volume 2, Photodetectors*, Springer, 2023, p. 23. DOI: 10.1007/978-3-031-20510-1_2.

[85]   "AQ6375B Long Wavelength Optical Spectrum Analyzer 1200 - 2400 nm." (2024), [Online]. Available: https://tmi.yokogawa.com/eu/solutions/discontinued/aq6375b-optical-spectrum-analyzer/ (visited on 01/12/2024).

[86]   M. Löffler-Mang, *Optische Sensorik*, 1st ed. Springer, 2012. DOI: 10.1007/978-3-8348-8308-7.

[87]   "Optical Spectrum Analysers - The Monochromator band pass filter." (2024), [Online]. Available: https://info.eu.tmi.yokogawa.com/acton/ct/19192/s-0087-1804/Bct/l-00d9/l-00d9:71c/ct13_0/1?sid=TV2%3A3r98ip8PV (visited on 01/02/2024).

[88]   A. Hemming, J. Richards, A. Davidson, N. Carmody, S. Bennetts, N. Simakov, and J. Haub, "99 W mid-IR operation of a ZGP OPO at 25 % duty cycle," *Opt. Express*, vol. 21, no. 8, p. 10062, 2013. DOI: 10.1364/OE.21.010062.

[89]   J. Šulc, M. Němec, D. Vyhlídal, H. Jelínková, K. Nejezchleb, and J. Polák, "Holmium doping concentration influence on Ho:YAG crystal spectroscopic properties," in *Solid State Lasers XXX: Technology and Devices*, vol. 11664, SPIE, 2021, p. 1166413. DOI: 10.1117/12.2578284.

[90]   D. Hanna, "Astigmatic Gaussian beams produced by axially asymmetric laser cavities," *IEEE J. Quantum Electron.*, vol. 5, no. 10, p. 483, 1969. DOI: 10.1109/JQE.1969.1075673.

[91] J. Kwiatkowski and J. Sotor, "Laser wavelength shift and dual-wavelength generation in continuous-wave operation of Ho:YAG laser pumped by thulium-doped fiber laser," *Opt. Laser Technol.*, vol. 146, p. 107544, 2022. DOI: 10.1016/j.optlastec.2021.107544.

[92] V. V. Vorob'ev, "Thermal blooming of laser beams in the atmosphere," *Prog. Quantum Electron.*, vol. 15, no. 1-2, p. 1, 1991. DOI: 10.1016/0079-6727(91)90003-Z.

[93] D. C. Smith, "High-power laser propagation: Thermal blooming," *Proc. IEEE*, vol. 65, no. 12, p. 1679, 1977. DOI: 10.1109/PROC.1977.10809.

[94] I. Gordon *et al.*, "The HITRAN2020 molecular spectroscopic database," *J. Quant. Spectrosc. Radiat. Transfer*, vol. 277, p. 107949, 2022. DOI: 10.1016/j.jqsrt.2021.107949.

[95] R. Kochanov, I. Gordon, L. Rothman, P. Wcisło, C. Hill, and J. Wilzewski, "HITRAN Application Programming Interface (HAPI): A comprehensive approach to working with spectroscopic data," *J. Quant. Spectrosc. Radiat. Transfer*, vol. 177, p. 15, 2016. DOI: 10.1016/j.jqsrt.2016.03.005.

[96] "HITRAN online - Definitions and Units: Line-by-line Parameters." (2024), [Online]. Available: https://hitran.org/docs/definitions-and-units/ (visited on 01/09/2024).

[97] A. J. Glass, "Thermal blooming in gases," *Opto-Electron.*, vol. 1, no. 4, p. 174, 1969. DOI: 10.1007/BF01834679.

[99] M. Tsunekane, N. Taguchi, T. Kasamatsu, and H. Inaba, "Analytical and experimental studies on the characteristics of composite solid-state laser rods in diode-end-pumped geometry," *IEEE J. Select. Topics Quantum Electron.*, vol. 3, no. 1, p. 9, 1997. DOI: 10.1109/2944.585807.

[100] R. Wilhelm, M. Frede, and D. Kracht, "Power Scaling of End-Pumped Solid-State Rod Lasers by Longitudinal Dopant Concentration Gradients," *IEEE J. Quantum Electron.*, vol. 44, no. 3, p. 232, 2008. DOI: 10.1109/JQE.2007.911702.

[101] S. C. Tidwell, J. F. Seamans, M. S. Bowers, and A. K. Cousins, "Scaling CW diode-end-pumped Nd:YAG lasers to high average powers," *IEEE J. Quantum Electron.*, vol. 28, no. 4, p. 997, 1992. DOI: 10.1109/3.135219.

[102] F. Hanson, "Improved laser performance at 946 and 473 nm from a composite Nd:$Y_3Al_5O_{12}$ rod," *Appl. Phys. Lett.*, vol. 66, no. 26, p. 3549, 1995. DOI: 10.1063/1.113812.

[103]   E. C. Honea, R. J. Beach, S. B. Sutton, J. A. Speth, S. C. Mitchell, J. A. Skidmore, M. A. Emanuel, and S. A. Payne, "115-W Tm:YAG diode-pumped solid-state laser," *IEEE J. Quantum Electron.*, vol. 33, no. 9, p. 1592, 1997. DOI: 10.1109/3.622641.

[104]   R. Weber, B. Neuenschwander, M. M. Donald, M. B. Roos, and H. P. Weber, "Cooling schemes for longitudinally diode laser-pumped Nd:YAG rods," *IEEE J. Quantum Electron.*, vol. 34, no. 6, p. 1046, 1998. DOI: 10.1109/3.678602.

[105]   R. J. Beach *et al.*, "High-average-power diode-pumped Yb:YAG lasers," in *Advanced High-Power Lasers*, vol. 3889, SPIE, 2000, p. 246. DOI: 10.1117/12.380891.

[106]   D. Kracht, R. Wilhelm, M. Frede, K. Dupré, and L. Ackermann, "407 W End-pumped Multi-segmented Nd:YAG Laser," *Opt. Express*, vol. 13, no. 25, p. 10140, 2005. DOI: 10.1364/OPEX.13.010140.

[107]   S. Hahn, M. Frede, J. Neumann, and D. Kracht, "High Power, Multi-Segmented Nd:YAG Laser, Longitudinally Pumped at 885 nm," in *Conference on Lasers and Electro-Optics*, Optica Publishing Group, 2009, p. CThR3. DOI: 10.1364/CLEO.2009.CThR3.

[108]   C. Evangelatos, P. Bakopoulos, G. Tsaknakis, D. Papadopoulos, G. Avdikos, A. Papayannis, and G. Tzeremes, "Continuous wave and passively Q-switched Nd:YAG laser with a multisegmented crystal diode-pumped at 885 nm," *Appl. Opt.*, vol. 52, no. 36, p. 8795, 2013. DOI: 10.1364/AO.52.008795.

[109]   Y. Huang and Y.-F. Chen, "High-power diode-end-pumped laser with multi-segmented Nd-doped yttrium vanadate," *Opt. Express*, vol. 21, no. 13, p. 16063, 2013. DOI: 10.1364/OE.21.016063.

[110]   Q. Shen *et al.*, "11-watt single-frequency 1342-nm laser based on multi-segmented Nd:YVO$_4$ crystal," *Opt. Express*, vol. 27, no. 22, p. 31913, 2019. DOI: 10.1364/OE.27.031913.

[111]   C. Jiang *et al.*, "High-power diode-end-pumped 1314 nm laser based on the multi-segmented Nd:YLF crystal," *Opt. Lett.*, vol. 48, no. 3, p. 799, 2023. DOI: 10.1364/OL.482169.

[112]   J. Dong, J. Cui, Y. Wen, C. Wu, and C. Wang, "High-effective mitigation of thermal effect in multi segment and multi concentration (MSMC) Tm:YAG crystal," *Infrared Phys. Technol.*, vol. 122, p. 104104, 2022. DOI: 10.1016/j.infrared.2022.104104.

[113]   J. Xie, M. Feng, D. Han, R. Xu, K. Zhang, J. Yang, Y. Tian, and F. Song, "Gradient doping composite multi-segmented slab lasers design optimization," *Opt. Laser Technol.*, vol. 168, p. 109826, 2024. DOI: 10.1016/j.optlastec.2023.109826.

[114] R. Wilhelm, D. Freiburg, M. Frede, and D. Kracht, "End-pumped Nd:YAG laser with a longitudinal hyperbolic dopant concentration profile," *Opt. Express*, vol. 16, no. 24, p. 20106, 2008. DOI: 10.1364/OE.16.020106.

[115] M. Wei, T. Cheng, R. Dou, Q. Zhang, and H. Jiang, "Superior performance of a 2 kHz pulse Nd:YAG laser based on a gradient-doped crystal," *Photon. Res.*, vol. 9, no. 7, p. 1191, 2021. DOI: 10.1364/PRJ.424989.

[116] R. Botha, W. Koen, M. Esser, C. Bollig, W. Combrinck, H. Von Bergmann, and H. J. Strauss, "High average power Q-switched 1314 nm two-crystal Nd:YLF laser," *Opt. Lett.*, vol. 40, no. 4, p. 495, 2015. DOI: 10.1364/OL.40.000495.

[117] S. Kurashkin, O. Martynova, D. Savin, E. Gavrishchuk, S. Rodin, and A. Savikin, "Doping profile influence on a polycrystalline Cr^{2+}:ZnSe laser efficiency," *Laser Phys. Lett.*, vol. 15, no. 2, p. 025002, 2018. DOI: 10.1088/1612-202X/aa9b25.

[118] M. Azrakantsyan, D. Albach, N. Ananyan, V. Gevorgyan, and J.-C. Chanteloup, "Yb^{3+}: YAG growth with controlled doping distribution using modified horizontal direct crystallization," *J. Cryst. Growth*, vol. 329, no. 1, p. 39, 2011. DOI: 10.1016/j.jcrysgro.2011.03.060.

[119] P. A. Budni, L. A. Pomeranz, M. L. Lemons, C. A. Miller, J. R. Mosto, and E. P. Chicklis, "Efficient mid-infrared laser using 1.9-μm-pumped Ho:YAG and $ZnGeP_2$ optical parametric oscillators," *J. Opt. Soc. Am. B*, vol. 17, no. 5, p. 723, 2000. DOI: 10.1364/JOSAB.17.000723.

[120] B.-R. Zhao, B.-Q. Yao, C.-P. Qian, G.-Y. Liu, Y. Chen, R.-X. Wang, T.-Y. Dai, and X.-M. Duan, "231 W dual-end-pumped Ho:YAG MOPA system and its application to a mid-infrared ZGP OPO," *Opt. Lett.*, vol. 43, no. 24, p. 5989, 2018. DOI: 10.1364/OL.43.005989.

[121] A. Dergachev, D. Armstrong, A. Smith, T. Drake, and M. Dubois, "3.4-μm ZGP RISTRA nanosecond optical parametric oscillator pumped by a 2.05-μm Ho:YLF MOPA system," *Opt. Express*, vol. 15, no. 22, p. 14404, 2007. DOI: 10.1364/OE.15.014404.

[122] W. Koen, "Middle-Infrared Laser Sources," Ph.D. dissertation, Stellenbosch University, 2016. DOI: 10.13140/RG.2.1.3105.2565.

[123] E. G. Víllora, P. Molina, M. Nakamura, K. Shimamura, T. Hatanaka, A. Funaki, and K. Naoe, "Faraday rotator properties of $\{Tb_3\}[Sc_{1.95}Lu_{0.05}](Al_3)O_{12}$, a highly transparent terbium-garnet for visible-infrared optical isolators," *Appl. Phys. Lett.*, vol. 99, no. 1, p. 011111, 2011. DOI: 10.1063/1.3609245.

[124] D. Vojna, O. Slezák, A. Lucianetti, and T. Mocek, "Verdet Constant of Magneto-Active Materials Developed for High-Power Faraday Devices," *Appl. Sci.*, vol. 9, no. 15, p. 3160, 2019. DOI: 10.3390/app9153160.

[125] S. Mi, J. Tang, D. Wei, B. Yao, J. Li, K. Yang, T. Dai, and X. Duan, "Thermal-birefringence-induced depolarization in a 450 W Ho:YAG MOPA system," *Opt. Express*, vol. 30, no. 12, p. 21501, 2022. DOI: 10.1364/OE.462617.

[126] R. Wilhelm, D. Freiburg, M. Frede, and D. Kracht, "Optimized multi-segmented crystal geometries for power scaling of end-pumped rod lasers," in *Conference on Lasers and Electro-Optics/Quantum Electronics and Laser Science Conference and Photonic Applications Systems Technologies*, Optica Publishing Group, 2006, p. JThC38. DOI: 10.1109/CLEO.2006.4628494.

[127] K. Goth, M. Rupp, M. Griesbeck, M. Eitner, M. Eichhorn, and C. Kieleck, "Limitations of homogeneous and segmented single-crystal compact TEM_{00}-mode Ho^{3+}:YAG laser resonators," *Appl. Phys. B*, vol. 129, no. 6, p. 95, 2023. DOI: 10.1007/s00340-023-08033-8.

[128] J. A. Caird, S. A. Payne, P. R. Staber, A. J. Ramponi, L. L. Chase, and W. F. Krupke, "Quantum electronic properties of the $Na_3Ga_2Li_3F_{12}$:Cr^{3+} laser," *IEEE J. Quantum Electron.*, vol. 24, no. 6, p. 1077, 1988. DOI: 10.1109/3.231.

[129] M. Rupp, M. Eichhorn, and C. Kieleck, "Iterative 3D modeling of thermal effects in end-pumped continuous-wave Ho^{3+}:YAG lasers," *Appl. Phys. B*, vol. 129, no. 1, p. 4, 2023. DOI: 10.1007/s00340-022-07939-z.

[130] S. Bigotta, G. Stöppler, J. Schöner, M. Schellhorn, and M. Eichhorn, "Novel non-planar ring cavity for enhanced beam quality in high-pulse-energy optical parametric oscillators," *Opt. Mater. Express*, vol. 4, no. 3, p. 411, 2014. DOI: 10.1364/OME.4.000411.

[132] J. Y. Liou, C. J. Chen, and M. Y. Hwang, "Misalignment characteristics of resonators formed by 90° cone and mirror," *Appl. Opt.*, vol. 19, no. 15, p. 2569, 1980. DOI: 10.1364/AO.19.002569.

[133] H. Li and Z. Cheng, "Output characteristics of right angle cone mirror cavity laser," *Chin. Opt. Lett.*, vol. 3, no. 11, p. 650, 2005.

[134] I.-C. Kuo and T. Ko, "Laser resonators of a mirror and corner cube reflector: analysis by the imaging method," *Appl. Opt.*, vol. 23, no. 1, p. 53, 1984. DOI: 10.1364/AO.23.000053.

[135] M. S. Scholl, "Ray trace through a corner-cube retroreflector with complex reflection coefficients," *J. Opt. Soc. Am. A*, vol. 12, no. 7, p. 1589, 1995. DOI: 10.1364/JOSAA.12.001589.

[136] W. Ke-Ying, Y. Su-Hui, Z. Chang-Ming, and W. Guang-Hui, "Single-Frequency Nd:YAG Ring Lasers with Corner Cube Prism," *Chin. Phys. Lett.*, vol. 17, no. 10, p. 728, 2000. DOI: 10.1088/0256-307x/17/10/010.

[137] G. Gould, S. Jacobs, P. Rabinowitz, and T. Shultz, "Crossed Roof Prism Interferometer*," *Appl. Opt.*, vol. 1, no. 4, p. 533, 1962. DOI: 10.1364/AO.1.000533.

[138] M. K. Chun and E. A. Teppo, "Laser resonator: an electrooptically Q-switched Porro prism device," *Appl. Opt.*, vol. 15, no. 8, p. 1942, 1976. DOI: 10.1364/AO.15.001942.

[139] J. G. Daly, "The Nd:YAG Laser Rangefinder/Designator," in *Scientific and Engineering Applications of Commercial Laser Devices*, vol. 0610, SPIE, 1986, p. 68. DOI: 10.1117/12.956386.

[140] J. P. Dudeja, "Nd:YAG Laser-Pumped Raman-Shifted Methane Laser as an Eye-safe Laser Rangefinder," *Def. Sci. J.*, vol. 39, no. 3, p. 221, 1989. DOI: 10.14429/dsj.39.4768.

[141] T. D. Cole, "NEAR laser rangefinder: A tool for the mapping and topologic study of asteroid 433 Eros," *Johns Hopkins Apl Technical Digest*, vol. 19, no. 2, p. 143, 1998.

[142] J. Beedell, "Nd:YAG based laser sources for targeting applications," Ph.D. dissertation, Heriot-Watt University, 2013.

[143] Y.-J. Huang, B.-Y. Huang, Y.-C. Lin, T.-D. Wang, and P.-T. Tai, "Development of a high-energy Q-switched slab laser for targeting designation," in *Electro-Optical and Infrared Systems: Technology and Applications XV*, vol. 10795, SPIE, 2018, p. 107950H. DOI: 10.1117/12.2325287.

[144] R. S. Afzal, "Mars Observer Laser Altimeter: laser transmitter," *Appl. Opt.*, vol. 33, no. 15, p. 3184, 1994. DOI: 10.1364/AO.33.003184.

[145]   D. M. Winker, W. H. Hunt, and C. A. Hostetler, "Status and performance of the CALIOP lidar," in *Laser Radar Techniques for Atmospheric Sensing*, vol. 5575, SPIE, 2004, p. 8. DOI: 10.1117/12.571955.

[146]   R. S. Afzal, A. W. Yu, J. L. Dallas, A. Melak, A. T. Lukemire, L. Ramos-Izqueirdo, and W. Mamakos, "The Geoscience Laser Altimeter System (GLAS) Laser Transmitter," *IEEE J. Select. Topics Quantum Electron.*, vol. 13, no. 3, p. 511, 2007. DOI: 10.1109/JSTQE.2007.896051.

[147]   J. F. Cavanaugh *et al.*, "The Mercury Laser Altimeter Instrument for the MESSENGER Mission," *Space Sci. Rev.*, vol. 131, no. 1, p. 451, 2007. DOI: 10.1007/s11214-007-9273-4.

[148]   J.-F. Lee and C.-Y. Leung, "Beam pointing direction changes in a misaligned Porro prism resonator," *Appl. Opt.*, vol. 27, no. 13, p. 2701, 1988. DOI: 10.1364/AO.27.002701.

[149]   J.-F. Lee and C.-Y. Leung, "Lateral displacement of the mode axis in a misaligned Porro prism resonator," *Appl. Opt.*, vol. 28, no. 24, p. 5278, 1989. DOI: 10.1364/AO.28.005278.

[150]   J.-F. Lee and C. Y. Leung, "Method of calculating the alignment tolerance of a Porro prism resonator," *Appl. Opt.*, vol. 28, no. 17, p. 3691, 1989. DOI: 10.1364/AO.28.003691.

[151]   I. A. Litvin, L. Burger, and A. Forbes, "Petal-like modes in Porro prism resonators," *Opt. Express*, vol. 15, no. 21, p. 14065, 2007. DOI: 10.1364/OE.15.014065.

[152]   L. Burger and A. Forbes, "A model of the transverse modes of stable and unstable porro-prism resonators using symmetry considerations," in *Laser Beam Shaping VIII*, vol. 6663, SPIE, 2007, p. 666305. DOI: 10.1117/12.734650.

[153]   E. R. Peck, "Polarization Properties of Corner Reflectors and Cavities∗," *J. Opt. Soc. Am.*, vol. 52, no. 3, p. 253, 1962. DOI: 10.1364/JOSA.52.000253.

[154]   Y.-D. Liu, C. Gao, and X. Qi, "Field rotation and polarization properties of the Porro prism," *J. Opt. Soc. Am. A*, vol. 26, no. 5, p. 1157, 2009. DOI: 10.1364/JOSAA.26.001157.

[155]   L. Burger and A. Forbes, "Porro prism lasers: a new perspective," in *Optical Technologies for Arming, Safing, Fuzing, and Firing IV*, vol. 7070, SPIE, 2008, p. 70700L. DOI: 10.1117/12.793702.

[156] J. Richards, "An improved prism for use in laser resonators," *Technical Memorandum ERL-0212-TM*, 1982.

[157] J. Richards, "Birefringence compensation in polarization coupled lasers," *Appl. Opt.*, vol. 26, no. 13, p. 2514, 1987. DOI: 10.1364/AO.26.002514.

[158] I. Singh, A. Kumar, and O. P. Nijhawan, "Design of a high-power Nd:YAG Q-switched laser cavity," *Appl. Opt.*, vol. 34, no. 18, p. 3349, 1995. DOI: 10.1364/AO.34.003349.

[159] Z. Alperovich, O. Buchinsky, S. Greenstein, and A. A. Ishaaya, "Misalignment sensitivity in an intra-cavity coherently combined crossed-Porro resonator configuration," *Laser Phys. Lett.*, vol. 14, no. 8, p. 085802, 2017. DOI: 10.1088/1612-202x/aa77c2.

[160] H. Yang, J. Meng, and W. Chen, "Characteristic analysis of a polarization output coupling Porro prism resonator," in *XX International Symposium on High-Power Laser Systems and Applications 2014*, vol. 9255, SPIE, 2015, p. 92553O. DOI: 10.1117/12.2064390.

[161] Y. P. Wang, T. Y. Dai, J. Wu, Y. L. Ju, and B. Q. Yao, "A Q-switched Ho:YAG laser with double anti-misalignment corner cubes pumped by a diode-pumped Tm:YLF laser," *Infrared Phys. Technol.*, vol. 91, p. 8, 2018. DOI: 10.1016/j.infrared.2018.03.020.

[162] D. Yan *et al.*, "Injection-seeded, Q-switched Ho:YAG laser based on alignment-insensitive corner cone reflectors," *Opt. Laser Technol.*, vol. 166, p. 109584, 2023. DOI: 10.1016/j.optlastec.2023.109584.

[163] A. Rapaport, L. Weichman, B. Brickeen, S. Green, and M. Bass, "Laser resonator design using optical ray tracing software: comparisons with simple analytical models and experimental results," *IEEE J. Quantum Electron.*, vol. 37, no. 11, p. 1401, 2001. DOI: 10.1109/3.958355.

[164] A. Forbes, L. Burger, and I. A. Litvin, "Modeling laser brightness from cross Porro prism resonators," in *Laser Beam Shaping VII*, vol. 6290, SPIE, 2006, p. 62900M. DOI: 10.1117/12.682843.

[165] J. W. Goodman, *Introduction to Fourier optics*, 2nd ed. McGraw-Hill, 1996.

[166] L. Agrawal, A. Bhardwaj, S. Pal, and A. Kumar, "Jones matrix formulation of a Porro prism laser resonator with waveplates: theoretical and experimental analysis," *Appl. Phys. B*, vol. 89, no. 2, p. 349, 2007. DOI: 10.1007/s00340-007-2801-9.

[167]   R. Saxena and P. P. Pathak, "Study of effects of wave plate orientation in cross porro prism diode pumped ND:YAG laser resonator," *Int. J. Latest Res. Sci. Technol.*, vol. 3, no. 3, p. 47, 2014. DOI: 10.1016/j.optlastec.2009.01.009.

[168]   K. Goth, M. Griesbeck, M. Eitner, H. Büker, M. Eichhorn, and C. Kieleck, "Alignment-insensitive end-pumped continuous-wave crossed-Porro prism Ho^{3+}:YAG laser," *Opt. Lett.*, vol. 47, no. 13, p. 3143, 2022. DOI: 10.1364/OL.459892.

[170]   B. M. Walsh, H. R. Lee, and N. P. Barnes, "Mid infrared lasers for remote sensing applications," *J. Lumin.*, vol. 169, p. 400, 2016. DOI: 10.1016/j.jlumin.2015.03.004.

[171]   E. E. Brown, Z. D. Fleischman, J. McKay, L. Merkle, U. Hommerich, W. Palosz, S. Trivedi, and M. Dubinskii, "Ho^{3+} doped low-phonon single crystals and chalcogenide glasses for mid-IR source application," *Opt. Mater. Express*, vol. 13, no. 5, p. 1307, 2023. DOI: 10.1364/OME.487911.

[172]   R. Moncorgé, A. Braud, P. Camy, J. L. Doualan, B. Denker, and E. Shklovsky, "Fluoride laser crystals," in *Handbook of Solid-State Lasers*, Woodhead Publishing, 2013, p. 28. DOI: 10.1533/9780857097507.1.28.

[173]   V. Fortin, M. Bernier, S. T. Bah, and R. Vallée, "30 W fluoride glass all-fiber laser at 2.94 µm," *Opt. Lett.*, vol. 40, no. 12, p. 2882, 2015. DOI: 10.1364/OL.40.002882.

[174]   F. Maes, V. Fortin, M. Bernier, and R. Vallée, "5.6 W monolithic fiber laser at 3.55 µm," *Opt. Lett.*, vol. 42, no. 11, p. 2054, 2017. DOI: 10.1364/OL.42.002054.

[175]   F. Maes, V. Fortin, S. Poulain, M. Poulain, J.-Y. Carrée, M. Bernier, and R. Vallée, "Room-temperature fiber laser at 3.92 µm," *Optica*, vol. 5, no. 7, p. 761, 2018. DOI: 10.1364/OPTICA.5.000761.

[176]   J. Li, D. D. Hudson, and S. D. Jackson, "High-power diode-pumped fiber laser operating at 3 µm," *Opt. Lett.*, vol. 36, no. 18, p. 3642, 2011. DOI: 10.1364/OL.36.003642.

[177]   R. Woodward, M. Majewski, G. Bharathan, D. Hudson, A. Fuerbach, and S. Jackson, "Watt-level dysprosium fiber laser at 3.15 µm with 73% slope efficiency," *Opt. Lett.*, vol. 43, no. 7, p. 1471, 2018. DOI: 10.1364/OL.43.001471.

[178]   V. Fedorov, I. Moskalev, M. Mirov, S. Mirov, T. Wagner, M. Bohn, P. Berry, and K. Schepler, "Energy scaling of nanosecond gain-switched Cr^{2+}:ZnSe lasers," in *Solid State Lasers XX: Technology and Devices*, vol. 7912, SPIE, 2011, p. 79121E. DOI: 10.1117/12.876700.

[179] D. Martyshkin, V. Fedorov, M. Mirov, I. Moskalev, S. Vasilyev, and S. Mirov, "High average power (35 W) pulsed Fe:ZnSe laser tunable over 3.8-4.2 µm," in *CLEO: Science and Innovations*, Optica Publishing Group, 2015, p. SF1F.2. DOI: 10.1364/CLEO_SI.2015.SF1F.2.

[180] J. Faist, F. Capasso, D. L. Sivco, C. Sirtori, A. L. Hutchinson, and A. Y. Cho, "Quantum Cascade Laser," *Science*, vol. 264, no. 5158, p. 553, 1994. DOI: 10.1126/science.264.5158.553.

[181] M. S. Vitiello, G. Scalari, B. Williams, and P. D. Natale, "Quantum cascade lasers: 20 years of challenges," *Opt. Express*, vol. 23, no. 4, p. 5167, 2015. DOI: 10.1364/OE.23.005167.

[182] M. Razeghi, Q. Lu, N. Bandyopadhyay, W. Zhou, D. Heydari, Y. Bai, and S. Slivken, "Quantum cascade lasers: from tool to product," *Opt. Express*, vol. 23, no. 7, p. 8462, 2015. DOI: 10.1364/OE.23.008462.

[183] "Mid-IR Lasers: Power and pulse capability ramp up for mid-IR lasers." (2014), [Online]. Available: https://www.laserfocusworld.com/lasers-sources/article/16550254/mid-ir-lasers-power-and-pulse-capability-ramp-up-for-mid-ir-lasers (visited on 03/22/2024).

[184] A. Mamrashev, N. Nikolaev, V. Antsygin, Y. Andreev, G. Lanskii, and A. Meshalkin, "Optical Properties of KTP Crystals and Their Potential for Terahertz Generation," *Crystals*, vol. 8, no. 8, p. 310, 2018. DOI: 10.3390/cryst8080310.

[185] K. W. Aniolek, T. J. Kulp, B. A. Richman, S. E. Bisson, P. E. Powers, and R. L. Schmitt, "Trace gas detection in the mid-IR with a compact PPLN-based cavity ring-down spectrometer," in *Application of Tunable Diode and Other Infrared Sources for Atmospheric Studies and Industrial Processing Monitoring II*, vol. 3758, SPIE, 1999, p. 62. DOI: 10.1117/12.366469.

[186] D. G. Lancaster, "Efficient Nd:YAG pumped mid-IR laser based on cascaded KTP and ZGP optical parametric oscillators and a ZGP parametric amplifier," *Opt. Commun.*, vol. 282, no. 2, p. 272, 2009. DOI: 10.1016/j.optcom.2008.09.064.

[187] G. W. Baxter, P. Schlup, and I. T. McKinnie, "Efficient, single frequency, high repetition rate, PPLN OPO pumped by a prelase Q-switched diode-pumped Nd:YAG laser," *Appl. Phys. B*, vol. 70, no. 2, p. 301, 2000. DOI: 10.1007/s003400050049.

[188] P. E. Britton, H. L. Offerhaus, D. J. Richardson, P. G. R. Smith, G. W. Ross, and D. C. Hanna, "Parametric oscillator directly pumped by a 1.55-μm erbium-fiber laser," *Opt. Lett.*, vol. 24, no. 14, p. 975, 1999. DOI: 10.1364/OL.24.000975.

[189] J. Liu, P. Tang, Y. Chen, C. Zhao, D. Shen, S. Wen, and D. Fan, "Highly efficient tunable mid-infrared optical parametric oscillator pumped by a wavelength locked, Q-switched Er:YAG laser," *Opt. Express*, vol. 23, no. 16, p. 20812, 2015. DOI: 10.1364/OE.23.020812.

[190] G. Hansson and D. D. Smith, "Mid-infrared-wavelength generation in 2-μm pumped periodically poled lithium niobate," *Appl. Opt.*, vol. 37, no. 24, p. 5743, 1998. DOI: 10.1364/AO.37.005743.

[191] L. Guo *et al.*, "Room temperature watt-level 3.87 μm MgO:PPLN optical parametric oscillator under pumping with a Tm:YAP laser," *Opt. Express*, vol. 28, no. 22, p. 32916, 2020. DOI: 10.1364/OE.409093.

[192] I. Elder, "Thulium fibre laser pumped mid-IR source," in *Laser Technology for Defense and Security V*, vol. 7325, SPIE, 2009, p. 73250I. DOI: 10.1117/12.818553.

[193] C.-P. Qian, B.-Q. Yao, B.-R. Zhao, G.-Y. Liu, X.-M. Duan, T.-Y. Dai, Y.-L. Ju, and Y.-Z. Wang, "High repetition rate 102 W middle infrared $ZnGeP_2$ master oscillator power amplifier system with thermal lens compensation," *Opt. Lett.*, vol. 44, no. 3, p. 715, 2019. DOI: 10.1364/OL.44.000715.

[194] M. A. Medina, M. Piotrowski, M. Schellhorn, F. R. Wagner, A. Berrou, and A. Hildenbrand-Dhollande, "Beam quality and efficiency of ns-pulsed high-power mid-IR ZGP OPOs compared in linear and non-planar ring resonators," *Opt. Express*, vol. 29, no. 14, p. 21727, 2021. DOI: 10.1364/OE.430717.

[195] A. V. Smith and D. J. Armstrong, "Nanosecond optical parametric oscillator with 90° image rotation: design and performance," *J. Opt. Soc. Am. B*, vol. 19, no. 8, p. 1801, 2002. DOI: 10.1364/JOSAB.19.001801.

[196] G. Arisholm, R. Paschotta, and T. Südmeyer, "Limits to the power scalability of high-gain optical parametric amplifiers," *J. Opt. Soc. Am. B*, vol. 21, no. 3, p. 578, 2004. DOI: 10.1364/JOSAB.21.000578.

[197] M. W. Haakestad, H. Fonnum, and E. Lippert, "Mid-infrared source with 0.2 J pulse energy based on nonlinear conversion of Q-switched pulses in $ZnGeP_2$," *Opt. Express*, vol. 22, no. 7, p. 8556, 2014. DOI: 10.1364/OE.22.008556.

[198]   A. Hildenbrand *et al.*, "Laser damage of the nonlinear crystals CdSiP$_2$ and ZnGeP$_2$ studied with nanosecond pulses at 1064 and 2090 nm," *Opt. Eng.*, vol. 53, no. 12, p. 122511, 2014. DOI: 10.1117/1.OE.53.12.122511.

[199]   L. Wang, T. Xing, S. Hu, X. Wu, H. Wu, J. Wang, and H. Jiang, "Mid-infrared ZGP-OPO with a high optical-to-optical conversion efficiency of 75.7 %," *Opt. Express*, vol. 25, no. 4, p. 3373, 2017. DOI: 10.1364/OE.25.003373.

[200]   O. L. Antipov, I. D. Eranov, and R. I. Kositsyn, "10-W mid-IR optical parametric oscillators based on ZnGeP$_2$ elements pumped by a fibre-laser-pumped Ho:YAG Laser. Experimental and numerical study," *Quantum Electron.*, vol. 47, no. 7, p. 601, 2017. DOI: 10.1070/QEL16366.

[201]   G. Arisholm, Ø. Nordseth, and G. Rustad, "Optical parametric master oscillator and power amplifier for efficient conversion of high-energy pulses with high beam quality," *Opt. Express*, vol. 12, no. 18, p. 4189, 2004. DOI: 10.1364/OPEX.12.004189.

[202]   G. Arisholm, E. Lippert, G. Rustad, and K. Stenersen, "Effect of resonator length on a doubly resonant optical parametric oscillator pumped by a multilongitudinal-mode beam," *Opt. Lett.*, vol. 25, no. 22, p. 1654, 2000. DOI: 10.1364/OL.25.001654.

[203]   M. Medina, "Investagation of OPO cavities for high average power generation in the mid-infrared," Ph.D. dissertation, Aix-Marseille Universitè, 2022.

Publications and Conference Contributions

Peer-Reviewed Publications (First Author)

<u>**K. Goth**</u>, M. Griesbeck, M. Eitner, H. Büker, M. Eichhorn, and C. Kieleck, "Alignment-insensitive end-pumped continuous-wave crossed-Porro prism Ho^{3+}:YAG laser," *Optics Letters*, vol. 47, no. 13, p. 3143, 2022. DOI: 10.1364/OL.459892.

<u>**K. Goth**</u>, M. Rupp, M. Griesbeck, M. Eitner, M. Eichhorn, and C. Kieleck, "Limitations of homogeneous and segmented single-crystal compact TEM_{00}-mode Ho^{3+}:YAG laser resonators," *Applied Physics B*, vol. 129, no. 6, p. 95, 2023. DOI: 10.1007/s00340-023-08033-8.

<u>**K. Goth**</u>, M. Eitner, M. Griesbeck, M. Rupp, D. Lorenz, J. Deutsch, M. Eichhorn, and C. Kieleck, "Beam quality improvement in a linear ZPG OPO pumped by a Q-switched compact high-power Ho^{3+}:YAG laser," *Optics Continuum*, vol. 3, no. 2, p. 112, 2024. DOI: 10.1364/OPTCON.505473.

Peer-Reviewed Publications (Co-Author)

M. Griesbeck, H. Büker, M. Eitner, <u>K. Goth</u>, P. Braesicke, M. Eichhorn, and C. Kieleck, "Mid-infrared optical parametric oscillator pumped by a high-pulse-energy, Q-switched Ho^{3+}:YAG laser," *Applied Optics*, vol. 60, no. 22, p. F21, 2021. DOI: 10.1364/AO.424039.

M. Rupp, <u>K. Goth</u>, M. Eichhorn, and C. Kieleck, "High average power Q-switched Ho^{3+}:YAG laser with a single-line emission at 2122 nm," *Optics Letters*, vol. 48, no. 21, p. 5619, 2023. DOI: 10.1364/OL.501824.

Conference Contributions

K. Goth, M. Griesbeck, M. Eitner, H. Büker, M. Eichhorn, and C. Kieleck, "Investigation of the Optical Gain in a Compact Ho^{3+}:YAG MOPA System," in *Optica Laser Congress 2021 (ASSL,LAC)*, Poster, Virtual, Oct. 2021, p. JM3A.6. DOI: 10.1364/ASSL.2021.JM3A.6.

K. Goth, M. Griesbeck, M. Eitner, **M. Eichhorn**, and C. Kieleck, "Comparison of crossed-Porro prism resonator design with conventional mirror resonator design in a Ho^{3+}:YAG laser," in *European Physical Journal Web of Conferences*, vol. 267, Hannover, Germany, Aug. 2022, p. 01019. DOI: 10.1051/epjconf/202226701019.

K. Goth, M. Griesbeck, M. Eitner, M. Eichhorn, and C. Kieleck, "Reduced Alignment Sensitivity and Pulsed Operation of Ho^{3+}:YAG Laser Porro Resonators," in *Optica Advanced Photonics Congress 2022*, Talk, Barcelona, Spain, Dec. 2022, p. ATu3A.3. DOI: 10.1364/ASSL.2022.ATu3A.3.

K. Goth, M. Griesbeck, M. Eitner, M. Eichhorn, and C. Kieleck, "Q-switched Ho^{3+}:YAG Porro resonators with improved alignment stability," in *SPIE Photonics West (Solid State Lasers XXXII: Technology and Devices)*, Talk, vol. 12399, San Francisco, USA, Jan. 2023, p. 1239909. DOI: 10.1117/12.2652592.

K. Goth, M. Griesbeck, M. Rupp, M. Eitner, M. Eichhorn, and C. Kieleck, "Power Limits of Compact Ho^{3+}:YAG Laser Resonators with Homogeneously Doped and Segmented Crystals," in *IEEE 2023 Conference on Lasers and Electro-Optics Europe & European Quantum Electronics Conference (CLEO/Europe-EQEC)*, Talk, Munich, Germany, Jun. 2023, p. 1. DOI: 10.1109/CLEO/Europe-EQEC57999.2023.10231704.

K. Goth, M. Rupp, M. Griesbeck, M. Eitner, M. Eichhorn, and C. Kieleck, "Power scaling of segmented and homogeneously doped Ho^{3+}:YAG laser resonators," in *SPIE Security + Defence (Technologies for Optical Countermeasures XIX)*, Talk, vol. 12738, Amsterdam, Netherlands, Sep. 2023, p. 127380E. DOI: 10.1117/12.2682141.

K. Goth, M. Rupp, M. Griesbeck, M. Eitner, M. Eichhorn, and C. Kieleck, "Investigation of High-Power Ho^{3+}:YAG Lasers With Homogeneous and Segmented Crystals," in *Optica Laser Congress 2023 (ASSL, LAC)*, Talk, Tacoma, USA, Oct. 2023, p. AM6A.7. DOI: 10.1364/ASSL.2023.AM6A.7.

K. Goth, I. Vergara, M. Griesbeck, M. Eitner, M. Rupp, M. Eichhorn, and C. Kieleck, "High-Beam Quality Highly-Efficient High-Average-Power Pulse Amplification in Ho^{3+}:YAG," in *Optica Laser Congress 2023 (ASSL, LAC)*, Poster, Tacoma, USA, Oct. 2023, p. JM4A.23. DOI: 10.1364/ASSL.2023.JM4A.23.

K. Goth, M. Eitner, M. Griesbeck, M. Rupp, J. Deutsch, M. Eichhorn, and C. Kieleck, "14 W linear ZGP OPO pumped by a Q-switched Ho^{3+}:YAG laser with a maximum energy of 2.2 mJ," in *SPIE Photonics West (Nonlinear Frequency Generation and Conversion: Materials and Devices XXIII)*, Talk, vol. 12869, San Francisco, USA, Jan. 2024, p. 1286906. DOI: 10.1117/12.2692202.

Awards

Best Student Paper Award for "Power scaling of segmented and homogeneously doped Ho^{3+}:YAG laser resonators" at *SPIE Security + Defence (Technologies for Optical Countermeasures XIX)*, Amsterdam, Netherlands, Sep. 2023

2023 Optica Laser Congress Student Paper Award for "Investigation of High-Power Ho^{3+}:YAG Lasers With Homogeneous and Segmented Crystals" at *Optica Laser Congress 2023 (ASSL, LAC)*, Tacoma, USA, Oct. 2023

List of Acronyms

AR	anti-reflective
AOM	acousto-optic modulator
CW	continuous wave
DFG	difference frequency generation
DR	doubly-resonant
EOM	electro-optic modulator
FWHM	full width at half maximum
Ho^{3+}:YAG	holmium-doped yttrium aluminum garnet
HR	highly reflective
IC	input coupling
MEMS	micro-electromechanical system
MOPA	master oscillator power amplifier
MWIR	mid-wave infrared
OC	output coupling
OOCE	optical-to-optical conversion efficiency
OPD	optical path difference
OPA	optical parametric amplification
OPG	optical parametric generation
OPO	optical parametric oscillator
OSA	optical spectrum analyzer

PBS	polarizing beam splitter
PEM	photoelectromagnetic
PPLN	periodically poled lithium niobate
RMS	root mean square
SR	singly-resonant
TFP	thin-film polarizer
TIR	total internal reflection
YAG	yttrium aluminum garnet
ZGP	zinc germanium phosphide
ZPS	zero phase shift

Acknowledgements

- My friends, who have been a source of distraction and always had an open ear for me, especially during the difficult phases of the thesis.

- My boyfriend Holger Bangert, who supported and motivated me throughout the entire duration of the PhD thesis.

I deeply appreciate the support I have received from all these people. Without them, it would not have been possible for me to carry out such work.

IRS

INSTITUTE OF CONTROL SYSTEMS

04

This series contains scientific reports on laser technology and optronics performed at or in cooperation with the IRS. The topics range from laser-related materials like crystals and glasses and their elaboration over laser physics and technologies up to laser and optronic applications.

Solid-state lasers based on holmium-doped yttrium aluminum garnet (Ho^{3+}:YAG) are promising laser sources in the 2 µm range. In this work, advanced concepts, which are intended to enable power scaling and an increased mechanical stability, are transferred to Ho^{3+}:YAG lasers. Regarding power scaling, these concepts include a segmented laser crystal designed for reducing the maximal temperature inside the crystal as well as a master oscillator power amplifier system when a preservation of the beam quality is desired. A Porro prism-based resonator geometry is investigated in detail with a focus on the prism quality, suitable resonator designs, and the alignment tolerance. As Q-switched 2 µm solid-state lasers are an ideal pump source for optical parametric oscillators based on zinc germanium phosphide, such an oscillator is designed and optimized.